
Assessing the macroscopicity of quantum mechanical superposition tests via hypothesis falsification

Der Fakultät für Physik der Universität Duisburg-Essen
vorgelegte Dissertation

von

Björn Schrinski

aus

Nettetal

zum Erwerb des

Doktors der Naturwissenschaften (Dr. rer. nat.)

Duisburg, den 27. Juni 2019

Datum der Disputation: 24. September 2019

Erstgutachter: Prof. Dr. Klaus Hornberger, Universität Duisburg-Essen

Zweitgutachter: Prof. Dr. Klemens Hammerer, Universität Hannover

DuEPublico

Duisburg-Essen Publications online

UNIVERSITÄT
DUISBURG
ESSEN

Offen im Denken

ub | universitäts
bibliothek

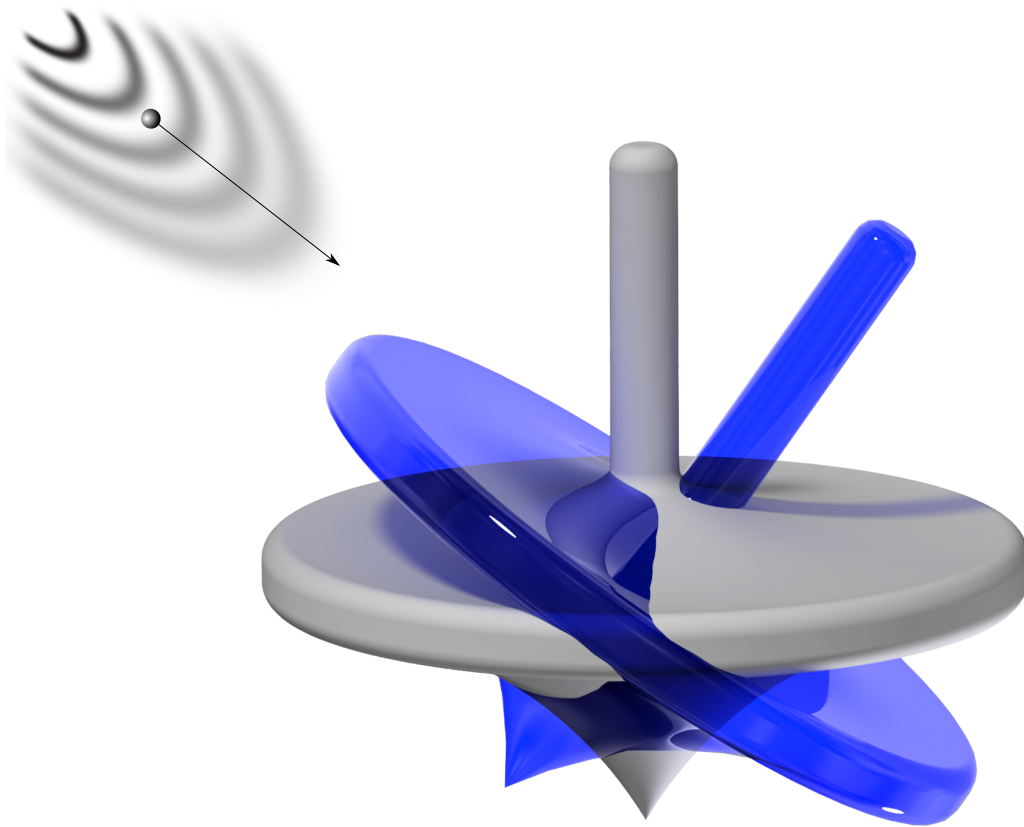
Diese Dissertation wird über DuEPublico, dem Dokumenten- und Publikationsserver der Universität Duisburg-Essen, zur Verfügung gestellt und liegt auch als Print-Version vor.

DOI: 10.17185/duepublico/70585

URN: urn:nbn:de:hbz:464-20191017-114700-9

Alle Rechte vorbehalten.

Assessing the macroscopicity
of quantum mechanical superposition tests
via hypothesis falsification



Björn Schrinski

Abstract

In this thesis I present a universal scheme to assess the macroscopicity of experimentally fabricated quantum superposition states based on the degree to which they probe the boundaries of quantum mechanics. The measure relies on the falsification of the weakest macrorealist modifications of quantum mechanics; it treats all experiments in an equal manner, regardless the actual form and size of the empirical data, using an uninformative approach to Bayesian inference. The versatility of this scheme is illustrated by applying it on state-of-the-art quantum tests where the study of minimal modifications of quantum mechanics often coincides with the examination of conventional decoherence effects. Finally, the environmental impact on orientational degrees of freedom, leading to diffusion, friction, and thermalization, are described analytically. Together with the formulation of minimal modifications of quantum mechanics applied to orientational degrees of freedom this paves the way for a thorough description of experiments with levitated nanorotors and the assessment of the respective macroscopicities.

Zusammenfassung

In dieser Arbeit stelle ich ein universales Verfahren vor, um die Makroskopizität experimentell realisierter Quanten-Superpositionszustände zu bestimmen, beruhend darauf, wie weit sie die Grenzen der Quantenmechanik durch empirische Beobachtung erweitern. Konkret basiert das Maß auf der Falsifizierung minimaler makrorealistischer Modifikationen der Quantenmechanik; es erlaubt durch einen nichtinformativen Ansatz im Rahmen der Bayesschen Statistik, alle denkbaren Experimente mit Datensätzen jeglicher Art und Größe objektiv miteinander zu vergleichen. Die breite Anwendbarkeit dieses Verfahrens wird an modernen Quantentests demonstriert. Deren Beschreibung unter Anwesenheit der oben genannten Modifikationen spielt auch abseits einer zu bestimmenden Makroskopizität eine Rolle, da sie zu Dekohärenzeffekten führen, welche auch durch konventionelle Quellen hervorgerufen sein können. Als Letztes analysiere ich die Zeitentwicklung von Orientierungsfreiheitsgraden starrer Körper sowohl unter diesen dekohärierenden Wechselwirkungen mit der Umgebung, die zu Diffusion, Reibung und Thermalisierung führen, als auch unter minimalen makrorealistischen Modifikationen, was erlaubt, auch für zukünftige Experimente mit levitierten nanometergroßen asymmetrischen Objekten Makroskopizitäten zu bestimmen.

Publications

Publications for which I contributed all calculations:

1. B. Schirnski, B. A. Stickler, and K. Hornberger, *Collapse-induced Orientational Localization of Rigid Rotors*, J. Opt. Soc. Am. B **34**, C1–C7 (2017)
2. B. Schirnski, K. Hornberger, and S. Nimmrichter, *Sensing spontaneous collapse and decoherence with interfering Bose-Einstein condensates*, Quantum Sci. Technol. **2**, 044010 (2017)
3. B. A. Stickler, B. Schirnski, and K. Hornberger, *Rotational friction and diffusion of quantum rotors*, Phys. Rev. Lett. **121**, 040401 (2018)
4. B. Schirnski, S. Nimmrichter, B. A. Stickler, and K. Hornberger, *Macroscopicity of quantum mechanical superposition tests via hypothesis falsification*, Phys. Rev. A **100**, 032111 (2019)

Publications for which I provided minor contributions:

1. B. A. Stickler, B. Papendell, S. Kuhn, B. Schirnski, J. Millen, M. Arndt and K. Hornberger, *Probing Macroscopic Quantum Superpositions with Nanorotors*, New J. Phys. **20**, 122001 (2018)

Contents

1. Introduction	1
2. Hypothesis test for classicalizing modifications of quantum mechanics	5
2.1. Macroscopicity measure via classicalizing modifications	5
2.1.1. Extensive difference and disconnectivity	5
2.1.2. Minimally invasive, macrorealist modifications of quantum me- chanics	7
2.1.3. Implications	9
2.1.4. Original definition of macroscopicity	11
2.2. Bayesian inference and the non-informative approach therein	12
2.2.1. Probability theory	13
2.2.2. Bayesian vs frequentist I: parameter inference	15
2.2.3. Uninformative prior distributions	17
2.2.4. Bayesian vs frequentist II: hypothesis testing	21
2.3. Hypothesis test of modified quantum mechanics	23
2.3.1. Formulation of the hypothesis test	23
2.3.2. Choosing a prior	25
2.3.3. General scheme for assessing macroscopicities	26
2.4. Case study: Molecule interferometry	28
2.4.1. Near-field Talbot-Lau interferometry	28
2.4.2. Kapitza-Dirac-Talbot-Lau Interferometer	31
2.4.3. Long baseline Universal Matter-wave Interferometer	33
2.4.4. Convergence of old and new definition of macroscopicity	36
2.5. Discussion	38
3. Quantum experiments in presence of classicalizing modifications	41
3.1. Interference of BEC in product and dual Fock states	41
3.1.1. Two-mode approximation in the Mach-Zehnder setup	41
3.1.2. Macroscopic wave function	44
3.1.3. BEC interference in second quantization	47
3.2. Ramsey interferometry with a number-squeezed BEC	52
3.2.1. Collective spin states	52
3.2.2. Measurement scheme	54
3.2.3. Classicalizing modifications in the collective spin picture	55
3.2.4. Death of entanglement I	57
3.2.5. Continuum approximation	59
3.2.6. Heating-induced particle loss	62

3.2.7. Assessing the macroscopicity	64
3.3. Leggett-Garg Test with an atomic random walk	65
3.3.1. Quantum random walks	65
3.3.2. Impact of the modification	67
3.3.3. Violating a Leggett-Garg inequality	69
3.3.4. Assessing the macroscopicity	70
3.4. Mechanical entanglement of photonic crystals	71
3.4.1. Measurement protocol	72
3.4.2. Classicalizing modifications in the phonon mode expansion	74
3.4.3. Diffusion regime	76
3.4.4. Experimentally achieved macroscopicity	78
3.4.5. Death of entanglement II	80
3.5. Discussion	81
4. Orientational coherence experiments	83
4.1. Theoretical background	83
4.1.1. Classical theory of rigid rotors	83
4.1.2. Quantum theory of rigid rotors	85
4.1.3. Calculation rules for angular momentum operators	86
4.2. Orientational decoherence, diffusion and thermalization	87
4.2.1. An orientational Caldeira-Leggett dissipator	87
4.2.2. General predictions of the orientational Caldeira-Leggett dissipator	90
4.2.3. Planar rotor	91
4.2.4. Linear rotor	94
4.3. Classicalizing modifications applied on orientational degrees of freedom . .	97
4.3.1. Orientational degrees of freedom under classicalizing modifications	97
4.3.2. Linear- and angular-momentum diffusion	99
4.3.3. Diffusion of planar rotors	103
4.3.4. Application: Orientational state revivals	105
4.4. Discussion	108
5. Conclusion and outlook	111
A. Experimental data from LUMI	113
B. Quantum experiments in presence of classicalizing modifications	117
B.1. BEC Interference	117
B.2. Mechanical entanglement of photonic crystals	118
B.2.1. Characteristic functions and symbols of mechanical oscillator states	118
B.2.2. The geometric factor $U_{<}(\sigma)$	119

C. Orientational coherence experiments	121
C.1. Orientational decoherence, diffusion and thermalization	121
C.1.1. Orientational Fokker-Planck equation of rigidly connected classical particles	121
C.1.2. General predictions and the classical limit of the orientational Caldeira-Leggett dissipator	122
C.1.3. Planar rotor	125
C.1.4. Linear rotor	126
C.2. Diffusion coefficients for cylinders	127
Bibliography	131

1. Introduction

The discovery of quantum mechanics unsettled the community of physicists and, even though its predictions are verified in countless experiments over and over again, the fundamental concepts coming along spark lively debates without cease. There seems to be a hierarchy in oddness between the exotic consequences of quantum mechanics (see Fig. 1.1): While the discrete nature of energy eigenstates, first discovered by Planck [1], or the fundamental uncertainty of incompatible observables, known as Heisenberg's uncertainty principle [2,3], were revolutionary at the time, nowadays they are well accepted and come almost natural. This can not be said about some other feature of quantum mechanics: The linear nature of the Schrödinger equation allows, in principle, for superpositions of matter over all length, time and mass scales, implying even quantum entanglement between particles on those same scales.

There are many approaches to explain the lack of superposition states on the macroscopic scale, such as decoherence theory [4–6], Bohmian mechanics [7,8], or gravitational collapse [9]. But the most drastic solution requires an objective intervention in unitary quantum dynamics that spontaneously destroys macroscopic superpositions [10–13], the most famous being the spontaneous continuous localization model (CSL) [12]. Those modifications of the Schrödinger equation, be they caused by gravitation or spontaneously, set themselves apart from interpretational explanations by the fact that they are empirically testable: Every collapse model is governed by a set of modification parameters and if the predictions do not fit the empirical observation those parameters are falsified.

Irrespectively of whether one sees such modifications of quantum mechanics as viable, there is a plethora of experiments which demonstrate that quantum mechanics is valid for ever higher mass, length, and time scales [19], and which serve to test these collapse models along the way: The matter wave interference of atoms [20–24] can be extended to composite nano-sized objects like molecules [25–28]. Interference by a simple overlap of wave packets or in a Ramsey scheme can be carried out with dilute Bose-condensed atoms coherently split between two spatial modes [29–33] that may even be number squeezed, which implies a significant amount of many-body entanglement [30,31]. Such collective quantum coherence was also observed in solids by interference experiments involving superpositions of counter-propagating superconducting loop currents [34,35] or nanobeam oscillation modes [36]. These kinds of experiments verify the superposition principle and thus serve to falsify the very prognosis collapse models are intended for. A distinct subset of experiments is solely designed to test some side effects of collapse models: While they destroy coherences these modifications unavoidably lead to an energy increase that can be tested [37–45] and as such purely classical observations can lead to the strongest restrictions on CSL [39,42] up to date.

1. Introduction

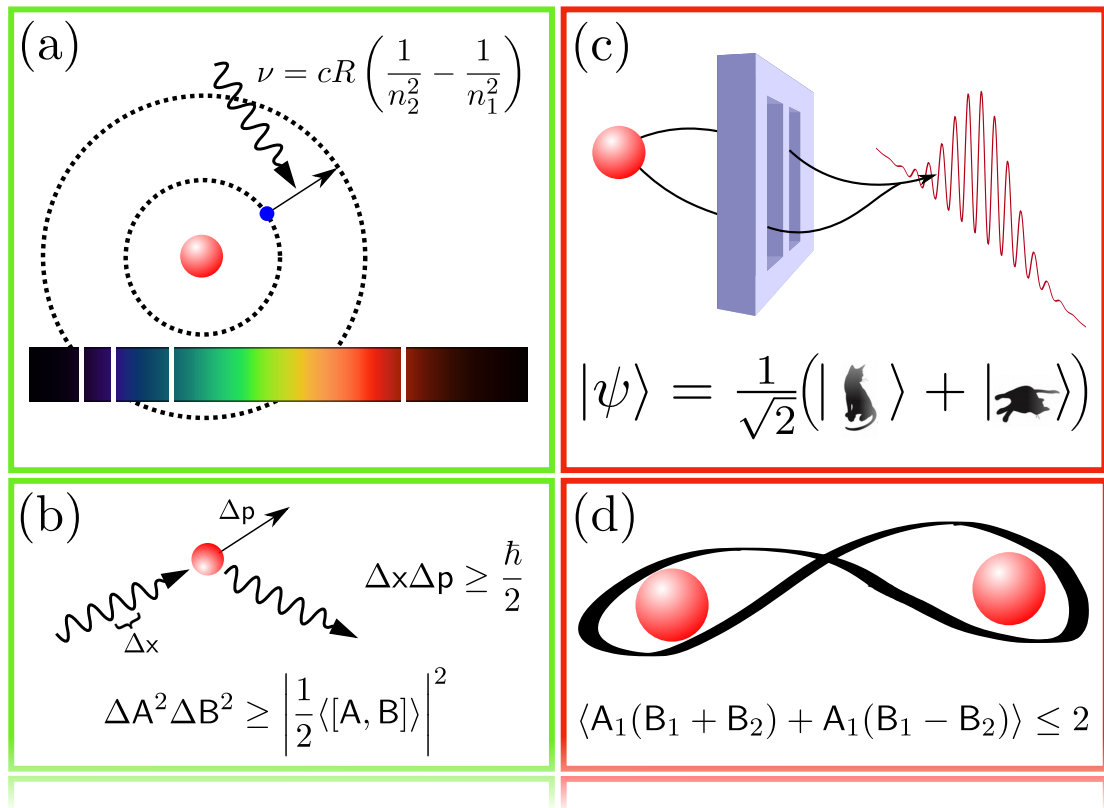


Figure 1.1.: Quantum mechanics leads to a whole range of unintuitive consequences. The most familiar ones are shown in this figure: (a) Quantized energy eigenstates can only be populated if the required energy is provided at once, a continuous energy transfer is not sufficient [14] unless it occurs fast enough to exploit the energy-time uncertainty. If a Hydrogen atom is exposed to a continuous spectrum of light only certain frequencies can be absorbed (Shown is the Balmer series ($n_1 = 2, n_2 > 2$) for absorption in the visible regime). (b) The smaller the wavelength of light the better it can resolve the position of a particle to be measured. But with increasing wave number also the momentum transfer increases and as such knowledge over position and momentum simultaneously is fundamentally bound by Heisenberg's theorem [2]. Regardless of any measurement back action the fundamental uncertainty is true for all non-commuting operators A and B , as first shown by Robertson [3]. (c) Particles can behave like waves and show interference effects, the most simple example being double slit experiments [15]. The statistics of such an experiment are generated by a probability density that does not arise just from missing information but as true fundamental uncertainty of quantum mechanics. Taking the linearity of quantum mechanics to the extreme leads to Schrödinger's famous Gedankenexperiment of living beings to be simultaneously dead and alive until measured [16]. (d) Entanglement of spatially separated quantum systems can lead to correlations that are classically impossible and violate Bell-CHSH inequalities [17, 18]. This entanglement between particles can in principle be maintained over arbitrary distances.

People do not need to be interested in those modifications to wonder how to quantify the degree to which experiments extend the confirmed regime of validity regarding quantum mechanics. Is a molecule with tens of thousands of atoms delocalized over nanometers more macroscopic than millions of atoms in a superposition of phonon modes in a solid body, as demonstrated with entangled micromechanical oscillators in Ref. [36], which in turn only have an amplitude of femtometers? Is a quantum random walk with an atom in a superposition of dozens of trajectories more macroscopic than a simple superposition of an atom on the meter scale? This question is frequently addressed [46–54] and while many approaches tend to focus on the abstract form of the quantum state in Hilbert space, for example under a resource theoretical perspective, one can return to the initial question that the experimentalist wants to answer in the first place: Is quantum mechanics valid on all scales? And if not, what is the alternative? In Ref. [51] such extensions of the von Neumann equation, referred to as minimally invasive, macrorealist modifications of quantum mechanics (MMM), were characterized and used to assess the macroscopicity of quantum tests: The more of these potential modifications are falsified the more macroscopic is the test since it implies the validity of quantum mechanics in a more macroscopic regime.

But the original formulation of the measure was not stated as a complete hypothesis test, an omission that will be remedied in this thesis [55]. This is done by means of a uninformative Bayesian hypothesis test that is directly applicable to all conceivable quantum tests since the only input in the statistical analysis are the likelihoods of experimental observations, unambiguously dictated by the MMM. The wide applicability of such a measure comes at the cost of being tedious to calculate since every (usually already rather complex) quantum state has to be evolved additionally under MMM and the implications must be compared with the empirical evidence. This alone makes for an interesting and demanding research topic [43, 55, 56], not least because many of the results can be applied to conventional decoherence sources, for example collisions with background gas.

Most quantum tests work with center-of-mass delocalization and only recently a new avenue appeared with the increasing control over orientational degrees of freedom in levitated optomechanics [57–62]. There is a prospect to reach the quantum ground state in such kinds of experiments very soon [63, 64] but this is not even necessary if one wants to observe quantum phenomena like state revivals because of the discrete momentum space [65]. For this relatively new field basic theoretical descriptions of orientational diffusion, friction, and thermalization in the quantum regime must be derived [66] as well as the impact of MMM on the orientational degrees of freedom be calculated [43].

This thesis is structured as follows: **Chapter 2** begins with a brief introduction to the original macroscopicity measure of Nimmrichter and Hornberger [51] and its general properties. It follows a short recapitulation of the essence of uninformative Bayesian inference and Bayesian hypothesis testing. Then I will establish a hypothesis test for MMM and show how to deduce a quantitative macroscopicity from it. Its use is demonstrated in a short case study regarding near-field interferometry. This will, among other things, clarify the connection to the original measure from Ref. [51].

In **Chapter 3** I will apply MMM to three conceptually vastly different quantum tests

1. Introduction

serving as a benchmark for the applicability of the robust hypothesis test from the preceding chapter: (i) Mach-Zehnder interferometry with Bose-Einstein condensates (BEC) prepared in all relevant forms of collective spin states with several thousands of atoms, (ii) atomic quantum random walks serving to violate Leggett-Garg inequalities, and (iii) entangled nanobeams verifying the collective superposition of millions of atoms in phonon modes excitations.

Chapter 4 translates the MMM to orientational degrees of freedom. Here, I will start with a short introduction to the complicated nature of the orientational degrees of freedom on a periodic configuration space with non trivial topology. Since the assessment of macroscopicity always relies on the identification of standard environmentally induced decoherence effects I will take a side trip to introduce the analytical treatment of general orientational diffusion, friction, and thermalization in the quantum regime. Finally, I derive the general MMM of the orientation state together with some implications for symmetric and linear rotors, especially for the newly proposed revival experiments of nanorotors [65].

Chapter 5 will conclude this thesis with a short outlook on possible future research on the topic of MMM and orientational degrees of freedom in the quantum regime.

2. Hypothesis test for classicalizing modifications of quantum mechanics

“The theory of inverse probability (Bayesian inference) is founded upon an error, and must be wholly rejected.”

— R. A. Fisher

In the introduction I briefly sketched the idea of how to assess the macroscopicity of quantum superposition experiments by falsifying stochastic extensions to regular quantum mechanics. In the current chapter this will be completed by formulating a proper hypothesis test within a Bayesian approach, highlighting its advantages, and additionally presenting a case study regarding near-field interferometry. I will start with a short introduction of the classicalizing modification defined in [51] that builds the foundation of the macroscopicity measure and is the primary object of research throughout this whole thesis.

2.1. Macroscopicity measure via classicalizing modifications

This section is dedicated to a short motivation and definition of the macroscopicity measure of Nimmrichter and Hornberger [51]. By closely following the notion of macroscopicity brought forward by Leggett [67] I will highlight the uniqueness of the measure from Ref. [51] when compared to measures focused more on the abstract Hilbert space in which the quantum mechanical state exists. As an alternative approach to macroscopicity, I will only briefly recapture the similarly popular measure of Fröwis and Dür [50], for an exhaustive compilation of macroscopicity measures I refer the reader to the review article of the same authors [54].

2.1.1. Extensive difference and disconnectivity

The literature on the quantification of Schrödinger cat sizes is huge [46–54] and (almost) always follows the same train of thought: What does one expect a true Schrödinger cat state to look like (high mass, large delocalization, etc.) and is there any functional dependency that returns a large value for these kind of states contrary to, say, a classically mixed state? An early and highly influential formulation was published by Leggett in Ref. [67], always having the simplest form of a superposition state in mind, $|\psi\rangle = (|\psi_a\rangle + |\psi_b\rangle)/\sqrt{2}$, by introducing the rather qualitative properties of *extensive difference* and *disconnectivity*. The former is the difference in value of an observable of choice that can be attributed to the two states, a simple example would be the spatial distance of the

2. Hypothesis test for classicalizing modifications of quantum mechanics

respective wave modes. The latter shall quantify the ‘degree of entanglement’ involved in $|\psi\rangle$, e.g. a N -particle GHZ state

$$|\psi\rangle_{\text{GHZ}} = \frac{1}{\sqrt{2}}(|\uparrow\rangle^{\otimes N} + |\downarrow\rangle^{\otimes N}), \quad (2.1)$$

where all N particles are maximally entangled has a higher disconnectivity than a product state $|\psi\rangle^{\otimes N}$ of particles in an individual superposition $|\psi\rangle = (|\uparrow\rangle + |\downarrow\rangle)/\sqrt{2}$. This inevitably requires a fleshed out resource theory regarding both entanglement as well as coherence and the connection to macroscopicity was only recently established [52, 53]. A short outline of what is commonly to be expected of a macroscopicity measure will prepare the finding that the measure advocated for in this thesis naturally fulfills these requirements of extensive difference and disconnectivity.

Disconnectivity is by far the more addressed property of a macroscopic quantum state. A popular example for a measure focused on disconnectivity is the quantum Fisher information (QFI), not to be confused with the Fisher information of classical probability theory discussed in Sec. 2.2.3. The idea to use the QFI as a measure of macroscopicity was first proposed by Fröwis and Dür [50]. They define the QFI¹ of an observable \mathbf{A} as

$$\mathcal{F}(\rho, \mathbf{A}) = 2 \sum_{i,j} \frac{(\pi_i - \pi_j)^2}{\pi_i + \pi_j} |\langle i|\mathbf{A}|j\rangle|^2, \quad (2.2)$$

using the spectral decomposition of the state operator ρ ,

$$\rho = \sum_i \pi_i |i\rangle\langle i|. \quad (2.3)$$

Then the definition of macroscopicity is as follows: Given a quantum state ρ the effective size (of a Schrödinger cat state) is defined as

$$N_{\text{eff}}^{\text{F}}(\rho) = \max_{\mathbf{A}} \mathcal{F}(\rho, \mathbf{A}) / (4N), \quad (2.4)$$

where N is the number of particles involved indexed with i and $\mathbf{A} = \sum_i \mathbf{A}^{(i)}$ is a sum of one-particle operators with norm $\|\mathbf{A}^{(i)}\| = 1$.

According to this measure a state is macroscopic if $N_{\text{eff}}^{\text{F}}(\rho) = \mathcal{O}(N^2)$ which is for example the case for a GHZ state (2.1) in a two-level system with $\mathbf{A} = \sum_i \sigma_z^{(i)}$. Here $\sigma_z^{(i)}$ are the Pauli matrix applied to the i th particle state. For a separable state in turn $N_{\text{eff}}^{\text{F}}(\rho_{\text{sep}}) = \mathcal{O}(N)$ and thus the QFI clearly addresses the idea of disconnectivity. On the other hand, extensive difference plays no role at all since it does not matter whether we have an entangled state of electron spins or the collective spin state of massive

¹Note that here the information aspect of the QFI, contrary to the case of the classical Fisher information used in Sec. 2.2.3, is irrelevant. The QFI is motivated as a quantum analogy of the classical case for example giving the Cramér-Rao bound for estimators of parameters θ parametrizing $\rho(\theta)$ [68]. Here the QFI is only considered because it shows the expected scaling properties, in this specific case regarding the entanglement of particles as explained further in the text.

2.1. Macroscopicity measure via classicalizing modifications

BEC as discussed in Sec. 3.2.1. This makes it somewhat unclear how to compare the macroscopicity of different species of quantum tests.

The QFI fulfills all requirements of a measure in accordance with coherence resource theories [52]. Simultaneously, the choice of the decomposition of the Hilbert space is crucial for the effective size returned by Eq. (2.4). It does matter hugely whether a molecule is chosen as a single particle or as an entangled conglomerate of atoms. But unintuitive results are achieved even when concentrating on comparable single particle states alone (which is just chosen for simplicity, the argumentation can be made for every N -particle pure state in every Hilbert space): Take for example a particle in a two-level system, once in a superposition of both states, $|\psi_a\rangle = (|\uparrow\rangle + |\downarrow\rangle)/\sqrt{2}$, and once simply in one of both states, $|\psi_a\rangle = |\uparrow\rangle$. Since both states are pure the Fisher information is simply the variance of the chosen A which in this case can always be expressed as a linear combination of Pauli matrices. But $|\psi_a\rangle$ is just a rotation of $|\psi_b\rangle$ on the Bloch sphere leaving the maximum variance unchanged. Taking both eigenstates $|\uparrow\rangle$ and $|\downarrow\rangle$ as being spatially separated this conflicts with the general perception of macroscopicity. This short example reveals one fundamental problem of coherence resource theory: The outcomes depend entirely on the basis choice and any state takes the form of a superposition in some specific basis.

2.1.2. Minimally invasive, macrorealist modifications of quantum mechanics

The measure of Nimmrichter and Hornberger [51] does not depend on such arbitrary choices of the decomposition of Hilbert space. It solely asks to what extent empirical evidence is compatible with just the slightest modification of quantum mechanics which leads to a classicalized dynamics on the macroscale. The more modifications are falsified the more macroscopic is the given quantum test.

The detailed derivation of minimally invasive, macrorealist modifications of quantum mechanics (MMM) is reported in Ref. [69] and I will only give a short outline of the cornerstones. Let us assume the real physics around us is not governed by the Schrödinger equation but by a nonlinear and stochastic extension thereof which effects Schrödinger-cat states to spontaneously collapse into one of its branches. All observable consequences of this dynamics are captured by the density operator $\rho = \mathbb{E}(|\psi\rangle\langle\psi|)$, where \mathbb{E} denotes the ensemble average over the stochastic trajectories $|\psi\rangle$. Thus we can rather focus on an extension of the von Neumann equation, the equivalent of the Schrödinger equation but for the density operator,

$$\partial_t \rho = \frac{1}{i\hbar} [\mathbf{H}, \rho] + \frac{1}{\tau_e} \mathcal{M}_\sigma \rho. \quad (2.5)$$

This is a Markovian master equation with additional generator \mathcal{M}_σ where I denoted the overall rate and as such the strength of the modification with $1/\tau_e$; all other parameters are summarized in σ . In the following three main requirements (i)–(iii) will be identified that shape the definite form of the MMM. The preservation of complete positivity demands \mathcal{M}_σ to be of Lindblad-type [70] and (i) Galilean invariance (required since both quantum mechanics and classical mechanics are Galilean invariant) restricts

2. Hypothesis test for classicalizing modifications of quantum mechanics

the Lindblad operators to be Weyl operators [71, 72] effecting phase-space kicks. Thus, for one particle the modification reads

$$\mathcal{M}_{\sigma\rho} = \int d^3\mathbf{s}d^3\mathbf{q} g_{\sigma}(\mathbf{s}, \mathbf{q}) \left[\mathbb{W}(\mathbf{s}, \mathbf{q})\rho\mathbb{W}^{\dagger}(\mathbf{s}, \mathbf{q}) - \rho \right], \quad (2.6)$$

with

$$\mathbb{W}(\mathbf{s}, \mathbf{q}) = \frac{m}{m_0} \exp \left[\frac{i}{\hbar} (\mathbf{p} \cdot \mathbf{s} - \mathbf{r} \cdot \mathbf{q}) \right]. \quad (2.7)$$

The Lindblad operator $\mathbb{W}(\mathbf{s}, \mathbf{q})$ leads to position and momentum translations by distance \mathbf{s} and \mathbf{q} , respectively, distributed by an isotropic probability density function $g_{\sigma}(\mathbf{s}, \mathbf{q}) = g_{\sigma}(s, q)$ as a consequence of rotational invariance.

For N particles in second quantization additional requirements are demanded: (ii) The single-particle MMM generator (2.6) shall be obtained by tracing out all $N - 1$ other particles which ensures that no uncorrelated system affects the time evolution due to the modification (innocent bystander criterion). (iii) Further, the center-of-mass degree of freedom of a rigid body must follow the same time evolution as a single particle with rescaled mass in such a way that it does not matter whether the particles are partitioned as one molecule, single atoms, or even nucleons and electrons (composition criterion). Together with the exchange symmetry of indistinguishable particles this leads to the second quantization version of the MMM,

$$\mathcal{M}_{\sigma\rho} = \int d^3\mathbf{s}d^3\mathbf{q} g_{\sigma}(s, q) \left[\mathbb{L}(\mathbf{q}, \mathbf{s})\rho\mathbb{L}^{\dagger}(\mathbf{q}, \mathbf{s}) - \frac{1}{2} \{ \mathbb{L}^{\dagger}(\mathbf{q}, \mathbf{s})\mathbb{L}(\mathbf{q}, \mathbf{s}), \rho \} \right], \quad (2.8)$$

with the Lindblad operator

$$\mathbb{L}(\mathbf{q}, \mathbf{s}) = \sum_{\alpha} \frac{m_{\alpha}}{m_0} \int d^3\mathbf{p} e^{i\mathbf{p} \cdot m_0\mathbf{s}/m_{\alpha}\hbar} \mathbf{c}_{\alpha}^{\dagger}(\mathbf{p}) \mathbf{c}_{\alpha}(\mathbf{p} - \mathbf{q}), \quad (2.9)$$

being summed over all involved particle species α (including spin degeneracy). The $\mathbf{c}_{\alpha}^{\dagger}(\mathbf{p})$ are creation operators in momentum space and m_0 is a reference mass that is set by convention to $m_0 = m_e$. I emphasize that the Lindblad term (2.9) is the indisputable result of the stated natural requirements (i)–(iii) and as such every single modification of standard quantum mechanics obeying the requirements must assume this shape.

Since the generator (2.8) can lead to diffusion in momentum and position with a strength given by the second moments of $g_{\sigma}(s, q)$ this distribution is simply assumed to be Gaussian with widths $\sigma = (\sigma_q, \sigma_s)$. Additionally, to avoid entering the relativistic regime, it was suggested in Ref. [51] to limit the widths by

$$\hbar/\sigma_q \lesssim 10 \text{ fm} \quad \text{and} \quad \sigma_s \lesssim 20 \text{ pm}. \quad (2.10)$$

In the case of large σ_q the associated momentum transfers may lead to a marked energy increase even though the respective inequality in Eq. (2.10) is met. Throughout this thesis this will be simply referred to as modification-induced heating, be it simply the kinetic energy of a free particle or the temperature of a solid body.

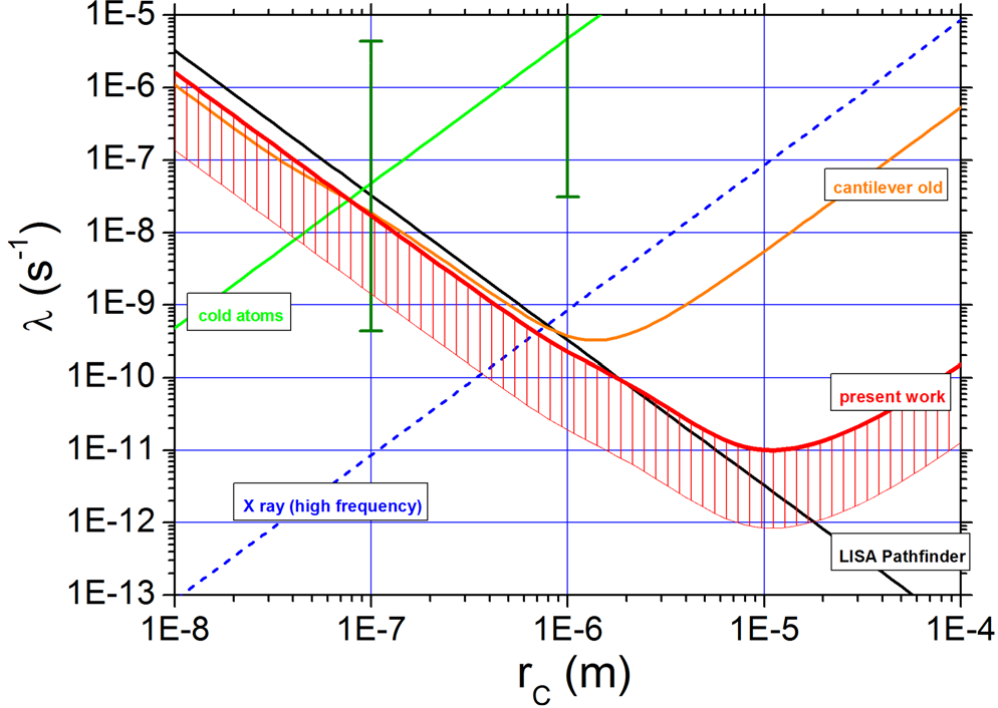


Figure 2.1.: This exclusion plot is taken from Ref. [42]. Together with the there found bounds by examining the heating of ultracold cantilevers (red) upper bounds from x-ray spontaneous emission experiments [74] (blue), cold atoms [75] (green), and center-of-mass diffusion of LISA Pathfinder [39] (black) are plotted. The vertical bars show proposed values inferred from latent image formation [76].

The MMM (2.8) are the inevitable consequence of the natural requirements (i)–(iii). It is only natural that as a result the widely studied collapse model of continuous spontaneous localization (CSL) [73] is a special case. This specific model with the characteristic length scale r_c and rate λ is obtained from the generator (2.8) by simply setting $g_\sigma(s, q) = \delta(s)f_\sigma(q)$, $\lambda = 1/\tau_e$, $r_c = \hbar/\sqrt{2}\sigma_q = 100$ nm, and the reference mass is changed to be the one of a nucleon. CSL is the most studied collapse model, but the majority of the work on exclusion of CSL parameters is done via unobserved heating. The result of different studies is typically combined in exclusion plots like the more recent one shown in Fig. 2.1, for which the specification on a fixed r_c is relaxed.

2.1.3. Implications

As already stated, the MMM lead to position and momentum diffusion. This can be most easily shown in the Heisenberg picture by applying the conjugated generator to the relevant observables. A direct calculation of the temporal change of expectation values, i.e. $\partial_t \langle A \rangle = \langle \mathcal{M}_\sigma^\dagger A \rangle$ if only the action of the MMM generator (2.6) is considered, yields

$$\langle \mathcal{M}_\sigma^\dagger \mathbf{r} \rangle = \langle \mathcal{M}_\sigma^\dagger \mathbf{p} \rangle = 0, \quad \langle \mathcal{M}_\sigma^\dagger \mathbf{r}^2 \rangle = 3\sigma_s^2 \quad \text{and} \quad \langle \mathcal{M}_\sigma^\dagger \mathbf{p}^2 \rangle = 3\sigma_q^2. \quad (2.11)$$

2. Hypothesis test for classicalizing modifications of quantum mechanics

The observation that an experiment clearly rules out the diffusion already suffices to falsify parameter ranges of (τ_e, σ) . In the course of establishing the hypothesis test in Sec. 2.3 I will propose conditioned likelihoods that disregard any information gain resulting from pure heating since we want to assess the quantum nature of an experiment and not some pure classical attribute.

Further, any spatial superposition state will decohere since

$$\frac{1}{\tau_e} \mathcal{M}_\sigma |\mathbf{r}\rangle \langle \mathbf{r}'| = \frac{m^2}{m_e^2 \tau_e} \left[e^{-(\mathbf{r}-\mathbf{r}')^2 \sigma_q^2 / 2\hbar^2} \int d^3 \mathbf{s} \frac{e^{-\mathbf{s}^2 / 2\sigma_s^2}}{\sqrt{2\pi\sigma_s^2}} |\mathbf{r}-\mathbf{s}\rangle \langle \mathbf{r}'-\mathbf{s}| - |\mathbf{r}\rangle \langle \mathbf{r}'| \right], \quad (2.12)$$

is clearly non-zero. The same holds for momentum superpositions, achieved by simply replacing $\mathbf{r} \rightarrow \mathbf{p}$, $\mathbf{s} \rightarrow \mathbf{q}$, and $\sigma_q \leftrightarrow \sigma_s$. The diffusion leading to Eq. (2.11) is identified by observing that entries $|\mathbf{r}\rangle \langle \mathbf{r}'|$ are replaced by neighboring entries $|\mathbf{r}-\mathbf{s}\rangle \langle \mathbf{r}'-\mathbf{s}|$, weighted with the Gaussian $\sim e^{-\mathbf{s}^2 / 2\sigma_s^2}$. This replenishment is suppressed by $e^{-(\mathbf{r}-\mathbf{r}')^2 \sigma_q^2 / 2\hbar^2}$ for coherences and vanishes entirely if $\mathbf{r}-\mathbf{r}' \gg \hbar/\sigma_q$. In this case the coherences decay with the full rate $m^2/m_e^2 \tau_e$ while they are practically unaffected in the opposite limit, $\mathbf{r}-\mathbf{r}' \ll \hbar/\sigma_q$. As such quantum mechanics is preserved for microscopic systems and maximally classicalized in the macroscopic realm, depending on the choice of σ . The scaling with the mass and with the spatial delocalization fulfills the requirement of extensive difference as demanded by Leggett.

The MMM naturally fulfill the scaling properties of other macroscopicity measures like the QFI discussed in the previous section, namely a quadratic scaling of the localization rate with the number of entangled particles, a direct consequence of the composition criterion. Take for example a NOON-state (the second quantization version of the GHZ-state (2.1)) of N bosons in two modes ϕ and χ , $|\text{NOON}\rangle = (|N_\phi, 0_\chi\rangle + |0_\phi, N_\chi\rangle)/\sqrt{2}$, for which one obtains

$$\begin{aligned} \langle N_\phi, 0_\chi | \mathcal{M}_\sigma \rho_{\text{NOON}} | 0_\phi, N_\chi \rangle &= \frac{N}{2} \int d^3 \mathbf{s} d^3 \mathbf{q} g_\sigma(s, q) \left[N \langle \phi | \mathbf{W}(\mathbf{s}, \mathbf{q}) | \phi \rangle \langle \chi | \mathbf{W}^\dagger(\mathbf{s}, \mathbf{q}) | \chi \rangle \right. \\ &\quad \left. - \frac{N-1}{2} (|\langle \phi | \mathbf{W}(\mathbf{s}, \mathbf{q}) | \phi \rangle|^2 + |\langle \chi | \mathbf{W}(\mathbf{s}, \mathbf{q}) | \chi \rangle|^2) - 1 \right], \end{aligned} \quad (2.13)$$

with $|\phi\rangle$ and $|\chi\rangle$ the first quantization states of the respective modes. If those modes are sufficiently well separated, i.e. $\Delta_x \gg \hbar/\sigma_q$ with Δ_x the distance of the modes, the coherences $|0_\phi, N_\chi\rangle \langle N_\phi, 0_\chi|$ decay proportional to N^2 modulo slight heating that can be ignored as long as $w_{\max} \ll \hbar/\sigma_q$, where w_{\max} is the maximum width of the modes. In the opposite limit of strong heating, all the expectation values in Eq. (2.13) are practically zero and all entries in ρ_{NOON} , be it populations or coherences, get depleted with the same rate. This is one example demonstrating how the composition criterion is fulfilled: It does not matter whether molecules are decomposed in atoms or nucleons. Simply imagine the two modes ϕ and χ as describing atoms of mass m composing a molecule localized at one place or the other. Then the term N^2 can be absorbed in the original mass scaling and as long as the MMM cannot excite the internal structure the decoherence will now scale with the whole mass $M = Nm$.

2.1. Macroscopicity measure via classicalizing modifications

Notice, that the entanglement can only enhance the effect of MMM if it is accompanied with a sufficient delocalization of the involved particles. Take as counter-example the maximally entangled state of two distinguishable particles a and b ,

$$|\psi\rangle = \frac{1}{\sqrt{2}}(|\phi_1\rangle_a|\chi_1\rangle_b + |\phi_2\rangle_a|\chi_2\rangle_b). \quad (2.14)$$

Even though the particles a and b may be separated by light years, only the spatial distance between ϕ_1 and ϕ_2 (or χ_1 and χ_2 for that matter) determines the localization rate. This property of the MMM will play a crucial role for the nanobeams in Sec. 3.4 which may in principle be entangled over meters but only involve superpositions on the sub-atomic length scale. As a consequence, entanglement will always be destroyed by the MMM simply because it requires superposition states to begin with, but it will never lead automatically to a quadratic scaling just like that.

We observe that the scaling behavior with entanglement is similar to the one of the QFI (2.2), the prime example of a proper coherence measure [52]. As such a macroscopicity measure using the falsification of MMM also fulfills the disconnectivity criterion formulated by Leggett but always in conjunction with the extensive difference criterion as explained above.

The MMM are not the only sources of decoherence and heating. The latter can also be produced by interaction with an uncontrolled environment [77]. It is crucial that whenever such conventional decoherence cannot be avoided in an experiment it should at least be correctly identified and implemented in the theoretical description of the conventional dynamics. Otherwise, the respective share on the classicalization effect would be fully attributed to the MMM.

2.1.4. Original definition of macroscopicity

Having discussed the basic implications of the MMM we can formulate a provisional hypothesis test as it was intended in Ref. [51]. The preposition that the true physics is indeed described by an extension of the von Neumann equation with the MMM generator (2.8), determined by a certain parameter set τ_e, σ , can, in the simplest way, be falsified as follows: Quantum coherences get destroyed by MMM depending on the choice of the parameters τ_e, σ and an observation of a distinct quantum interference pattern thus falsifies a certain range of this parameter region which is incompatible with the empirical data. The larger this region is the more macroscopic a quantum test can be viewed. To reduce this volume to a single number the authors of Ref. [51] suggested to define macroscopicity as the largest excluded τ_e maximized over σ (as long as σ is in the allowed regime (2.10)) on a decadic logarithmic scale

$$\mu = \max_{\sigma} \log_{10} \left(\frac{\tau_e}{1 \text{ s}} \right). \quad (2.15)$$

Of course the devil is in the detail, specifically in how one has to ascertain the incompatibility of empirical observation and theoretical prediction. The default way is, as always, to simply calculate expectation values, for example to extract visibilities of

2. Hypothesis test for classicalizing modifications of quantum mechanics

interference patterns, and compare it with the experimental data leaving all statistical and error analysis to the experimentalist (if it is carried out at all). One determines for every σ the τ_e that would theoretically lead to the measured visibility or the like and every smaller classicalization time parameter than τ_e is excluded as it would have led to an even stronger decay. Because there are always imperfections in every quantum test there will never be a perfect experimental result and thus a finite largest excluded τ_e exists.

A popular example is a simple formula that can be derived for a wide range of matter-wave interference experiments [51]

$$\mu \simeq \log_{10} \left[\left| \frac{1}{\log(f/f_{\text{theo}})} \right| \left(\frac{m}{m_e} \right)^2 \frac{t_{\text{tot}}}{1 \text{ s}} \right], \quad (2.16)$$

with the mass of the particle m , the total flight time t_{tot} , f the measured visibility, and f_{theo} the theoretically predicted visibility without MMM. This visibility f has to be extracted from the data, in the simplest form with a fit, *with confidence*, taking for example the preferred most conservative confidence interval of the resulting parameter distribution. I allocate the portrayed conservative approach to *frequentist* inference, which is based on the idea that repeated measurements lead to a certain confidence about the possible range of the examined parameters, giving a prognosis what to expect from additional measurements. I will loosely refer to an approach as frequentist inference whenever no prior is involved, which would define it as Bayesian. Direct comparisons between both main branches of statistics are made in Secs. 2.2.2, 2.2.4, and 2.4.4 by means of specific examples.

Needles to say, the resulting macroscopicity can vary even for the same experiment depending on the method of statistical analysis used for attaining confidence. A separate approach may be well justified, but in the extreme case different experiments are not comparable at all just because a specific frequentist analysis technique is only applicable on the one or the other. Moreover, in some experiment it may even be unclear which observable one should look at, e.g. in the quantum random walk in Sec. 3.3. For this reason I formulated a Bayesian non-informative hypothesis test of MMM that gets rid of all those frequentist ambiguities. A frequentist approach may very well be the preferred way to go for a specific example, but fails to objectively compare all conceivable quantum tests.

2.2. Bayesian inference and the non-informative approach therein

In the previous section I introduced the MMM and the general idea how to assess macroscopicity by ruling out regions in the underlying parameter space by means of empirical observations made in a quantum test. Usually the associated observables depend monotonously on the classicalization time parameter τ_e of the MMM, so that all τ_e leading to stronger modifications are falsified. The common procedure is that theorists

calculate suitable expectation values and compare them with the respective data provided from the experimentalist. This way any error analysis is left for the experimentalist to take care of, if one is interested in such things at all². Apart from the fact that this procedure is not the proper way to perform hypothesis tests, it very much relies on the existence of a monotonous observable, e.g. visibilities.

The next section 2.3 is dedicated to opening up a new perspective by formulating a Bayesian hypothesis test, regarding the preposition that MMM of quantum mechanics is the correct description of nature. The falsification of this hypothesis shall be the indicator for high macroscopicity, as formulated in Sec. 2.3. To set the stage I start in this current section with an introduction to probability theory and in particular uninformative Bayesian inference, loosely following Ref. [77, 78].

2.2.1. Probability theory

Before diving into the Bayesian framework I present with a short summary how statistical quantities are defined throughout this thesis. The sample space Ω is the set of all possible outcomes a random experiment can produce. The subsets of Ω will be denoted with upper case letters like A , that are in the simplest case elementary events or, at the opposite extreme, the whole sample space Ω . They form a σ -algebra \mathcal{A} with three properties [77]:

- The sample space Ω and the empty set belong to the system of events, i.e. $\Omega \in \mathcal{A}$ and $\emptyset \in \mathcal{A}$.
- If $A_1 \in \mathcal{A}$ and $A_2 \in \mathcal{A}$ then also the union $A_1 \cup A_2$, the intersection $A_1 \cap A_2$, and the difference $A_1 \setminus A_2$ belong to \mathcal{A} .
- If we have a countable collection of events $A_1, A_2, \dots, A_n, \dots \in \mathcal{A}$, then also their union $\cup_{n=1}^{\infty} A_n$ belongs to \mathcal{A} .

These properties ensure that we can define measures that assign non-negative and real numbers to the subsets of \mathcal{A} , for example probabilities. The sample space Ω can be continuous or discrete, but whenever outcomes of real physical experiments are considered we can assume the sample space to be discrete when necessary to simplify calculations (otherwise drawing limits can become a tedious business). The reason is that the resolution of every real experiment is fundamentally finite. The realizations of events will be denoted with lower case letters like a , and it can be either a single event or a tuple $a = (a_1, a_2, \dots)$ of consecutive experimental runs that are not correlated. On the other hand, when talking about the A s I will from now on always consider them as disjoint elementary subsets.

Random variables can be introduced mapping the events A to real numbers $X : \Omega \rightarrow \mathbb{R}$, like mapping heads and tails to 0 and 1 when tossing a coin. I will use A synonymously for events and random variables since we will never be interested in expectation values

²The reader will have a tough time to ever find exclusion curves in plots like Fig. 2.1 showing error bars.

2. Hypothesis test for classicalizing modifications of quantum mechanics

and the like but only in the probabilities

$$P(A|B, I) \tag{2.17}$$

of events to occur, given B and the so called *background information* I . Throughout this thesis I will always include I in the conditional probabilities since, to quote Ref. [78], *there is no such thing as an unconditional probability*. The background information I includes all the fixed parameters that are not a subject of investigation like the free Hamiltonian, type and number of particles involved and so on. The probability maps the σ -algebra of the sample space to non-negative, real numbers $P : \Omega \rightarrow \mathbb{R}_0^+$ that are normalized with respect to all elementary (and thus disjoint) events,

$$\sum_A P(A|B, I) = 1, \quad \int dA p(A|B, I) = 1, \tag{2.18}$$

or any combination of continuous and discrete regions. B can be an adjustable parameter to control the mapping or is itself an event from another sample space so that Eq. (2.17) is a conditional probability

$$P(A|B, I) = \frac{P(A, B|I)}{P(B|I)}, \tag{2.19}$$

where $P(A, B|I)$ is the probability of both events to occur simultaneously.

Technically, there is no real difference between random variable and parameter, it all depends on what one wants to learn about A and B . In reality the physical parameter a statistician wants to infer has (ideally) a true value and is not distributed over a range of possible realizations. To once again quote Ref. [78], in Bayesian theory the probability *is considered as a degree of belief in the truth of a proposition*, or in other words, the amount of belief whether the physical parameter assumes the value A_1 or A_2 . The reader should note that this perception is independent from the notion of whether true randomness exists or if it is just a result of missing information (many would argue that this true randomness is provided by the indeterminism of quantum mechanics).

The simplest way to obtain a probability (2.17) in a quantum mechanical measurement is by means of a projective measurement,

$$P(A|B, I) = \langle \psi_A | \rho(B, I) | \psi_A \rangle, \tag{2.20}$$

that in the case of a pure state, $\rho(B, I) = |\psi(B, I)\rangle\langle\psi(B, I)|$, reduces to Born's rule

$$P(A|B, I) = |\langle \psi_A | \psi(B, I) \rangle|^2. \tag{2.21}$$

The event A is then simply the notion that the quantum state is $|\psi_A\rangle$. B is the unknown parameter (or set of parameters) we may want to infer while I includes all remaining parameters that are needed to evolve ρ through time (mass, charge, and so on). In the most general case the probabilities can be assessed with help of a positive operator valued measure (POVM), so that

$$P(A|B, I) = \text{tr} [\rho(B, I) F_A], \quad \text{with} \quad \sum_A F_A = \mathbb{1}, \tag{2.22}$$

which ensures together with $\text{tr} \rho(B, I) = 1$ the normalization (2.18).

2.2.2. Bayesian vs frequentist I: parameter inference

The most common task in the field of statistics is parameter inference, i.e. finding the probability $P(a|b, I)$ of a parameter A to assume the value a given realizations b in an experiment. A simple example would be drawing balls from an urn, then A could be the proportion of red balls and b is the result of drawing a certain amount of balls to somehow infer the value a . In the best case the statistical dependency is known, that is we know the conditional probability $P(b|A, I)$ how the realizations b are produced for different A , but if that is not the case we enter the field of nonparametric statistics [79]. I can safely assume always to know the dependency of B on A since there is always a physical model involving the unitary Hamiltonian, to the best of my knowledge of course, and the MMM generator (2.8) that precisely determines $P(B|A, I)$ via the POVM (2.22). From this point onwards I will refer to the parameter that is to be inferred only by its realizations, i.e. lower case letters (here a). There is no real necessity to differentiate between possible events and realizations since a physical parameter can only be realized once taking a specific value (in contrast to experimental observations that can be made over and over again with different outcomes).

There are two main approaches to parameter inference: Bayesian and frequentist. I want to start with the more unambiguous one which is, and this may come as a surprise, the Bayesian inference. Using the most straightforward rule for probabilities, the product rule directly following from the conditional probability (2.19),

$$P(a, b|I) = P(a|b, I)P(b|I) = P(b|a, I)P(a|I), \quad (2.23)$$

one arrives at the key statement of Bayesian inference, Bayes' theorem

$$P(a|b, I) = \frac{P(b|a, I)P(a|I)}{P(b|I)}. \quad (2.24)$$

There is nothing controversial about Bayes' theorem as it directly follows from fundamental rules of probability theory. It states how a *prior* probability $P(a|I)$ is updated by observation of a realization b and the respective *likelihood* $P(b|a, I)$ of a to lead to this certain b . The resulting updated probability $P(a|b, I)$ is called the *posterior* while $P(b|I) = \sum_a P(b|a, I)P(a|I)$ provides the normalization and is of no further importance for the qualitative characteristics of $P(a|b, I)$. The posterior $P(a|b, I)$ includes the new information gained in an experiment and is maybe shifted to a different region of A or is simply refined to allow for an even more educated guess of the true value a . Most of the time the parameter space to be inferred is continuous for which $P(a|b, I)$ and $P(a|I)$ simply have to be replaced by $p(a|b, I)$ and $p(a|I)$, respectively, and $P(b|I) = \int da P(b|a, I)p(a|I)$.

The bone of contention is the interpretation of Bayes' theorem and its usage, especially regarding the involvement of subjective belief that irritates scientists that follow the so-called *frequentist* approach to statistics. Nevertheless, particularly if only scarce data is available there is no way around Bayesian inference if one wants to arrive at any meaningful conclusion. Additionally, in the limit of infinitely many runs, the opposite of scarce data, the posterior becomes independent of the prior under very general

2. Hypothesis test for classicalizing modifications of quantum mechanics

conditions [79–82] and asymptotically assumes a Gaussian distribution around the true parameter a_0 that produced the data, known as Bernstein-von-Mises theorem. This Bayesian consistency requires for example a non-zero prior distribution around a_0 and a finite sample space from which the b are drawn to converge almost surely (which means that for continuous sample spaces only subsets with measure zero may fail the consistency). Still, the sheer possibility to start with any favored prior distribution leads to the impression that the Bayesian approach is arbitrary. That this is not the case when following the uninformative prior approach will be demonstrated in the next subsection but first let us take a look at some frequentist techniques.

Bayesian inference will only make use of Bayes' theorem (2.24) but in the case of frequentist inference there are as many possible approaches as there are frequentist statisticians (which may be a slight exaggeration), prominent examples are parameter estimation theories using the maximum likelihood estimator (MLE) or least squares fits (which is used as an example for comparison in Sec. 2.2.4). As such it does not make much sense to aim for a quantitative comparison between Bayesian and frequentist inference in general (which is not even possible at the current state of research in my opinion). As a recurring theme I will rather demonstrate the failing of common frequentist techniques when we try to use them in a broad application like the macroscopicity measure where we need a robust inference for all conceivable quantum tests.

MLE is maybe the most straightforward parameter estimation. As the name suggests it simply returns the value a that has the largest likelihood to produce the observed data. Technically, this results in the a that maximizes $P(b|a, I)$, or the logarithm of the likelihood which is often used to simplify the calculation but leads to the same result because of the monotonicity of the logarithm. The attentive reader may notice that this is nothing else but Bayesian inference using Eq. (2.24) but with a flat prior and taking the maximum value of the resulting posterior. Some would say that due to the flat prior the subjectivity of Bayesian inference is gone (we will learn in the following section that this is surely not the case) and MLE is a true frequentist procedure. But at this point the true problems only begin when studying the MMM: It is very much possible that an experiment shows quite a good quantum signature coming close to the theoretically expected value (a good example is the near-field interferometer LUMI at the end of this chapter) which leads to $\tau_e \rightarrow \infty$ being the most likely parameter to have produced the data. The MLE will return just this since it does not include any statistical error analysis ignoring the shot-noise of finite data, which makes it unsuitable for the macroscopicity measure.

Such an error analysis is provided by a least squares fit that measures the distance between the likelihood $P(b|a, I)$ and a normalized experimentally observed histogram:

$$\text{Dist}(a) = \sum_B [h(B) - P(B|a, I)]^2, \quad (2.25)$$

where $h(B)$ is the normalized value of the histogram column at the event B . The a resulting in the minimum $\text{Dist}(a)$ is identified as most likely and one can even give confidence intervals for a when assuming that the fluctuations of $h(B)$ are normally

distributed³ [83]. Still when handling the MMM we have a similar problem as in the case of MLE since for $\tau_e \rightarrow \infty$ there are infinitely many classicalization time scales leading to practically the same result. An alternative to circumvent this problem would be (and this is actually the common practice) to fit the resulting form of $P(B|\tau_e, \sigma, I)$ not regarding τ_e but substituting it with simple coefficients: instead of $P(B|\tau_e, \sigma, I) = \sum_k^K c_k(\tau_e) f_k(B, \sigma, I)$ we assume the c_k to be the parameters we infer instead of τ_e , leading to $P(B|c_1, \dots, c_K, \sigma, I) = \sum_k^K c_k f_k(B, \sigma, I)$. Subsequently, the τ_e is determined via identification with the most likely c_k while conservative estimations are taken from the confidence intervals of the c_k . An example is shown in Sec. 2.2.4 with Eq. (2.72). This reduces the functional complexity of the inferred parameter and with it the unfavorable scaling of $\tau_e \rightarrow \infty$. Apart from the fact that this approach is dubious in some sense it is not clear if it fairly handles different experiments with different $P(B|\tau_e, \sigma, I)$.

These were only two simple alternatives to Bayesian inference. Surely there are many more from which some may be perfectly suitable to estimate MMM parameters when applied to certain quantum tests. And as long as one uses consistent estimators all approaches should converge to the same values in the limit of infinitely large data. So why even bother with the question which inference technique one should use? Because I will show that Bayesian inference is effortlessly applicable to all conceivable experiments without the subjectivity that is often attributed to it.

2.2.3. Uninformative prior distributions

The typical field of application for Bayesian inference is either scarce data that relies on educated input from scratch or the combination with previously obtained results to draw a bigger picture. This idea of incorporating external and possibly subjective information is the prominent cause for refusal of the Bayesian approach. But there was and is great effort in the Bayesian community to make the whole procedure as objective as possible. Since the prior distribution is the only source of ambiguity it is also the target of this endeavor and the first realization one arrives at is the fact that there is no universal prior that is objective for all kind of applications.

Naively, one might claim that the flat prior $p(a|I) = \text{const.}$ (that can incidentally lead to non-normalizable posteriors) carries the least amount of information about the parameter. It is easy to see why this is not the case by studying simple scenarios. Take for example a binomially distributed probability

$$P(K|q, I) = \binom{n}{K} q^K (1-q)^{(n-K)}, \quad (2.26)$$

that, depending on the parameter $0 \leq q \leq 1$, produces random variables in the range of integers $0 \leq K \leq n$. The background information I would in this case simply be the maximum value n and one might want to infer the value q of the parameter by performing several runs drawing $k = \{k_1, k_2, \dots\}$.

³In this case and if $P(B|a, I)$ is linear in a the minimum $\text{Dist}(a)$ is assumed for the same a found by the MLE [83].

2. Hypothesis test for classicalizing modifications of quantum mechanics

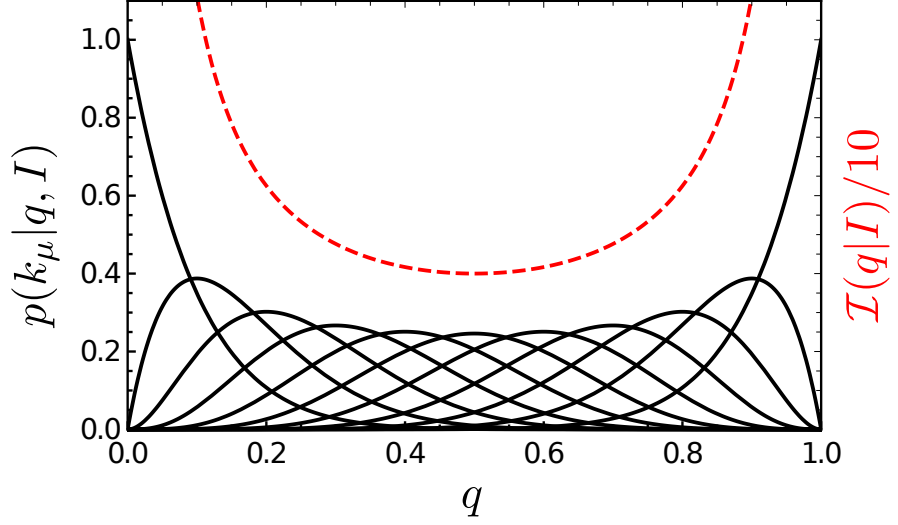


Figure 2.2.: Shown are the likelihoods (2.26) of a Binomial distribution with $n = 10$ as function of the parameter q for different realizations k_μ . The black, solid curves depict $k_\mu = 0, 1, \dots, 10$ from left to right while the red, dashed curve is one tenth of the respective Fisher information (2.28) of the binomial distribution (2.26), being $\mathcal{I}(q|I) = 1/q(1 - q)$. Normalizing the shown likelihoods of q reveals for example a standard deviation of $\Delta q = 0.14$ for $P(5|q, I)$ and a standard deviation of $\Delta q = 0.077$ for $P(0|q, I)$ and $P(10|q, I)$.

Bayesian inference would then update any prior distribution $p(q|I)$ to

$$p(q|k, I) \propto P(k|q, I)p(q|I) = \prod_{\mu} P(k_\mu|q, I)p(q|I). \quad (2.27)$$

Inserting a given k_μ into Eq. (2.26) reveals that the inference of q varies strongly in its quality depending on which random variable is obtained, compare Fig. 2.2. One observes that different k_μ infer different posterior probability distributions for q , but some k_μ lead to more vague conclusions (observations at $k_\mu \simeq n/2$) while other yield a more peaked distribution (observations at the margins, e.g. $k_\mu = 0$). In the case of Eq. (2.26) realizations at the margins of the possible range of k are only assumed if q itself is very close to the boundaries of its distribution while other values are likely to occur for broad ranges of q .

This idea of more or less informative events is quantified by the Fisher information [78]

$$\mathcal{I}(a|I) = \langle (\partial_a \log[p(B|a, I)])^2 \rangle_B = \sum_B p(B|a, I) (\partial_a \log[p(B|a, I)])^2. \quad (2.28)$$

The Fisher information plays an important role in Bayesian consistency since from the Bernstein-von-Mises theorem follows that the posterior for $\ell \rightarrow \infty$ many observations approaches a Gaussian distribution [80]

$$p(a|b, I) \simeq \sqrt{\frac{\ell \mathcal{I}(a_0|I)}{2\pi}} \exp \left[-\ell \mathcal{I}(a_0|I) \frac{(a - a_0)^2}{2} \right], \quad (2.29)$$

2.2. Bayesian inference and the non-informative approach therein

centered around the true a_0 with a width given by the Fisher information at this value. A similar statement can be made about frequentist parameter estimation: For unbiased estimators, meaning they likewise approach the true value a_0 for an experimental sample of size $\ell \rightarrow \infty$, the minimum variance is also given by the Fisher information [78],

$$\Delta^2 \hat{a} \geq \frac{1}{\ell \mathcal{I}(a|I)}, \quad (2.30)$$

known as Cramer-Rao bound. It states that the estimation \hat{a} of the parameter a scatters at least with variance (2.30) around the true value a_0 .

From the definition of the Fisher information (2.28) one can directly infer that likelihoods with sharp peaks at regions where $p(B|a, I)$ has high mass carry a large amount of Fisher information about this parameter region. The Fisher information is plotted for the binomial distribution (2.26), where $a = q$ and $B = K$, as red, dashed curve in Fig. 2.2. This indicates that indeed the sample space K carries more information about the margins of the parameter space q . Now, interpreting the flat prior as the posterior of a previous experiment it thus carries some amount of information simply by giving all q the same probability in contrast to their differing likelihood.

Thus, the goal is to find for every experimental trial the proper, *non-informative* prior that carries the least amount of inference if understood as a result of previous experiments. We can expect the prior to depend on the individual likelihood describing the measurement. For example, if we reparametrize $q = \cos^2(\theta)$ (leading to a simple form of the likelihoods found for Mach-Zehnder interferometry with BEC in Sec. 3.1 and Sec. 3.2) the resulting Fisher information turns uniform on θ , strongly deviating from the Fisher information plotted in Fig. 2.2. Thus, there must not be a universal prior, let alone a flat prior, that can claim to be non-informative in all random experiments. The specific, non-informative prior on the other hand should ideally fulfill two conditions: (i) It should not depend on the parametrization, e.g. in the case of a binomial distribution (2.26) on choosing q or $\cos^2 \theta$ as relevant parameter, (ii) it should consider the deviating amount in information gain due to different observations, i.e. the degree of refinement when updating from prior to posterior on the actual observable that was measured. These two issues are addressed by *Jeffreys' prior* and the *reference prior*.

Jeffreys' prior addresses the problem of informative priors by using the Fisher information itself. By defining the prior simply as [84]

$$p(a|I) \propto \sqrt{\mathcal{I}(a|I)} \quad (2.31)$$

it incorporates the amount of information carried by the observables b directly into the prior distribution. The square root additionally serves to ensure invariance under reparametrization of a , since

$$\begin{aligned} p(a|I) = p(a'|I) \left| \frac{\partial a'}{\partial a} \right| &\propto \sqrt{\mathcal{I}(a'|I)} \left| \frac{\partial a'}{\partial a} \right|^2 = \sqrt{\left\langle \left(\frac{\partial}{\partial a'} \log[P(B|a', I)] \right)^2 \left| \frac{\partial a'}{\partial a} \right|^2 \right\rangle_B} \\ &= \sqrt{\left\langle \left(\frac{\partial}{\partial a} \log[P(B|a, I)] \right)^2 \right\rangle_B} = \sqrt{\mathcal{I}(a|I)}. \end{aligned} \quad (2.32)$$

2. Hypothesis test for classicalizing modifications of quantum mechanics

As such Jeffreys' prior addresses issue (i) since every physical problem leads to the same prior distribution regardless how the likelihoods are parametrized.

The reference prior formalizes the notion of information gain (ii). Not every event leads to the same amount of refinement from the prior to the posterior. This can be quantified with help of the Kullback-Leibler divergence [85] (in a physical context better known as relative entropy),

$$K(p||q) = \int da p(a|I) \log \left[\frac{p(a|I)}{q(a|I)} \right] \geq 0, \quad (2.33)$$

that measures how one probability density $p(a|I)$ differs from another one $q(a|I)$. It is always positive⁴ but not symmetric under exchange of the probability distributions. If this divergence between a prior and a posterior is high one could conclude a large information gain from the data. From this, it is natural to demand a maximalization of the Kullback-Leibler divergence from prior to posterior, averaged over the whole sample space Ω of B weighted by $P(B|I) = \int da P(B|a, I)p(a|I)$:

$$K_{\text{av}}[p(a|I)] = \sum_B P(B|I) \int da p(a|B, I) \log \left[\frac{p(a|B, I)}{p(a|I)} \right]. \quad (2.34)$$

Since $P(B|a, I)$ is known and $p(a|B, I) = P(B|a, I)p(a|I)/P(B|I)$ an unambiguous maximalization with respect to $p(a|I)$ is possible, but this problem is in general not analytically tractable.

Fortunately, it can be shown [86, 87] in the asymptotic limit, where we have $k \rightarrow \infty$ experimental repetitions with $b \rightarrow \mathbf{b} = (b_1, b_2, \dots, b_k)$, that Jeffreys' prior (2.31) maximizes Eq. (2.34) in the one dimensional case. This leads to

$$\begin{aligned} K_{\text{av}}[p(a|I)] &= \sum_{\mathbf{b}} P(\mathbf{b}|I) \int da p(a|\mathbf{b}, I) \log \left[\frac{p(a|\mathbf{b}, I)}{p(a|I)} \right] \\ &= \int da p(a|I) \log \left\{ \frac{\exp \left[\sum_{\mathbf{b}} P(\mathbf{b}|I) \int da p(a|\mathbf{b}, I) \log p(a|\mathbf{b}, I) \right]}{p(a|I)} \right\}, \end{aligned} \quad (2.35)$$

that is maximized for

$$p(a|I) \sim \exp \left[\sum_{\mathbf{b}} P(\mathbf{b}|I) \underbrace{\int da p(a|\mathbf{b}, I) \log p(a|\mathbf{b}, I)}_{=-H[p(a|\mathbf{b}, I)]} \right], \quad (2.36)$$

where $H[\cdot]$ is the information entropy of a probability distribution.

Assuming the posterior distribution $p(a|\mathbf{b}, I)$ in the first term to be the result of $k \rightarrow \infty$ inference steps the asymptotic limit is according to the Bernstein-von-Mises theorem as already stated before a (arbitrarily narrow) Gaussian (2.29),

$$p(a|\mathbf{b}, I) \simeq \sqrt{\frac{k\mathcal{I}[a_0(\mathbf{b})|I]}{2\pi}} \exp \left[-k\mathcal{I}[a_0(\mathbf{b})|I] \frac{(a - a_0(\mathbf{b}))^2}{2} \right], \quad (2.37)$$

⁴This can easily be verified by noting $\log(x) \leq x - 1$ to arrive at $K(p||q) \geq - \int da p(a|I)[q(a|I)/p(a|I) - 1] = 0$.

2.2. Bayesian inference and the non-informative approach therein

depending on the Fisher information of a_0 which is the true value that produced the data \mathbf{b} . The entropy of a Gaussian with width w is $\log(2\pi ew^2)/2$ and as such

$$H[p(a|\mathbf{b}, I)] \simeq \frac{1}{2} \log(2\pi e/k) - \frac{1}{2} \log \mathcal{I}[a_0(\mathbf{b})|I], \quad (2.38)$$

where we can ignore the first, parameter-independent term in the maximalization process. Since $P(\mathbf{b}|a)$ will for large k be concentrated around the generating a we have

$$\sum_{\mathbf{b}} P(\mathbf{b}|a, I) \log \sqrt{\mathcal{I}[a_0(\mathbf{b})|I]} \simeq \log \sqrt{\mathcal{I}[a|I]}, \quad (2.39)$$

so that Jeffreys' prior indeed maximizes Eq. (2.35).

The identity of Jeffreys' prior and the reference prior is true if, and only if, there are no so-called nuisance parameters [86]. Nuisance parameters are additional dimensions in the parameter space a that are of no particular interest and therefore marginalized at the end of the inference. Take for example the MMM parameter space (τ_e, σ) where we could perform Bayesian inference for the whole three-dimensional parameter space and subsequently integrate over σ since the macroscopicity is defined primarily by falsification of classicalization time parameter τ_e . Not only does this approach disagree with the original definition of the largest excluded τ_e maximized over σ it would also force us to make a choice between maximalization of the Kullback-Leibler divergence between prior and posterior on the one side, and invariance under reparametrization on the other side.

2.2.4. Bayesian vs frequentist II: hypothesis testing

The hypothesis test in the Bayesian way can be obtained by following Bayes' theorem (2.24). Even though hypotheses H_μ with $\mu = 1, 2, \dots$ are no random objects, we can quantify the amount of belief that H_1 is more plausible than H_2 . This leads to

$$P(H_\mu|d, I) = \frac{P(d|H_\mu, I)P(H_\mu|I)}{p(d|I)}, \quad (2.40)$$

where d is the data set observed in an experiment. To assess whether H_1 or H_2 is more plausible given the data d obtained in an experiment, one can simply calculate the odds ratio

$$o := \frac{P(H_1|d, I)}{P(H_2|d, I)} = \frac{P(d|H_1, I)}{P(d|H_2, I)} \underbrace{\frac{P(H_1|I)}{P(H_2|I)}}_{o_{\text{P}}}, \quad (2.41)$$

where o_{P} denotes prior odds whether one favors one or the other hypothesis prior to the incorporation of d . If the odds ratio o falls below some suitable threshold value one can favor H_2 over H_1 with the respective amount of belief. Eq. (2.41) is the starting point for every Bayesian hypothesis test and from here onwards one has to examine special cases.

Before that, I would like to discuss the obvious question that might be in the reader's mind: Why not simply use a frequentist hypothesis test for the hypothesis of MMM being

2. Hypothesis test for classicalizing modifications of quantum mechanics

true for certain parameter sets (τ_e, σ) ? The short answer is that, contrary to the Bayesian way, a frequentist hypothesis test is entirely unpractical in its overall implementation. This is due to the key feature of frequentist hypothesis testing a la Fisher [78]: One can only falsify hypotheses, in particular, it is not possible to compare the plausibility of two different hypotheses in a frequentist setting like in Eq. (2.41). Therefore, one defines a null hypothesis H_0 for the sole purpose to falsify it. Falsification is achieved provided

$$P(d|H_0, I) < \alpha, \quad (2.42)$$

where α is the significance level that is typically rather low, e.g. 5%, so that falsification due to pure chance is avoided. This is close to the idea of the MLE identifying the probability of the hypothesis directly with the likelihood of it to produce the data d . Since the idea of the macroscopicity measure [51] is to falsify the MMM it seems quite natural to simply define the existence of a set of parameters (τ_e, σ) as null hypothesis H_0 and show that its probability falls below some chosen α .

However, the problems with this approach manifest when real applications are studied. Then the probability $P(d|H_0, I) = \prod_k^K P(d_k|H_0, I)$ associated with accumulating more and more independent data decreases arbitrarily just alone from the fact that in every non-trivial case $P(d_k|H_0, I) < 1$. There is for any non-trivial case a size K^* beyond which for *any* observation $d(K^*)$ we obtain $P(d(K^*)|H_0, I) < \alpha$. To get around this problem Fisher brought forward the concept of a *test of significance* [88], that simply cumulates all the probabilities for events that are at least as extreme, i.e. even more unlikely, as the observed d , so that we have to replace Eq. (2.42) by

$$\tilde{P}(d, H_0, I) = \sum_{P(D|H_0, I) \leq P(d|H_0, I)}^{\infty} P(D|H_0, I) < \alpha. \quad (2.43)$$

This quantity is easy to evaluate for, say, a simple Bernoulli processes like tossing a single coin. If the null hypothesis H_0 is assuming a fair coin and one obtains 600 heads shown in 1000 trials then $P(600|H_0, N = 1000, I) < 5\%$, as for any other number of heads for this many trials, but also $1 - \sum_{n=401}^{599} P(n|H_0, N = 1000, I) < 5\%$. In other words, the probability of all events even more unlikely than showing 600 times heads *combined* is still below the significance level α . For tossing coins, the case is clear since the probability of landing more than 600 times on the same side of the coin becomes monotonously smaller when considering a fair coin.

To see that already a slightly more complicated problem renders a frequentist hypothesis test impractical I next consider the quantum random walk discussed in Sec. 3.3. Without going into much detail one expects two different probability distributions whether or not the walk is quantum or classical and the MMM continuously mediate from one to the other. In the four-step walk there are five possible sites for every atom to arrive at. If 627 runs are performed, as in the experiment described below, there are

$$\binom{627+4}{627} = 6\,542\,880\,015 \quad (2.44)$$

2.3. Hypothesis test of modified quantum mechanics

possible ways to distribute the 627 outcomes to five bins and thus there are the same amount of elementary events D . According to the concept of the test of significance for every outcome one would have to calculate whether it is more unlikely than the actually measured one d , $P(D|H_0, I) < P(d|H_0, I)$. Moreover, even if one somehow manages to sort all events the resulting hierarchy of probabilities is certainly not consistent for all MMM parameters (τ_e, σ) and has to be assessed over and over again. In contrast, for the Bayesian hypothesis test only $P(d|H_1, I)$ and $P(d|H_2, I)$ have to be calculated once for every MMM parameter set.

2.3. Hypothesis test of modified quantum mechanics

Having argued that non-informative Bayesian hypothesis testing is a viable way to compare hypotheses regarding the parameters of a probability distribution in an objective manner I must cast it into a general scheme that can be applied to assess macroscopicities of quantum superposition tests. This description of a macroscopicity measure driven by hypothesis falsification was published in Ref. [55].

2.3.1. Formulation of the hypothesis test

The hypothesis to be falsified is the notion that our physical world as probed in laboratory experiments on all scales is described by the von Neumann equation for the density operator augmented by a MMM generator (2.8). The modification shall have a certain strength to make predictions with meaningful deviations from standard quantum mechanics. This directly translates to a classicalization time parameter τ_e being smaller than some certain τ_e^* since smaller time parameter produce a stronger classicalization dynamics. The precise hypothesis I chose spells:

$H_{\tau_e^}$: Given a classicalizing modification (2.8) with parameters σ , the dynamics of the system state ρ_t are determined by Eq. (2.5) with a modification time scale $\tau_e \leq \tau_e^*$.*

An experiment showing quantum signatures is unlikely to happen for strong modifications. With this spelled out hypothesis one is able to calculate the exact likelihood of any MMM to produce the data d observed and in turn, via Bayesian inference, to calculate the probability of the hypothesis to be true.

The goal of a quantum experiment can now be viewed as confirming that the hypothesis $H_{\tau_e^*}$ is false. At this point an extensive discussion could be started to justify the *proper* way to test hypotheses for any given experiment but to ensure comparability we want to stipulate one scheme for all quantum tests. In the previous section I made a case for the versatility of Bayesian hypothesis testing as it is directly applicable in contrast to a frequentist approach. This makes it most suitable to be used in the wider framework of a macroscopicity measure that shall be used to assess all conceivable quantum experiments.

For the Bayesian hypothesis test one calculates the *odds ratio* between two hypotheses one wants to compare. In our case we want to know if $H_{\tau_e^*}$ or its complement $\bar{H}_{\tau_e^*}$ is

2. Hypothesis test for classicalizing modifications of quantum mechanics

more plausible,

$$o(\tau_e^*|d, \sigma, I) = \frac{P(H_{\tau_e^*}|d, \sigma, I)}{P(\overline{H}_{\tau_e^*}|d, \sigma, I)}, \quad (2.45)$$

given an observed set of data d . If this odds ratio falls below some acceptable value o_m we can favor $\overline{H}_{\tau_e^*}$ over $H_{\tau_e^*}$ and reject the hypothesis with the respective amount of believe. The odds ratio (2.45) can be reshaped with the help of Bayes' theorem as

$$o(\tau_e^*|d, \sigma, I) = \frac{P(d|H_{\tau_e^*}, \sigma, I) P(H_{\tau_e^*}, \sigma, I)}{P(d|\overline{H}_{\tau_e^*}, \sigma, I) P(\overline{H}_{\tau_e^*}, \sigma, I)}. \quad (2.46)$$

The second quotient is the *prior odds* and can be used to implement some prior favoritism of one hypothesis over the other, for example due to findings in previous experiments. This is unwanted at this point as the macroscopicity of an experiment should be independent from previous experiments. To avoid favoring $H_{\tau_e^*}$ over its complement the quotient is set to unity.

At this point we have to express the prepositions of $H_{\tau_e^*}$ and $\overline{H}_{\tau_e^*}$ by using the marginalization rule

$$P(d|H, \sigma, I) = \int d\tau_e P(d|H, \sigma, I, \tau_e)p(\tau_e|H, \sigma, I), \quad (2.47)$$

on τ_e :

$$\begin{aligned} o(\tau_e^*|d, \sigma, I) &= \frac{\int_0^\infty d\tau_e P(d|H_{\tau_e^*}, \sigma, I, \tau_e)p(\tau_e|H_{\tau_e^*}, \sigma, I)}{\int_0^\infty d\tau_e P(d|\overline{H}_{\tau_e^*}, \sigma, I, \tau_e)p(\tau_e|\overline{H}_{\tau_e^*}, \sigma, I)} \\ &= \frac{\int_0^{\tau_e^*} d\tau_e P(d|\sigma, I, \tau_e)p(\tau_e|\sigma, I)}{\int_{\tau_e^*}^\infty d\tau_e P(d|\sigma, I, \tau_e)p(\tau_e|\sigma, I)}. \end{aligned} \quad (2.48)$$

Here I utilized that $p(\tau_e|H_{\tau_e^*}, \sigma, I) = p(\tau_e|H_{\tau_e^*})p(\tau_e|\sigma, I)$ factorizes, because the uninformative prior distribution of τ_e should not depend on the hypothesis chosen, and that the likelihood $P(d|H_{\tau_e^*}, \sigma, I, \tau_e)$ does not explicitly depend on $H_{\tau_e^*}$.

All one has to do now is to calculate the posterior distribution

$$p(\tau_e|d, \sigma, I) \propto P(d|\tau_e, \sigma, I)p(\tau_e|\sigma, I). \quad (2.49)$$

It consists of two ingredients: (i) The first factor is the likelihood of the parameters (τ_e, σ, I) to produce the data set d measured in the experiment,

$$P(d|\tau_e, \sigma, I) = \prod_k^N P(d_k|\tau_e, \sigma, I). \quad (2.50)$$

The data $d = \{d_1, d_2, \dots, d_N\}$ is typically gathered in N independent runs, where d_k denotes a set of (possibly correlated) measurement outcomes with every experimental run further refining the posterior probability density. The likelihood $P(d|\tau_e, \sigma, I)$ is unambiguously defined by the MMM (2.8) applied to the quantum dynamics of the system

2.3. Hypothesis test of modified quantum mechanics

and can be calculated in principle, even though it may be hard. (ii) On the other hand, the prior distribution $p(\tau_e|\sigma, I)$ involves a certain degree of subjectivity. It is the key feature of Bayesian inference to include prior beliefs into the process; especially in the case of sparse data this helps to acquire meaningful results [78]. However, typical physics experiments with hundreds or thousands of experimental runs result in the opposite of scarce data and in the asymptotic limit of infinitely many data points the posterior turns independent of the prior distribution under very general conditions [80]. Still it is preferable to get rid of any ambiguity produced by the prior and this matter is addressed in the next subsection.

2.3.2. Choosing a prior

The choice of the prior distribution $p(\tau_e|\sigma, I)$ is driven by the aim to evaluate all experiments equally and fairly with one another. As discussed in Sec. 2.2.3 there exists no universally non-informative prior, like for example the flat prior, that could be applied to every likelihood when calculating the posterior (2.49). The most reasonable choice would then be to use the reference prior. This prior maximizes the information gain in the update from prior to posterior by maximizing the Kullback-Leibler-divergence and the reverse conclusion would be that this prior carries the least amount of information as possible for every experiment individually. In the present case of a single relevant parameter the reference prior even coincides with Jeffreys' prior (2.31) rendering it invariant under re-parametrization of the MMM. Hence, it is irrelevant whether one uses the timescale τ_e or rate $\lambda = 1/\tau_e$ (as in the model on Continuous Spontaneous Localization) or any other power of τ_e as the fundamental parameter of the MMM. I therefore argue that Jeffreys' prior

$$p(\tau_e|\sigma, I) = \sqrt{\left\langle \left(\frac{\partial}{\partial \tau_e} \log[P(D|\tau_e, \sigma, I)] \right)^2 \right\rangle_D}. \quad (2.51)$$

is the natural choice to be used in the hypothesis test.

Even though all case studies in Sec. 2.4 and Sec. 3 demonstrate that Jeffreys' prior can be straightforwardly implemented for a vast variety of different experiments, we have to make sure that Jeffreys' prior is applicable to *any* conceivable quantum experiment. In particular any inferred posterior distribution (2.49) must always be positive and normalizable.

The likelihood is per construction bound to fulfill $0 \leq P(D|\tau_e, \sigma, I) \leq 1$ (since we can always assume the sample space D to be discrete) and $\sum_D P(D|\tau_e, \sigma, I) = 1$, thus there is always a D_c for which $\lim_{\tau_e \rightarrow \infty} P(D_c|\tau_e, \sigma, I) = \text{const}$. This requires the prior to decay as $\tau_e^{-1-\epsilon}$, with $\epsilon > 0$ to ensure that the posterior (2.49) is integrable. In the limit $\tau_e \rightarrow \infty$ the modification becomes arbitrarily weak and the general solution of the master equation (2.5) can be expanded into a Dyson series up to the first relevant order. The likelihood then reads as

$$P(D|\tau_e, \sigma, I) = P_\infty(D|I) + \frac{1}{\tau_e} q(D|\sigma, I) + \mathcal{O}(1/\tau_e^2). \quad (2.52)$$

2. Hypothesis test for classicalizing modifications of quantum mechanics

Inserting this series into the definition of Jeffreys' prior (2.51) yields

$$p(\tau_e|\sigma, I) \stackrel{\tau_e \rightarrow \infty}{\sim} \begin{cases} \tau_e^{-3/2} & \exists D_0 : P_\infty(D_0|I) = 0, \\ \tau_e^{-2} & \text{else.} \end{cases} \quad (2.53)$$

Together with a constant likelihood this is sufficient for the posterior to decay fast enough in the limit $\tau_e \rightarrow \infty$ and thus be integrable.

In the opposite limit, $\tau_e \rightarrow 0$, the posterior is allowed to diverge as $\tau_e^{-(1-\epsilon)}$ with $\epsilon > 0$ to ensure integrability. I use that the likelihood $P(D|\tau_e, \sigma, I)$ continuously approaches some limiting classical probability,

$$P(D|\tau_e, \sigma, I) \simeq P_0(D|\sigma, I) + \tau_e^\alpha \tilde{q}(D|\sigma, I) \quad \text{for } \tau_e \rightarrow 0, \quad (2.54)$$

where $\alpha > 0$ may depend on D . Inserting this into the definition of Jeffreys' prior (2.51) yields

$$p(\tau_e|\sigma, I) \stackrel{\tau_e \rightarrow 0}{\sim} \begin{cases} \tau_e^{-(1-\alpha_{\min}/2)} & \exists D_0 : P_0(D_0|I) = 0, \\ \tau_e^{-(1-\alpha_{\min})} & \text{else.} \end{cases} \quad (2.55)$$

Here, $\alpha_{\min} > 0$ is the minimal α obtained over the range of all possible D . This is an integrable divergence so that the lower boundary of τ_e does not impair the integrability of the posterior. To rule out any divergences of the prior in the interior of the interval $[0, \infty)$ we exploit the non-negativity of the likelihood $P(D|\tau_e, \sigma, I)$. It may vanish, and thus potentially lead to a diverging quotient obtained in Eq. (2.51) after differentiating the logarithm, but because it must be a local minimum its first derivative must be zero as well and its second derivative must be non-negative. L'Hospital's rule then states that the posterior stays finite for all values $\tau_e \in (0, \infty)$.

In the upcoming scenarios it is typical for an experiment to consist of several measurement protocols (for example different waiting times in a time integrated interferometer), indicated here by the index k . Direct calculation reveals that Jeffreys' prior results in a weighting of the different Fisher informations,

$$p(\tau_e|\sigma, I) \propto \sqrt{\sum_k N_k \mathcal{I}(\tau_e|\sigma, I_k)}, \quad (2.56)$$

where N_k is the number of experimental runs with the respective $P(D_k|\tau_e, \sigma, I_k)$. This simple form of Jeffreys' prior (2.56) for a combination of different likelihoods can be obtained by noting that $\langle \partial_{\tau_e} \log[P(D_k|\tau_e, \sigma, I_k)] \rangle_{D_k} = 0$ in any case since the normalization of the probability distribution $P(D_k|\tau_e, \sigma, I_k)$ must be preserved for all τ_e .

2.3.3. General scheme for assessing macroscopicities

In the previous two subsections I derived the general form of the hypothesis test that now has to be specified to return a distinctive value for the macroscopicity reached in a given experiment. For this purpose, I choose the threshold odds that is required to

2.3. Hypothesis test of modified quantum mechanics

safely reject a hypothesis $H_{\tau_e^*}$ as $o_m = 1 : 19$. This directly translates to calculating the lowest five percent quantile of the posterior distribution,

$$P(\tau_e \leq \tau_m | d, \sigma, I) \equiv \int_0^{\tau_m} p(\tau_e | d, \sigma, I) = 5\%. \quad (2.57)$$

This identifies the hypothesis H_{τ_m} that is just rejected and all hypotheses with $\tau_e^* \leq \tau_m$ lead to an odds ratio smaller than o_m and are even more unlikely.

In close analogy to the original measure in Ref. [51] the macroscopicity is defined as the greatest excluded modification time scale $\tau_m(\sigma)$ maximized over the modification parameters σ on a decadic logarithmic scale,

$$\mu_m = \max_{\sigma} \left[\log_{10} \left(\frac{\tau_m(\sigma)}{1 \text{ s}} \right) \right]. \quad (2.58)$$

And just as the original measure of macroscopicity it ranks superposition experiments according to the degree to which they are at odds with our classical perception since the respective hypotheses of classicalizing MMM are rejected by empirical observation.

As discussed in Sec. 2.1.3 the MMM not only lead to decoherence but also to an energy increase depending on the parameter τ_e, σ by construction. The definition of macroscopicity (2.58) cannot distinguish whether modifications are falsified by an experiment because it shows a genuine quantum superposition effect or merely because no heating due to the mentioned energy increase is observed, be it even with extreme accuracy. Therefore, the measure must only be applied to experiments that undeniably show genuine quantum signatures. But even for those genuine quantum experiments the measurements may include or even be dominated by information about the absence of modification-induced heating.

To fairly address this issue it is necessary to filter out any information regarding the overall energy increase of the system. This is achieved by dividing the observables in subsets d yielding information about quantum coherence and d_{heat} providing only information about the energy gain. The likelihood $P(D, d_{\text{heat}} | \tau_e, \sigma, I)$ must be conditioned on the data d_{heat} measured in the experiment,

$$P(D | \tau_e, \sigma, I, d_{\text{heat}}) = \frac{P(D, d_{\text{heat}} | \tau_e, \sigma, I)}{P(d_{\text{heat}} | \tau_e, \sigma, I)}. \quad (2.59)$$

This effectively transfers any witnessed lack of heating to the background information I and the conditioned likelihood (2.59) ensures that only verified quantum effects enter the measure of macroscopicity. In most quantum superposition tests this is naturally incorporated in the measurement scheme since only the conditional measurements are reported, see for example the evaluation of entangled nanobeams in Sec. 3.4. Contrarily, an example where this separation of observables is necessary for the macroscopicity to not be dominated by classical observations is shown in Sec. 3.2 where interfering BEC are studied.

The formal framework is now completed and the assessment of macroscopicity can be phrased in a general scheme as follows:

2. Hypothesis test for classicalizing modifications of quantum mechanics

1. Determine the Hamiltonian, environmental decoherence channels, and quantum measurement protocol, and use these to calculate the likelihood $P(D|\tau_e, \sigma, I)$ in presence of the modification (2.8). If appropriate use Eq. (2.59) to focus on data demonstrating quantum coherence.
2. Calculate Jeffreys' prior (2.56).
3. Determine the posterior distribution via Bayesian updating (2.49) to extract $\tau_m(\sigma)$ via Eq. (2.57).
4. Find the maximum of the function $\tau_m(\sigma)$, which determines the macroscopicity (2.58).

Naturally, the first thing to do now is to put this scheme on trial with interference experiments for a comparison with the original formulation in Ref. [51].

2.4. Case study: Molecule interferometry

Molecule interferometry [25–28] is arguably one of the strongest contribution to the expansion of the quantum realm, or rather its validation, more and more to the macroscopic regime. In any case it leads, according to Ref. [51], to the highest macroscopicities in state of the art quantum tests. As a quantum test exhibiting an interference visibility that can directly be evaluated by Eq. (2.16) it serves as a benchmark to compare the old definition for macroscopicity with the Bayesian scheme developed in the previous section. The two experiments in question are near field interference experiments performed in Vienna: the Kapitza-Dirac-Talbot-Lau Interferometer (KDTLI) [28] and the Long baseline Universal Matter-wave Interferometer (LUMI) [89].

2.4.1. Near-field Talbot-Lau interferometry

Near-field interferometry is discussed in depth in Refs. [69,90] and I will only report the key results here. The exact setup probing Talbot-Lau interferometry as it is done in the so-called KDTLI and LUMI is shown in Fig. 2.3. It consists of three gratings with equal distance $L_1 = L_2 = L$ and equal grating period d_g , the center grating being a standing laser wave. The resulting interference pattern at the position of the third grating is probed by altering the lateral position x_S of the third grating, which leads to a varying intensity S of the particles stream behind it. The functional dependency $S(x_S)$ can be expanded in Fourier components

$$S(x_S) = \sum_{\ell} S_{\ell} \exp \left[\frac{2\pi i \ell}{d_g} (x_S + \delta x) \right]. \quad (2.60)$$

The value δx is an absolute offset in the lateral position typically not reported by the experimentalists and therefore determined by a fit. The different Fourier components

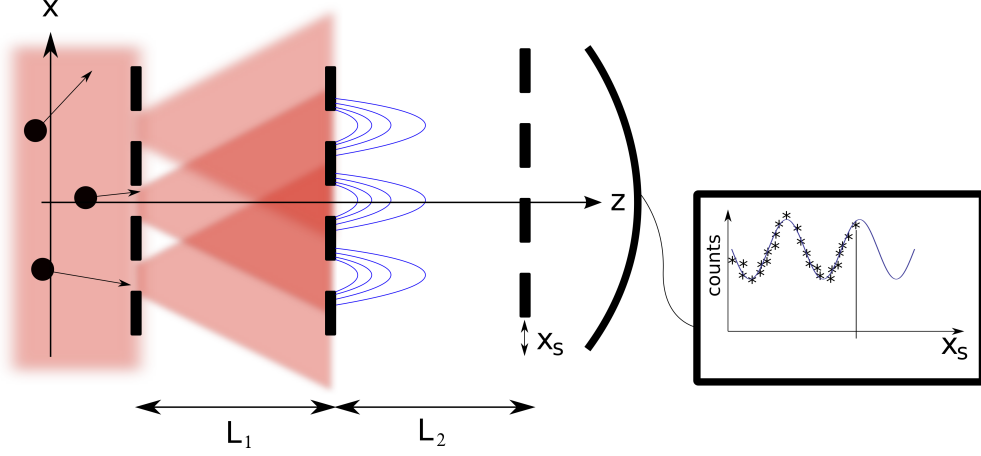


Figure 2.3.: Schematic representation of the Talbot-Lau interferometer discussed in the text and taken from Ref. [91]. Molecules from an incoherent source traverse three gratings with period d from which the second one is a standing laser wave in the studied setups. The distances are equal, $L_1 = L_2$. The two first gratings produce an interference pattern at the position of the third grating that can be scanned by changing the lateral position x_S of the third grating. Molecules traversing the last grating are counted and the current varies with the position x_S verifying interference.

depend crucially on a whole set of parameters [69]:

$$S_\ell = f_1 f_3 \text{sinc}(\pi \ell f_1) \text{sinc}(\pi \ell f_3) e^{\beta \phi_0 [\cos(\pi \ell T / T_T) - 1]} \left[\frac{\beta + \sin(\pi \ell T / T_T) - \beta \cos(\pi \ell T / T_T)}{\beta - \sin(\pi \ell T / T_T) - \beta \cos(\pi \ell T / T_T)} \right]^\ell \times J_{2\ell} \left\{ \text{sgn} \left[\beta - \sin \left(\frac{\pi \ell T}{T_T} \right) - \beta \cos \left(\frac{\pi \ell T}{T_T} \right) \right] \phi_0 \sqrt{\sin^2 \left(\frac{\pi \ell T}{T_T} \right) - 4\beta^2 \sin^4 \left(\frac{\pi \ell T}{T_T} \right)} \right\}, \quad (2.61)$$

with $J_{2\ell}(\cdot)$ being Bessel functions, $\beta = n_0/2\phi_0$, and all relevant parameters listed in Tab. 2.1.

Eq. (2.61) takes photon absorption at the laser grating into account which is necessary in the two experimental realizations discussed below. The simplified case without photon absorption is obtained by setting $\beta = 0$,

$$\tilde{S}_\ell = f_1 f_3 \text{sinc}(\pi \ell f_1) \text{sinc}(\pi \ell f_3) J_{2\ell} \left[\phi_0 \sin \left(\frac{\pi \ell T}{T_T} \right) \right]. \quad (2.62)$$

It is important to note that Talbot-Lau interferometry allows for a classical shadow pattern that can be obtained by ballistic particle trajectories that are reflected by the gratings. This leads to a third set of Fourier coefficients

$$S_\ell^{\text{cl.}} = f_1 f_3 \text{sinc}(\pi \ell f_1) \text{sinc}(\pi \ell f_3) J_{2\ell} \left[\phi_0 \frac{\pi \ell T}{T_T} \right], \quad (2.63)$$

2. Hypothesis test for classicalizing modifications of quantum mechanics

grating distance	L
molecule mass	m
opening fraction of the μ th grating	f_μ
beam waist	w_y
molecule velocity	v_z
polarizability of the molecule	α
laser power of the second grating	P
absorption cross section	σ_{abs}
grating period	d_g
time of flight	$T = L/v_z$
Talbot time	$T_T = md_g^2/2\pi\hbar$
phase shift	$\phi_0 = 8\sqrt{2\pi}\alpha P/\hbar c w_y v_z$
maximum mean number of absorbed photons	$n_0 = 8 d_g \sigma_{\text{abs}} P / \sqrt{2\pi}^3 \hbar c w_y v_z$

Table 2.1.: Experimental parameters required to calculate the Fourier coefficients (2.61).

which deviates sufficiently well from the quantum case to allow for differentiation as demonstrated in Figs. 2.4 and 2.5 for the two studies KDTLI and LUMI.

Since the Fourier coefficients for $|\ell| > 1$ are in our case orders of magnitudes smaller than S_0 and S_1 the signal is in practice sinusoidal,

$$S(x_S) \simeq f_1 f_3 \left\{ 1 + \mathcal{V}_{\text{sin}} \sin \left[\frac{2\pi}{d_g} (x_S + \delta x) \right] \right\}. \quad (2.64)$$

The overall prefactor $f_1 f_3$ is of no importance for determining the likelihoods later on.

With Eq. (2.64) we have the pure quantum mechanical description of the Talbot-Lau interferometer signal but we also need the alteration of this signal if MMM are present. Fortunately, this was already calculated in Ref. [69] for vanishing position kicks σ_s . The latter are indeed negligible since the relevant path separations in the interferometer are far above the femtometer scale. The momentum displacements lead to a diminished visibility factor \mathcal{V}_{sin} with [69]

$$\mathcal{V}_{\text{sin,MMM}} = \mathcal{V}_{\text{sin}} \exp \left\{ -2 \frac{T}{\tau_e} \left(\frac{m}{m_e} \right)^2 \left[1 - \frac{\sqrt{\pi} \hbar T_T}{\sqrt{2} d_g \sigma_q T} \operatorname{erf} \left(\frac{d_g \sigma_q T}{\sqrt{2} \hbar T_T} \right) \right] \right\}. \quad (2.65)$$

Thus, due to the incoherent momentum kicks the sinusoidal signal can vanish entirely for $\tau_e \rightarrow 0$. Notice further, that $\mathcal{V}_{\text{sin,MMM}}$ can simply be averaged over any distribution of masses m or velocities v_z since S_0 only depends on f_1 and f_3 .

We are ready to put MMM to the test with help of Eqs. (2.64) and (2.65). Either, by exposing different grating positions x_S to a constant stream of molecules for the same amount of time and calculating the likelihood of the count distribution observed. Alternatively, one can measure the number of particles traversing the third grating compared to the number of particles that did not pass the grating and calculate the likelihood of those absolute numbers and combine it for different grating positions. Both schemes are studied in the next two subsections.

2.4.2. Kapitza-Dirac-Talbot-Lau Interferometer

In Ref. [28] $C_{284}H_{190}F_{320}N_4S_{12}$ -molecules with a total mass of 10 123 u were interfered in a Talbot-Lau setup with a grating distance $L = 0.105$ m. Two exemplary data sets are shown in Fig. 2.4: 42 different lateral grating positions x_S were adjusted and exposed to a beam of molecules with constant intensity and the particles passing the setup during a fixed duration time for every x_S were counted. This allows us to write the periodic probability for molecules to be detected as

$$p(x_S|\tau, \sigma, I) \sim 1 + \mathcal{V}_{\text{sin,MMM}} \sin \left[\frac{2\pi}{d_g}(x_S + \delta x) \right]. \quad (2.66)$$

For fixed mass m and velocity v_z of the interfered molecules Jeffreys' prior (2.51) can be analytically derived as

$$p(\tau_e|\sigma, I) \sim \sqrt{\int_0^{2\pi} dx_S p(x_S|\tau_e, \sigma, I) [\partial_{\tau_e} \log p(x_S|\tau_e, \sigma, I)]^2} \sim \frac{\tilde{T}}{\tau_e^2} \sqrt{\frac{1}{\sqrt{1 - \mathcal{V}_{\text{sin}}^2 e^{-4\tilde{T}/\tau_e}} - 1}}, \quad (2.67)$$

with the characteristic timescale

$$\tilde{T} = T \left(\frac{m}{m_e} \right)^2 \left[1 - \frac{\sqrt{\pi} \hbar T_T}{\sqrt{2} d_g \sigma_q T} \operatorname{erf} \left(\frac{d_g \sigma_q T}{\sqrt{2} \hbar T_T} \right) \right]. \quad (2.68)$$

Since per construction $\mathcal{V}_{\text{sin}} < 1$ the prior distribution (2.67) decays in the limits $\tau_e \rightarrow \infty$ and $\tau_e \rightarrow 0$ quadratically and exponentially, respectively, and therefore ensures integrability as already shown in Sec. 2.3.2 for the general case. The prior for the actual setup is only numerically achievable and shown in Fig. 2.4, because for the KDTLI one has to average $\mathcal{V}_{\text{sin,MMM}}$ over a velocity distribution.

All that is left to do according to Eq. (2.49) is to multiply the likelihoods (2.66) of the data shown in Fig. 2.4 with Jeffreys' prior (2.67). The lowest five percent quantile of the resulting posterior has then to be maximized with respect to σ_q . This is achieved for $\sigma_q \gtrsim 10^3 \hbar T_T / d_g T$ which results in $\tilde{T} \simeq T(m/m_e)^2$. This σ_q is many orders of magnitude smaller than the actual momentum of the molecules so we can safely assume that the momentum translations induced by the MMM do not disintegrate the molecule for any τ_e in the range depicted in Fig. 2.4 (c).

Finally, the resulting posteriors from updating Jeffreys' prior with the data depicted in Fig. 2.4 (a) are shown in Fig. 2.4 (c) and the lowest five percent quantiles lead to macroscopicities of $\mu_m = 12.2$ and $\mu_m = 12.5$. In principle the likelihoods of both data sets could be merged to determine a third macroscopicity but the resulting value would be lower than the macroscopicity of the data at $P = 1$ W alone. Naturally, the additional incorporation of a worse data set (in the sense that it would imply a lower macroscopicity) can correct the determined τ_m to lower values.

2. Hypothesis test for classicalizing modifications of quantum mechanics

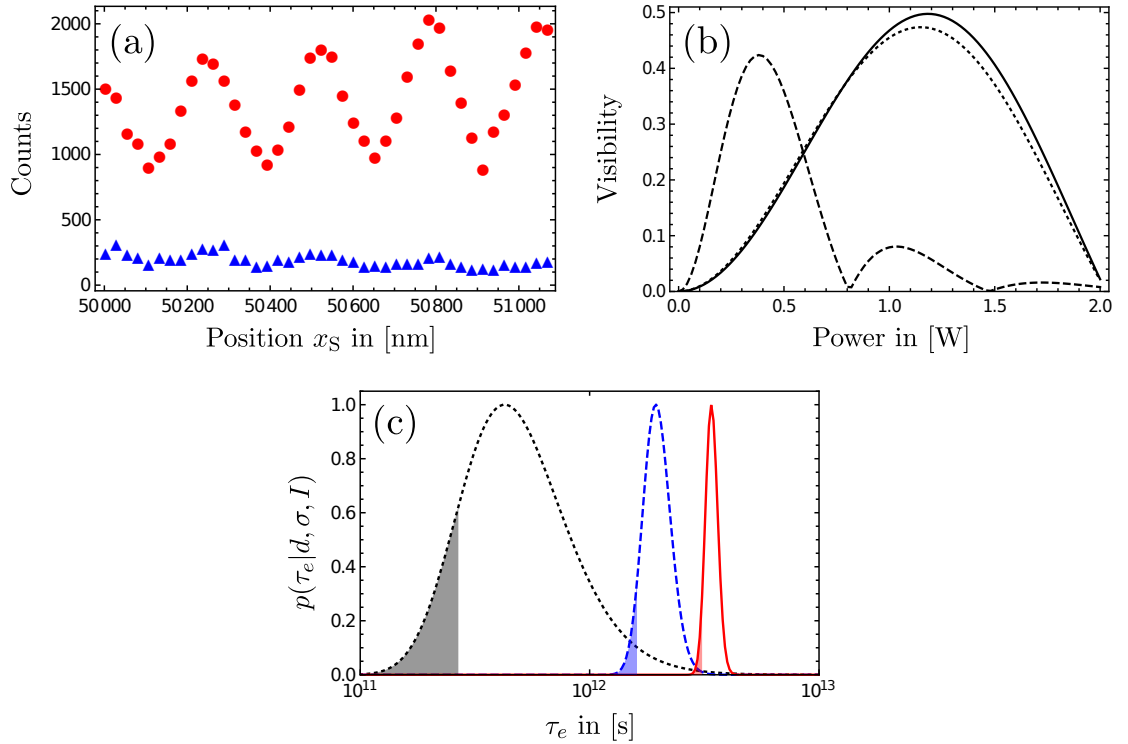


Figure 2.4.: (a) Shown are two count distributions measured in Ref. [28] as a function of the grating position x_S , for a grating laser power of 1 W (circles) and for a laser power of 0.84 W (triangles). In the latter case considerably fewer particles arrived at the detector behind the third grating because of a lower integration time and a lower overall intensity in the particle beam. (b) The theoretically achievable visibility (2.64) for the quantum case (dotted line considering absorption, solid line without considering absorption) is sufficiently higher than the classical expected value (dashed line) in the relevant power region. In both cases MMM will induce a loss in contrast eventually leading to a constant signal in the limit $\tau_e \rightarrow 0$. Note that both visibility curves for the quantum case lead to considerably larger values than the theoretically achievable visibility reported in [28]. (c) Shown are Jeffreys' prior (dotted line) as well as the posterior distributions achieved by updating the prior with the two data sets shown in (a) at $P = 0.84$ W (dashed line) and $P = 1$ W (solid line). All distributions are normalized to their maximum value and the lowest five percent quantiles are marked by the shaded areas. One observes that both posterior distributions are shifted to the quadratically suppressed region of the prior, suggesting a genuine quantum interference, and are converged to a large extent compared to the prior, suggesting that more data points will not substantially improve the macroscopicity.

grating distance	$L = 0.105 \text{ m}$
molecule mass	$\bar{m} = 10\,123 \text{ u}$
opening fraction of the gratings	$f_1 = f_3 = 0.42$
beam waist	$w_y = 9.45 \times 10^{-4} \text{ m}$
molecule velocity	$v_z = 85 \pm 12.74 \text{ m/s}$
polarizability of the molecule	$\alpha = 410 \times 10^{-30} \text{ m}^3 \times 4\pi\epsilon_0$
Laser power at the second grating	$P = 0.84 \text{ W}, 1 \text{ W}, 1.33 \text{ W}$
absorption cross section	$\sigma_{\text{abs}} = 1.7 \times 10^{-21} \text{ m}^2$
grating period	$d_g = 2.66 \times 10^{-7} \text{ m}$

Table 2.2.: Experimental parameters for the KDTLI setup in Ref. [28].

2.4.3. Long baseline Universal Matter-wave Interferometer

In the case of LUMI [89] we do not have one specific type of molecule that is interfered but a distribution of different masses, shown in Fig. 2.5 (a). The different sharp peaks in the mass spectrum are associated with the loss of several side-arms with about 460 atomic mass units per arm. For the expected visibility \mathcal{V}_{sin} one therefore has to average over the mass spectrum additionally to the averaging over the velocity distribution. The result is shown in Fig. 2.5 (b).

Contrarily to the KDTLI from the previous subsection, the intensity of the molecule stream in the LUMI is no longer stable for different lateral grating positions x_S . Because of that, one can no longer simply multiply the likelihoods (2.66) of different grating positions since these likelihoods are no longer proportional to Eq. (2.64) because of varying intensities. As a remedy, I use reference data that was collected for periods of time where the laser grating was turned off. This resulted in a constant signal as can be confirmed theoretically by setting $\phi_0(P = 0) = 0$ in the Fourier coefficients (2.61). So for each grating position x_S two numbers of arriving molecules were measured at the detector: N_d and N_0 during periods in which the laser grating was turned on or off, respectively. From this I can deduce that whenever N_d particles traversed the third grating at the same time $N_0/f_3 - N_d$ particles were blocked. Thus, for every grating position x_S there are only two possible events (passed/blocked) and the measurement scheme can be understood as dichotomous. This dichotomous measurement can be used for the hypothesis test, together with all the dichotomous measurements at other grating positions without needing an overall constant particle intensity.

The likelihoods of the dichotomous measurements can be inferred by the already known Eq. (2.64), the intensity of particles detected behind the third grating, and

$$S_{\text{tot}} - S(x_S) = f_1 \left[1 - f_3 - f_3 \mathcal{V}_{\text{sin,MMM}} \cos \left(\frac{2\pi}{d_g} x_S \right) \right], \quad (2.69)$$

the intensity of particles blocked by the third grating. The total intensity S_{tot} is simply found by setting $f_3 = 1$ in Eq. (2.61). Thus, for every grating position x_S we have in

2. Hypothesis test for classicalizing modifications of quantum mechanics

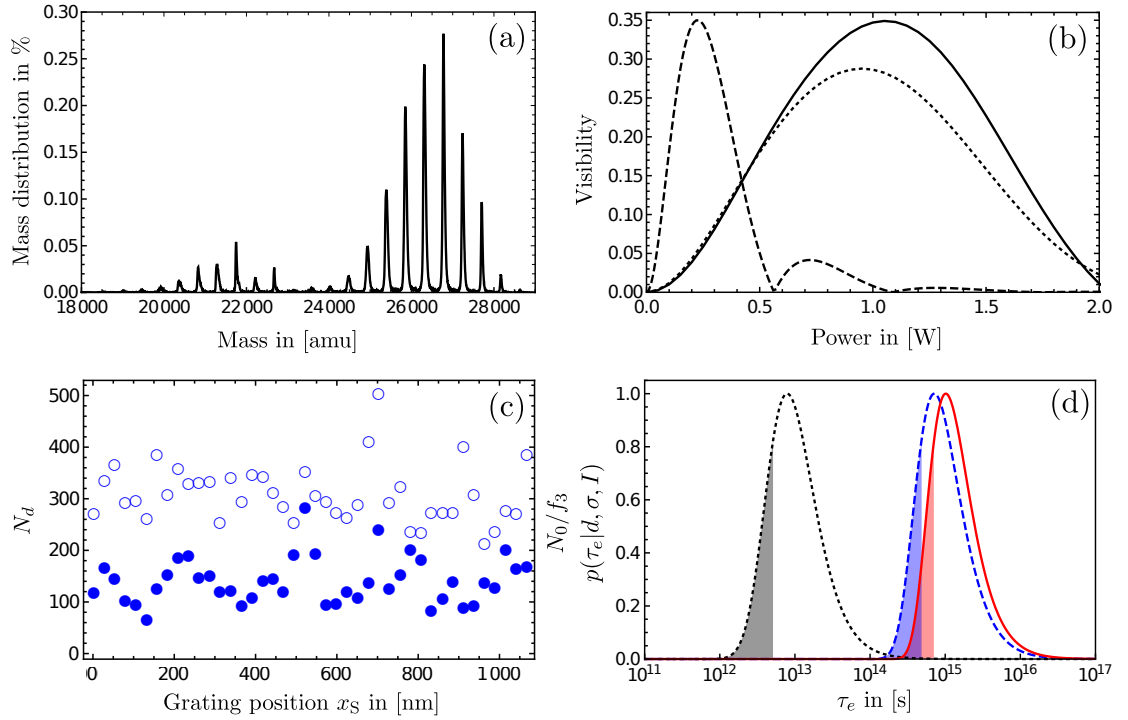


Figure 2.5.: (a) Mass distribution of the molecules used in the LUMI experiment. (b) The theoretically achievable visibility (2.64) for the quantum case (dotted line with photon absorption, solid line without photon absorption) is sufficiently higher than the classical expected value (dashed line) in the relevant power region. In both cases MMM will induce a loss in contrast eventually leading to a constant signal in the limit of short classicalization time scales. (c) Shown are the number of molecules detected in one specific run after the third grating with an operating (not operating) laser grating at 1 W marked by full circles (empty circles and rescaled by $1/f_3$) as function of the position x_S of the third grating. (d) The posterior distributions $p(\tau_e | \sigma, I)$ are achieved by Bayesian updating of Jeffreys prior (dotted line) of $p(t | x_S, \tau_e, \sigma, I)$. While the blue dashed posterior is achieved by using the data shown in (c) the red posterior is a result of updates over a whole range of different laser powers P for which the data is shown in App. A (I take the data sets 1, 5, 7, 10, 11, 13, 16, and 22, omitting sets with appreciable noise). All probability densities are normalized to their maximum value, and their lowest five percent quantile is marked by the shaded areas. In contrast to the results for the KDTLI shown in Fig. 2.4 (c) here the posterior distribution do not substantially converge. Nevertheless, the shift to much large values of τ_e demonstrates a genuine quantum interference.

2.4. Case study: Molecule interferometry

grating distance	$L = 0.981 \text{ m}$
mean molecule mass	$m = 25\,675.1 \text{ u}$
opening fraction of the gratings	$f_1 = f_3 = 0.43$
beam waist	$w_y = 7.3 \times 10^{-4} \text{ m}$
molecule velocity	$v_z = 256 \pm 50 \text{ m/s}$
polarizability at $m = 27\,714 \text{ u}$	$\alpha = 1320 \times 10^{-30} \text{ m}^3 \times 4\pi\epsilon_0$
Laser power at the second grating	0.4–1.2 W
absorption cross section	$\sigma_{\text{abs}} = 1.6 \times 10^{-20} \text{ m}^2$
grating period	$d_g = 2.66 \times 10^{-7} \text{ m}$

Table 2.3.: Experimental parameters for the LUMI setup in Ref. [89]. The polarizability changes with the mass and decreases quasi linearly with every arm of $\sim 460 \text{ amu}$ while the absorption cross section is quasi constant [89]

addition to the probability

$$p(+|x_S, \tau_e, \sigma, I) = S(x_S)/f_1 \quad (2.70)$$

for molecules to traverse the grating the probability

$$p(-|x_S, \tau_e, \sigma, I) = (S_{\text{tot}} - S(x_S))/f_1 \quad (2.71)$$

to be blocked by the third grating.

Calculating the probabilities $p(+|x_S, \tau_e, \sigma, I)$ and $p(-|x_S, \tau_e, \sigma, I)$ for the parameters of the LUMI that are shown in Tab. 2.3 and processing the set of data points shown in Fig. 2.5 (c) leads to the blue, dashed posterior shown in Fig. 2.5 (d). Taking the data sets 1, 5, 7, 10, 11, 13, 16, and 22 in App. A into account results in the red, solid posterior with a macroscopicity of $\mu_m = 14.8$. This is achieved by the maximum excluded τ_m found once again by setting $\sigma_q \gg \hbar T_T/dT$ for all masses and velocities. We observe that the posterior $p(\tau_e|\sigma, I)$ is strongly shifted rightwards away from the prior distribution, clearly indicating a quantum signature (since large values of τ_e , and therefore weak MMM, are more likely).

On the other hand, the posterior hardly converged at all and if we would be truly interested to find the classicalization time parameter τ_e (and not just assess a macroscopicity of the experiment), the number of data points would be not sufficient to provide a conclusive result. Nevertheless, the $\tau_e = 10^{14.8} \text{ s}$ ruled out for $\sigma_q \gg \hbar T_T/dT$ can be assumed to be a conservative estimation as it is certainly underestimated by (i) choosing Jeffreys' prior which is strongly suppressed in the relevant region of τ_e and by (ii) taking the lowest five percent quantile. Note finally, that for the LUMI with its whole range of different masses and by taking data from different laser powers $P = 0.2 - 1.8 \text{ W}$ there is no obvious way to calculate the macroscopicity μ in the original manner intended in [51] via Eq. (2.16). This will also be discussed in more detail in the next section. As such it is the first of a long parade of experiments profiting from the new approach via hypothesis testing.

2.4.4. Convergence of old and new definition of macroscopicity

It is impossible to compare the two definitions of macroscopicity Eq. (2.15) and Eq. (2.58), standing for the frequentist and Bayesian approach, in general. While the statistical errors are inherently and consistently addressed by Bayesian inference, there are innumerable conceivable approaches for calculating macroscopicities in a frequentist framework via the old definition. Options range from different appropriate estimators to the choice of confidence intervals as discussed in Sec. 2.2.2. In every case we can expect convergence in the limit of an infinite amount of experimental data, first because of the consistency of Bayesian inference which is always fulfilled under very general assumptions as already stated in Sec. 2.2.1, and second due to the existence of consistent parameter estimators, e.g. the maximum likelihood estimator that amounts to Bayesian inference with a flat prior thus eligible for Bayesian consistency.

Such convergence is exemplarily shown in Fig. 2.6 where I *simulated* different scenarios of the LUMI measurement schemes from the previous section. Taking the same relative molecule intensities for different grating positions x_S and $P = 1$ W as in the actual experiment I simulated different total count numbers from several hundreds to millions (being subsets of the same total data set) for different ‘true’ MMM parameters τ_e and $\sigma_q = 10^3 \hbar T_T / dT$. The frequentistically excluded time parameters are determined with help of a least squares fit to the normalized interference signal using a general sine function

$$S(x_S) = c_1 + c_2 \sin\left(\frac{2\pi}{d_g} x_S + \delta x\right), \quad (2.72)$$

with parameters c_k instead of τ_e . The τ_e is then inferred simply by comparison with the 95% confidence interval of the fitted parameters, $\mathcal{V}_{\text{sin,MMM}} = |c_2/c_1|$, to be in some sense consistent with the lowest five percent quantile from Bayesian inference. This is a very naive approach but comes close to the standard procedure. I found in all cases a convergence to the true value of τ_e with which I created the data. The rate of this convergence decreases for increasing values of the true τ_e , implying that for better interference signals it is ever harder to come to a conclusive τ_m . The overall convergence of Bayesian inference and the result of a fit to the normalized interference signal additionally confirms that the description with the dichotomous sample space for each laser power is correct.

The comparison with the frequentistically achieved macroscopicities by means of a fit shows no monotonicity in contrast to the values achieved by the Bayesian hypothesis test. Especially the data points for a large true value of $\tau_e = 10^{16}$ s exhibit inconsistent scattering. Mind, that every point in Fig. 2.6 resembles just a single data set to provide a first impression of the consistency and at least several hundreds sets per data point would be necessary to observe the reduced scattering with increasing number of observations. Nevertheless it is noteworthy that even for a low amount of data the hypothesis test preserves the monotonicity which cannot be said about the frequentist fit even though here the 95% confidence interval is used as well.

Comparing the posteriors in Fig. 2.7 (e) for $\tau_e = 10^{15}$ and $\tau_e = 10^{16}$ with the result of the actual experiment shown in Fig. 2.5 (d) suggests that the number of detection

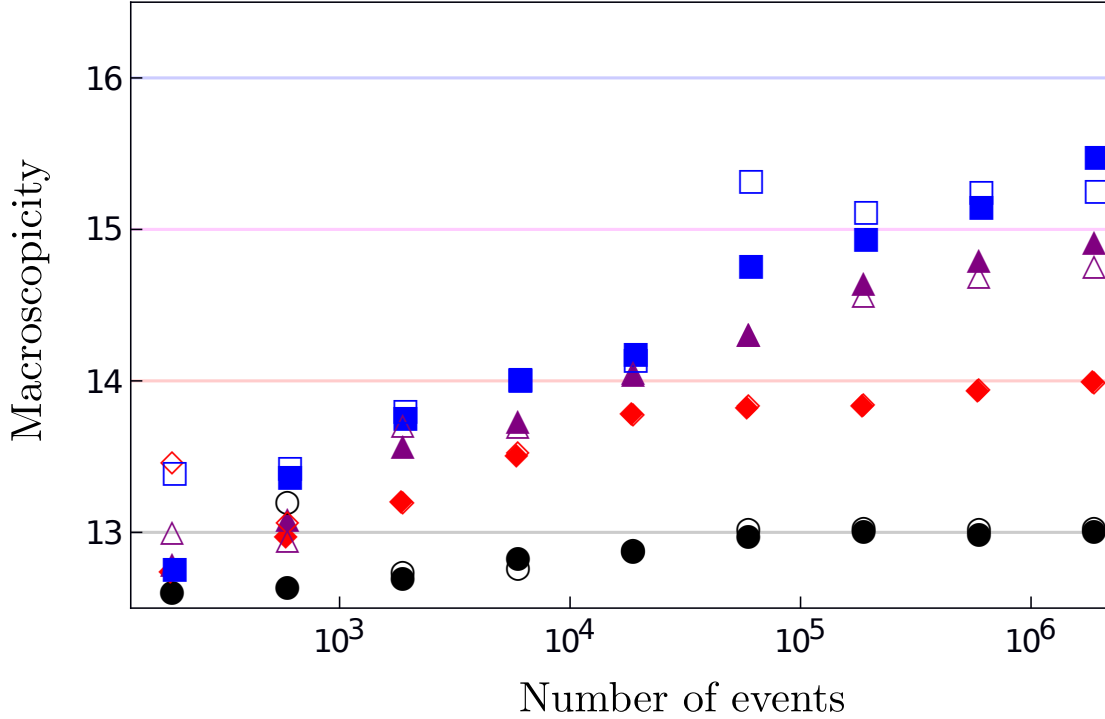


Figure 2.6.: (a) Convergence of old and new definition of macroscopicity. Shown are the macroscopicities obtained for simulated data obtained for MMM parameters $\tau_e = 10^{13} s, 10^{14} s, 10^{15} s, 10^{16} s$ at $\sigma_q = 10^3 \hbar T_T / dT$ for the LUMI measurement scheme as discussed in the main text. The values correspond to the lower five percent quantiles τ_m of the posterior $p(\tau_e | \sigma_q \gtrsim 10^3 \hbar T_T / dT, I)$ achieved by Bayesian inference (filled markers). They should be compared with the respective value corresponding to the macroscopicity calculated with Eq. (2.58) (empty markers). The latter is determined by the lower 95% confidence interval from a least squares fit of the renormalized raw data. One observes that increasing numbers of simulated events the τ_m converge to the true value with decreasing rate the weaker the MMM and thus the closer the interference contrast comes to the theoretically possible value shown in Fig. 2.5 (b). Thanks to Jeffreys' prior and by choosing the lowest five percent quantile the assessed macroscopicity via Bayesian hypothesis testing is always underestimated. In particular, it is not rewarding to use sparse data.

2. Hypothesis test for classicalizing modifications of quantum mechanics

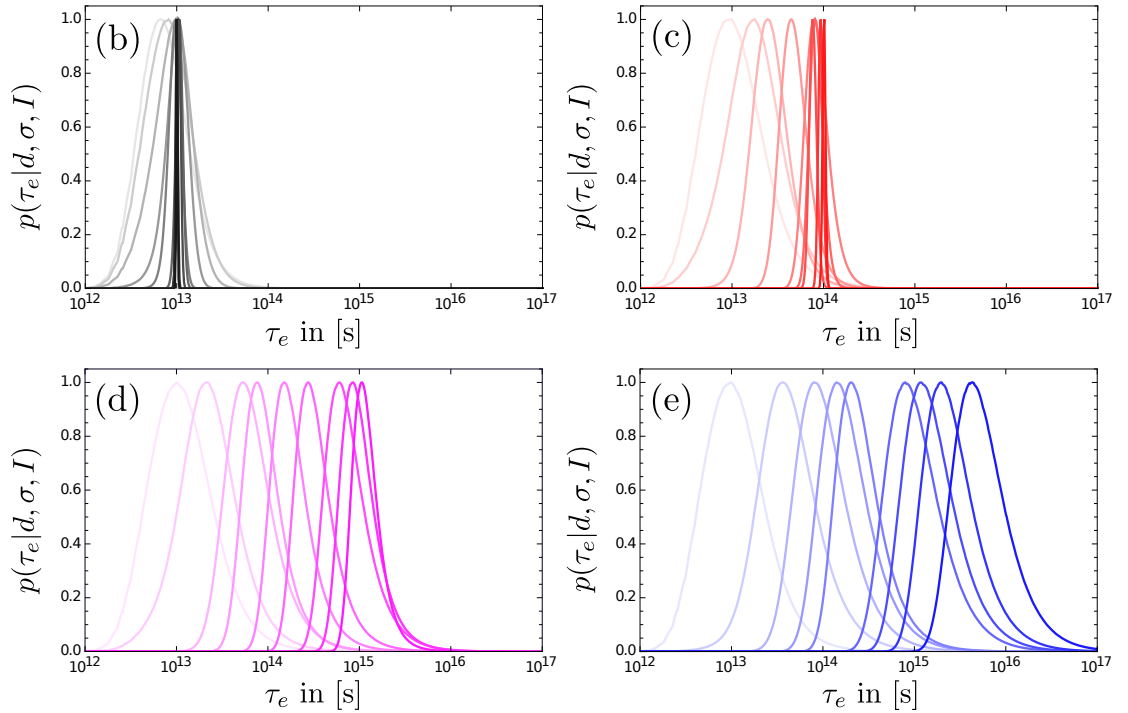


Figure 2.7.: Here I plot the posteriors leading to the filled data points shown in Fig. 2.6 where (a)–(d) correspond to the data sets of true classicalization times $\tau_e = 10^{13} \text{ s}, 10^{14} \text{ s}, 10^{15} \text{ s}, 10^{16} \text{ s}$ in ascending order. The darker the lines the more events are incorporated in the inference.

events of about 10^5 is simply not large enough to come to a conclusive result (if one would be interested in the true value of τ_e) and it is to be expected that one order of magnitude more data points could push the macroscopicity even further than the found $\mu = 14.8$. An objective criterion for the situation that enough data is collected is a lower five percent quantile that does not fluctuate noticeably over an order of magnitude of data.

2.5. Discussion

We learned in this chapter that the falsification of MMM parameters can be performed in an objective manner using an uninformative Bayesian hypothesis test, independently of the shape and size of the data produced in any quantum test. We can rely on the consistency of Bayesian inference both with frequentist methods and, more importantly, with the true value of the underlying parameter τ_e . The latter consistency was demonstrated for the specific scenario of the LUMI in Sec. 2.4.4 and for the general case in Refs. [80] in the shape of the Bernstein-von-Mises theorem. In this Sec. 2.4.4 the flip side of the automatic incorporation of statistical errors in the Bayesian approach became apparent: The weaker the modifications the more difficult it gets to identify the exact

deviation from the undisturbed signal and therefore the more data points are needed to sufficiently converge the posterior. This is stated again by the Bernstein-von-Mises theorem that predicts the widths of the resulting Gaussian to be inversely proportional to the size of the sample and the Fisher information at the true value. Thus, the further away from the main body of Jeffreys' prior the true value is (implying a low Fisher information) the more repetitions of the experiment are needed. On the other hand this restricts the maximum macroscopicity achievable in a quantum experiment with a finite data set, preventing it from assuming infinite values.

From the case studies here and the evaluations in the next chapter we can identify the two driving factors for a large macroscopicity: (i) The lowest five percent quantile of Jeffreys' prior provides a reference macroscopicity (or minimal macroscopicity) of a given experiment. Even before a single event is observed, it allows us to obtain a rough estimate for the macroscopicity reached in a successful quantum experiment determined by the usual suspects: mass, interference time, delocalization distance, and so on. (ii) The quality of the quantum signature, e.g. the ratio between expected and measured visibility, can further enhance this prior macroscopicity, in principle to infinity but practically on an ever slower pace.

One might argue that an experiment with macroscopic parameters would achieve large macroscopicities simply by means of the prior macroscopicity without ever showing a genuine quantum signal. But this is no specific feature of Bayesian inference and can be witnessed for frequentist approaches as well. As stated in Ref. [51] the assessment of macroscopicity is conditioned on the fact that a genuine quantum effect has been observed (E.g. the fit of a sine to a single digits histogram would not be accepted by any physicist as a quantum interference even though it may lead to a finite visibility). For the hypothesis test brought forward here the case is clear: if the posterior is shifted to regions quadratically suppressed by Jeffreys' prior the quantum nature of the signal is satisfactorily demonstrated. This is the case for all experiments discussed in the scope of this thesis. Note, that this verification of a genuine interference signal has to be made additionally to the notion whether a quantum or classical observable is available in the first place.

I have to address one last issue of the macroscopicity measure that is independent from the choice of exact definition (2.15) or (2.58): The measure does in principle not reward any effort to limit environmental decoherence sources if those are correctly implemented in the theoretical description of the time evolution. For example, assume the near-field interferometry discussed in this chapter was performed with a poor vacuum leading to relevant decoherence due to scattering which is fully incorporated using collisional decoherence theory [92, 93]. This would simply reduce the interference visibility by another multiplicative factor. Just assuming for the moment there was a true set of MMM parameters the resulting τ_m would converge to the same value both in presence and absence of background gas. Fortunately, such a poor control of the environment in the experiment comes at a price: The lower the visibility becomes due to the additional decoherence the more data points are needed for a sufficient inference because of the flat background.

3. Quantum experiments in presence of classicalizing modifications

In this chapter I will present how minimally invasive, macrorealist modifications of quantum mechanics (MMM), as defined by Eq. (2.8), influence the time evolution of several non-trivial quantum tests, including large spatial superpositions of (partially entangled) BEC in Sec. 3.1 and 3.2, Leggett-Garg tests by means of quantum random walks in optical lattices in Sec. 3.3, and entanglement of motional modes of two massive crystals in Sec. 3.4. The respective results enable me to further show how the macroscopicity measure defined in Sec. 2.3 works in practice. Since the modified time evolution can often also be understood as an outcome of general decoherence channels the here reported findings are relevant beyond assessing the achieved macroscopicity (for example for single particles the MMM generator (2.6) is equivalent to a special case of collisional interaction with a gaseous environment).

3.1. Interference of BEC in product and dual Fock states

The motivation for the macroscopicity measure established in Ref. [51] was to objectify the notion of truly macroscopic quantum effects. An example for the necessity of such a measure is given in this section where I examine the BEC interference experiment reported in Ref. [33]. The authors managed to create a quantum superposition state on a half meter scale, but they were unable create a phase-stable interference pattern, which provoked a discussion on the validity of their claims [94, 95]. In what follows this controversy will be resolved especially in regard to the predictions of MMM; the results are published in Ref. [56].

3.1.1. Two-mode approximation in the Mach-Zehnder setup

Indistinguishable particles can be assigned to two categories: In the case of *bosons* the permutation of two particles in any given state preserves the sign (the state is symmetric), in the case of *fermions* such a permutation changes the sign (the state is anti-symmetric). This symmetry of states involving bosons is sufficient to derive the Bose-Einstein statistics for non-interacting particles in thermal equilibrium which states that the average occupation of a state with energy ϵ_i is [96, 97]

$$\langle n_i(\tilde{\mu}) \rangle = \frac{1}{e^{(\epsilon_i - \tilde{\mu})/k_B T} - 1}. \quad (3.1)$$

The chemical potential $\tilde{\mu}$ is implicitly given by the total number of particles $\sum_i \langle n_i(\tilde{\mu}) \rangle = N$. For high temperatures Eq. (3.1) turns into the Boltzmann distribution but below

3. Quantum experiments in presence of classicalizing modifications

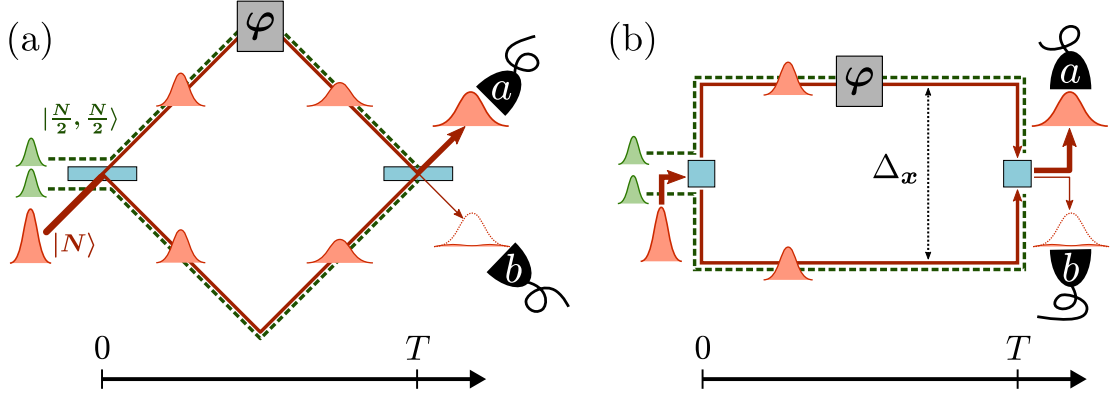


Figure 3.1.: Generic two-arm Mach-Zehnder interferometer. (a) A BEC with N atoms (red, solid) is coherently split into a superposition of two modes with distinct momenta at the first beamsplitter. After a reflection at time $T/2$ they recombine at a second beamsplitter. Variation of the relative phase φ , a sum of the two phase-shifts at the first and second beamsplitter and during the free time evolution, determines the probability of the atoms to arrive at detector a or b . If this phase cannot be stabilized the resulting statistics may not be distinguishable from the interference of two independent BEC with $N/2$ atoms in each Mach-Zehnder arm (green, dashed). (b) Same scheme as before but with a constant arm separation $\Delta_x = \Delta_p T/2\sqrt{3}m$. Regarding the effect of MMM both schemes are equivalent as shown in the main text.

some critical temperature T_c the ground state is macroscopically occupied, i.e. $\langle n_0(\mu) \rangle$ is on the order of N , referred to as *Bose-Einstein condensation*. The first such BEC with matter was created by Cornell, Wiemann, and Ketterle using Rubidium and Natrium [98, 99].

The dynamics of indistinguishable particles is most easily described in second quantization, avoiding the symmetrization of the state by hand. Then the only information the *Fock state* $|n_a, n_b, \dots\rangle$ possesses is how many particles n are in the modes a, b and so on. The Mach-Zehnder interferometer depicted in Fig. 3.1 can be traversed by three relevant many particle states. In the two-mode picture these states are characterized by different occupations of the single-particle wave functions $\psi_{a,b}(\mathbf{r}, t)$ that here depend explicitly on time to reflect the free motion and dispersion in each arm of the interferometer. As such the creation and annihilation operators, for example expressed in the momentum basis,

$$c_a^\dagger = \int d\mathbf{p} \psi_a(\mathbf{p}, t) c^\dagger(\mathbf{p}), \quad (3.2)$$

still fulfill the required commutation relation of bosons, $[c_a, c_b^\dagger] = \delta_{a,b}$, as long as the states are (in principle) orthogonal for all times, $\int d\mathbf{p} \psi_a(\mathbf{p}, t) \psi_b^*(\mathbf{p}, t) = 0$.

In the ideal scenario (unitary dynamics of a BEC at $T = 0$ and no interactions) each atom is in a superposition between the two modes after passing the first beamsplitter. In the case of a BEC with N particles occupying the same superposition the resulting

3.1. Interference of BEC in product and dual Fock states

many particle state is a *product state* (PS),

$$|\Psi_{\text{PS}}(\phi)\rangle = \frac{1}{\sqrt{2^N N!}} \left(c_a^\dagger + e^{i\phi} c_b^\dagger \right)^N |\text{vac}\rangle, \quad (3.3)$$

with the bosonic annihilation operators c_a and c_b of the modes a and b behind the second beamsplitter, respectively. This product state is also called *coherent spin state* and will be discussed in detail in Sec. 3.2 when dealing with interference of squeezed collective spin states. Just like in the one-particle case the relative phase ϕ can be tuned to control the statistics of atom-counts recorded in the two detectors placed behind the second beamsplitter. This second beamsplitter transforms the creation operators as

$$\begin{aligned} c_a^\dagger &= \cos \theta c_{a,\text{out}}^\dagger + e^{i\alpha} \sin \theta c_{b,\text{out}}^\dagger \\ c_b^\dagger &= -e^{-i\alpha} \sin \theta c_{a,\text{out}}^\dagger + \cos \theta c_{b,\text{out}}^\dagger. \end{aligned} \quad (3.4)$$

Plugging the transformation (3.4) into Eq. (3.3) reveals how the amplitudes of modes a, out and b, out can be controlled by tuning ϕ and α .

If ϕ cannot be stabilized and varies from shot to shot in a quasi random fashion the state is appropriately described by a phase averaged PS,

$$\rho_{\text{PAPS}} = \frac{1}{2\pi} \int_0^{2\pi} d\phi |\Psi_{\text{PS}}(\phi)\rangle \langle \Psi_{\text{PS}}(\phi)|. \quad (3.5)$$

In contrast to the ideal PS, this *phase averaged product state* (PAPS) would not lead to a stable interference pattern and the visibility would be zero right from the start since $|\langle c_a^\dagger c_b \rangle| = 0$. The two modes would still interfere due to the indistinguishability of the involved bosons, but this feature can also be attributed to the final state discussed in this section: the dual Fock state (DFS). Here two individually prepared BEC each with $N/2$ particles occupy each interferometer arm and arrive at the second beamsplitter to interfere, compare Fig. 3.1. The DFS,

$$|\Psi_{\text{DFS}}\rangle = \frac{1}{(N/2)!} \left(c_a^\dagger c_b^\dagger \right)^{N/2} |\text{vac}\rangle, \quad (3.6)$$

has no phase information whatsoever and the detection events of the interference fluctuate from shot to shot just like in the case of the PAPS.

This similarity between PAPS and DFS left the authors of Ref. [94] in doubt whether a superposition state was verified at all by the data produced in Ref. [33]. In reality there is a slight difference between the two states, as already apparent in the bunching and anti-bunching described by the second order correlations $\langle c_a^\dagger c_a^\dagger c_a c_a \rangle$, $\langle c_b^\dagger c_b^\dagger c_b c_b \rangle$, and $\langle c_a^\dagger c_b^\dagger c_a c_b \rangle$. We will see below that especially for small particle numbers there is a clear distinction between PAPS and DFS rooted in the Hong-Ou-Mandel effect [100]. As shown in Fig. 3.2 this effect leads to apparent deviations for single digit numbers of particles but becomes irrelevant for $N \rightarrow \infty$. In Sec. 2.3 I already argued that such a collective observable (like correlation functions) should not be used to study the effect of MMM on an interference experiment for assessing a macroscopicity, but rather the likelihoods of single events should be acquired. The corresponding count statistics $P(n_a)$ of n_a atoms from the condensate to be detected by detector a (and thus $N - n_a$ particles detected by detector b if no particles are lost) will be the main result of this section.

3. Quantum experiments in presence of classicalizing modifications

3.1.2. Macroscopic wave function

Before entering the full second quantization picture, I want to motivate two simplifications with help of the single-particle description of the Mach-Zehnder interferometer. Especially for many particles $N \gg 1$ a macroscopic wave function obeying the single-particle Schrödinger-equation is a viable approximation to describe the mean field statistics of the BEC [101]. The interaction between the individual particles of the BEC can be incorporated on the level of the macroscopic wave function with help of the Gross-Pitaevskii equation that reads [102, 103]

$$i\hbar\partial_t\psi(\mathbf{r}, t) = \left[-\frac{\hbar^2}{2m}\nabla_{\mathbf{r}}^2 + V(\mathbf{r}, t) + g|\psi(\mathbf{r}, t)|^2 \right] \psi(\mathbf{r}, t). \quad (3.7)$$

It adds to the single-particle Schrödinger equation of the macroscopic wave function a non-linear self-interaction which in general requires a numerical approach. In the current scenario we can assume the free BEC to be dilute enough that particle-particle interaction can be neglected. In Sec. 3.2, where the BEC is confined to a double well potential, I will approximate the interaction between the particles by means of a chemical potential linear in the particle number. This sufficiently describes the relevant impact [31, 104] and still allows for analytical solutions.

In first quantization the effect of MMM is most easily calculated with help of the characteristic function that reads

$$\chi(x, p) = \int dx_0 e^{ipx_0/\hbar} \langle x_0 + x/2 | \rho | x_0 - x/2 \rangle. \quad (3.8)$$

For the characteristic function the time evolution with MMM generator (2.6) and kinetic energy simply becomes

$$\partial_t^{\mathcal{M}_\sigma} \chi(x, p) = \frac{m_e^2}{m^2} \frac{e^{-x^2\sigma_q^2/2\hbar^2} - 1}{\tau_e} \chi(x, p) - \frac{p}{m} \partial_x \chi(x, p). \quad (3.9)$$

It suffices to describe solely the motion along the axis on which the spatial delocalization takes place, from now on referred to as x -axis. The other two axes are only relevant when discussing heating as will be done later on the way. The two modes after the first beamsplitter are assumed to be Gaussians with the same widths w_x and a relative momentum displacement of Δ_p , thus $\psi_a(x) = (2\pi w_x^2)^{-1/4} \exp(-x^2/4w_x^2)$ and $\psi_b(x) = \exp(i\Delta_p x/\hbar) \psi_a(x)$ operating in the rest frame of arm a . This is allowed since the MMM are invariant under Galilean transformation and any gradients in the gravitational potential can be absorbed in the relative phase ϕ .¹ After time $T/2$ the relative motion of the wave packets is reversed by applying a momentum displacement of $-2\Delta_p$ on mode b mirroring the movement and allowing to implement a second beamsplitter at time T .

First, I want to discuss the relevance of dispersion on the Gaussian wave packets. The free time evolution not only separates the modes spatially due to the superposition in

¹In fact, atom or BEC interferometers are especially suited and used to measure exactly this gradient [20, 22, 105].

3.1. Interference of BEC in product and dual Fock states

momentum, it also disperses the modes over time because of the finite extension of the wave packets. Since the MMM induces momentum diffusion it will indirectly enhance the dispersion effect. As a consequence, the overlap with the freely dispersed wave function gets diminished additionally which has to be assessed quantitatively. The time evolution (3.9) evolves any characteristic function χ_0 to

$$\chi_t(x, p) = \exp \left[\frac{m_e^2}{m^2} \int_0^t \frac{dt'}{\tau_e} \left(e^{-\sigma_q^2(x-pt'/m)^2/2\hbar^2} - 1 \right) \right] \chi_0 \left(x - \frac{pt}{m}, p \right). \quad (3.10)$$

We can immediately deduce from Eq. (3.10) that dispersion plays no role in the strong depletion regime, $\hbar/\sigma_q \ll w_x$, since the reduction effect is already at its maximum with $\chi_t(x, p) = e^{-t/\tau_e} \chi_0 \left(x - \frac{pt}{m}, p \right)$. Any impact from an enhanced dispersion therefore relatively increases until we reach the regime of diffusive heating with $\hbar/\sigma_q \gg w_x$ for which one can expand the expression (3.10) as

$$\chi_t(x, p) \simeq \exp \left[-\frac{m_e^2}{m^2} \frac{\sigma_q^2 t}{2\hbar^2 \tau_e} \left(x^2 - \frac{xpt}{m} + \frac{p^2 t^2}{3m^2} \right) \right] \chi_0 \left(x - \frac{pt}{m}, p \right). \quad (3.11)$$

To identify the correction terms when implementing the MMM correctly I calculate the overlap with the freely evolved characteristic function. This leads for a Gaussian wave function after the duration T of the experiment to

$$\begin{aligned} & \int \frac{dx dp}{2\pi\hbar} \chi_T(-x, -p) \chi_T^{\text{free}}(x, p) \\ & \simeq \left\{ 1 + 2 \left(\frac{\sigma_q w_x}{\hbar} \right)^2 \frac{m_e^2 T}{m^2 \tau_e} \left[1 + \frac{1}{6} \left(\frac{\hbar T}{m w_x^2} \right)^2 + \frac{T}{24\tau_e} \left(\frac{\sigma_q T}{m w_x} \right)^2 \right] \right\}^{-1/2}. \end{aligned} \quad (3.12)$$

The higher powers in T are the corrections due to the dispersion of the wave packets. Their influence depends on the ratio between the interference time T and the characteristic free dispersion time scale $t_d = m w_x^2 / \hbar$ of a Gaussian wave. With $T = 2.08$ s [33] and an extension of the Gaussian on the millimeter scale it follows that $T \ll t_d$ and the dispersion enhancement is negligible. The transition between the strong depletion and diffusive regime in the heating of populations $P_a = |\psi_a\rangle\langle\psi_a|$ can be described by

$$\langle P_a(T) \rangle \simeq \langle \psi_a | \rho_0 | \psi_a \rangle \exp \left[-\frac{m_e^2 T}{m^2 \tau_e} \left(1 - e^{-w_x^2 \sigma_q^2 / 2\hbar^2} \right) \right] \equiv \langle \psi_a | \rho_0 | \psi_a \rangle H(\sigma_q, \tau_e), \quad (3.13)$$

where slight deviations at $\hbar/\sigma_q \sim w_x$ can be beared with on the logarithmic scale. As stated before, we are only interested in the motion along the x -axis since that is the relevant axis where the superposition takes place. But in contrast to the decoherence the heating occurs in all three dimension which leads to the same term (3.13) but with $w_x \rightarrow \sqrt{w_x^2 + w_y^2 + w_z^2}$.

The second simplification motivated in this section is the introduction of a constant spatial delocalization shown in Fig. 3.1 (b) rather than the superposition state with linearly increasing and decreasing distance shown in 3.1 (a). I will demonstrate that

3. Quantum experiments in presence of classicalizing modifications

the latter scenario can be effectively substituted by a static arm separation leading to the same observable effects. First of all the overall heating is not affected by the type of delocalization (linearly or constant) but only by the mode widths. Thus, the only interesting quantity is the robustness of coherences like $M_{ab} = |\psi_a\rangle\langle\psi_b|$. To determine the decay in the coherences I calculate the overlap with the projector of the undisturbed counterpart only affected by free time evolution

$$\langle M_{ab}(T) \rangle = \langle \psi_a | \rho_0 | \psi_b \rangle \int \frac{dx dp}{2\pi\hbar} M_{ab}(-x, -p, T) M_{b,a}^{\text{free}}(x, p, T) \quad (3.14)$$

Calculating the characteristic symbol of the coherence M_{ab} leads to

$$M_{ab}(x, p) = \exp \left[-\frac{x^2}{8w_x^2} - \frac{(p - \Delta_p)^2 w_x^2}{2\hbar^2} - i \frac{\Delta_p x}{2\hbar} \right] \quad (3.15)$$

Integrating the time evolution (3.9) for time $T/2$, subsequently modeling the reflection of mode b with a momentum displacement $-2\Delta_p$, and as a last step integrating again for $T/2$ leads to

$$M_{ab}(x, p, T) = e^{i\Delta_p(x+pT/2m)/\hbar} R \left(x + \frac{p - \Delta_p}{m} T, p - 2\Delta_p \right) R \left(x + \frac{pT}{2m}, p \right), \quad (3.16)$$

where

$$R(x, p) = \exp \left[\frac{m_e^2}{m^2} \left(\int_0^{T/2} \frac{dt}{\tau_e} e^{-\sigma_q^2(x-pt/m)^2/2\hbar^2} - \frac{T}{2\tau_e} \right) \right]. \quad (3.17)$$

Assuming orthogonality of the two modes a, b the overlap (3.14) becomes

$$\begin{aligned} \langle M_{ab}(T) \rangle &\simeq \langle \psi_a | \rho_0 | \psi_b \rangle \int \frac{dx dp}{2\pi\hbar} M_{ab}(-x, -p, T) M_{a,b}^*(x, p) e^{-i\Delta_p(x+pT/2m)/\hbar} \\ &\simeq \langle \psi_a | \rho_0 | \psi_b \rangle \exp \left\{ -\frac{m_e^2}{m^2} \frac{T}{\tau_e} \left[1 - \frac{\sqrt{2\pi} m \hbar}{\sigma_q \Delta_p T} \operatorname{erf} \left(\frac{\sigma_q \Delta_p T}{2\sqrt{2} m \hbar} \right) \right] \right\}. \end{aligned} \quad (3.18)$$

The last approximation was achieved by assuming a much larger arm separation than wave packet size, $\Delta_p T/2m \gg w_x$, and a negligible dispersion as already argued before. Calculating the same overlap with a constant spatial superposition Δ_x ,

$$M_{ab}(x, p) = \exp \left[-\frac{(x - \Delta_x)^2}{8w_x^2} - \frac{p^2 w_x^2}{2\hbar^2} + i \frac{p \Delta_x}{2\hbar} \right], \quad (3.19)$$

leads under the same assumptions to

$$\langle M_{ab}(T) \rangle \simeq \langle \psi_a | \rho_0 | \psi_b \rangle \exp \left[-\frac{m_e^2}{m^2} \frac{T}{\tau_e} \left(1 - e^{-\Delta_x^2 \sigma_q^2 / 2\hbar^2} \right) \right] \equiv \langle \psi_a | \rho_0 | \psi_b \rangle D(\sigma_q, \tau_e). \quad (3.20)$$

Comparing the expressions (3.18) and (3.20) reveals that the maximum dephasing rate of $1/\tau_e$, obtained for $\sigma_q \gg m\hbar/\Delta_p T$ and $\sigma_q \gg \hbar/\Delta_x$, is the same in both cases. In the opposite limit, where $\sigma_q \ll m\hbar/\Delta_p T$ and $\sigma_q \ll \hbar/\Delta_x$, an expansion in σ_q shows a coincidence of both expressions if $\Delta_x = \Delta_p T/2\sqrt{3}m$. Only during the transition from one limit to the other at $\sigma_q \Delta_x \sim \hbar$ deviations may occur that are irrelevant at least on the logarithmic scale on which the macroscopicity measure operates.

3.1.3. BEC interference in second quantization

To elaborate on the distinction between the three relevant many particle states PS, PAPS and DFS one has to enter the second quantization description that automatically incorporates the indistinguishability of the involved bosonic Rubidium atoms. As a start I will calculate the first and second order expectation values already briefly discussed in the introduction section followed by a thorough calculation of the count statistics that will conclude the discussion.

Expressing the creation and annihilation operators appearing in the Lindblad operator (2.9) in terms of the spatial field operators $\psi(\mathbf{r})$ leads for the MMM generator (2.8) to

$$\begin{aligned} \mathcal{M}_{\sigma\rho} = & \frac{m^2}{\tau_e m_e^2} \int d\mathbf{r} d\mathbf{r}' e^{-(\mathbf{r}-\mathbf{r}')^2/2\hbar^2} \\ & \times \left[\psi^\dagger(\mathbf{r})\psi(\mathbf{r})\rho\psi^\dagger(\mathbf{r}')\psi(\mathbf{r}') - \frac{1}{2} \left\{ \psi^\dagger(\mathbf{r}')\psi(\mathbf{r}')\psi^\dagger(\mathbf{r})\psi(\mathbf{r}), \rho \right\} \right] \end{aligned} \quad (3.21)$$

This can be applied to the output mode operators that are obtained after the recombining beamsplitter as

$$\begin{aligned} \mathbf{c}_{a,\text{out}}^\dagger &= \cos\theta \mathbf{c}_a^\dagger - e^{i\alpha} \sin\theta \mathbf{c}_b^\dagger \\ \mathbf{c}_{b,\text{out}}^\dagger &= e^{-i\alpha} \sin\theta \mathbf{c}_a^\dagger + \cos\theta \mathbf{c}_b^\dagger, \end{aligned} \quad (3.22)$$

where

$$\mathbf{c}_a^\dagger = \frac{1}{\sqrt{2\pi w_x^2}} \int dx e^{-x^2/4w_x^2} \psi^\dagger(x) \quad \text{and} \quad \mathbf{c}_b^\dagger = \frac{1}{\sqrt{2\pi w_x^2}} \int dx e^{-(x-\Delta_x)^2/4w_x^2} \psi^\dagger(x), \quad (3.23)$$

with $\Delta_x = \Delta_p T / 2\sqrt{3}m$ as motivated in the last subsection. The beamsplitter phase α can be absorbed via $\varphi = \phi - \alpha$ and in the following the beamsplitter is assumed to be balanced with $\theta = \pi/4$.

Applying the generator (3.21) leads in the Heisenberg picture to

$$\begin{aligned} \langle \mathbf{c}_{a,\text{out}}^\dagger \mathbf{c}_{a,\text{out}} \rangle &= \left\langle \frac{\mathbf{c}_a^\dagger \mathbf{c}_a + \mathbf{c}_b^\dagger \mathbf{c}_b}{2} \right\rangle H(\sigma_q, \tau_e) - \left\langle \frac{e^{i\alpha} \mathbf{c}_b^\dagger \mathbf{c}_a + e^{-i\alpha} \mathbf{c}_a^\dagger \mathbf{c}_b}{2} \right\rangle D(\sigma_q, \tau_e) \\ \langle \mathbf{c}_{b,\text{out}}^\dagger \mathbf{c}_{b,\text{out}} \rangle &= \left\langle \frac{\mathbf{c}_a^\dagger \mathbf{c}_a + \mathbf{c}_b^\dagger \mathbf{c}_b}{2} \right\rangle H(\sigma_q, \tau_e) + \left\langle \frac{e^{i\alpha} \mathbf{c}_b^\dagger \mathbf{c}_a + e^{-i\alpha} \mathbf{c}_a^\dagger \mathbf{c}_b}{2} \right\rangle D(\sigma_q, \tau_e), \end{aligned} \quad (3.24)$$

with $H(\sigma_q, \tau_e)$ and $D(\sigma_q, \tau_e)$ defined by Eq. (3.13) and Eq. (3.20), respectively. This can be calculated by simple application of the commutation rules of the mode creation and annihilation operators (3.22) in Eq. (3.21).

Keep in mind that the expectation values can be calculated without dispersion as the effect is negligible. Starting with the PS the particle number expectation value oscillates as a function of the phase φ ,

$$\langle \mathbf{c}_{a,\text{out}}^\dagger \mathbf{c}_{a,\text{out}} \rangle_{\text{PS}} = \frac{N}{2} [H(\sigma_q, \tau_e) - \cos(\varphi) D(\sigma_q, \tau_e)]. \quad (3.25)$$

3. Quantum experiments in presence of classicalizing modifications

The average value of $N/2$, approached after the second term vanishes due to decoherence, is additionally reduced on a much longer time scale because of heating provided $\hbar/\sigma_q \gg w_x$. For the PAPS and DFS this is the only effect occurring since there was never any phase information and the first order coherence $\langle c_a^\dagger c_b \rangle$ is zero from the start. Notice that the depletion rate of the output mode occupation in Eq. (3.24) does not depend on the actual number of atoms in the state and that the normalized expectation value decays in the same way. Since the N atoms are in a product state they behave independently, comparable to performing the same experiment sequentially N times with only one atom.

The second order correlation functions can be calculated in the same straightforward manner, the general scheme for arbitrary orders of correlation function is explained in Appendix B.1. For a PS the unnormalized probabilities to detect two particles in the same or in different arms are

$$\langle c_{a,\text{out}}^\dagger c_{a,\text{out}}^\dagger c_{a,\text{out}} c_{a,\text{out}} \rangle_{\text{PS}} = \frac{N(N-1)}{8} \left[3H\left(\sigma_q, \frac{\tau_e}{2}\right) + \cos(2\varphi)D\left(\sigma_q, \frac{\tau_e}{4}\right) - 4\cos(\varphi)D(\sigma_q, \tau_e) \right] \quad (3.26)$$

and

$$\langle c_{a,\text{out}}^\dagger c_{b,\text{out}}^\dagger c_{b,\text{out}} c_{a,\text{out}} \rangle_{\text{PS}} = \frac{N(N-1)}{8} \left[H\left(\sigma_q, \frac{\tau_e}{2}\right) - \cos(2\varphi)D\left(\sigma_q, \frac{\tau_e}{4}\right) \right], \quad (3.27)$$

respectively. The same correlation functions for the PAPS can be immediately derived by averaging over φ to arrive at

$$\begin{aligned} \langle c_{a,\text{out}}^\dagger c_{a,\text{out}}^\dagger c_{a,\text{out}} c_{a,\text{out}} \rangle_{\text{PAPS}} &= \frac{3N(N-1)}{8} H\left(\sigma_q, \frac{\tau_e}{2}\right) \\ \langle c_{a,\text{out}}^\dagger c_{b,\text{out}}^\dagger c_{b,\text{out}} c_{a,\text{out}} \rangle_{\text{PAPS}} &= \frac{N(N-1)}{8} H\left(\sigma_q, \frac{\tau_e}{2}\right). \end{aligned} \quad (3.28)$$

Comparison with a DFS containing $N/2$ particles in each arm,

$$\begin{aligned} \langle c_{a,\text{out}}^\dagger c_{a,\text{out}}^\dagger c_{a,\text{out}} c_{a,\text{out}} \rangle_{\text{DFS}} &= \frac{N(3N-2)}{8} H\left(\sigma_q, \frac{\tau_e}{2}\right) \\ \langle c_{a,\text{out}}^\dagger c_{b,\text{out}}^\dagger c_{b,\text{out}} c_{a,\text{out}} \rangle_{\text{DFS}} &= \frac{N(N-2)}{8} H\left(\sigma_q, \frac{\tau_e}{2}\right), \end{aligned} \quad (3.29)$$

reveals that they differ only by $N/8$ in the prefactor. Consequently, only for small particle numbers a clear distinction between both states can be made, as illustrated in Fig. 3.2. For realistic BEC interferometer setups with $N \gg 1$ this correlator cannot distinguish the states.

This treatment can now be expanded to correlation functions of arbitrary order until one ultimately arrives at the count statistics or, to remain in the language of the Bayesian hypothesis test introduced in Sec. 2.3, at the likelihoods of the MMM parameter to produce the events in every interferometer run. This likelihood to detect n_a particles in output mode a and $N - n_a$ particles in output mode b given (τ_e, σ, I) is

$$P(n_a, N | \tau_e, \sigma, I) = \frac{\langle (c_{a,\text{out}}^\dagger)^{n_a} (c_{b,\text{out}}^\dagger)^{N-n_a} | \text{vac} \rangle \langle \text{vac} | (c_{a,\text{out}})^{n_a} (c_{b,\text{out}})^{N-n_a} \rangle}{n_a! (N - n_a)!} \quad (3.30)$$

3.1. Interference of BEC in product and dual Fock states

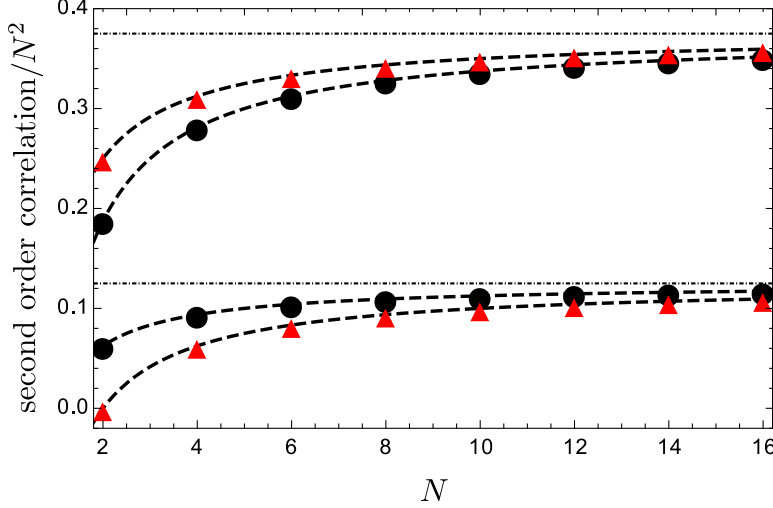


Figure 3.2.: The normalized second order correlation functions of PAPS (circles) from Eq. (3.28) and DFS (triangles) from Eq. (3.29) become less and less distinguishable with increasing particle number N . The upper and lower data refer to the probability to detect two atoms in the same or in different modes, respectively. The dashed curves are plotted to guide the eye, and the dash-dotted lines are the asymptotes achieved by letting $N \rightarrow \infty$ in Eqs. (3.28)-(3.29).

Depending on the condensate state this N -th order expectation value comprises phase-independent terms, only affected by heating induced depletion, and terms oscillating with multiples of φ , affected additionally by dephasing. For the PS this leads to

$$P_{\text{PS}}(n_a, N | \tau_e, \sigma, I) = \frac{1}{2^{2N}} \binom{N}{n_a} \sum_{k, k'=0}^{n_a} (-)^{k-k'} \binom{n_a}{k} \binom{n_a}{k'} \sum_{\ell, \ell'=0}^{N-n_a} \binom{N-n_a}{\ell} \binom{N-n_a}{\ell'} \times \begin{cases} H(\sigma_q, \frac{\tau_e}{N}) & \text{if } k + \ell = k' + \ell', \\ e^{i(k+\ell-k'-\ell')\varphi} D(\sigma_q, \frac{\tau_e}{|k+\ell-k'-\ell'|^2}) & \text{otherwise.} \end{cases} \quad (3.31)$$

The dephasing process for $N = 30$ atoms is depicted in Fig. 3.3. Consistently we have $\sum_{n_a} P_{\text{PS}}(n_a, N | \tau_e, \sigma, I) = H(\sigma_q, \tau_e/N)$, thus the normalization is affected only by the overall depletion. The strong scaling of $P(N | \tau_e, \sigma, I)$ with τ_e/N arises from the requirement of *all* N particles to remain in the condensate. The cumulative case considering all intermediate numbers of remaining atoms is considered later on.

To get the analogous expression for the PAPS one has to phase-average Eq. (3.31) to arrive at

$$P_{\text{PAPS}}(n_a, N | \tau_e, \sigma, I) = \frac{H(\sigma_q, \tau_e/N)}{\pi n_a! (N - n_a)!} \Gamma\left(n_a + \frac{1}{2}\right) \Gamma\left(N - n_a + \frac{1}{2}\right) \xrightarrow{N \gg 1} \frac{H(\sigma_q, \tau_e/N)}{\pi \sqrt{n_a (N - n_a)}}. \quad (3.32)$$

3. Quantum experiments in presence of classicalizing modifications

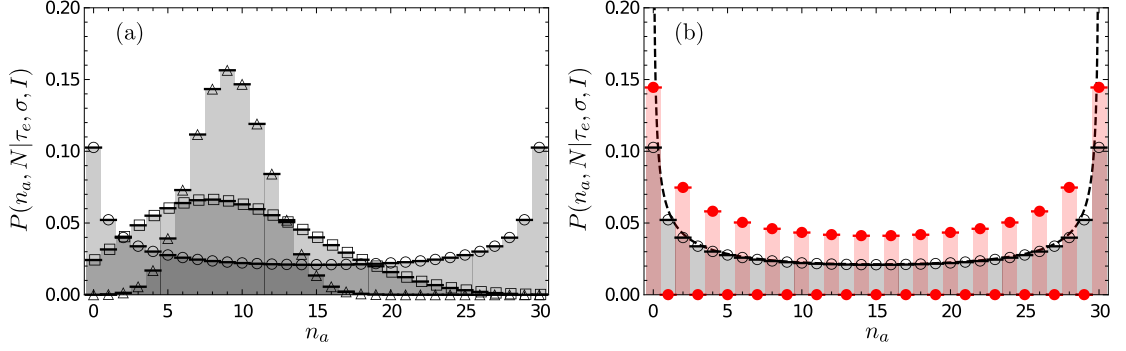


Figure 3.3.: (a) Atom count distribution of a PS (3.31) for 30 particles and $\varphi = -3\pi/8$. While the triangles show the initial state the squares correspond to a dephasing after $T = 0.2\tau_e$ at a moderate dephasing strength $\sigma_q\Delta_x/\hbar = 1$ while assuming negligible heating losses, $H(\sigma_q, \tau_e/30) \simeq 1$. The open dots mark the fully dephased PAPS that is also shown in (b) together with the count statistics of a DFS (3.33) that exhibits the typical Hong-Ou-Mandel dips. Both are (on average in the case of the DFS) very well approximated by the classical intensity distribution (dashed line).

The many-atom expression, $N \gg 1$, is achieved by using Stirling's approximation of the Gamma function. The depletion factor aside, this likelihood is a discrete version of the classical expression $P_{\text{cl}}(I_a|I_0) = 1/\pi\sqrt{I_a(I_0 - I_a)}$. The latter describes the distribution of intensities I_a of classical waves in one output port of a balanced beamsplitter receiving two input beams of equal intensity $I_0/2$ but with a random phase difference [100]. It was also used in the data analysis of Ref. [33]. The classical density distribution is plotted in Fig. 3.3 for $N = 30$ as a dashed line to highlight the excellent agreement with the discrete PAPS and with the DFS, for which the count statistics are given next.

For even N , to ensure same number of particles in each independent BEC, the likelihood for n_a reads

$$P_{\text{DFS}}(n_a, N|\tau_e, \sigma, I) = H\left(\sigma_q, \frac{\tau_e}{N}\right) \begin{cases} \frac{(2j)!\Gamma(N/2-j+1/2)}{\sqrt{\pi}2^{2j}(j!)^2(N/2-j)!} & \text{if } n_a = 2j \text{ even,} \\ 0 & \text{otherwise.} \end{cases} \quad (3.33)$$

The Hong-Ou-Mandel effect which we already observed explicitly for two particles with help of the correlation functions (3.29) is present in the count statistics as a generalized Hong-Ou-Mandel effect, see Ref. [100]. The case of undepleted distributions of DFS with unbalanced population $N_a \neq N_b$, as well as their different HOM signatures, are examined in detail in the same reference. In the limit of many atoms, $N \gg 1$, one can once again approximate with Stirling's formula to arrive at

$$P_{\text{DFS}}(2j, N \gg 1|\tau_e, \sigma, I) \simeq 2P_{\text{cl}}(2j, N)H(\sigma_q, \tau_e/N). \quad (3.34)$$

This coincides with the many atom limit of the PAPS, implying that the two are indistinguishable in the low order correlation functions. But measuring on the single atom level would allow one to tell apart both phase independent condensate states thanks to the generalized Hong-Ou-Mandel effect.

3.1. Interference of BEC in product and dual Fock states

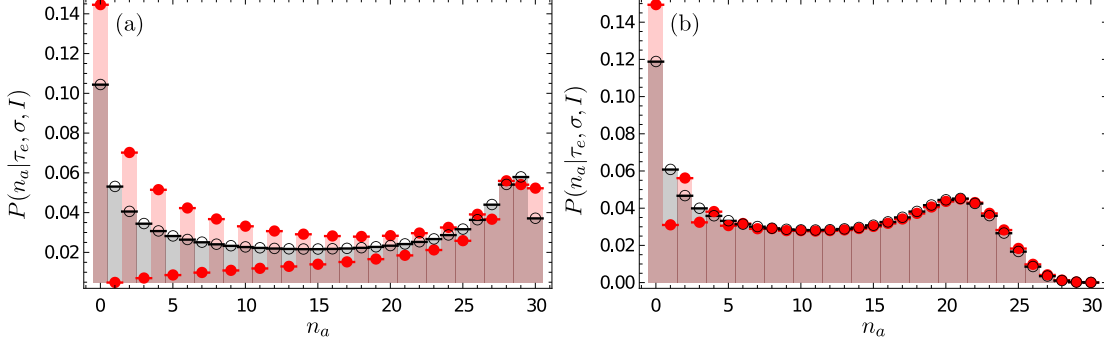


Figure 3.4.: Shown is the count statistics for dephased PS (3.36), open dots, and DFS (3.37), filled dots, with particle loss. (a) If only one particle on average is lost the Hong-Ou-Mandel dips at the higher end of the spectrum are already lost. (b) If on average 25% of the condensate is lost almost all of the DFS signature is gone and it is indistinguishable from the PAPS except for very small n_a . Note that for particle loss $n_a + n_b = N$ is no longer fulfilled which leads to the asymmetry in the distributions.

In reality the atom number in the condensate gets diminished because of the MMM induced heating and instead of Eq. (3.30) we have a sum over all possible remaining number of particles N_d reaching the final beamsplitter,

$$P(n_a|\tau_e, \sigma, I) = \sum_{N_d=0}^N P(n_a, N|\tau_e, \sigma, I) = \sum_{N_d=0}^N P(n_a|N_d, \tau_e, \sigma, I)P(N_d|\tau_e, \sigma, I). \quad (3.35)$$

Here $P(n_a|N_d, \tau_e, \sigma, I) = [P(n_a, N_d|\tau_e, \sigma, I)]_{H=1}$ are simply the undepleted count probabilities. In an experiment where the initial atom number N is not precisely known an additionally convolution with an appropriate distribution in N can be implemented.

Calculating the resulting likelihood (3.35) for n_a alone is in case of a PS, and therefore for a PAPS as well, equal to a Bernoulli process characterized by the survival probability $H = H(\sigma_q, \tau_e)$

$$P_{\text{PS}}(n_a|\tau_e, \sigma, I) = \sum_{N_d}^N \binom{N}{N_d} H^{N_d} (1-H)^{N-N_d} P_{\text{PS}}(N_a|N_d, \tau_e, \sigma, I). \quad (3.36)$$

In complete analogy to Eq. (3.35) the likelihood for the DFS is equal to two independent depletion processes removing atoms in each of the two independent condensates,

$$P_{\text{DFS}}(n_a|\tau_e, \sigma, I) = \sum_{N_a, N_b=0}^{N/2} \binom{N/2}{N_a} \binom{N/2}{N_b} H^{N_a+N_b} (1-H)^{N-N_a-N_b} P(n_a|N_a, N_b, \tau_e, \sigma, I). \quad (3.37)$$

In this full scenario the Hong-Ou-Mandel dips vanish rather quickly due to the summation over different numbers of remaining particles as shown in Fig. 3.4. There, the DFS

3. Quantum experiments in presence of classicalizing modifications

is compared to a PS in the two scenarios $H = 1 - 1/30$ and $H = 0.75$ which resembles an average loss of a single particle or 25% of the condensate, respectively (dephasing plays no role in the case of DFS and PAPS).

In principle, the count statistics (3.36) for the PS can be used as a likelihood for the Bayesian hypothesis test motivated in the previous chapter to assess macroscopicities as it is the exact solution for Mach-Zehnder interferometry with product states (or coherent quasi spin states in two modes) in presence of MMM. But since in reality thousands of atoms are involved in such a setup, the exact solution is not really necessary as long as no measurement precision on the single atom level is achieved. More practicable is the continuum approximation brought forward in the next section where it is derived to describe squeezed states.

3.2. Ramsey interferometry with a number-squeezed BEC

We learned in the previous section according to the measure defined in Sec. 2 that interference of a product state is not more macroscopic than the consecutive interference of the involved single particles. In the case of number-squeezed BEC that were interfered by the authors of Ref. [31] the quantum state is no longer separable. Rather it indicates a high depth of entanglement as shown in [106–108] and will be explained below. This may lead to an enhanced macroscopicity compared to even the ideal phase stable superposition state discussed in the previous section. This section draws on results of my master thesis [109] which discussed the effect of MMM on collective spin states. The results presented in this section are published in Ref. [55].

3.2.1. Collective spin states

In close analogy to the quasi-spin representation of single particles in two level configurations one can formulate a collective spin state of a many particle state where all particles are restricted to the same two level system. One starts defining quasi angular momentum operators acting on the collective pseudospin similar to Pauli matrices [110]:

$$\begin{aligned} J_x &= \frac{1}{2} \left(c_a^\dagger c_b + c_b^\dagger c_a \right) \\ J_y &= \frac{1}{2i} \left(c_a^\dagger c_b - c_b^\dagger c_a \right) \\ J_z &= \frac{1}{2} \left(c_a^\dagger c_a - c_b^\dagger c_b \right), \end{aligned} \quad (3.38)$$

where $c_{a,b}$ are the annihilation operators of the two modes. The quasi angular momentum operators (3.38) fulfill the angular momentum commutation relations $[J_\lambda, J_\mu] = i\epsilon_{\lambda,\mu,\nu} J_\nu$ and the simultaneous eigenstates of J^2 with eigenvalues $J(J+1)$ and J_z with eigenvalues m are denoted as Dicke states

$$|J, m\rangle = \frac{(c_a^\dagger)^{J+m} (c_b^\dagger)^{J-m}}{\sqrt{(J+m)!(J-m)!}} |\text{vac}\rangle, \quad (3.39)$$

3.2. Ramsey interferometry with a number-squeezed BEC

where $J = N/2$.

Product states of N atoms in a superposition between the two modes a, b read in this basis as

$$\begin{aligned} |\theta, \phi\rangle &\equiv \frac{1}{\sqrt{(2J)!}} \left(\cos\left(\frac{\theta}{2}\right) c_a^\dagger + e^{i\phi} \sin\left(\frac{\theta}{2}\right) c_b^\dagger \right)^{2J} |\text{vac}\rangle \\ &= \sum_{m=-J}^J \binom{2J}{J+m} \cos^{J-m}\left(\frac{\theta}{2}\right) \sin^{J+m}\left(\frac{\theta}{2}\right) e^{-i(J+m)\phi} |J, m\rangle. \end{aligned} \quad (3.40)$$

They are referred to as *coherent spin states* (CSS) and form an overcomplete basis. They can be represented on a general Bloch sphere (see Fig. 3.7), whose polar angle θ indicates the relative population in a and b , while the azimuth ϕ denotes the relative phase of the superposition state².

The name CSS reflects the fact that the state (3.40) is a discretized version of the ordinary coherent state in Fock space. This can be observed for

$$|\theta, \phi = 0\rangle = \sum_{k=0}^N \sqrt{\binom{N}{k} \sin^{2k}\left(\frac{\theta}{2}\right) \cos^{2N-2k}\left(\frac{\theta}{2}\right)} \frac{(c_a^\dagger)^k (c_b^\dagger)^{N-k}}{\sqrt{k!(N-k)!}} |\text{vac}\rangle, \quad (3.41)$$

by taking the limit $N \rightarrow \infty$ for $N \sin^{2k}(\theta/2) = \text{const}$. The Binomial distribution in Eq. (3.41) then turns asymptotically into a Poisson distribution and Eq. (3.41) becomes

$$|\alpha\rangle = \exp\left[-\frac{1}{2}|\alpha|^2\right] \sum_{k=0}^{\infty} \frac{\alpha^k}{\sqrt{k!}} |k\rangle, \quad \text{with } |k\rangle = \frac{(c_a^\dagger)^k (c_b^\dagger)^{N-k}}{\sqrt{k!(N-k)!}} |\text{vac}\rangle \quad (3.42)$$

and $\alpha = \sqrt{N} \sin^k(\theta/2)$. The general case for $|\theta, \phi \neq 0\rangle$ can be obtained by applying $e^{i\phi J_z}$ on Eq. (3.42). With $J_z |k\rangle = (k - N/2) |k\rangle$ we then get $\alpha = \sqrt{N} \sin^k(\theta/2) e^{i\phi}$ and a global phase $e^{-iN\phi/2}$. Equation (3.42) is the well known coherent state [111] with minimal and symmetric uncertainties in amplitude. It is in some sense the most classical quantum state.

Just like this coherent state the CSS (3.40) also shows minimal and symmetric uncertainties but now with respect to the angular momentum operators which do not commute. E.g. for $\theta = \pi/2$ and $\phi = 0$ this leads to $\Delta J_z^2 = \Delta J_y^2 = |\langle J_x \rangle|/2 = J/2$ whereas $\Delta J_x^2 = J^2$. This type of uncertainties can also be obtained for other values of θ, ϕ perpendicular to the main spin direction and thus in general for linear combinations of the J_μ .

Just as a regular coherent state (3.42) can be squeezed to shift the symmetry in uncertainty more in favor of a narrow variance in particle number *or* in phase the CSS can be squeezed to lower the variance of one of the perpendicular angular momenta,

²It should be re-emphasized that the J_μ are only quasi angular momentum operators without a respective conjugate orientation space. Especially the angles θ, ϕ on the general Bloch sphere are *not* conjugated to any projections of the angular momenta as it is the case for the Euler angles of a real orientational state in Sec. 4.

3. Quantum experiments in presence of classicalizing modifications

which we want to call J_{\min} , below $J/2$. This can be achieved by applying nonlinear squeezing operators [112, 113] and the resulting *squeezed spin states* (SSS) are useful tools for metrology [114–116] or are more robust against dephasing processes [31, 104]. Either way, due to the squeezing the resulting state is no longer a product state [106] and the *depth of entanglement* achieved can be assessed quantitatively [107, 108] by identifying the largest subsets for which the state is not separable which will be explained in Sec. 3.2.4. This level of non-separability increases with the squeezing parameter

$$\xi^2 = 2(\Delta J_{\min})^2/J \quad (3.43)$$

as long as the perpendicular variance does not increase too much.

From the discussion in Sec. 2.1 we learned that entanglement in general leads to a higher vulnerability of states against the MMM-induced decoherence, which suggests SSS to be good candidates to falsify a great range of modification parameters. Macroscopicity measures that use for example the Quantum Fisher Information [50] would even certify an increased macroscopicity alone from the existence of such a squeezed state since the QFI increases with decreasing ξ . This can be verified easily by exploiting the fact that the squeezed state is still pure and therefore the QFI is simply the largest variance of the collective spin (see Sec. 2.1.1). The variance perpendicular to the main spin direction and J_{\min} increases due to squeezing and according to Eq. (2.4) one has to maximize the QFI with respect to the sum of single particle operators, here leading to a linear combination of the J_{μ} . Thus, the connection between squeezing and effective size according to [50] is obvious.

To remain in the spirit of the original macroscopicity measure [51] and the scheme established in Sec. 2.3 I will discuss the consequences of squeezing on the measurement protocol and the impact on the probabilities of the different observables measured in an experiment.

3.2.2. Measurement scheme

The experiment reported in Ref. [31] consists of a number-squeezed ($J_{\min} = J_z$) BEC of about 1200 ^{87}Rb atoms occupying the two lowest eigenstates of a double well potential. The latter have a slight energy gap ϵ because the whole potential is tilted in the gravitational potential. The free time evolution $\mathcal{L}\rho = -i[\mathbf{H}, \rho]/\hbar$ further involves the interaction between the atoms which leads in lowest approximation to the Hamiltonian [104]

$$\mathbf{H} = \epsilon J_z + \hbar\zeta J_z^2. \quad (3.44)$$

Here, $\zeta = d\tilde{\mu}/d(\hbar m)|_{m=0}$ is the change of the chemical potential $\tilde{\mu}$ with the occupation difference m at an even distribution in both modes. The first term in Eq. (3.44) leads to a rotation of the state with an angular frequency ϵ/\hbar around the z -axis of the general Bloch sphere. The second term leads to dispersion as if the two poles of the general Bloch sphere were twisted in opposite directions. This is the very mechanism used to create *one-axis-twisting* [112] by increasing ζ for a short time, e.g. by tightening the potential. Certainly this dispersion during the free interference time is uncalled for and the number squeezing is implemented to counter the effect.

3.2. Ramsey interferometry with a number-squeezed BEC

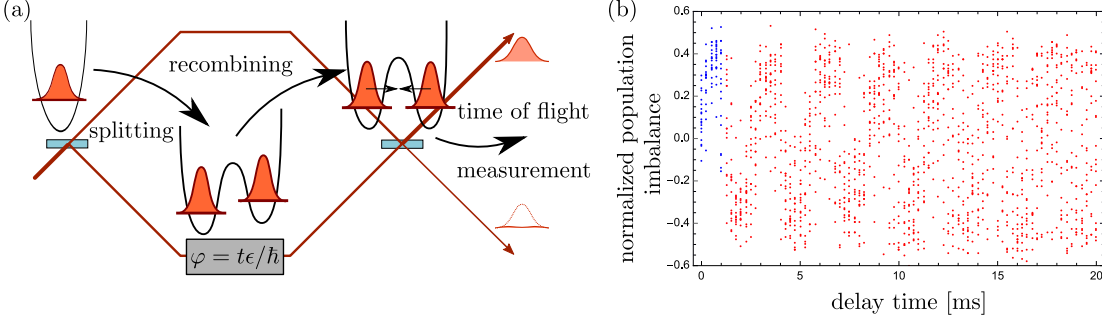


Figure 3.5.: (a) Shown is a schematic illustration of the double-well BEC interference experiment [31] following a Ramsey interference scheme as described in the main text. The BEC is initially split into a superposition between slightly detuned left and right double-well states, then number squeezed, then let to freely evolve for a delay time, before a final $\pi/2$ -pulse (recombiner) converts the phase difference between the states into an occupation difference. (b) Time-of-flight measurement data of the occupation imbalance versus delay time (from Ref. [31]).

The measurement protocol, shown in Fig. 3.5, resembles a Ramsey interferometer and is executed as follows: The BEC is prepared in the CSS $|\theta = \pi/2, \phi = 0\rangle$ (splitting), corresponding to a superposition between the double wells, and then squeezed in z -direction, i.e. in the population difference. After a free evolution under Eq. (3.44) a $\pi/2$ -rotation around the x -axis is performed (recombining) so that the phase distribution is converted to a distribution in the mode occupation difference. The double-well potential is then switched off and the two modes depart from each other with a relative momentum. After some time of flight the number difference is read out by fluorescence photon counting.

This protocol determines the likelihood (2.50) required for the hypothesis test as

$$P(m|\tau_e, \sigma, I) = \sum_{J=0}^{\infty} \langle J, m | e^{-i\pi J_x/2} \rho_t e^{i\pi J_x/2} | J, m \rangle, \quad (3.45)$$

being the likelihood for a certain set of MMM parameters to lead to the particle difference m between the modes. The sum over J accounts for the possibility that particles are removed from the BEC due to the MMM-induced heating. This and the overall MMM-induced decoherence are now incorporated by adding the Lindblad generator to the free time evolution (3.44).

3.2.3. Classicalizing modifications in the collective spin picture

Since all relevant length scales are on the micrometer level we can neglect spatial displacements and set $g_\sigma(s, q) = f_\sigma(q)\delta(s)$ in Eq. (2.8). Further, the creation and annihilation operators in the Lindblad operator (2.9) can be expanded in the eigenstates of the double-well potential,

$$\mathbf{c}^{(\dagger)}(\mathbf{p}) = \sum_{\mu} \psi_{\mu}^{(*)}(\mathbf{p}) \mathbf{c}_{\mu}^{(\dagger)}. \quad (3.46)$$

3. Quantum experiments in presence of classicalizing modifications

For the moment I will neglect all contributions of other modes besides the two ground states of the double-well potential. This is valid if the momentum displacements are too weak to scatter particles out of the condensate.

We arrive at a Lindblad generator

$$\mathcal{M}_\sigma \rho = \frac{4m_{\text{Rb}}^2}{\tau_e m_e^2} \int d^3 \mathbf{q} f_\sigma(q) \left[\mathbf{A}(\mathbf{q}) \rho \mathbf{A}^\dagger(\mathbf{q}) - \frac{1}{2} \{ \mathbf{A}^\dagger(\mathbf{q}) \mathbf{A}(\mathbf{q}), \rho \} \right], \quad (3.47)$$

with Lindblad operators

$$\begin{aligned} \mathbf{A}(\mathbf{q}) = & \frac{1}{2} \int d^3 \mathbf{p} \left(\psi_a^*(\mathbf{p} - \mathbf{q}) \psi_a(\mathbf{p}) \mathbf{c}_a^\dagger \mathbf{c}_a + \psi_a^*(\mathbf{p} - \mathbf{q}) \psi_b(\mathbf{p}) \mathbf{c}_a^\dagger \mathbf{c}_b \right. \\ & \left. + \psi_b^*(\mathbf{p} - \mathbf{q}) \psi_a(\mathbf{p}) \mathbf{c}_b^\dagger \mathbf{c}_a + \psi_b^*(\mathbf{p} - \mathbf{q}) \psi_b(\mathbf{p}) \mathbf{c}_b^\dagger \mathbf{c}_b \right). \end{aligned} \quad (3.48)$$

By using the fact that $\mathbf{c}_a^\dagger \mathbf{c}_a + \mathbf{c}_b^\dagger \mathbf{c}_b = \text{const.}$ and $\psi_b(\mathbf{r}) = \psi_a(\mathbf{r} - \Delta_x \mathbf{e}_x) \in \mathbb{R}$ Eq. (3.48) can be expressed by the angular momentum operators (3.38) as

$$\mathbf{A}(\mathbf{q}) = a_x(\mathbf{q}) \mathbf{J}_x + a_z(\mathbf{q}) \mathbf{J}_z, \quad (3.49)$$

with

$$\begin{aligned} a_x(\mathbf{q}) &= \langle \psi_a | \mathbf{W}(\mathbf{q}) | \psi_b \rangle \\ a_z(\mathbf{q}) &= i \sin \left(\frac{\Delta_x q_x}{2\hbar} \right) e^{i\Delta_x q_x / 2\hbar} \langle \psi_a | \mathbf{W}(\mathbf{q}) | \psi_a \rangle, \end{aligned} \quad (3.50)$$

where $\mathbf{W}(\mathbf{q}) = \exp(i\mathbf{q} \cdot \mathbf{r} / \hbar)$ is the momentum transfer operator.

The operator (3.49) is a sum of two angular momentum operators widely used to model disturbance channels when describing collective spin states [113, 117]: \mathbf{J}_x induces rotations around the x -axis, or *spin-flips*, and the \mathbf{J}_z induces rotations around the z -axis, or *phase flips*. These quantum channels lead to a smearing of any state perpendicular to the mentioned axes. In this specific case the spin-flips are strongly suppressed as there is practically no spatial overlap between the two ground modes, so that $a_x(\mathbf{q}) \ll a_z(\mathbf{q})$ irrespective of the size of \mathbf{q} . This implies that $\langle \mathbf{J}_z^2 \rangle_t$, and therefore the initial squeezing ξ , remains constant.

We could calculate a macroscopicity with help of expression (2.16) by simply identifying the visibility associated with the interference pattern shown in Fig. 3.5. This visibility would scale with $\langle \mathbf{J}_y \rangle_t$ which decays under the influence of the MMM as

$$\langle \mathbf{J}_y \rangle_t = e^{-\Gamma_P t / 2} \langle \mathbf{J}_y \rangle_{f,t}, \quad \text{with} \quad \Gamma_P = \frac{4m_{\text{Rb}}^2}{\tau_e m_e^2} \int d^3 \mathbf{q} f_\sigma(q) |a_z(\mathbf{q})|^2. \quad (3.51)$$

Here, $\langle \mathbf{J}_y \rangle_{f,t}$ denotes expectation values under the free time evolution produced by the Hamiltonian (3.44); an analogous equation holds for $\langle \mathbf{J}_x \rangle_t$. We observe that the phase-flip decay rate (or dephasing rate) Γ_P does not depend on the degree of squeezing.

3.2. Ramsey interferometry with a number-squeezed BEC

The same holds true for the induced diffusion in the azimuthal plane. Monitoring the diffusion with help of the second moments reveals

$$\langle J_y^2 \rangle_t = \frac{1}{2} \langle J_x^2 + J_y^2 \rangle_{f,t} - \frac{e^{-2\Gamma_P t}}{2} \langle J_x^2 - J_y^2 \rangle_{f,t}, \quad (3.52)$$

and

$$\langle J_x^2 \rangle_t = \frac{1}{2} \langle J_x^2 + J_y^2 \rangle_{f,t} - \frac{e^{-2\Gamma_P t}}{2} \langle J_y^2 - J_x^2 \rangle_{f,t}. \quad (3.53)$$

For realistic amounts of squeezing (For example $\xi = 0.41$ at $J = 600$ in Ref. [31]) the state is still distributed narrowly in the mean spin direction it holds that $\langle J_x^2 \rangle_{f,t} \approx J^2$ and the change of second moments due to the MMM is independent of squeezing as well.

The resulting independence of the visibility from squeezing implies that single particle observables do not profit from any depth of entanglement macroscopicity-wise according to the original measure leading to Eq. (2.16). To calculate the macroscopicity via Eq. (2.58) we still require the likelihoods of all possible particle differences (3.45). I will derive them in Sec. 3.2.5 after shortly discussing the loss of entanglement in the squeezed BEC that can already be observed with help of the collective observables.

3.2.4. Death of entanglement I

The depth of entanglement was brought forward in Ref. [107]. This entanglement measure is based on a simple inequality of angular momentum operators, namely [118]

$$\langle J_x \rangle^2 + \langle J_y^2 \rangle + \langle J_z^2 \rangle \leq J(J+1). \quad (3.54)$$

Together with Heisenberg's uncertainty $\Delta J_y^2 \Delta J_z^2 \leq \langle J_x \rangle^2 / 4$ and with $\langle J_z^2 \rangle \geq \Delta J_z^2$, we arrive at

$$\Delta J_z^2 (J(J+1) - \langle J_x \rangle^2 - \Delta J_z^2) \geq \frac{1}{4} \langle J_x \rangle^2, \quad (3.55)$$

which implies a lower bound on ΔJ_z^2 via

$$\Delta J_z^2 \geq \frac{1}{2} \left(J(J+1) - \langle J_x \rangle^2 - \sqrt{(J(J+1) - \langle J_x \rangle^2)^2 - \langle J_x \rangle^2} \right). \quad (3.56)$$

For large J this comes close to the tight minimum found with numerical methods and shown in Fig. 3.6.

Now the authors of Ref. [107] deduced that whenever a collective spin state is separable,

$$\rho = \sum_k p_k \rho_1^{(k)} \otimes \rho_2^{(k)} \otimes \dots \otimes \rho_N^{(k)}, \quad \sum_k p_k = 1, \quad (3.57)$$

3. Quantum experiments in presence of classicalizing modifications

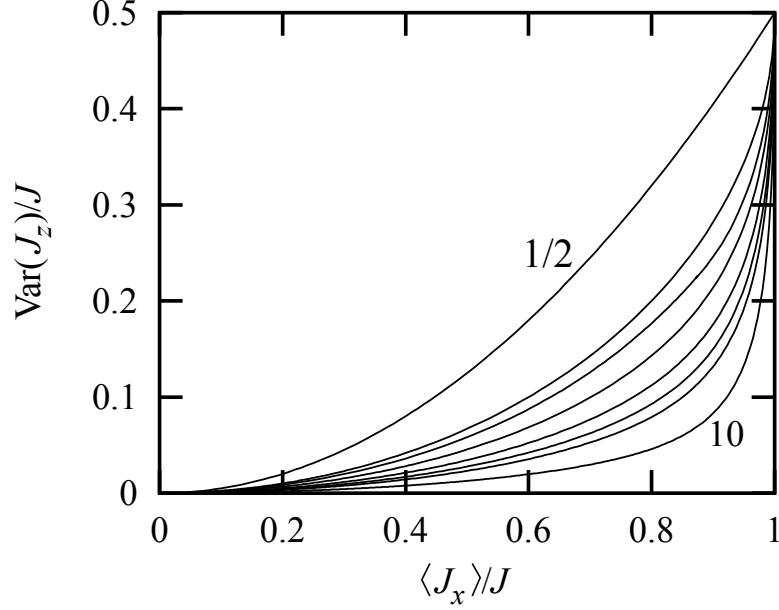


Figure 3.6.: Shown are the minimal ΔJ_z^2 as a function of $\langle J_x \rangle$ normalized by J and found numerically via Lagrange multipliers. Starting from above, the curves represent $j = 1/2, 1, 3/2, 2, 3, 4, 5, 10$. If the observation in an experiment leads to a point above the respective curve (but under the one resembling the next smaller j) the state is entangled at the $(2j - 1)$ -particle level. The Plot is taken from Ref. [107] and reduced to the here relevant statements while interchanging J_x and J_z to better fit to the relevant direction of squeezing in this section.

its variance must be greater or equal to the sum of the individual one-particle variances. From this follows

$$\Delta J_z^2 \geq \sum_k p_k \sum_i^N j F_j \left(\frac{\langle J_x \rangle_i^{(k)}}{j} \right), \quad (3.58)$$

with F_j being the numerical result shown in Fig. 3.6 as function of the individual $\langle J_x \rangle_i$. If the inequality (3.58) is not fulfilled the state is definitely entangled but we can go even further: Since all F_j are convex one can move both sums in Eq. (3.58) into the argument of F_j to arrive at

$$\Delta J_z^2 \geq J F_j \left(\frac{\langle J_x \rangle}{J} \right). \quad (3.59)$$

Sweeping through the different F_j from above we eventually arrive at a j for which the inequality (3.59) holds, meaning that the state is entangled at least on the $(2j - 1)$ -particle level. Thus, even by measuring solely collective observables one can qualitatively estimate the depth of entanglement in the condensate.

Turning back to the MMM, we can directly observe the impact on the entanglement depth with help of Eq. (3.51). Even though the variance in z -direction is not affected

3.2. Ramsey interferometry with a number-squeezed BEC

by MMM the state is smeared out over the equator eventually leading to $\langle J_x \rangle \rightarrow 0$ so that Eq. (3.59) will hold for every j . As such the MMM verifiably lead to a *death of entanglement* once again underlining the classicalizing nature of the modifications. Note however that the verification of entanglement via Eq. (3.59) only goes in one direction; states that fulfill the inequality are not automatically separable, but possible entanglement is simply not verified.

3.2.5. Continuum approximation

For a product state the discrete likelihood (3.45) would be as easy to calculate as the expression (3.31), but the nonlinear squeezing of the initial state complicates the calculation tremendously. To alleviate this, I will use a continuum approximation in the the tangent plane of the general Bloch sphere as sketched in Fig. 3.7. Since $J \gg 1$ we can replace the discrete and bounded (J_y, J_z) by continuous and unbounded (j_y, j_z) and use that $\langle [J_y, J_z] \rangle = i \langle J_x \rangle \simeq iJ$ is no longer operator valued. A squeezed binomial distribution is still very well approximated by a Gaussian and thus one can write the Wigner function of the state in the tangent plane as

$$w_0(j_y, j_z) = \frac{1}{\sqrt{4\pi^2 \langle J_y^2 \rangle_0 \langle J_z^2 \rangle_0}} \exp \left[-\frac{1}{2} \frac{j_y^2}{\langle J_y^2 \rangle_0} - \frac{1}{2} \frac{j_z^2}{\langle J_z^2 \rangle_0} \right]. \quad (3.60)$$

Of course, also in the continuous case the free time evolution produced by the Hamiltonian (3.44) leads to free rotation and dispersion. Together with the diffusion induced by the phase flip operator in the Lindblad operator (3.49) the modified von Neumann equation reads

$$\partial_t \rho = \frac{1}{i\hbar} [\varepsilon j_z + \hbar \zeta j_z^2, \rho] + \Gamma_P \left[j_z \rho j_z - \frac{1}{2} \{j_z^2, \rho\} \right] \quad (3.61)$$

For the Wigner function 3.60 this leads to the following differential equation

$$\begin{aligned} \partial_t w_t(j_y, j_z) &= \frac{1}{2\pi} \int dq e^{-iq_z j_y} \left\langle j_z - \frac{q}{2} \left| \partial_t \rho \right| j_z + \frac{q}{2} \right\rangle \\ &= - \left(\frac{\varepsilon}{\hbar} + 2\zeta j_z \right) \partial_{j_y} w_t(j_y, j_z) + \frac{\Gamma_P}{2} \partial_{j_y}^2 w_t(j_y, j_z). \end{aligned} \quad (3.62)$$

Equation (3.62) is solved by

$$w_t(j_y, j_z) = \frac{1}{\sqrt{4\pi^2 \left(\langle J_y^2 \rangle_0 + \Gamma_P J^2 t \right) \langle J_z^2 \rangle_0}} \exp \left[-\frac{1}{2} \frac{(j_y - \varepsilon t / \hbar - 2\zeta j_z t)^2}{\langle J_y^2 \rangle_0 + \Gamma_P J^2 t} - \frac{1}{2} \frac{j_z^2}{\langle J_z^2 \rangle_0} \right], \quad (3.63)$$

implying that the marginal distribution of j_z remains unaffected by the dynamics as already stated in the preceding subsection.

3. Quantum experiments in presence of classicalizing modifications

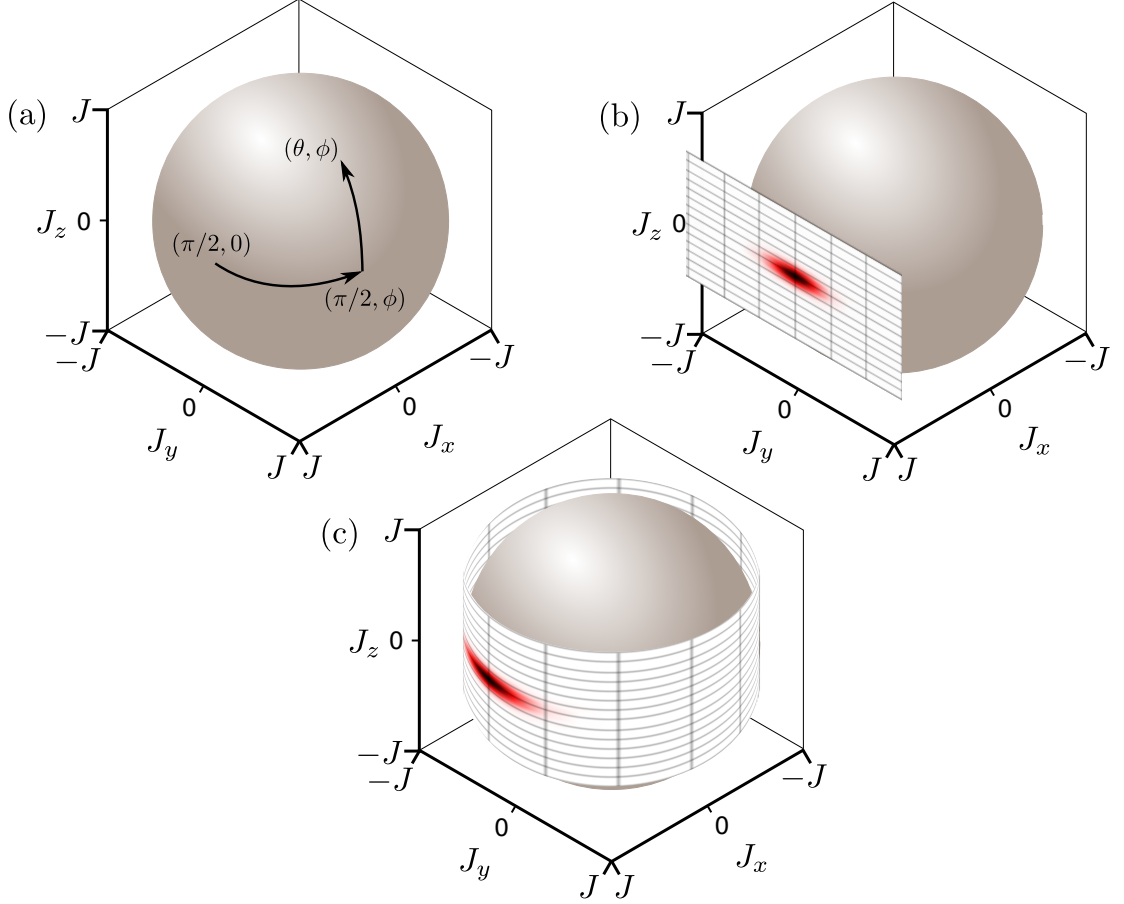


Figure 3.7.: (a)-(c) The continuum approximation maps a well localized state onto the tangent plane of the general Bloch sphere. After applying the time evolution (3.62) the resulting state is wrapped back onto the sphere.

The $\pi/2$ -rotation around the x -axis in Eq. (3.45) is performed by simply exchanging j_y and j_z in Eq. (3.63). Further, the populations in m are obtained after an integration over j_y . Finally, we are still in the flat plane (or now rather a flat line after the marginalization) and the distribution in j_z has to be wrapped back onto the sphere by using $\sin(j_z) = m/J$. Because of the periodicity one has to sum over $j_z + 2\pi k$ with $k \in \mathbb{Z}$ eventually resulting in the continuous probability density approximating the likelihood (3.45),

$$p_J(m|\tau_e, \sigma, I) = \frac{\Theta(J^2 - m^2)}{2\pi\sqrt{J^2 - m^2}} \left[\vartheta_3 \left(\frac{\arcsin(m/J) - \epsilon t/\hbar}{2}, g(t) \right) + \vartheta_3 \left(\frac{\pi - \arcsin(m/J) - \epsilon t/\hbar}{2}, g(t) \right) \right]. \quad (3.64)$$

Here, $\Theta(\cdot)$ denotes the Heaviside function and ϑ_3 the Jacobi-theta function of the third

3.2. Ramsey interferometry with a number-squeezed BEC

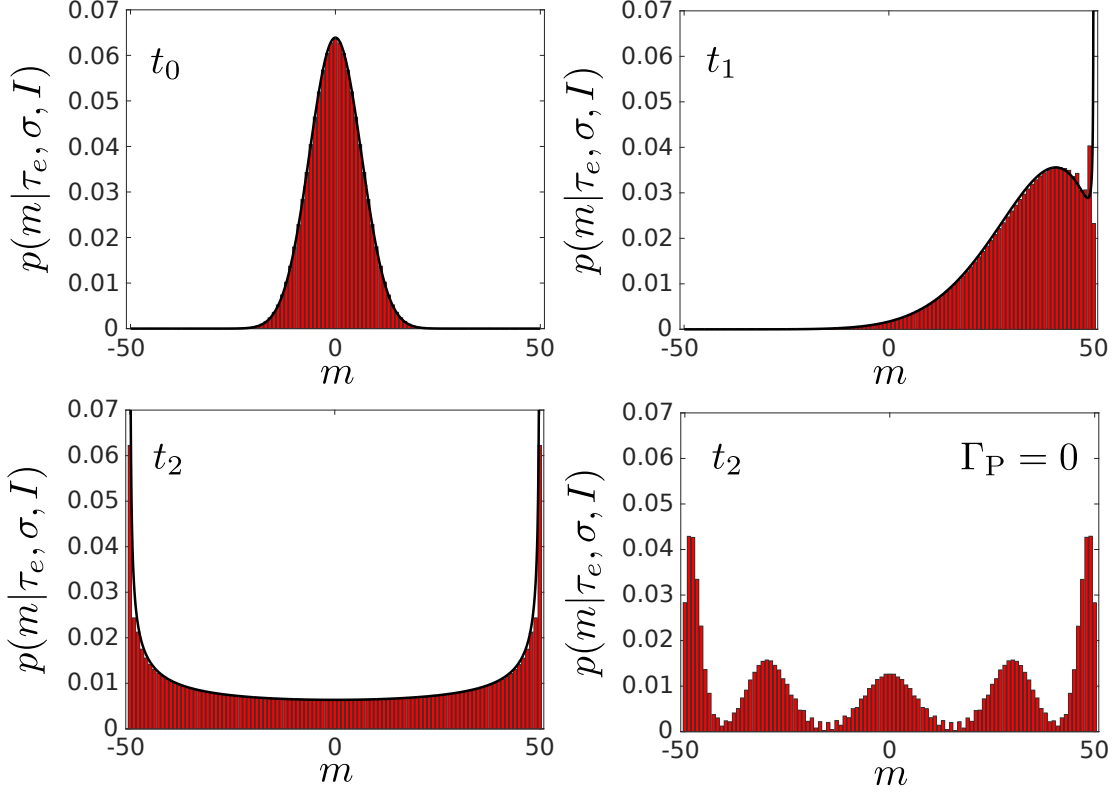


Figure 3.8.: The result of the continuum approximation (shown here with black lines) is compared to exact numerical calculation of probabilities of number differences (red histogram) revealing very good agreement. These numerics are obtained for $N = 100$ particles and an initial variance of $\Delta J_z^2 = N/5$, thus a number squeezed state is at hand which was produced by means of one-axis-squeezing [112]. The different times are $t_0 = 0$, $t_1 = 5.25 \pi \hbar / \epsilon$, and $t_2 = 400 \pi \hbar / \epsilon$ and the parameters are $\Gamma_P = \zeta = 0.002 \epsilon / \hbar$. At time t_2 the distribution practically assumes the steady state of full dephasing. Without phase diffusion (partial) revivals take place, for example at the time t_2 shown in the last graphic. A complete revival of the initial state occurs at $t = 10^3 \pi \hbar / \epsilon$ when the smallest angular momentum $m = 1$ performs a complete rotation due to the dispersion with $e^{im\zeta t} = 1$.

kind,

$$\vartheta_3(u, q) = \sum_{n=-\infty}^{\infty} q^{n^2} e^{2inu}, \quad (3.65)$$

which reflects the periodicity of the problem. The dependence on the initial state is contained in the function

$$g(t) = \exp \left[-\frac{\langle J_y^2 \rangle_0}{2J^2} - \frac{\Gamma_P t}{2} - 2\zeta^2 t^2 \langle J_z^2 \rangle_0 \right]. \quad (3.66)$$

3. Quantum experiments in presence of classicalizing modifications

Note that Eq. (3.64) is the result for any generic dephasing effect leading to a Lindblad generator with the Lindblad operator J_z , for example due to collisions with a gaseous environment. It provides an adequate approximation as evident by comparison with the exact numerical results shown in Fig. 3.8. The only drawback of this method is the loss of the discrete nature of the angular momenta which prevents any (partial) quantum revivals. This is of no concern in the here discussed experimental scheme from Ref. [31] but calls for a more elaborated approach if any revival experiments with squeezed collective spin states shall be studied under the influence of MMM.

Evaluation of Eq. (3.64) may now be carried out if particle loss can be ignored. Unfortunately however over the whole range of σ any relevant decoherence effect (generated by adaption of τ_e) is accompanied by considerable heating. Even though we are not interested in ruling out MMM parameters by unobserved heating the particle loss in the current scenario cannot simply be factorized and must be implemented in the description.

3.2.6. Heating-induced particle loss

Particles may be scattered into excited states by the MMM and by neglecting any back scattering into the condensate, which would be a justified assumption for large σ_q , one arrives at an exponential decay of the ground state populations,

$$\langle \mathbf{c}_a^\dagger \mathbf{c}_a \rangle_t = e^{-\Gamma_L t} \langle \mathbf{c}_a^\dagger \mathbf{c}_a \rangle_0, \quad \langle \mathbf{c}_b^\dagger \mathbf{c}_b \rangle_t = e^{-\Gamma_L t} \langle \mathbf{c}_b^\dagger \mathbf{c}_b \rangle_0, \quad (3.67)$$

with loss rates

$$\begin{aligned} \Gamma_L &= \frac{m_{\text{Rb}}^2}{\tau_e m_e^2} \int d^3 \mathbf{q} f_\sigma(q) \left[1 - |\langle \psi_a | \mathbf{W}(\mathbf{q}) | \psi_a \rangle|^2 \right] \\ &= \frac{m_{\text{Rb}}^2}{\tau_e m_e^2} \int d^3 \mathbf{q} f_\sigma(q) \left[1 - |\langle \psi_b | \mathbf{W}(\mathbf{q}) | \psi_b \rangle|^2 \right], \end{aligned} \quad (3.68)$$

since we can still use $\psi_b(\mathbf{r}) = \psi_a(\mathbf{r} - \Delta_x \mathbf{e}_x)$.

The particle loss leads to a shrinking of the generalized Bloch sphere. This results in an overall increase of the normalized second moments even for unsqueezed states since in this case the variance increases only as \sqrt{N} . Apart from the particle loss itself we thus have to incorporate of this heating-induced broadening of the normalized distribution.

To calculate the change of the variance in any \mathbf{J}_n , i.e. the angular momentum component in direction \mathbf{n} , I draw on results from Ref. [113]. There, by tracing out $2(J_0 - J)$ lost particles, the authors obtained

$$\frac{\langle J_n^2 \rangle_J}{J^2} = \frac{2J - 1}{2J_0 - 1} \frac{\langle J_n^2 \rangle_{J_0}}{J_0 J} + \frac{J_0 - J}{J(2J_0 + 1)} \simeq \frac{\langle J_n^2 \rangle_{J_0}}{J_0^2} + \frac{J_0 - J}{2J_0 J}, \quad (3.69)$$

where J and J_0 is the current and initial collective spin, respectively, and I used $J, J_0 \gg 1$. The brackets $\langle \cdot \rangle_J$ denote expectation values in the subspace of $2J$ particles. Since $J \leq J_0$ we can directly infer that the normalized variance $\langle J_n^2 \rangle_J / J^2$ only increases due to particle

3.2. Ramsey interferometry with a number-squeezed BEC

loss. By inserting $J = J_0 \exp^{-\Gamma_L t}$ and expanding linearly in t in the case of moderate particle loss one obtains for all normalized second moments that

$$\frac{\langle J_{\mathbf{n}}^2 \rangle_J}{J^2} \simeq \frac{\langle J_{\mathbf{n}}^2 \rangle_{J_0}}{J_0^2} + \frac{\Gamma_L t}{2J_0}. \quad (3.70)$$

This broadening is strongly suppressed for $J_0 \gg 1$. But, since it no longer only affects the equatorial variances but also the one in z -direction, the non-commutativity with the dispersion due to the Hamiltonian (3.44) has to be addressed.

If diffusion takes place perpendicular to the shearing in the plane due to the Hamiltonian (3.44), one has to consider the following differential equation

$$\partial_t w_t(j_y, j_z) = -2\zeta j_z \partial_{j_y} w_t(j_y, j_z) + \frac{\Gamma_L}{4} \partial_{j_z}^2 w_t(j_y, j_z). \quad (3.71)$$

This is solved by

$$w_t(j_y, j_z) = \frac{1}{4\pi^2} \int dp_y dp_z dj'_y dj'_z w_0(j'_y, j'_z) e^{i(j_y - 2\zeta j_z t)p_y - izp_z - ip_y j'_y + ip_z j'_z} \\ \times \exp \left[-J^2 \Gamma_L \left(\frac{p_z^2}{4} t - \frac{\zeta p_y p_z}{2} t^2 - \frac{\zeta^2 p_y^2}{3} t^3 \right) \right], \quad (3.72)$$

found with help of a twofold Fourier transform. Taking the initial distribution $w_0(j_y, j_z)$ to be a Gaussian with widths σ_y and σ_z and integrating j_z yields the marginal distribution

$$w_t(j_y) = \int dz w_t(j_y, j_z) = \frac{1}{\sqrt{2\pi\sigma_y^2(t)}} \exp \left[\frac{j_y^2}{2\sigma_y^2(t)} \right], \quad (3.73)$$

with variance

$$\sigma_y^2(t) = \sigma_y^2 + 4\zeta^2 t^2 \left(\sigma_z^2 + \frac{J^2 \Gamma_L t}{6} \right). \quad (3.74)$$

Thus, the Gaussian shape is preserved and since the diffusion along the equator and the rotation with constant velocity ϵ/\hbar commutes with the Diffusion and Dispersion in Eq. (3.71) the end result takes again the form of Eq. (3.64), but with

$$g(t) = \exp \left[-\frac{\langle J_y^2 \rangle_0}{2J_0^2} - \frac{\Gamma_P t}{2} - \frac{\Gamma_L t}{4J_0} - 2\zeta^2 t^2 \left(\langle J_z^2 \rangle_0 + \frac{\Gamma_L J_0 t}{6} \right) \right]. \quad (3.75)$$

This approximation will fail for strong particle loss not only because of Eq. (3.70) becoming invalid but also because the change in chemical potential can no longer be linearized and ζ is no longer constant.

Just as in the case of product states in Sec. 3.1 the distribution of the remaining particles is binomial with the survival chance of every particle being $p = e^{-\Gamma_L t}$. This leads to the final likelihood

$$p(m|\tau_e, \sigma, I) = \sum_{J=0}^{J_0} \binom{J_0}{J} (1 - e^{-\Gamma_L t})^J (e^{-\Gamma_L t})^{J_0 - J} p_J(m|\tau_e, \sigma, I), \quad (3.76)$$

where $p_J(m|\tau_e, \sigma, I)$ is given by Eqs. (3.64) and (3.75) and $p_0(m|\tau_e, \sigma, I) = \delta(m)$.

3. Quantum experiments in presence of classicalizing modifications

3.2.7. Assessing the macroscopicity

All that is left to determine the macroscopicity of the experiment in Ref. [31] is to plug the experimental parameters and measured data into the final likelihood (3.76). The number-squeezed ($\xi = 0.41$) BEC consists of $N = 2J_0 \simeq 1200$ ^{87}Rb atoms and the spatial separation of the two ground state wave functions is $\Delta_x \simeq 2 \mu\text{m}$. The energy gap is $\epsilon/\hbar = 2.19 \text{ kHz}$ and the first order corrections due to the particle-particle interaction was measured as $\zeta = 4 \text{ Hz}$.

The two ground states can be approximated harmonically with frequencies $\omega_x/2\pi = 1.44 \text{ kHz}$, $\omega_y/2\pi = 1.84 \text{ kHz}$, and $\omega_z/2\pi = 13.2 \text{ Hz}$, so that the z -motion in the cigar-shaped potential is quasi-free. With the widths of the ground state wave functions $\sigma_{x,y} = \sqrt{\hbar/2m_{\text{Rb}}\omega_{x,y}}$ this leads to the following phase-flip and loss rates,

$$\begin{aligned}\Gamma_{\text{P}} &= \frac{2m_{\text{Rb}}^2}{\tau_e m_e^2} \frac{1 - \exp[-\Delta_x^2 \sigma_q^2 / (4\sigma_q^2 \sigma_x^2 + 2\hbar^2)]}{\sqrt{(1 + 2\sigma_q^2 \sigma_x^2 / \hbar^2)(1 + 2\sigma_q^2 \sigma_y^2 / \hbar^2)}} \\ \Gamma_{\text{L}} &= \frac{m_{\text{Rb}}^2}{\tau_e m_e^2} \left(1 - \frac{1}{\sqrt{(1 + 2\sigma_q^2 \sigma_x^2 / \hbar^2)(1 + 2\sigma_q^2 \sigma_y^2 / \hbar^2)}} \right),\end{aligned}\quad (3.77)$$

that are plotted in Fig. 3.9.

As already indicated in the previous section, the experimental parameters given above lead to a non-negligible particle loss rate because the $\sigma_{x,y}$ are not much smaller than Δ_x . The measured total particle number thus has a significant impact on the hypothesis test even though this particular observable does not verify quantum coherence. In order to only take the observables affected by coherence into account one must use a conditioned likelihood (2.59) as discussed in Sec. 2.3.3. Doing so transfers the overall particle number remaining in the condensate to the background information and one rather calculates the modification-induced loss of interference visibility given that a certain particle number was detected. Formally this is achieved by dividing Eq. (3.76) by the probability

$$P(D_{\text{heat}}|\tau_e, \sigma, I) = \sum_{J=[0.9J_0]}^{J_0} \binom{J_0}{J} (e^{\Gamma_{\text{L}} t} - 1)^J e^{-J_0 \Gamma_{\text{L}} t} \quad (3.78)$$

that not more than 10% of the particles are scattered out of the two ground states, $D_{\text{heat}} := \{J \geq 0.9J_0\}$. This threshold value can be taken as a conservative estimate since the fluctuation in the number of trapped particles is at most 10% from run to run.

The 1438 data points shown in Fig. 3.5 (b) can now be used to perform the Bayesian hypothesis test. As one would expect by conditioning on the remaining particle number the greatest τ_m maximized over σ is achieved for the maximum value of the phase flip rate $\Gamma_{\text{P}} \simeq 1.7/\tau_e$ at the modification parameter $\sigma_q \simeq \hbar/0.77 \text{ mm}$. For this value the particle loss rate is an order of magnitude smaller ($\Gamma = 0.11/\tau_e$) but would still dominate the hypothesis test if it was not filtered out by the conditioning (2.59). The resulting macroscopicity is $\mu_{\text{m}} = 8.5$ as can be checked with the lowest five percent quantile of the posterior in Fig. 3.9.

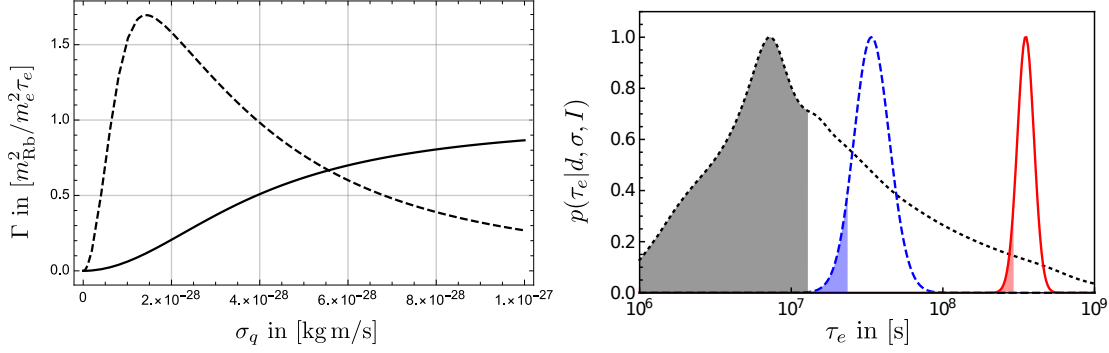


Figure 3.9.: Left: Plotted are the phase-flip and loss rates Γ_P (dashed line) and Γ_L (solid line) according to Eq. (3.77). Right: Shown is the posterior distribution of the classicalization timescale τ_e (red solid line) as obtained via Bayesian updating of Jeffreys' prior (black dashed line) with the measurement data shown in Fig. 3.5 (b). If only the blue data points up to 1 ms from the same source are used the blue intermediate distribution is obtained. The shaded areas indicate the lowest five percent quantiles and all distributions are normalized to the same maximum value.

As already suggested by the assessment of the single particle observables (3.51), the number-squeezing has little to negligible effect on the macroscopicity achieved in these kind of Ramsey interferometer experiments. This is indicated by a comparison with a simple atom interferometer using single Rubidium atoms, for which an estimation with the original macroscopicity measure (2.16) would return $\mu = 8.5$ as well, if an interference visibility $f = 0.2$ after $t = 20$ ms was assumed.

3.3. Leggett-Garg Test with an atomic random walk

Leggett-Garg (LG) inequalities [119, 120] may be viewed as a time-resolved version of the Bell inequalities [17, 18] defining how correlation functions must behave according to classical statistics. The violation of both kinds of inequalities is seen as a fundamental test to verify the validity of quantum mechanics on macroscopic scales. Quantum random walks (QRW) are a popular playing field to demonstrate the unintuitive results of quantum interference as it so strongly deviates from the classical statistics of a Galton board [121]. The violation of LG inequalities with such a QRW is a complex matter and thus promises to be an ideal benchmark for the applicability of the hypothesis test as it was defined in Sec. 2.3. The results presented in this section are published in Ref. [55].

3.3.1. Quantum random walks

The key feature of a QRW distinguishing it from a classical random walk is that the walker simultaneously follows all possible trajectories in a coherent superposition instead of just randomly deciding at every branch which path to take. This is the reason why often times the attribute “random” is dropped and the process is referred to simply as quantum walk. So instead of turning up at a single location like a classical walker the

3. Quantum experiments in presence of classicalizing modifications

quantum walker is in a spatial superposition of all possible sites and only the measurement localizes the wave function to a distinct position. As we will see later, this leads to significant deviations from a classically expected distribution if one gathers statistics by performing many of those walks.

The exemplary setup studied here is reported in Ref. [122] and involves QRWs of ^{133}Cs atoms. These atoms can be prepared essentially in two internal hyperfine states. The hyperfine states determine which external potential the atom senses, and with help of an optical lattice of two circularly polarized laser beams the two internal states can be individually shifted in their position. In this way a spatial delocalization over a distance d can be achieved during the time span T_d .

Every step in the QRW is then performed by first applying a unitary θ -pulse during the time span T_r that can be written in the spin basis of the hyperfine states as

$$C = \begin{pmatrix} \cos(\theta/2) & -\sin(\theta/2) \\ \sin(\theta/2) & \cos(\theta/2) \end{pmatrix}. \quad (3.79)$$

By choosing $\theta = \pi/2$ the operator (3.79) resembles a fair coin flip with equal amplitudes as it was used for the LG test in Ref. [122]. The ramping process delocalizing the state is described by applying

$$U_d = e^{ip_x d/2\hbar} \quad (3.80)$$

on the upper internal state and U_d^\dagger on the lower internal state, resulting in a total delocalization over the range d . Combining both operations in the case of a $\pi/2$ -pulse simply results in

$$S = \frac{1}{\sqrt{2}} \begin{pmatrix} U_d & -U_d \\ U_d^\dagger & U_d^\dagger \end{pmatrix}, \quad (3.81)$$

describing a single step of the QRW performed in [122].

The final state of a four-fold QRW is then $\rho = S^4 \rho_0 (S^\dagger)^4$ being a 2×2 matrix containing coherences associated with spatial delocalizations over a range of up to $4d$. The measuring process is modeled by the ideal likelihood

$$P(\ell|\tau_e, \sigma, I) = \text{tr}_{\text{spin}}(\langle \ell d | \rho | \ell d \rangle), \quad (3.82)$$

with lattice sites $\ell \in \{-2, -1, 0, 1, 2\}$. Here I assumed that the wave function of the particle is localized well enough to clearly identify the lattice and the actual form of the wave function is of no importance. The measurement destroys all coherences and as a result the classical binomial distribution is expanded by only two possible classes of trajectories shown in Fig. 3.11 that survive the measurement: (With trajectories I denote the transformation history of a single dyad, e.g. $|0, \uparrow\rangle\langle 0, \uparrow| \rightarrow |1, \uparrow\rangle\langle -1, \downarrow| \rightarrow |0, \downarrow\rangle\langle -2, \downarrow| \rightarrow \dots$) (i) The wave function is split at the first or second opportunity and immediately recombines afterwards, still having time to align the internal hyperfine state. (ii) The wave function splits at the first step after which the two parts are displaced left or right in parallel in the second step and recombine in the third step to once again have the chance

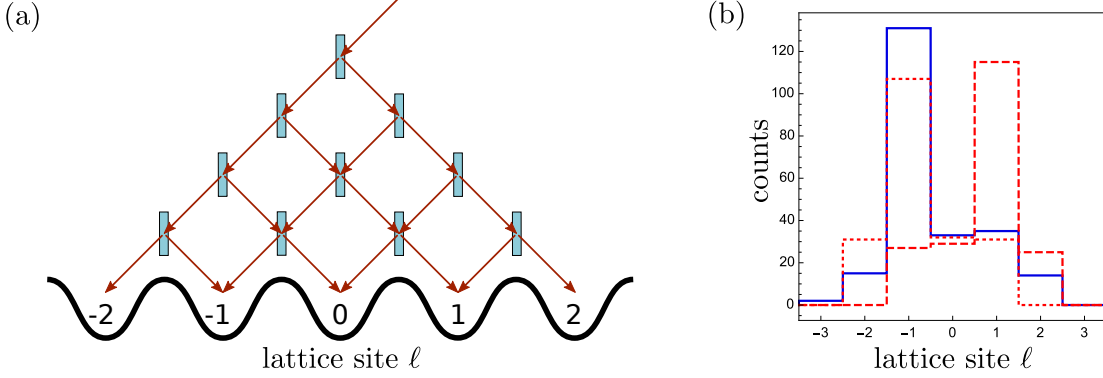


Figure 3.10.: (a) Sketch of a four-fold QRW where the atom takes all possible paths simultaneously until it is measured at the five possible lattice sites ℓ . (b) Shown are histograms of count distributions measured in Ref. [122]. The blue solid line resembles the full walk with the atom being initially in the upper hyperfine state. When the measurements were additionally post-selected whether the first step was taken to the left (right) the red dotted (dashed) histogram can be generated with the data.

to align the spin degree of freedom in the last step. The resulting ideal distribution for the QRW is shown in Fig. 3.11 exhibiting a distinct peak that can be considered as a quantum signature.

3.3.2. Impact of the modification

Since the relevant length scales in the QRW are above nanometers the spatial displacements can be disregarded by setting $\sigma_s = 0$. Further we can neglect heating for the relevant range of σ_q as will be argued in the next subsection when the experimental parameters are incorporated. The treatment of the coherences in the final ρ can straightforwardly be calculated as it was done in Sec. 3.1.2 by imposing several momentum displacements to portray the ramping and the resting during the $\pi/2$ -pulse³. In its entirety this calculation is not necessary since most coherences vanish anyway in the measurement (3.82). With the populations being unaffected by the MMM, since we neglect heating, only the decoherence of the two classes of trajectories (i) and (ii) discussed in the last subsection and depicted in Fig. 3.11 has to be calculated.

In both cases the MMM only affect the dyads during the periods of spatial delocalization. This deviates from the scenario resulting in Eq. (3.18) only in the fact that instead of a mirroring of the momentum by a displacement of $-2\Delta_p$ a displacement of $-\Delta_p$ is applied. This reflects the transition to a resting at constant distance in the spatial delocalization instead of an immediate re-approachment. After this time of constant spatial superposition t , being $t = T_r$ for trajectories of type (i) and $t = 2T_r + T_d$ for trajectories of type (ii), a second momentum displacement $-\Delta_p$ is imposed to rejoin the branches of

³Note, that the approximation with a collective macroscopic wave function in Sec. 3.1.2 is perfectly suitable here since in this experiment there is actually only one particle involved.

3. Quantum experiments in presence of classicalizing modifications

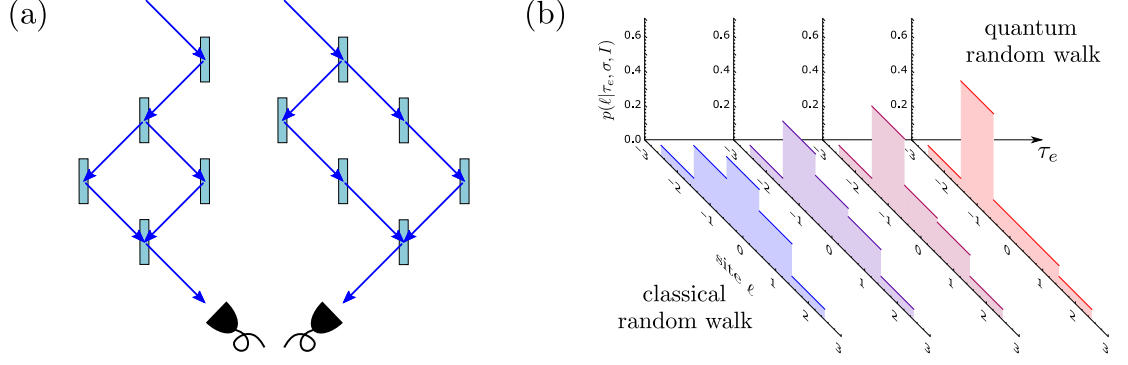


Figure 3.11.: (a) As discussed in the text, only two kinds of interfering trajectories contribute to the final measurement: (i) A delocalization over one lattice distance d is joint at the next opportunity, (ii) the delocalization is maintained for one additional step. (b) Lattice sites populations (3.84) for different MMM parameters. The modifications gradually transforms from a perfect quantum distribution ($\tau_e \rightarrow \infty$, far right) to the classical binomial distribution ($\tau_e \rightarrow 0$, far left). The parameters are chosen as $\sigma_q = 10 \hbar/d$ and $\tau_e m_e^2/m_{Cs}^2 = 1 \mu\text{s}, 50 \mu\text{s}, 100 \mu\text{s}, 10 \text{ms}$ from left to right.

the wave function. In dependence on t the coherences are reduced by the factor

$$R(t) = \exp \left[-\frac{2T_d m_{Cs}^2}{\tau_e m_e^2} \left(1 - \frac{\sqrt{\pi} \hbar}{\sqrt{2} d \sigma_q} \operatorname{erf} \left(\frac{d \sigma_q}{\sqrt{2} \hbar} \right) \right) \right] \exp \left[-\frac{t m_{Cs}^2}{\tau_e m_e^2} \left(1 - \exp \left(-\frac{d^2 \sigma_q^2}{2 \hbar^2} \right) \right) \right]. \quad (3.83)$$

Naturally, the impact of MMM increases for longer ramping and resting times.

The four-step QRW in Ref. [122] was initialized with the atom being in the upper hyperfine state. Applying the unitary transformation (3.81) four times and calculating the populations (3.82) leads to

$$P(-2|\tau_e, \sigma, I) = \frac{1}{16}, \quad (3.84a)$$

$$P(-1|\tau_e, \sigma, I) = \frac{1}{4} + \frac{1}{4}R(T_r) + \frac{1}{8}R(T_d + 2T_r) \quad (3.84b)$$

$$P(0|\tau_e, \sigma, I) = \frac{3}{8} - \frac{1}{4}R(T_r), \quad (3.84c)$$

$$P(1|\tau_e, \sigma, I) = \frac{1}{4} - \frac{1}{8}R(T_d + 2T_r), \quad (3.84d)$$

$$P(2|\tau_e, \sigma, I) = \frac{1}{16}. \quad (3.84e)$$

This follows by simply weighting all summands stemming from trajectories (i) or (ii) with the respective coherence reduction factor (3.83). If the atom would have been initially in the lower hyperfine state the distribution would be mirrored, and an initial superposition of both internal degrees of freedom would result in the familiar double-peaked distribution. Eq. (3.84) gradually transforms from QRW probabilities ($\tau_e \rightarrow \infty$,

3.3. Leggett-Garg Test with an atomic random walk

i.e. $R(t) = 1$) to classical random walk probabilities ($\tau_e \rightarrow 0$, i.e. $R(t) = 0$). This transition is also depicted in Fig. 3.11 exemplarily for $\hbar/\sigma_q = d/10$, clearly showing the classicalizing effect of the MMM.

The LG test discussed in the next subsection requires in addition to the genuine four step QRW two conditioned walks which effectively resemble a three-step QRW. A postselection was imposed by tracing out all trajectories with the atom traveling right (or left) at the first step, which is achieved by transferring the respective branch far away in the potential. The resulting conditioning leads to the following three-step distribution

$$P_L(-2|\tau_e, \sigma, I) = P_R(2|\tau_e, \sigma, I) = \frac{1}{8}, \quad (3.85a)$$

$$P_L(-1|\tau_e, \sigma, I) = P_R(1|\tau_e, \sigma, I) = \frac{3}{8} + \frac{1}{4}R(T_r), \quad (3.85b)$$

$$P_L(0|\tau_e, \sigma, I) = P_R(0|\tau_e, \sigma, I) = \frac{3}{8} - \frac{1}{4}R(T_r), \quad (3.85c)$$

$$P_L(1|\tau_e, \sigma, I) = P_R(-1|\tau_e, \sigma, I) = \frac{1}{8}, \quad (3.85d)$$

$$P_L(2|\tau_e, \sigma, I) = P_R(-2|\tau_e, \sigma, I) = 0, \quad (3.85e)$$

with the subscript L (R) denoting that the first step was performed to the left (right). Since the random walk effectively starts one step later only trajectories of type (i) contribute to the likelihoods (3.85).

3.3.3. Violating a Leggett-Garg inequality

The main motivation for the QRW performed in Ref. [122] was to execute a LG test with help of correlation functions obtained by the ideal ($\tau_e \rightarrow \infty$) QRW likelihoods (3.84) and (3.85). The specific LG inequality studied was of the simplest kind [120],

$$K = \langle Q(t_2)Q(t_1) \rangle + \langle Q(t_3)Q(t_2) \rangle - \langle Q(t_3)Q(t_1) \rangle \leq 1, \quad (3.86)$$

where the $Q(t_i) = \pm 1$ are outcomes of measurements performed at times $t_i \leq t_{i+1}$. The derivation of Eq. (3.86) is grounded on two principles: (A1) *macroscopic realism*, meaning that a system is at all times in one *or* the other state, e.g. in $Q(t_i) = -1$ *or* $Q(t_i) = +1$. (A2) *Noninvasive measurability*, allowing undisturbing and arbitrarily precise measurements of the system. Both assumptions are at odds with quantum mechanics since (A1) does not allow for quantum superpositions and (A2) is not compatible with the measurement projection postulate.

In reality one can never be certain that any violation of (A2) is grounded in a genuine effect of quantum mechanics and does not have a trivial cause. To circumvent this the experimenter can ensure (A2) with help of *ideal negative measurements* [119] and only test (A1). This was implemented in Ref. [122] via the postselection stated above that does not disturb the coherent process in the QRW: For example, if the internal state of the atom is \uparrow in the first step the respective potential is shifted five lattice sites instead of one, removing it from the final measurement without measuring, and thus collapsing

3. Quantum experiments in presence of classicalizing modifications

it, this early in the walk. The delocalization over this many lattice sites does not play a role for the macroscopicity since the respective coherences are traced out after the fourth step.

The t_i for the LG inequality (3.86) were chosen as $t_1 = 0$, $t_2 = 26 \mu\text{s}$, and $t_3 = 104 \mu\text{s}$ so that at t_1 one step and at t_2 the whole QRW is performed. Further, the $Q(t_i)$ were defined as follows: $Q(t_0)$ and $Q(t_1)$ are always set to unity, regardless of the actual state of the atom. $Q(t_2)$ returns -1 if the atom ends up at lattice sites $\ell \leq 0$ and $+1$ for $\ell > 0$. Inserted into Eq. (3.86) together with the probabilities (3.84) and (3.85) leads to

$$\sum_{\ell=-2}^2 \text{sgn}(\ell) \left(P(\ell|\tau_e, \sigma, I) - \frac{1}{2} [P_L(\ell|\tau_e, \sigma, I) + P_R(\ell|\tau_e, \sigma, I)] \right) \leq 0. \quad (3.87)$$

This can be rephrased solely with the reduction factors (3.83) to simply state

$$R(T_r) + R(T_d + 2T_r) \leq 0, \quad (3.88)$$

which is, in theory, always violated unless $\tau_e \rightarrow 0$. However, in a real experiment measurement errors and a finite number of runs would always lead to deviations from a perfect result.

If desired one could now calculate excluded MMM parameters according to the spirit of the original macroscopicity measure in [51] by comparing the theoretical predictions $K(\tau_e, \sigma)$ with the experimentally achieved (3.86) of $K^* = 1.435 \pm 0.074 > 1$. Every $K(\tau_e, \sigma) < K^*$ would then be excluded. But as already stated in Sec. 2.4.4, this raises ambiguities: Can the visibility V of an interference experiment be compared to K without further ado? Is the error bar achieved by, for example, fitting a sine to achieve a visibility fairly comparable with the ± 0.074 found here by bootstrapping, or should rather a Monte Carlo resampling with ± 0.068 be used as it was computed in [122] as well? To avoid these ambiguities I will in the next subsection process the experimental parameters and the measured data according to the scheme presented in Sec. 2.3.

3.3.4. Assessing the macroscopicity

The relevant experimental parameters reported in [122] are as follows: The displacement and resting time are $T_d = 21 \mu\text{s}$ and $T_r = 5 \mu\text{s}$, the distance between the lattice sites is $d = 433 \text{ nm}$, and the potential depth at each lattice site is $80 \mu\text{K}$. When maximizing the effect of MMM with respect to σ one observes that the term in round brackets in the reduction factor (3.83) already saturates to unity for $\hbar/\sigma_q = d/10$. All that is left to do is to multiply the likelihoods of the in total 627 QRW. Together with Jeffreys' prior (2.56) this leads to the posterior depicted in Fig. 3.12 and a macroscopicity of $\mu_m = 7.1$.

It is necessary to retroactively confirm that for $\sigma_q = 10 \hbar/d$ heating is negligible and to thus legitimize the description of the preceding subsections. To be on the safe side, the heating rate is calculated conservatively with help of the 5% quantile of Jeffreys' prior ($\tau_e \simeq 9.85 \cdot 10^5 \text{ s}$). Since Bayesian updating of a true quantum experiment shifts the distribution to higher τ_e (and thus weaker modifications) this overestimates the induced heating. The said choice of MMM parameters results in a temperature increase

3.4. Mechanical entanglement of photonic crystals

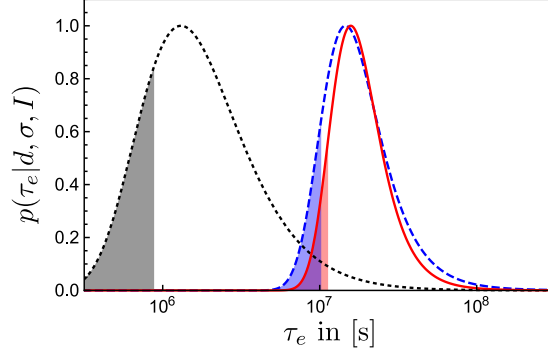


Figure 3.12.: Calculating Jeffreys prior (2.56) for 230 four-step QRW with likelihoods (3.84) and in total 397 three-step QRW with likelihoods (3.85) at $\sigma_q = 10 \hbar/d$ leads to the dotted prior. Updating with only the blue histogram from Fig. 3.10 leads to the blue dashed posterior while taking all data into account leads to the red solid distribution. The shaded regions mark the lowest five percent quantile of each probability distribution and all are normalized to their respective maximum.

of $\Delta T = \sigma_q^2 m_{\text{Cs}} t_2 / 2\tau_e m_e^2 k_B \approx 6 \mu\text{K}$ over the duration t_2 of the whole experiment which amounts to less than $1/13$ of the potential depth. Note that here in the QRW setup, in contrast to the Ramsey interferometry with number-squeezed BEC in Sec. 3.2 where the atom numbers were measured after some time of flight, particles are not required to remain in the ground state. As long as they are well localized, which can be assumed if they are as deeply trapped in the potential as in this scenario, it allows to definitely assign them to one lattice site after the measurement. As a consequence no conditioning (2.59) on heating is required to calculate the likelihood, but since the QRW is a single atom experiment it would not matter anyway because the conditioning factorizes in this simple case.

3.4. Mechanical entanglement of photonic crystals

Intuitively a quantum superposition experiment is more macroscopic the higher the delocalized mass. In case of the macroscopicity defined via the exclusion of MMM this is clearly incorporated by the quadratic scaling m^2/m_e^2 . So it suggests itself that the collective movement of billions of atomic masses in a phononic mode is a macroscopic quantum state if brought into a superposition as it was done in Ref. [36]. On the other hand, the spatial extensions of these kinds of modes is merely on the femtometer scale and this calls for a thorough assessment via the hypothesis test to clarify the objective macroscopicity of these kinds of superposition tests involving phonon modes. The results presented in this section are published in Ref. [55].

3. Quantum experiments in presence of classicalizing modifications

3.4.1. Measurement protocol

The experiment performed by the authors of Ref. [36] aimed to verify the entanglement of millions of atomic mass units in two nanobeams. The superposition state carrying this entanglement involves a specific phonon mode excited in one of the two beams and is created by Stokes scattering of a single pump photon in a Mach-Zehnder like configuration, compare Fig. 3.13. The same mode can then be relaxed back into the ground state via stimulated emission induced by a read photon traversing the same Mach-Zehnder type setup. Then instead of the pump (read) photon the scattered (anti-)Stokes photon enters the second beamsplitter of the structure. With help of a coincidence measurement of both scattered photons after the second beamsplitter the entanglement can be witnessed with help of certain correlation functions.

For this entanglement witness and for the hypothesis test described in Sec. 2.3 one requires the likelihood of the different coincidence outcomes to occur given the MMM parameters,

$$P(\pm_1, \pm_2 | \tau_e, \sigma, I) = \text{tr} (|\pm_1, \pm_2\rangle \langle \pm_1, \pm_2 | \rho_{\text{fin}}). \quad (3.89)$$

Here, the index in \pm_i denotes the Stokes (1) and anti-Stokes (2) photon, while + (−) refers to the upper (lower) detector, see Fig. 3.13. ρ_{fin} is the total final state including both oscillators and both scattered photons. At the start of the experiment this total state is excited by the pump photon to the following two-level superposition state

$$|\psi\rangle_{t=0} = \frac{1}{2} \left[|+\rangle_1 \left(|1, 0\rangle + e^{i\phi} |0, 1\rangle \right) + |-\rangle_1 \left(|1, 0\rangle - e^{i\phi} |0, 1\rangle \right) \right] |\text{vac}\rangle_2, \quad (3.90)$$

with ϕ the initial relative phase. After the excitation the state (3.90) evolves and accumulates a phase additional to ϕ because of a slight mismatch in the energy of both involved phonon modes. Additionally, the MMM act on the oscillator thereby decohering the state and possibly exciting the relevant phonon modes further to arbitrary occupations $|k, \ell\rangle$.

After a certain time t the read photon passes the interferometer and induces a de-excitation of the oscillators in the mixed state ρ_t as described above. This can be modeled with help of a read operator $\rho_{\text{fin}} = R\rho_t R^\dagger / \mathcal{N}$, where I introduced a normalization factor $\mathcal{N} = \text{tr}(R^\dagger R\rho_t)$ to account for the fact that only coincidence measurements are considered in the likelihoods (3.89) that imply a successful relaxation of one of the phonon modes. Since the read out process can be executed with a tunable phase θ on the first beamsplitter, the application of R on an arbitrary total state leads to

$$R|\pm\rangle_1 |k, \ell\rangle |\text{vac}\rangle_2 = \frac{|\pm\rangle_1}{\sqrt{2k+2\ell}} \left[\sqrt{k} |k-1, \ell\rangle (|+\rangle_2 + |-\rangle_2) + e^{i\theta} \sqrt{\ell} |k, \ell-1\rangle (|+\rangle_2 - |-\rangle_2) \right], \quad (3.91)$$

for $(k, \ell) \neq (0, 0)$. With a small chance the MMM can transfer the oscillator states into the ground state for which $R|\pm\rangle_1 |0, 0\rangle |\text{vac}\rangle_2 = 0$ will not lead to a coincidence measurement which is absorbed in the normalization \mathcal{N} .

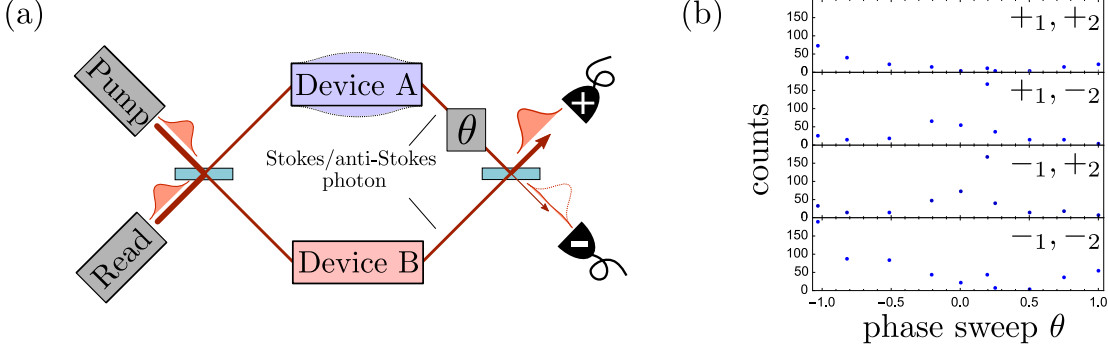


Figure 3.13.: (a) A pump photon enters the first beamsplitter and subsequently traverses the two nanobeam devices where it can induce a Stokes process. This entangles both harmonic oscillator in a superposition of the first (second) phononic mode being in the ground state (first excited state) *and* vice versa. The Stokes scattered photon is detected after entering a second beamsplitter. A read photon also enters the setup through the first beamsplitter and may induce an anti-Stokes process in one of the excited phonon modes. The resulting scattered photon is once again detected after traversing the second beamsplitter. (b) By tuning the relative phase θ of the anti-Stokes scattered photon the probabilities for different coincidence measurements can be controlled. With the experimentally observed data shown here the authors of Ref. [36] were able to verify the entanglement in the nanobeams with help of suitable correlation functions.

As the MMM only acts on the oscillators it is beneficial to rewrite the likelihoods (3.89) as a generalized measurement

$$P(\pm_1, \pm_2 | \tau_e, \sigma, I) = \text{tr}(\mathbf{F}_{\pm_2} \rho_t^{(\pm_1)}) / \mathcal{N} \quad (3.92)$$

with the conditioned oscillator state

$$\rho_t^{(\pm_1)} = \langle \pm | {}_1 \langle \text{vac} | {}_2 \rho_t | \text{vac} \rangle_2 | \pm \rangle_1 \quad (3.93)$$

and

$$\begin{aligned} \mathbf{F}_{\pm_2} &= \text{tr}_1(\langle \text{vac} | {}_2 \mathbf{R}^\dagger | \pm \rangle_2 \langle \pm | {}_2 \mathbf{R} | \text{vac} \rangle_2) \\ &= \frac{1}{2} \left(\sum_{k=1, \ell=0}^{\infty} \frac{k}{k+\ell} |k, \ell\rangle \langle k, \ell| + \sum_{k=0, \ell=1}^{\infty} \frac{\ell}{k+\ell} |k, \ell\rangle \langle k, \ell| \right. \\ &\quad \pm \sum_{k=1, \ell=0}^{\infty} e^{i\theta} \frac{\sqrt{k(\ell+1)}}{k+\ell} |k, \ell\rangle \langle k-1, \ell+1| \\ &\quad \left. \pm \sum_{k=0, \ell=1}^{\infty} e^{-i\theta} \frac{\sqrt{(k+1)\ell}}{k+\ell} |k, \ell\rangle \langle k+1, \ell-1| \right). \end{aligned} \quad (3.94)$$

In this way all information regarding the anti-Stokes photon is incorporated in \mathbf{F}_{\pm_2} and only the oscillator modes remain that are relevant for the modification. The time evolution under the MMM producing the state (3.93) is calculated in the next subsection.

3. Quantum experiments in presence of classicalizing modifications

3.4.2. Classicalizing modifications in the phonon mode expansion

To describe the impact of the MMM generator (2.8) on some part of the oscillator state $|k, \ell\rangle\langle k', \ell'|$ I will transform the state as well as the Lindblad operator (2.9) into the phase space description of the phonon mode, which is, after all, a simple harmonic oscillator. Since the atoms in both nanobeams are sufficiently localized and distinguishable one can approximate the Lindblad operator (2.9) in first quantization as

$$L(\mathbf{q}, \mathbf{s}) = \sum_n \frac{m_n}{m_e} \exp \left[-i \frac{\mathbf{r}_n \cdot \mathbf{q} - \mathbf{p}_n \cdot \mathbf{s}}{\hbar} \right]. \quad (3.95)$$

The question is how the position and momentum operators \mathbf{r}_n and \mathbf{p}_n can be expressed by the one-dimensional phase space operators \mathbf{Q} and \mathbf{P} of the oscillator.

For this purpose one can quantize the classical displacement field $\mathbf{u}(\mathbf{r}, t)$. For an isotropic elastic medium the Lagrangian density can be expressed by $\mathbf{u}(\mathbf{r}, t)$ via [123]

$$\begin{aligned} \mathcal{L} &= \frac{\rho}{2} \dot{\mathbf{u}}^2(\mathbf{r}, t) - V[\mathbf{u}(\mathbf{r}, t)] \\ &= \frac{\rho}{2} \dot{\mathbf{u}}^2(\mathbf{r}, t) - \frac{1}{4} \sum_{klmn=1}^3 \left(\frac{\lambda}{2} \delta_{kl} \delta_{mn} + \mu \delta_{km} \delta_{ln} \right) \left(\frac{\partial u_k}{\partial x_l} + \frac{\partial u_l}{\partial x_k} \right) \left(\frac{\partial u_m}{\partial x_n} + \frac{\partial u_n}{\partial x_m} \right), \end{aligned} \quad (3.96)$$

where λ and μ are the Lamé coefficients describing linear response to normal and shear strain. The equations of motion can directly be deduced from the Lagrangian density as

$$\frac{\partial}{\partial t} \frac{\partial \mathcal{L}}{\partial (\partial u_i / \partial t)} + \sum_{j=1}^3 \frac{\partial}{\partial x_j} \frac{\partial \mathcal{L}}{\partial (\partial u_i / \partial x_j)} - \frac{\partial \mathcal{L}}{\partial u_i} = 0, \quad (3.97)$$

leading to Navier's equation [123]

$$\rho \frac{\partial^2 \mathbf{u}}{\partial t^2} = \mu \nabla^2 \mathbf{u} + (\lambda + \mu) \nabla (\nabla \cdot \mathbf{u}). \quad (3.98)$$

Navier's equation is solved by means of mode functions

$$\mathbf{u}_k(\mathbf{r}, t) = \sqrt{\frac{\hbar}{2\rho V_k \omega_k}} \mathbf{w}_k(\mathbf{r}) (e^{-i\omega_k t} a_k + e^{i\omega_k t} a_k^*), \quad (3.99)$$

defined as the eigenfunctions of the differential operator appearing at the left hand side in Eq. (3.98) with the eigenvalues $-\omega_k^2 \rho$. The exact form of the $\mathbf{w}_k(\mathbf{r})$ is determined by the boundary conditions. One has

$$\mathbf{u}_k(\mathbf{r}, t) = 0 \quad (3.100)$$

on fixed surfaces and

$$\sum_{j=1}^3 T_{ij} n_j = 0 \quad (3.101)$$

3.4. Mechanical entanglement of photonic crystals

on free surfaces, where \mathbf{n} is the normal vector and

$$T_{ij} = -\lambda\delta_{ij}\nabla \cdot \mathbf{u} - \mu \left(\frac{\partial u_i}{\partial x_j} + \frac{\partial u_j}{\partial x_i} \right) \quad (3.102)$$

is the stress tensor fully characterized by the Lamé coefficients.

Quantization of the mode variables $a_k \rightarrow \mathbf{a}_k$ has to be accompanied by a proper normalization. The total displacement $\mathbf{u}(\mathbf{r}, t) = \sum_k \mathbf{u}_k(\mathbf{r}, t)$ has the mean energy

$$\langle E \rangle_t = \left\langle \int d^3\mathbf{r} \left[\frac{\rho}{2} \dot{\mathbf{u}}^2(\mathbf{r}, t) + V[\mathbf{u}(\mathbf{r}, t)] \right] \right\rangle_t = \sum_k \frac{\hbar\omega_k}{V_k} \int d^3\mathbf{r} \mathbf{w}_k^2(\mathbf{r}) a_k^* a_k. \quad (3.103)$$

The mean energy shall be given by the occupation operators, requiring $\langle E \rangle_t = \sum_k \hbar\omega_k a_k^* a_k$, which sets the mode Volume to $\int d^3\mathbf{r} \mathbf{w}_k^2(\mathbf{r}) = V_k$. Given this normalization the quantization $a_k \rightarrow \mathbf{a}_k$ of phonon modes can be carried out pragmatically.

The position operator of individual particles can now be expressed by the displacement modes as

$$\mathbf{r}_n = \mathbf{r}_n^{(0)} + \sum_k \mathbf{w}_k(\mathbf{r}_n^{(0)}) \mathbf{Q}_k, \quad (3.104)$$

where the operator valued amplitude of the oscillator mode is the usual combination of creation and annihilation operators

$$\mathbf{Q}_k = \sqrt{\frac{\hbar}{2\rho V_k \omega_k}} (\mathbf{a}_k + \mathbf{a}_k^\dagger). \quad (3.105)$$

After expressing the individual positions \mathbf{r}_n by phonon amplitudes the same has to be done for the individual momenta \mathbf{p}_n in the Lindblad operator (3.95). For this purpose one determines the classical momentum density

$$\boldsymbol{\pi}_k(\mathbf{r}, t) = \rho \frac{\partial}{\partial t} \mathbf{u}_k(\mathbf{r}, t) = i \sqrt{\frac{\hbar\rho\omega_k}{2V_k}} \mathbf{w}_k(\mathbf{r}) (e^{i\omega_k t} \mathbf{a}_k^* - e^{-i\omega_k t} \mathbf{a}_k). \quad (3.106)$$

Thanks to the normalization by V_k the quantized momentum density $\boldsymbol{\Pi}_k(\mathbf{r}, t)$ fulfills the expected commutator relations

$$\int d^3\mathbf{r} [\mathbf{u}_k(\mathbf{r}, t), \boldsymbol{\Pi}_k(\mathbf{r}, t)] = \int d^3\mathbf{r} \frac{w_k^2(\mathbf{r})\hbar}{2V_k} [e^{i\omega_k t} \mathbf{a}_k^\dagger + e^{-i\omega_k t} \mathbf{a}_k, e^{i\omega_k t} \mathbf{a}_k^\dagger - e^{-i\omega_k t} \mathbf{a}_k] = i\hbar. \quad (3.107)$$

To arrive at the momentum displacement of the individual atom we integrate over the respective volume \mathcal{V}_n it occupies in which a constant displacement is assumed (excluding

3. Quantum experiments in presence of classicalizing modifications

optical modes⁴ oscillating on the lattice constant length scale of the crystal):

$$\mathbf{p}_n = \sum_k \int_{V_n} d^3r \Pi_k(\mathbf{r}, t) \simeq \sum_k i \sqrt{\frac{\hbar \omega_k m_n^2}{2 \varrho V_k}} \mathbf{w}_k(\mathbf{r}_n^{(0)}) (\mathbf{a}_k^\dagger - \mathbf{a}_k) = \sum_k \frac{m_n}{\varrho V_k} \mathbf{w}_k(\mathbf{r}_n^{(0)}) P_k. \quad (3.108)$$

Thus, the momentum displacement is rescaled by the effective mass ρV_k of the mode, which is on the order of the nanobeam mass. Hence even though the mode amplitude may be on the femtometer scale (which is in the range of allowed MMM parameter σ_s) the possible MMM effect of spatial displacements is reduced by over six orders of magnitude and therefore negligible. This stark contrast to the momentum displacements can be understood by noting that the femtometer movement of a single atom in its harmonic potential is not comparable to the mode energy, while a momentum transfer on the order of $\sim \sqrt{\hbar \rho V_k \omega_k} / 2$ on a single atom propagates noticeably through the mode.

The Lindblad operator (3.95) then takes on the form

$$\begin{aligned} \mathbf{L}(\mathbf{q}) &\simeq \sum_n \frac{m_n}{m_e} \exp \left[-\frac{i}{\hbar} \left(\mathbf{r}_n^{(0)} + \sum_k \mathbf{w}_k(\mathbf{r}_n^{(0)}) \mathbf{Q}_k \right) \cdot \mathbf{q} \right] \\ &= \frac{1}{m_e} \int d^3\mathbf{r} \varrho(\mathbf{r}) \exp \left[-\frac{i}{\hbar} \left(\mathbf{r} + \sum_k \mathbf{w}_k(\mathbf{r}) \mathbf{Q}_k \right) \cdot \mathbf{q} \right], \end{aligned} \quad (3.109)$$

where $\varrho(\mathbf{r}) = \sum_n m_n \delta(\mathbf{r} - \mathbf{r}_n^{(0)})$ denotes the exact discrete mass density of the oscillator that can be replaced by a continuous, homogeneous mass density if the characteristic length scale \hbar/σ_q cannot resolve the lattice constant of the crystal [38].

3.4.3. Diffusion regime

The Lindblad operator (3.109) looks scary as it couples the different modes. But in the diffusive regime, when $\sigma_q \ll \sqrt{2\rho V_k \omega \hbar}$, the exponential function can be expanded to first order and the modes decouple. As will be shown later, this is the only relevant regime as stronger modifications would lead to significant heating, destroying the crystal instead of decohering the phonon modes. Since we are only interested in the resonant mode regarding the pump and read photons all other modes can be traced out. I therefore drop the index of the remaining mode amplitude \mathbf{Q} and respective quantities if no distinction is necessary. After the diffusive expansion the Lindblad operator (3.109) effectively takes on the much easier form

$$\mathbf{L}(\mathbf{q}) = -\frac{i}{\hbar} [\tilde{\mathbf{w}}_\varrho(\mathbf{q}) \cdot \mathbf{q}] \mathbf{Q}, \quad (3.110)$$

⁴Those optical modes are of no relevance for the measurement protocol described in 3.4.1. And even if they are occupied to a considerable extent due to MMM there is no coupling in the diffusion regime and as we will learn in Sec. 3.4.3 this is the only relevant regime.

3.4. Mechanical entanglement of photonic crystals

where I introduced

$$\tilde{\mathbf{w}}_{\varrho}(\mathbf{q}) = \frac{1}{m_e} \int d^3\mathbf{r} \varrho(\mathbf{r}) \mathbf{w}(\mathbf{r}) e^{-i\mathbf{r}\cdot\mathbf{q}/\hbar}. \quad (3.111)$$

As promised in the last subsection, the transition to the mode amplitude \mathbf{Q} and momentum \mathbf{P} significantly simplifies the description of the MMM effect as we can work with the characteristic function

$$\chi_t(\mathbf{Q}, \mathbf{P}) = \int d^2\mathbf{Q}' e^{i\mathbf{P}\cdot\mathbf{Q}'/\hbar} \left\langle \mathbf{Q}' + \frac{\mathbf{Q}}{2} \left| \rho_t \right| \mathbf{Q}' - \frac{\mathbf{Q}}{2} \right\rangle. \quad (3.112)$$

It captures the relevant phonon modes of both nanobeams with $\mathbf{Q} = (Q_1, Q_2)$ and $\mathbf{P} = (P_1, P_2)$, effectively resembling a two-dimensional oscillator. Transforming of the free time evolution and the MMM generator (2.8) with Lindblad operator (3.110) into this characteristic phase space yields

$$\partial_t \chi_t(\mathbf{Q}, \mathbf{P}) = \left(-\frac{1}{\varrho V_m} \mathbf{P} \cdot \nabla_{\mathbf{Q}} + \varrho V_m \mathbf{Q} \cdot \Omega^2 \nabla_{\mathbf{P}} - \frac{U(\sigma) \mathbf{Q}^2}{\tau_e} \right) \chi_t(\mathbf{Q}, \mathbf{P}). \quad (3.113)$$

The diagonal matrix Ω contains the two slightly detuned frequencies of both oscillators, and assuming the nanobeams being separated by more than \hbar/σ_q one gets

$$U(\sigma) = \frac{1}{2\hbar^2} \int d^3\mathbf{q} f_{\sigma}(q) |\tilde{\mathbf{w}}_{\varrho}(\mathbf{q}) \cdot \mathbf{q}|^2. \quad (3.114)$$

The time evolution (3.113) allows for an analytical solution that reads

$$\chi_t(\mathbf{Q}, \mathbf{P}) = \exp \left[-\frac{U(\sigma)}{\tau_e} \int_0^t dt' \mathbf{Q}_{t'}^2 \right] \chi_0(\mathbf{Q}_t, \mathbf{P}_t), \quad (3.115)$$

with

$$\begin{aligned} \mathbf{Q}_t &= \cos(\Omega t) \mathbf{Q} + \frac{1}{\varrho V_m} \Omega^{-1} \sin(\Omega t) \mathbf{P} \\ \mathbf{P}_t &= \cos(\Omega t) \mathbf{P} - \varrho V_m \Omega \sin(\Omega t) \mathbf{Q}, \end{aligned} \quad (3.116)$$

where V_m is the relevant mode volume.

Later when the macroscopicity of the experiment is assessed a maximalization over σ_q has to be performed. From Eqs. (3.114) and (3.115) we can deduce that larger σ_q lead to a stronger effect of the modification. On the other hand, this leads to ever stronger heating of the nanobeams which can, of course, be dealt with by means of a conditioned likelihood (2.59) that incorporates the knowledge about an intact crystal into the background information to not dominate the hypothesis test. And just as the heating eventually diminishes the phase diffusion rate in Sec. 3.2, here in this case it prevents any decoherence as the atoms are removed from the crystal by the strong momentum displacements.

To incorporate this particle loss I simply split the MMM generator (2.8) in two parts: $\mathcal{M}_{\sigma}^{\leq}$ induces momentum transfers $|\mathbf{q}| < q_c$ that most likely leave the atom in the crystal,

3. Quantum experiments in presence of classicalizing modifications

and $\mathcal{M}_\sigma^>$ with $|\mathbf{q}| > q_c$ removing the atom into the vacuum. The time evolution involving the resulting sum

$$\begin{aligned} \mathcal{M}_\sigma \rho_t = & \int_{q < q_c} d^3 \mathbf{q} f_\sigma(q) \left[\mathbf{L}(\mathbf{q}) \rho \mathbf{L}^\dagger(\mathbf{q}) - \frac{1}{2} \left\{ \mathbf{L}^\dagger(\mathbf{q}) \mathbf{L}(\mathbf{q}), \rho \right\} \right] \\ & + \int_{q > q_c} d^3 \mathbf{q} f_\sigma(q) \left[\mathbf{L}(\mathbf{q}) \rho \mathbf{L}^\dagger(\mathbf{q}) - \frac{1}{2} \left\{ \mathbf{L}^\dagger(\mathbf{q}) \mathbf{L}(\mathbf{q}), \rho \right\} \right] \end{aligned} \quad (3.117)$$

can be expanded into a Dyson series to arrive at

$$\rho_t = \exp \left[\frac{t}{i\hbar} \mathcal{H} + \frac{t}{\tau_e} \mathcal{M}_\sigma^< \right] \rho_0 + \tilde{\rho}. \quad (3.118)$$

Here, only the first term is compatible with a coincidence measurement (3.89) and its reduced trace can simply be absorbed in the normalization constant \mathcal{N} . By this approach the loss of even a single atom is not consistent with the coincidence detection, which can be understood as a conservative estimation. Overall, the analytical description with Eq. (3.115) remains valid after replacing Eq. (3.114) by

$$U_<(\sigma) = \frac{1}{2\hbar^2} \int_{q < q_c} d^3 \mathbf{q} f_\sigma(q) |\tilde{\mathbf{w}}_\varrho(\mathbf{q}) \cdot \mathbf{q}|^2. \quad (3.119)$$

The critical momentum transfer q_c can be estimated with help of the cohesive energy $E_b = 4.6 \text{ eV}$ [124] in Silicon crystals as $q_c = \sqrt{2m_{\text{Si}} E_b}$.

3.4.4. Experimentally achieved macroscopicity

The calculation of the likelihoods (3.92) translated to the characteristic phase space picture is simply the overlap integral

$$P(\pm_1, \pm_2 | \tau_e, \sigma, I) = \int d^2 \mathbf{Q} d^2 \mathbf{P} \chi_t^{\pm_1}(\mathbf{Q}, \mathbf{P}) \eta^{\pm_2}(\mathbf{Q}, \mathbf{P}), \quad (3.120)$$

with $\chi_t^{\pm_1}(\mathbf{Q}, \mathbf{P})$ and $\eta^{\pm_2}(\mathbf{Q}, \mathbf{P})$ being the characteristic symbols of the state (3.93) and the projector (3.94), respectively. Two additional simplifications can be exploited at this point: First, the oscillator frequencies of $\omega \simeq 2\pi \times 5 \text{ GHz}$ are so large on the timescale t of the experiment, $\omega t \gg 1$, that the time dependent phase space coordinates (3.116) can be safely averaged in the exponent of Eq. (3.115), leading to

$$\chi_t(\mathbf{Q}, \mathbf{P}) \approx \exp \left[-\frac{U_<(\sigma)t}{2\tau_e} (\mathbf{Q}^2 + \varrho^2 V_m^2 (\Omega^{-1} \mathbf{P})^2) \right] \chi_0(\mathbf{Q}_t, \mathbf{P}_t). \quad (3.121)$$

Second, since the MMM cannot create coherences it suffices to only keep the off-diagonal terms in the projector (3.94) that are initially populated. This significantly simplifies the projector to

$$\mathbb{F}_{\pm_2} = \frac{1}{2} \left(\mathbb{1} - |0, 0\rangle \langle 0, 0| \pm e^{i\theta} |1, 0\rangle \langle 0, 1| \pm e^{-i\theta} |0, 1\rangle \langle 1, 0| \right). \quad (3.122)$$

3.4. Mechanical entanglement of photonic crystals

The characteristic symbol of the projector (3.122) and the characteristic function of the state (3.93) are given in App. B.2.1. Calculating the overlap (3.120) of those results in the likelihoods

$$P(\pm_1, \pm_2 | \tau_e, \sigma, I) = \frac{1}{4\mathcal{N}} + \frac{(\pm_1)(\pm_2)4 \cos(\theta - \Delta\Omega t) - 2\xi t/\tau_e - \xi^2 t^2/\tau_e^2}{\mathcal{N}(2 + \xi t/\tau_e)^4}. \quad (3.123)$$

Here, $\Delta\Omega = 2\pi \times 45$ MHz is the frequency mismatch between the two oscillators and I abbreviated $\xi = 2U_{<}(\sigma)\hbar/\rho V_m \omega$.

The dimensionless parameter ξ contains via $U_{<}(\sigma)$ the only dependence on the actual shape of the phonon modes. Those phonon modes in Ref. [36] are characterized by an effective mass $\rho V_m \simeq 9 \times 10^{-17}$ kg and have the mechanical frequency $\omega \simeq 2\pi \times 5$ GHz. To calculate the geometry factor (3.119) and with it the time evolution of the oscillator states one requires the displacement field that is determined by the complicated geometry of the photonic crystal. Since the resulting mode is only numerically accessible and as I expect the details of the mode function to be of only minor relevance I will substitute it with an analytically tractable case possessing the essentially same physical characteristics. The chosen shape is a $L_x \times L_y \times L_z$ cuboid with the same number of atoms that contribute to the elastic deformation in the nanobeam and the simplest longitudinal mode with

$$\mathbf{w}(\mathbf{r}) = \mathbf{e}_z \sin\left(\frac{\pi z}{L_z}\right), \quad (3.124)$$

mimicking the breathing mode. To match the effective mass and frequency of the oscillators with the speed of sound $v = 8433$ m/s and density $\rho = 2300$ kg/m³ the sides of the cuboid must be $L_x \times L_y \times L_z \approx 0.31 \mu\text{m} \times 0.31 \mu\text{m} \times 0.84 \mu\text{m}$. With these one can straightforwardly derive the geometry factor (3.119) that is reported in App. B.2.2.

At this point all ingredients are at hand to perform the hypothesis test. The phase- and time-sweep measurement protocols reported in [36] can be handled by variation of θ and t , respectively. The initial phase ϕ is not reported but can simply be deduced to be $\phi \simeq 1.8$ rad $- \Delta\Omega \times 123$ ns via optimization. Plugging the data into the likelihoods (3.123) results together with Jeffreys' prior to the posteriors shown in Fig. 3.14. They lead to the maximal macroscopicity of $\mu_m = 7.8$ at $\hbar/\sigma_q \simeq \sqrt{\hbar^2/2m_{\text{Si}}E_b}$. It may be somewhat surprising that the macroscopicity of an experiment involving billions of atomic mass units in an entangled superposition does not lead to a significantly higher macroscopicity than the previously discussed single atom interference experiment. But since the delocalization extends only on femtometers the MMM can only diffusively decohere the quantum state. Already deep in this diffusive regime the decoherence rate is capped as the momentum transfer rather removes particles from the crystal. It is consistent with this picture that the maximum excluded time parameter $\tau_m = 6.6 \times 10^7$ s is achieved at $\hbar/\sigma_q \simeq \sqrt{\hbar^2/2m_{\text{Si}}E_b}$ where the transition to pure heating takes place.

3. Quantum experiments in presence of classicalizing modifications

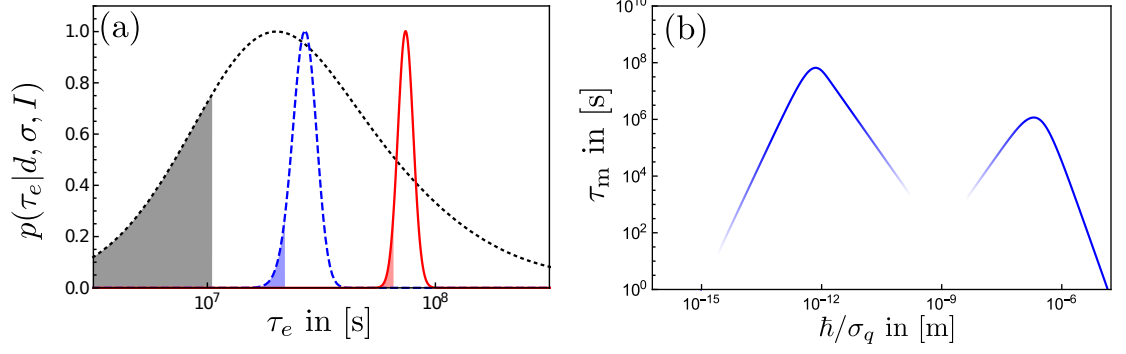


Figure 3.14.: (a) Bayesian updating of Jeffreys' prior (dotted line) calculated for the likelihood (3.123). If only data from the phase sweep, depicted in Fig. 3.13, is incorporated the blue dashed posterior emerges. If additional data from varying the time delay t is included the final red solid posterior is obtained. All probability densities are normalized to their maximum value and the shaded regions indicate the lowest five percent quantile. (b) The largest excluded time parameter τ_m is achieved for $\hbar/\sigma_q \simeq \sqrt{\hbar^2/2m_{\text{Si}}E_b}$ from which point onwards particles are removed from the crystal for increasing σ_q . Another local maximum is obtained when \hbar/σ_q is on the scale of the crystal elongation. The shaded areas indicate where the analytical expressions shown in App. B.2.2 are no longer valid: If \hbar/σ_q is on the order of Ångström the mass can no longer be taken as continuous and if \hbar/σ_q is in the low femtometer regime the diffusive approximation fails.

3.4.5. Death of entanglement II

The main goal in Ref. [36] was to verify the entanglement between the nanobeams with help of the measurable entanglement witness [125]

$$R_m(\theta, \pm_2) = 4 \frac{g_{+1, \pm_2}(\theta) + g_{-1, \pm_2}(\theta) - 1}{(g_{+1, \pm_2}(\theta) - g_{-1, \pm_2}(\theta))^2}, \quad \text{with} \quad g_{\pm_1, \pm_2} = \frac{\langle c_{\pm_1}^\dagger c_{\pm_2}^\dagger c_{\pm_1} c_{\pm_2} \rangle}{\langle c_{\pm_1}^\dagger c_{\pm_1} \rangle \langle c_{\pm_2}^\dagger c_{\pm_2} \rangle}, \quad (3.125)$$

where the c_{\pm_j} are the annihilation operators in the two detector modes while $j = 1(2)$, as before, denotes the pump (read) photon. $R_m(\theta, \pm_2)$ is the measurable upper bound of a tight entanglement witness and whenever $R_m(\theta, \pm_2) < 1$ it verifies entanglement of the micromechanical oscillators.

The second order correlation functions in the witness (3.125) are nothing else but the coincidence measurement probabilities already reported by Eq. (3.123) in presence of the modification. The first order correlation functions are just the sum of Eq. (3.123) over \pm_1 or \pm_2 , respectively. The MMM gradually flattens both types of correlation functions and as a result, $R_m(\theta, \pm_2)$ eventually diverges with decreasing τ_e and at some point passes the threshold of unity. As before in the case of collective spin states in Sec. 3.2.4, this does not inevitably result in a separable state but the entanglement is simply no longer verifiable. In the end, the entanglement witness relies heavily on the phase stability which is the first victim when exposed to MMM, underlining once again its classicalizing nature.

3.5. Discussion

Throughout this chapter I demonstrated the impact of MMM on several relevant quantum tests, always leading to a loss of coherence and a gradual heating of the whole system. As a direct consequence, quantum features like entanglement or the falsification of macrorealism are no longer verifiable, be it via depth of entanglement (3.59), Leggett-Garg inequalities (3.86), or entanglement witnesses driven by correlation functions (3.125). This confirms the status of MMM as classicalizing modifications. At the same time the assessment of macroscopicity via the hypothesis test relieves one from the necessity of such ‘witnesses of quantumness’. As long as the measured data leads to posterior distributions that shift to smaller τ_e the quantum nature of the experiment is sufficiently demonstrated.

Especially the assessment of the collective spin states in Sec. 3.2 reveals the effort one has to put in to disclose the likelihoods of different measurement events used in the hypothesis test from Sec. 2.3. This is in contrast to simpler derivations of expectation values of collective observables to rule out MMM parameters. It is the price one has to pay to be comparable to more abstract quantum experiments like the QRW or the entangled nanobeams that rely on the assessment via likelihoods. At the end of the day, estimations with the original scheme (2.16) may turn out to be sufficient if applicable, as shown in Sec. 2.4.3 and 3.2.7.

Even though the quantum tests analyzed in this chapter are totally different from one another, the resulting macroscopicities are surprisingly close on the logarithmic scale. The main reason, apart from the convenient combination of masses and coherence times by chance, is the reduction of information by assessing the macroscopicity with the maximum time parameter τ_m as a function of σ in Eq. (2.58). As long as a maximalization of the decoherence time scale τ_e is achieved it is no longer relevant which value the respective σ assumes, rendering it somewhat irrelevant if the delocalization takes place over a few micrometers or on the half meter scale. Only if the delocalization is so small the length scale really matters, as in the case of the phonon modes of the entangled nanobeams, where larger σ_q would lead to an incompatible heating.

By including information about the delocalization length scale in the macroscopicity measure it partly loses its simplicity (at least it is no longer condensed to a single number). Moreover, it is not so clear how to consistently implement the range of excluded MMM length scales into the calculation, the simplest reason being that in the general case it is not even possible to calculate the effect of MMM for all σ . But just to have a slight impression of further differentiation it may be beneficial to additionally note the smallest σ_q for which the time parameter assumes its maximum. The resulting two dimensional map of experiments discussed in this thesis is shown in Fig. 3.15. Whenever quantum tests are compared in their macroscopicity this will open up a new layer of differentiation, maybe even allowing people who emphasize more on the spatial dimension of a superposition experiment to focus on this aspect. The large macroscopicities of the KDTLI and the LUMI for example are found at more than three orders of magnitude larger σ_q than the interference of squeezed spin states. Surely, this assessment would once again be impossible for macroscopicity measures based for example on the QFI

3. Quantum experiments in presence of classicalizing modifications

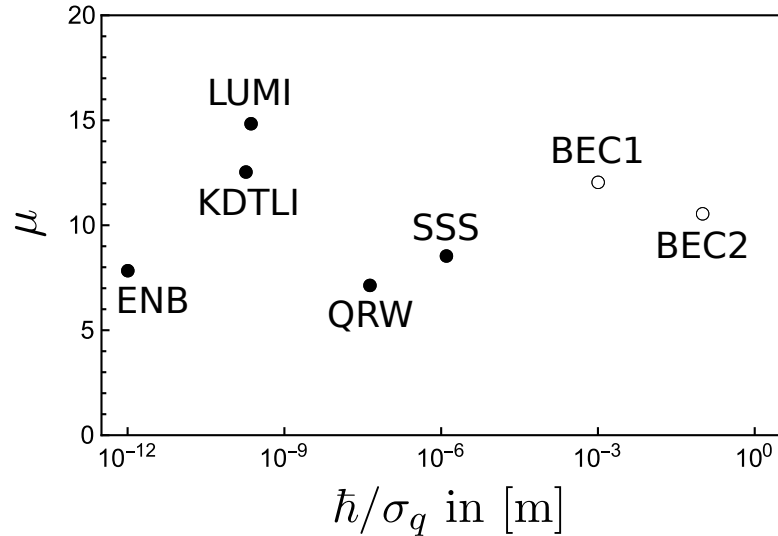


Figure 3.15.: Map of the macroscopicities of the different discussed experiments as a function of the critical length scale \hbar/σ_q on which they first achieve the maximum excluded τ_m : Kapitza-Dirac-Talbot-Lau Interferometer (KDTLI) from Sec. 2.4.2, Long baseline Universal Matter-wave Interferometer (LUMI) from Sec. 2.4.3, squeezed spin states (SSS) from Sec. 3.2, quantum random walks (QRW) from Sec. 3.3, and entangled nanobeams (ENB) from Sec. 3.4. The empty circles mark the hypothetical positions of a BEC delocalized up to half a meter discussed in Sec. 3.1 if a stable phase could be maintained. BEC1 and BEC2 refer to two experimental setups with different maximum delocalizations reported in [33]. One could additionally include exclusion curves like in Fig. 2.1 to highlight which portion of the MMM parameter space as a whole is excluded by the different experiment. I refrain from doing so since not all of the shown experiments are evaluable on the whole range of σ_q .

(2.4) using an abstract Hilbert space independent from the actual time and length scales of the quantum delocalization.

4. Orientational coherence experiments

The last years witnessed a tremendous progress in the manipulation of rotational and orientational degrees of freedom in experiments working with levitated asymmetric nanorotors [57–62]. The quantum regime seems to be within grasp [63, 64] and effects like revivals of orientation states, already shown for small molecules [126–128], may be witnessed soon for nanorotors with tens of millions of atomic mass units. This calls for an all quantum mechanical description, including the interaction with the surroundings leading to decoherence, diffusion and friction, as well as the formulation of the minimally invasive, macrorealist modifications of quantum mechanics (MMM) defined by Eq. (2.8) acting on these orientational degrees of freedom to some day assess the macroscopicity of quantum tests with levitated nanorods.

4.1. Theoretical background

The quantization of orientational degrees of freedom is a complicated matter due to the finite and topologically non-trivial configuration space. It is, in its entirety, by no means covered by the standard curriculum and therefore calls for a thorough introduction into the underlying theory. I will refrain from doing so and only introduce the absolute basic definitions used in the theoretical description to come. Interested readers are referred to Ref. [129] that will be the source for the statements in this section. The reduction to collective orientational degrees of freedom and angular momenta will assume the rotors to be rigid bodies and neglect the internal degrees of freedom.

4.1.1. Classical theory of rigid rotors

The orientation of a rigid body is determined by the relation of its body-fixed frame, denoted by the orthonormal Cartesian basis $\mathbf{n}_1, \mathbf{n}_2, \mathbf{n}_3$, to the space-fixed frame, denoted by $\mathbf{e}_1, \mathbf{e}_2, \mathbf{e}_3$. A specific orientation Ω , e.g. encoded in the Euler angles specified below, is then obtained by applying the respective rotation matrix $R(\Omega)$ on any point in the body-fixed frame:

$$\mathbf{n}_\mu = R(\Omega)\mathbf{e}_\mu, \quad (4.1)$$

with

$$R^T(\Omega)R(\Omega) = \mathbb{1} \quad \text{and} \quad \det R(\Omega) = 1, \quad (4.2)$$

where $R(0) = \mathbb{1}$ leaves the body-fixed frame and space fixed frame aligned.

4. Orientational coherence experiments

The relevant parametrization of orientations throughout this thesis will be the Euler parametrization $\Omega = (\alpha, \beta, \gamma)$ where any rotation can be factorized as three consecutive rotations around (i) the space-fixed 3-axis \mathbf{e}_3 with α , (ii) the interim body-fixed 2-axis \mathbf{n}_ξ , also called nodal line, with β , and (iii) finally around the resulting body-fixed 3-axis \mathbf{n}_3 with γ . There are alternative conventions with altering rotation-axes and sequences but we will stick to this so-called z - y - z convention, in the space fixed frame written as [129]

$$\mathbf{R}(\Omega) = \begin{pmatrix} \cos \alpha \cos \beta \cos \gamma - \sin \alpha \sin \gamma & -\cos \alpha \cos \beta \sin \gamma - \sin \alpha \cos \gamma & \cos \alpha \sin \beta \\ \sin \alpha \cos \beta \cos \gamma + \cos \alpha \sin \gamma & -\sin \alpha \cos \beta \sin \gamma + \cos \alpha \cos \gamma & \sin \alpha \sin \beta \\ -\sin \beta \cos \gamma & \sin \beta \sin \gamma & \cos \beta \end{pmatrix}, \quad (4.3)$$

if relevant for the calculations to come. Most of the results, however, are presented in a coordinate-free fashion anyway.

The Lagrange function of the freely rotating rigid top reads [129]

$$\begin{aligned} \mathcal{L}(\Omega, \dot{\Omega}) = T(\Omega, \dot{\Omega}) &= \frac{1}{2} \sum_{i=1}^3 I_i \tilde{\omega}_i^2 \\ &= \frac{1}{2} \left[\dot{\alpha}^2 (I_1 \sin^2 \beta \cos^2 \gamma + I_2 \sin^2 \beta \sin^2 \gamma + I_3 \cos^2 \beta) \right. \\ &\quad + \dot{\beta}^2 (I_1 \sin^2 \gamma + I_2 \cos^2 \gamma) + \dot{\gamma}^2 I_3 + 2\dot{\alpha}\dot{\gamma} I_3 \cos \beta \\ &\quad \left. + 2\dot{\alpha}\dot{\beta} (I_2 - I_1) \sin \beta \sin \gamma \cos \gamma \right], \end{aligned} \quad (4.4)$$

with I_μ being the moments of inertia and $\tilde{\omega}_{1,2,3}$ the body fixed components of the angular velocity. The latter is expressed in Euler angles as

$$\tilde{\omega}_1 = \dot{\beta} \sin \gamma - \dot{\alpha} \sin \beta \cos \gamma, \quad \tilde{\omega}_2 = \dot{\beta} \cos \gamma + \dot{\alpha} \sin \beta \sin \gamma, \quad \tilde{\omega}_3 = \dot{\alpha} \cos \beta + \dot{\gamma}. \quad (4.5)$$

From the Lagrange function we can deduce the canonically conjugate momenta of the Euler angles Ω via $p_\mu = \partial/\partial\dot{\mu} L(\Omega, \dot{\Omega})$ to be

$$\begin{aligned} p_\alpha &= \dot{\alpha} (I_1 \sin^2 \beta \cos^2 \gamma + I_2 \sin^2 \beta \sin^2 \gamma + I_3 \cos^2 \beta) \\ &\quad + \dot{\beta} (I_2 - I_1) \sin \beta \sin \gamma \cos \gamma + \dot{\gamma} I_3 \cos \beta = \mathbf{J} \cdot \mathbf{e}_3 \\ p_\beta &= \dot{\alpha} (I_2 - I_3) \sin \beta \sin \gamma \cos \gamma + \dot{\beta} (I_1 \sin^2 \gamma + I_2 \cos^2 \gamma) = \mathbf{J} \cdot \mathbf{n}_\xi \\ p_\gamma &= I_3 (\dot{\alpha} \cos \beta + \dot{\gamma}) = \mathbf{J} \cdot \mathbf{n}_3. \end{aligned} \quad (4.6)$$

As indicated by the second equalities in Eq. (4.6) they are the projection of the total angular momentum \mathbf{J} onto the rotation axes with respect to which the Euler angles are defined. Thus, one can directly identify the components of the angular momentum operator as

$$\begin{aligned} J_1 &= -p_\alpha \cos \alpha \cot \beta - p_\beta \sin \alpha + p_\gamma \frac{\cos \alpha}{\sin \beta} \\ J_2 &= -p_\alpha \sin \alpha \cot \beta - p_\beta \cos \alpha + p_\gamma \frac{\sin \alpha}{\sin \beta} \\ J_3 &= p_\alpha \end{aligned} \quad (4.7)$$

in the space-fixed frame, and

$$\begin{aligned}\tilde{J}_1 &= p_\gamma \cos \gamma \cot \beta + p_\beta \sin \gamma - p_\alpha \frac{\cos \gamma}{\sin \beta} \\ \tilde{J}_2 &= -p_\gamma \sin \gamma \cot \beta + p_\beta \cos \gamma + p_\alpha \frac{\sin \gamma}{\sin \beta} \\ \tilde{J}_3 &= p_\gamma\end{aligned}\tag{4.8}$$

in the body-fixed frame. With the definition of $R(\Omega)$, $p_{\alpha,\beta,\gamma}$ and \mathbf{J} we have all the essential classical quantities at hand whenever a comparison with the classical dynamics is sought. In the next subsection I will present the quantum mechanical counterparts.

4.1.2. Quantum theory of rigid rotors

The Euler angle operators $\Omega = (\alpha, \beta, \gamma)$ have a continuous spectrum of eigenvalues, analogous to the position operators in Cartesian space, with eigenstates $|\Omega\rangle = |\alpha, \beta, \gamma\rangle$. These provide an orthonormal Hilbert basis so that

$$\langle \Omega | \Omega' \rangle = \frac{\delta_{2\pi}(\alpha - \alpha') \delta_\pi(\beta - \beta') \delta_{2\pi}(\gamma - \gamma')}{\sin \beta},\tag{4.9}$$

with the periodic Delta-distributions $\delta_\phi(x) = \delta(x \bmod \phi)$, and

$$\mathbb{1} = \int d\Omega |\Omega\rangle \langle \Omega| = \int_0^{2\pi} d\alpha \int_0^\pi d\beta \int_0^{2\pi} d\gamma \sin \beta |\alpha, \beta, \gamma\rangle \langle \alpha, \beta, \gamma|.\tag{4.10}$$

The conjugated momentum operators to the Euler angle operators are [129]

$$\begin{aligned}\mathbf{p}_\alpha &= -i\hbar \frac{\partial}{\partial \alpha} \\ \mathbf{p}_\beta &= -i\hbar \left(\frac{\partial}{\partial \beta} + \frac{1}{2} \cot \beta \right) \\ \mathbf{p}_\gamma &= -i\hbar \frac{\partial}{\partial \gamma}.\end{aligned}\tag{4.11}$$

These commute with each other, $[\mathbf{p}_\mu, \mathbf{p}_\nu] = 0$, and, because of the compact configuration space defined by the Euler angles, have a discrete set of eigenvalues

$$\begin{aligned}\mathbf{p}_\alpha |m_\alpha, m_\beta, m_\gamma\rangle &= \hbar m_\alpha |m_\alpha, m_\beta, m_\gamma\rangle \\ \mathbf{p}_\beta |m_\alpha, m_\beta, m_\gamma\rangle &= 2\hbar m_\beta |m_\alpha, m_\beta, m_\gamma\rangle \\ \mathbf{p}_\gamma |m_\alpha, m_\beta, m_\gamma\rangle &= \hbar m_\gamma |m_\alpha, m_\beta, m_\gamma\rangle.\end{aligned}\tag{4.12}$$

The corresponding eigenstates are given by

$$\langle \Omega | m_\alpha, m_\beta, m_\gamma \rangle = \frac{e^{im_\alpha \alpha}}{\sqrt{2\pi}} \frac{e^{2im_\beta \beta}}{\sqrt{\pi \sin \beta}} \frac{e^{im_\gamma \gamma}}{\sqrt{2\pi}}.\tag{4.13}$$

4. Orientational coherence experiments

Analogous to the classical description we can now derive the angular momentum operators \mathbf{J} by means of the momenta conjugated to the Euler angles (4.11). Applying Weyl-ordering and expressing the result in the orientation basis leads to the angular momentum operators in the space-fixed frame

$$\begin{aligned} J_1 &= i\hbar \left(\cot \beta \cos \alpha \frac{\partial}{\partial \alpha} + \sin \alpha \frac{\partial}{\partial \beta} - \frac{\cos \alpha}{\sin \beta} \frac{\partial}{\partial \gamma} \right) \\ J_2 &= i\hbar \left(\cot \beta \sin \alpha \frac{\partial}{\partial \alpha} - \cos \alpha \frac{\partial}{\partial \beta} - \frac{\sin \alpha}{\sin \beta} \frac{\partial}{\partial \gamma} \right) \\ \tilde{J}_3 &= -i\hbar \frac{\partial}{\partial \alpha}, \end{aligned} \quad (4.14)$$

and

$$\begin{aligned} \tilde{J}_1 &= i\hbar \left(\frac{\cos \gamma}{\sin \beta} \frac{\partial}{\partial \alpha} - \sin \gamma \frac{\partial}{\partial \beta} - \cos \gamma \cot \beta \frac{\partial}{\partial \gamma} \right) \\ \tilde{J}_2 &= i\hbar \left(-\frac{\sin \gamma}{\sin \beta} \frac{\partial}{\partial \alpha} - \cos \gamma \frac{\partial}{\partial \beta} + \sin \gamma \cot \beta \frac{\partial}{\partial \gamma} \right) \\ \tilde{J}_3 &= -i\hbar \frac{\partial}{\partial \gamma}, \end{aligned} \quad (4.15)$$

that are the angular momentum operators in the body-fixed frame.

J_3 , \tilde{J}_3 , and J^2 are a complete set of commuting observable with eigenvalues

$$\begin{aligned} J_3 |j, m, k\rangle &= m |j, m, k\rangle \\ \tilde{J}_3 |j, m, k\rangle &= k |j, m, k\rangle \\ J^2 |j, m, k\rangle &= j(j+1) |j, m, k\rangle. \end{aligned} \quad (4.16)$$

This provides a third orthogonal eigenbasis

$$\langle j, m, k | j', m', k' \rangle = \delta_{j,j'} \delta_{m,m'} \delta_{k,k'} \quad (4.17)$$

$$\sum_{j \in \mathbb{N}_0} \sum_{m=-j}^j \sum_{k=-j}^j |j, k, m\rangle \langle j, k, m| = \mathbb{1}, \quad (4.18)$$

It is worth noting that the $|j, m, k\rangle$ are only eigenstates of the Hamiltonian for the symmetric top. There exists no simple analytical equation for the eigenvalues of an asymmetric top. As a consequence, even though all results given in this chapter will be applicable to an arbitrary tensor of inertia, explicit examples will only be given for linear or planar rotors, reducing the relevant eigenstates to $|j, m\rangle$ or $|m\rangle$, respectively.

4.1.3. Calculation rules for angular momentum operators

In contrast to the Cartesian momentum operators the angular momentum operators (4.14) do not commute with one another, $[J_\mu, J_\nu] = i\hbar \epsilon_{\mu\nu\lambda} J_\lambda$. This substantially complicates the forthcoming calculations. It is therefore appropriate to give a little overview

4.2. Orientational decoherence, diffusion and thermalization

$\epsilon_{\mu\nu\lambda}R_{\alpha\mu}R_{\beta\lambda} = \epsilon_{\alpha\gamma\beta}R_{\gamma\nu} \Leftrightarrow \epsilon_{\mu\nu\lambda}R_{\alpha\mu}^T R_{\beta\lambda}^T = \epsilon_{\alpha\gamma\beta}R_{\gamma\nu}^T$
$R_{\mu\nu}R_{\mu\lambda} = R_{\mu\nu}^T R_{\mu\lambda}^T = \mathbb{1}_{\nu\lambda}$
$[R_\mu, R_\nu] = 0$
$J_\mu = \sum_\nu R_{\mu\nu} \tilde{J}_\nu$
$\tilde{J}_\mu = \sum_\nu R_{\nu\mu} J_\nu$
$[J_\mu, J_\nu] = i\hbar\epsilon_{\mu\nu\lambda}J_\lambda$
$[\tilde{J}_\mu, \tilde{J}_\nu] = -i\hbar\epsilon_{\mu\nu\lambda}\tilde{J}_\lambda$
$[J_\mu, \tilde{J}_\nu] = 0$
$[J_\mu, R_{\nu\lambda}] = i\hbar\epsilon_{\mu\nu\alpha}R_{\alpha\lambda} \Rightarrow [J_\mu, R_{\mu\nu}] = [J_\mu, R_{\mu\nu}^T] = 0$
$[\tilde{J}_\mu, R_{\nu\lambda}] = -i\hbar\epsilon_{\mu\lambda\alpha}R_{\nu\alpha}$
$[\tilde{J}_\mu, \mathbf{a}] = -i\hbar(\mathbf{n}_\mu \times \mathbf{a})$
$[J_\mu, \mathbf{a}] = -i\hbar(\mathbf{e}_\mu \times \mathbf{a})$

Table 4.1.: Formulary of different calculation rules involving rotation matrix operators and angular momenta. For brevity I replaced $R = R(\Omega)$, \mathbf{a} is a vector with arbitrary orientation, and as always I use the Einstein summation convention.

of useful relations, some more, some less apparent. This is done in Table 4.1, mostly in terms of the different components which allow for a more straightforward calculation. All the relations shown in Tab. 4.1 are obtained by using the Euler representations of R , J_μ , and \tilde{J}_μ .

4.2. Orientational decoherence, diffusion and thermalization

To adequately describe the impact of classicalizing modifications (2.8) on the orientational degrees of freedom and the resulting macroscopicity of experiments based upon them, it is, as always, beneficial to describe the quantum mechanical system as in much detail as possible. This includes the interaction with the environment that will in general decohere the state even in absence of the modifications. As a consequence, any underestimation of this environmental decoherence would lower the macroscopicity of a given experiment, as it would attribute it to the MMM.

The correct description of orientational thermalization is of huge importance not only for assessing macroscopicities: It is an essential tool for studies based on rotational control of molecules and nanoparticles [57–62] and the results of this section are published in Ref. [66].

4.2.1. An orientational Caldeira-Leggett dissipator

The study of orientational decoherence and diffusion is a relatively new field [130–132]. My contribution was an extension of the general decoherence framework to additionally describe friction and eventually thermalization with a surrounding bath. For this pur-

4. Orientational coherence experiments

pose it is instrumental to start from the full many-body Caldeira-Leggett dissipator in Lindblad form [77, 133] for N (distinguishable) particles

$$\mathcal{C}\rho = \frac{1}{i\hbar} \left[\sum_{n=1}^N \frac{\gamma_n}{4} (\mathbf{r}_n \cdot \mathbf{p}_n + (\mathbf{r}_n \cdot \mathbf{p}_n)^\dagger), \rho \right] + \frac{2k_B T}{\hbar^2} \sum_{n=1}^N m_n \gamma_n \left(\mathbf{L}_n \cdot \rho \mathbf{L}_n^\dagger - \frac{1}{2} \left\{ \mathbf{L}_n^\dagger \cdot \mathbf{L}_n, \rho \right\} \right), \quad (4.19)$$

with

$$\mathbf{L}_n = \mathbf{r}_n + \frac{i\hbar}{4m_n k_B T} \mathbf{p}_n. \quad (4.20)$$

It describes the isotropic diffusion and friction of every particle with individual damping rate γ_n ¹. It can be derived for example by means of scattering theory involving test particles in an ideal background gas [134, 135]. The shape of Eq. (4.19) clearly displays the Lindblad-type of the master equation implying with $\gamma_n > 0$ the complete positivity of the time evolution [70].

Another popular way to write the dissipator (4.19) is

$$\mathcal{C}\rho = - \sum_{n,\mu} \left(\frac{k_B T}{\hbar^2} \gamma_n m_n [r_{n,\mu}, [r_{n,\mu}, \rho]] + \frac{i\gamma_n}{2\hbar} [r_{n,\mu}, \{p_{n,\mu}, \rho\}] + \frac{\gamma_n}{16m_n k_B T} [p_{n,\mu}, [p_{n,\mu}, \rho]] \right), \quad (4.21)$$

where μ labels the Cartesian components of the operators. This splits the dissipator into three terms with distinct physical meanings: (i) The first double-commutator describes momentum diffusion with $\langle \mathcal{C}_1^\dagger \mathbf{p}_n \rangle = 0$ and $\langle \mathcal{C}_1^\dagger \mathbf{p}_{n,\mu}^2 \rangle = 2k_B T \gamma_n m_n \equiv D_n$. (ii) The second term describes friction, since $\langle \mathcal{C}_2^\dagger \mathbf{p}_n \rangle = -\gamma_n \langle \mathbf{p}_n \rangle$, and (iii) the last term spatial diffusion with $\langle \mathcal{C}_3^\dagger \mathbf{r}_n \rangle = 0$ and $\langle \mathcal{C}_3^\dagger r_{n,\mu}^2 \rangle = \gamma_n \hbar^2 / 8m_n k_B T$. This spatial diffusion is strongly suppressed by the appearance of \hbar^2 in the numerator, it thus plays only a minor role at low temperatures and its main purpose is to ensure the complete positivity of the whole dissipator. It even vanishes in the classical limit obtained by setting $\hbar \rightarrow 0$ in the Wigner phase space representation of the single particle time evolution,

$$\partial_t^{\mathcal{C}} w_n(\mathbf{r}, \mathbf{p}) \stackrel{\hbar \rightarrow 0}{=} k_B T \gamma_n m_n \nabla_{\mathbf{p}}^2 w_n(\mathbf{r}, \mathbf{p}) + \gamma_n \nabla_{\mathbf{p}} \cdot [\mathbf{p} w_n(\mathbf{r}, \mathbf{p})]. \quad (4.22)$$

In the original derivation of the Caldeira-Leggett dissipator the term leading to spatial diffusion is missing, compromising the complete positivity of the according time evolution.

Equation (4.22) leads to thermalization but not to a stationary state per se. Without an external potential the marginal distribution in the momenta will become stationary but the spatial dispersion will smear the state into infinity. Only if the spatial motion

¹The complicated notation with a conjugate transposition in the commutator is in principle not necessary since it is simply $(\mathbf{r}_n \cdot \mathbf{p}_n)^\dagger = \mathbf{p}_n \cdot \mathbf{r}_n$. This notation will be relevant later when the individual position and momentum operators are expressed by collective degrees of freedom.

4.2. Orientational decoherence, diffusion and thermalization

is contained, for example by a harmonic potential, any state thermalizes eventually assuming the stationary state

$$w_n^{\text{eq}}(\mathbf{r}, \mathbf{p}) \propto e^{-[\mathbf{p}_n^2/2m_n + V(\mathbf{r})]/k_B T}, \quad (4.23)$$

as can be directly checked by inserting into $\partial_t w_n(\mathbf{r}, \mathbf{p}) = \partial_t^{\mathcal{C}} w_n(\mathbf{r}, \mathbf{p}) + \partial_t^{\text{free}} w_n(\mathbf{r}, \mathbf{p})$, with the free time evolution

$$\partial_t^{\text{free}} w_n(\mathbf{r}, \mathbf{p}) = -\frac{\mathbf{p}_n}{m_n} \cdot \nabla_{\mathbf{r}} w_n(\mathbf{r}, \mathbf{p}) + [\nabla_{\mathbf{r}} V(\mathbf{r})] \cdot \nabla_{\mathbf{p}} w_n(\mathbf{r}, \mathbf{p}). \quad (4.24)$$

We will see later that due to the compact configuration space of the orientation state there is no need for an additional potential to thermalize the orientational phase space distribution to a steady state.

The goal of this subsection is to turn Eq. (4.19), describing the $3N$ degrees of freedom exposed to diffusion and friction, into a dissipator only accounting for the collective orientation and angular momentum of a rigid body composed of N particles. For this purpose I will now reduce the degrees of freedom in Eq. (4.19) via the replacements

$$\mathbf{r}_n = \mathbf{R}(\Omega) \mathbf{r}_n^{(0)} \quad \text{and} \quad \mathbf{p}_n = -m_n \mathbf{R}(\Omega) \mathbf{r}_n^{(0)} \times \mathbf{R}(\Omega) I_0^{-1} \mathbf{R}^T(\Omega) \mathbf{J}. \quad (4.25)$$

The new expression for the momentum operator \mathbf{p}_n is motivated by the classical $\mathbf{p}_n = m_n \mathbf{r} \times \tilde{\omega}$ ensures that $\mathbf{J} = \sum_n \mathbf{r}_n \times \mathbf{p}_n$. Its non-hermitian form is the reason for the unorthodox notation in the commutator Eq. (4.19), which, as a byproduct, now vanishes.

Inserting the new positions and momenta (4.25) into Eqs. (4.19) and (4.20) leads to

$$\mathcal{D}\rho = \frac{2k_B T}{\hbar^2} \sum_{n=1}^N m_n \gamma_n \left[\mathbf{R}(\Omega) \mathbf{K}_n \cdot \rho \mathbf{K}_n^\dagger \mathbf{R}^T(\Omega) - \frac{1}{2} \left\{ \mathbf{K}_n^\dagger \cdot \mathbf{K}_n, \rho \right\} \right], \quad (4.26)$$

where $\mathbf{K}_n = \mathbf{r}_n^{(0)} + i\hbar I_0^{-1} \mathbf{R}^T(\Omega) \mathbf{J} \times \mathbf{r}_n^{(0)} / 4k_B T$. This intermediate step makes it easier to see that one can perform the sum over all particles with help of the tensor

$$\tilde{\mathcal{D}}_0 = k_B T \sum_{n=1}^N m_n \gamma_n \mathbf{r}_n^{(0)} \otimes \mathbf{r}_n^{(0)} = \sum_{k=1}^3 \tilde{D}_k \mathbf{d}_k^{(0)} \otimes \mathbf{d}_k^{(0)}, \quad (4.27)$$

where $\mathbf{d}_k^{(0)}$ are the eigenvectors of $\tilde{\mathcal{D}}_0$. The summation leads to the main result of this section, the orientational Caldeira-Leggett dissipator

$$\mathcal{D}\rho = \sum_{k=1}^3 \frac{2\tilde{D}_k}{\hbar^2} \left[\mathbf{A}_k \cdot \rho \mathbf{A}_k^\dagger - \frac{1}{2} \left\{ \mathbf{A}_k^\dagger \mathbf{A}_k, \rho \right\} \right], \quad (4.28)$$

with Lindblad operators

$$\mathbf{A}_k = \mathbf{d}_k(\Omega) - \frac{i\hbar}{4k_B T} \mathbf{d}_k(\Omega) \times \mathbf{I}^{-1}(\Omega) \mathbf{J}. \quad (4.29)$$

4. Orientational coherence experiments

Here, $\mathbf{d}_k(\Omega) = \mathbf{R}(\Omega)\mathbf{d}_k^{(0)}$ and $\mathbf{I}^{-1}(\Omega) = \mathbf{R}(\Omega)\mathbf{I}_0^{-1}\mathbf{R}^T(\Omega)$ are the rotated counterparts of the unrotated expressions.

The $\mathbf{d}_k(\Omega)$ are also the eigenvectors of the diffusion matrix $\mathbf{D}(\Omega)$ which is linked to $\tilde{\mathbf{D}}_0$ via

$$\mathbf{D}(\Omega) = \sum_{k=1}^3 \tilde{D}_k [\mathbb{1} - \mathbf{d}_k(\Omega) \otimes \mathbf{d}_k(\Omega)]. \quad (4.30)$$

From this follows the relation of eigenvalues $D_k = \tilde{D}_i + \tilde{D}_j$, or the other way around $\tilde{D}_k = (D_i + D_j - D_k)/2$, with (i, j, k) being permutations of $(1, 2, 3)$. For the dissipator (4.28) to be positive requires $\tilde{D}_k \geq 0$ and thus $D_i + D_j \geq D_k$, which is a strong constraint on the diffusion tensor but already observed for isotropic diffusion in the classical regime, as shown in App. C.1.1.

4.2.2. General predictions of the orientational Caldeira-Leggett dissipator

Before I exemplarily apply this heuristically derived dissipator on two scenarios, namely the planar and linear rotor, I want to ensure that the dissipator (4.28) in general leads to the desired diffusion, friction, and thermalization. This includes the correct Ehrenfest equations for \mathbf{J} and \mathbf{J}^2 , as well as the steady state energy. Furthermore, the classical limit is calculated to verify quantum-to-classical consistency.

All the relevant quantities can be calculated straightforwardly by following the commutator relations summarized in Tab. 4.1. An exemplary calculation for the first moment of \mathbf{J} is shown in App. C.1.2 resulting in

$$\langle \mathcal{D}^\dagger \mathbf{J} \rangle = -\langle \Gamma(\Omega) \mathbf{J} \rangle + \mathcal{O}(\hbar), \quad (4.31)$$

with the friction tensor

$$\Gamma(\Omega) = \frac{1}{k_B T} \mathbf{D}(\Omega) \mathbf{I}^{-1}(\Omega). \quad (4.32)$$

The corresponding calculation for the tensor $\mathbf{J} \otimes \mathbf{J}$ and as a special case for its second moments reveals

$$\langle \mathcal{D}^\dagger \mathbf{J} \otimes \mathbf{J} \rangle = -\langle \Gamma(\Omega) \mathbf{J} \otimes \mathbf{J} + \mathbf{J} \otimes \mathbf{J} \Gamma^T(\Omega) \rangle + 2\langle \mathbf{D}(\Omega) \rangle + \mathcal{O}(\hbar) \quad (4.33)$$

and

$$\langle \mathcal{D}^\dagger \mathbf{J}^2 \rangle = -2\langle \mathbf{J} \cdot \Gamma(\Omega) \mathbf{J} \rangle + 2\text{Tr}[\mathbf{D}(\Omega)] + \mathcal{O}(\hbar). \quad (4.34)$$

As one would expect, any net angular momentum gets diminished until $\langle \mathcal{D}^\dagger \mathbf{J} \rangle = 0$ while the second moment approaches an equilibrium value as soon as $\langle \mathbf{J} \cdot \Gamma(\Omega) \mathbf{J} \rangle = \text{Tr}[\mathbf{D}(\Omega)] + \mathcal{O}(\hbar)$, where any angular momentum gain due to diffusion is compensated by the friction. From this we can directly calculate the steady state energy of the rotor to be

$$\langle \mathbf{H} \rangle = \frac{1}{2} \langle \mathbf{J} \cdot \mathbf{I}(\Omega)^{-1} \mathbf{J} \rangle = \frac{f}{2} k_B T + \mathcal{O}(\hbar), \quad (4.35)$$

4.2. Orientational decoherence, diffusion and thermalization

where $f = \text{rank}[\mathbf{I}(\Omega)]$ denotes the number of rotational degrees of freedom.

The calculation of the classical limit of Eq. (4.28) is accomplished with help of the Wigner function for the rotation state [129, 136] in close analogy to the calculation of Eq. (4.22). Derivation of the time evolution of this orientational Wigner function while simultaneously sending \hbar to zero is demonstrated in App. C.1.2. It leads to the orientational Fokker-Planck equation

$$\partial_t^{\mathcal{P}} w(\Omega, \mathbf{J}) \stackrel{\hbar \rightarrow 0}{=} \nabla_{\mathbf{J}} \cdot [\Gamma(\Omega) \mathbf{J} w(\Omega, \mathbf{J})] + \nabla_{\mathbf{J}} \cdot \mathbf{D}(\Omega) \nabla_{\mathbf{J}} w(\Omega, \mathbf{J}). \quad (4.36)$$

Naturally, this equation is also obtained by inserting the classical version (simply replacing the operators with scalars) of the position and momentum operators (4.25) into Eq. (4.22) as shown in App. C.1.1. More importantly, Eq. (4.36) can be microscopically derived in a classical derivation for arbitrarily shaped particles in a rarefied gas [137] indicating the consistency of the here presented heuristic derivation with first principles calculations.

It is easy to show via integration by parts that Eq. (4.36) reproduces the equations of motions for the semiclassical expectation values (4.31)-(4.34). Moreover, calculating the steady state of Eq. (4.36) results in the Gibbs state including only the free rotational energy,

$$w(\Omega, \mathbf{J}) \propto \exp \left[-\frac{\mathbf{J} \cdot \mathbf{I}^{-1}(\Omega) \mathbf{J}}{2k_{\text{B}}T} \right]. \quad (4.37)$$

The quantum version of the Gibbs state (4.37), i.e.

$$\rho_{\text{G}} = \exp[-\mathbf{H}/k_{\text{B}}T], \quad (4.38)$$

inserted into the dissipator (4.28) turns out to be stationary as well, apart from corrections in higher orders of the reciprocal temperature (see App. C.1.2). As a consequence, any stationary state is approximated by the Gibbs state for high enough temperatures when sufficiently many angular momentum eigenstates are populated such that the discrete nature of the Hilbert space is negligible. However, as we will see by studying the exemplary cases in the next subsections, the Gibbs state is practically indistinguishable from the true steady state deep in the quantum regime.

4.2.3. Planar rotor

A rigid rotor can be approximated as a planar rotor if its motion is sufficiently confined to a single plane and the orientation can be described by a single angle α . Aligning this plane with the space-fixed xy -plane one can write the orientational state as $\mathbf{e}_r(\alpha) = \mathbf{e}_1 \cos \alpha + \mathbf{e}_2 \sin \alpha$. The angular momentum operator only has one entry \mathbf{p}_α that is perpendicular to the plane, $\mathbf{J} = \mathbf{e}_3 \mathbf{p}_\alpha$. The only remaining Lindblad operator (4.29) takes on the simple form

$$\mathbf{A} = \mathbf{e}_r(\alpha) + \frac{i\hbar}{4k_{\text{B}}T\mathbf{I}} \mathbf{e}_\phi(\alpha) \mathbf{p}_\alpha, \quad (4.39)$$

4. Orientational coherence experiments

with $\mathbf{e}_\phi(\alpha) = \mathbf{e}_3 \times \mathbf{e}_r(\alpha)$ and the diffusion tensor and the tensor of inertia reduced to scalars D and I , respectively.

The exact stationary state produced by Eq. (4.39) and the free Hamiltonian $H = \mathbf{p}_\alpha^2/2I$ can be calculated explicitly. In order to do this it is helpful to note that the unitary part of the time evolution demands the steady state to be diagonal in the momentum basis,

$$\rho_{\text{eq}} = \sum_{m_\alpha \in \mathbb{Z}} \rho_{\text{eq}}^{m_\alpha} |m_\alpha\rangle \langle m_\alpha|. \quad (4.40)$$

In the following, I will drop the index α as there is only one quantum number. Plugging Eq. (4.40) into the orientational Caldeira-Leggett equation with Lindblad operator (4.39) leads to coupling solely of neighboring entries in the populations ρ_{eq}^m , see App. C.1.3. Starting with the requirement $\langle m=0 | \mathcal{D}\rho | m=0 \rangle \stackrel{!}{=} 0$ one can then iteratively deduce the equilibrium state as

$$\rho_{\text{eq}}^m = \frac{1}{Z} \binom{2\xi}{|m|}^2 \binom{2\xi + |m|}{|m|}^{-2} \simeq \frac{1}{2^{2\xi}} \binom{2\xi}{\xi + m}, \quad (4.41)$$

with $\xi = 2Ik_B T/\hbar^2$. Here, the approximation is obtained by dropping the orientational diffusion term in Eq. (4.28) proportional to $1/T$. Both expressions approach the Gibbs state $\rho_{\text{eq}}^m \propto \exp(-m^2/\xi)$ for $\xi \rightarrow \infty$, as evident by Stirling's formula.

In order to describe a thermalization process over time we utilize the Wigner function of the orientation state [136]. For a planar rotor with single degree of freedom α it reads

$$w_m(\alpha) = \frac{1}{2\pi} \int_{-\pi}^{\pi} d\alpha_0 e^{im\alpha_0} \left\langle \alpha - \frac{\alpha_0}{2} \left| \rho \right| \alpha + \frac{\alpha_0}{2} \right\rangle. \quad (4.42)$$

Application of the dissipator (4.28) with Lindblad operators (4.39) leads to

$$\begin{aligned} \partial_t^{\mathcal{D}} w_m(\alpha) = & \frac{\Gamma}{2} [(m+1)w_{m+1}(\alpha) - (m-1)w_{m-1}(\alpha)] + D \frac{w_{m+1}(\alpha) - 2w_m(\alpha) + w_{m-1}(\alpha)}{\hbar^2} \\ & - \frac{\hbar^2 \Gamma}{4k_B T I} \left\{ m^2 w_m(\alpha) - \frac{(m+1)^2}{2} w(\alpha, m+1) - \frac{(m-1)^2}{2} w(\alpha, m-1) \right. \\ & \left. - \frac{1}{4} \partial_\alpha^2 \left[w_m(\alpha) + \frac{1}{2} w_{m+1}(\alpha) + \frac{1}{2} w_{m-1}(\alpha) \right] \right\}. \end{aligned} \quad (4.43)$$

The term proportional to \hbar^2 is once again a product of the orientational diffusion and can be neglected if small deviations from a perfectly positive state during the thermalization process can be beared with. The remaining terms then resemble a one-dimensional Fokker-Planck equation (4.36) with discretized derivatives thus once more showing consistency in the classical limit.

To illustrate the thermalization dynamics the initial state is chosen to be a superposition of two quasi-Gaussians centered at angular momenta $\pm m_0$,

$$\psi(\alpha) = \frac{\cos(\alpha m_0) \exp(\cos \alpha / 4\sigma^2)}{\sqrt{\pi I_0(1/2\sigma^2)}}, \quad (4.44)$$

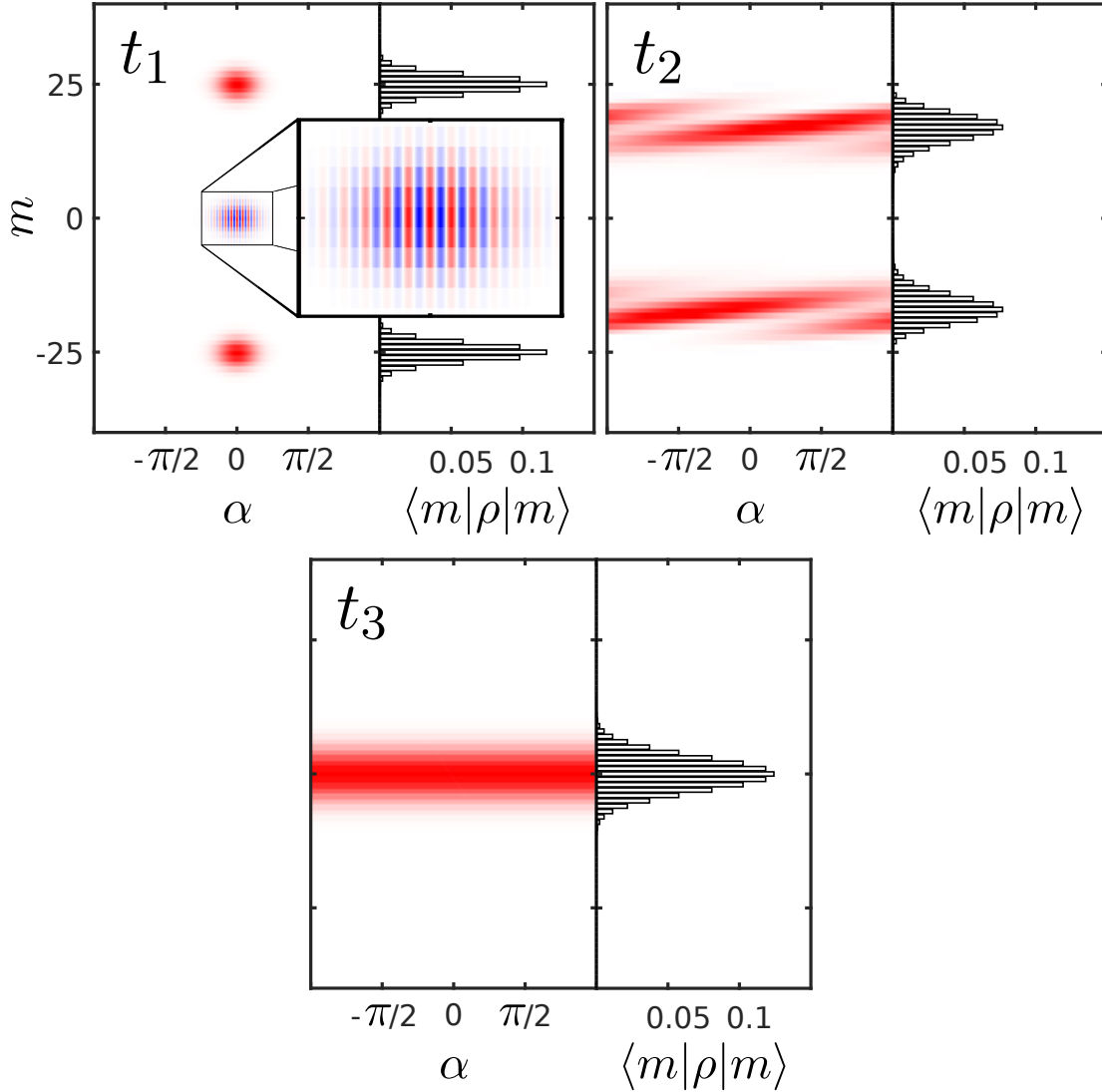


Figure 4.1.: Shown is an exemplary thermalization process of a planar rotor state with the free Hamiltonian $H = \mathbf{p}_\alpha^2/2I$ and the dissipator (4.28), visualized by the Wigner phase space function [136]. The initial state at $t_1 = 0$ is given by Eq. (4.45) and exhibits a fringe structure with negative values in blue typical for superposition states. The initial values are chosen to be $m_0 = 25$, $\sigma = 0.2$, $\xi = 20$, and $\Gamma = \hbar/\pi I$. The state first turns into a mixture indicated by the vanishing fringes at $t_2 = 4\pi I/10\hbar$ and then, on a much longer timescale, thermalizes with the environment. The steady state is virtually reached at $t_3 = 4\pi I/\hbar$ and well approximated by the Gibbs state (4.38).

4. Orientational coherence experiments

with the corresponding Wigner function

$$w_m(\alpha) = \frac{1}{4\pi I_0(1/2\sigma_2)} \sum_k I_k \left(\frac{\cos \alpha}{2\sigma_2} \right) \left\{ 2 \operatorname{sinc} \left[\pi \left(m + \frac{k}{2} \right) \right] \cos(2m_0\alpha) \right. \\ \left. + \operatorname{sinc} \left[\pi \left(m - m_0 + \frac{k}{2} \right) \right] + \operatorname{sinc} \left[\pi \left(m + m_0 + \frac{k}{2} \right) \right] \right\}. \quad (4.45)$$

The time evolution of this state is depicted in Fig. 4.1. It first decoheres into a mixture and then, on a much longer timescale $1/\Gamma$, thermalizes with the environment to produce the steady state (4.41).

4.2.4. Linear rotor

We can gain one level of generality by switching from a planar rotor to a linear rotor. It can be understood as a infinitely thin rotor (because of a negligible thickness compared to its length) with a two-dimensional orientational degree of freedom encoded by the direction of its symmetry axis $\mathbf{m}(\Omega)$, with $\Omega = (\alpha, \beta)^2$. The various tensors describing the properties of the linear rotor and its coupling to the bath are just slightly more complicated than in the case of the planar rotor since there is only one independent entry in the rank-2 matrices,

$$\begin{aligned} \mathbf{I}(\Omega) &= I[\mathbb{1} - \mathbf{m}(\Omega) \otimes \mathbf{m}(\Omega)], \\ \Gamma(\Omega) &= \Gamma[\mathbb{1} - \mathbf{m}(\Omega) \otimes \mathbf{m}(\Omega)], \\ \mathbf{D}(\Omega) &= D[\mathbb{1} - \mathbf{m}(\Omega) \otimes \mathbf{m}(\Omega)]. \end{aligned} \quad (4.46)$$

Similar to the planar rotor we obtain only a single Lindblad operator

$$\mathbf{A} = \mathbf{m}(\Omega) - \frac{i\hbar}{4k_B T I} \mathbf{m}(\Omega) \times \mathbf{J}. \quad (4.47)$$

Inserting the Lindblad operator (4.47) into Eq. (4.28) results in

$$\begin{aligned} \mathcal{D}\rho &= \frac{2D}{\hbar^2} [\mathbf{m}(\Omega) \cdot \rho \mathbf{m}(\Omega) - \rho] - \frac{i\Gamma}{2\hbar} [\mathbf{m}(\Omega) \times \mathbf{J} \cdot \rho \mathbf{m}(\Omega) + \mathbf{m}(\Omega) \cdot \rho \mathbf{J} \times \mathbf{m}(\Omega)] \\ &\quad - \frac{\Gamma}{8k_B T I} \left[\mathbf{m}(\Omega) \times \mathbf{J} \cdot \rho \mathbf{J} \times \mathbf{m}(\Omega) - \frac{1}{2} \{ \mathbf{J} \cdot \mathbf{m}(\Omega) \otimes \mathbf{m}(\Omega) \mathbf{J} - \mathbf{J}^2, \rho \} \right], \end{aligned} \quad (4.48)$$

describing in order of appearance momentum diffusion, friction, and orientational diffusion. The last one may, as always, be neglected resulting in minor violations of the state positivity during the time evolution.

Like in the case of the planar rotor, one can determine the equilibrium state by noting that the free Hamiltonian $\mathbf{H} = \mathbf{J}^2/2I$ only commutes with a state diagonal in the angular momenta. As before this results in a coupled set of equations that can be solved as

$$\rho_{\text{eq}} = \sum_{\ell m} \rho_{\text{eq}}^{\ell m} |\ell m\rangle \langle \ell m| \quad \text{with} \quad \rho_{\text{eq}}^{\ell m} = \frac{1}{Z} \binom{2\xi}{\ell}^2 \binom{2\xi + \ell + 1}{\ell}^{-2}, \quad (4.49)$$

²In the case of a linear rotor the Euler angles α, β are identical with the azimuthal and polar angles ϕ, θ .

4.2. Orientational decoherence, diffusion and thermalization

with $\xi = 2Ik_{\text{B}}T/\hbar^2$. Again Stirling's formula can be used to show that Eq. (4.49) approaches the Gibbs state $\rho_{\text{eq}}^{\ell m} \sim \exp[-\ell(\ell+1)/\xi]$ for $\xi \rightarrow \infty$.

To demonstrate the thermalization process of the linear rotor I choose an orientational superposition state

$$\langle \Omega | \psi_0 \rangle \sim \exp[-|\mathbf{e}_3 \times \mathbf{m}(\Omega)|^2/2\sigma^2], \quad (4.50)$$

being a superposition of pointing upwards and downwards in z -direction. The time evolution is shown in Fig. 4.2 with help of three snapshots and a plot of the important system parameters of the linear rotor, namely the energy, entropy and purity. The latter reflects the fast decay of coherences $\sim 2D/\hbar^2$ and only on the larger timescale $1/\Gamma$ the rotor slowly thermalizes with the environment as evident by the saturation of the energy. In the depicted scenario the bath temperature enters via $\xi = 10$ which leads to a thermal occupation number as low as $\bar{\ell} = 2.7$. Even though the resulting equilibrium state lies deep in the quantum regime it is already well approximated by the Gibbs state $\rho_{\text{eq}}^{\ell m} \sim \exp[-\ell(\ell+1)/\xi]$.

For azimuthally symmetric rotors like the linear rotor the interaction with its surroundings only depend on the orientation of the symmetry axis $\mathbf{m}(\Omega)$ [132]. As a direct consequence of the angular momentum diffusion the localization rate of coherences of different orientations, $\partial_t \langle \Omega | \rho | \Omega' \rangle = -F(\Omega, \Omega') \langle \Omega | \rho | \Omega' \rangle$, is

$$F(\Omega, \Omega') = \frac{2D}{\hbar^2} [1 - \mathbf{m}(\Omega) \cdot \mathbf{m}(\Omega')]. \quad (4.51)$$

It is maximized if the symmetry axes are anti-parallel and the orientational delocalization is at its maximum. This should not be the case if the nanorotor is inversion symmetric and the interaction with the bath can not tell both orientations apart. This can easily be fixed by implementing a quadratic dependence of the Lindblad operators in the particle orientation similar to how it is obtained if the inversion symmetry is considered in the microscopic derivation [132]. This yields the alternative dissipator

$$\mathcal{D}\rho = \frac{D}{\hbar^2} \text{Tr} \left[\mathbf{B}\rho\mathbf{B}^\dagger - \frac{1}{2} \{ \mathbf{B}^\dagger \mathbf{B}, \rho \} \right], \quad (4.52)$$

with now tensorial Lindblad operators (therefore the matrix trace $\text{Tr}(\cdot)$)

$$\mathbf{B} = \mathbf{m}(\Omega) \otimes \mathbf{m}(\Omega) - \frac{i\hbar}{2k_{\text{B}}T} \mathbf{m}(\Omega) \otimes \mathbf{m}(\Omega) \times \mathbf{I}^{-1}(\Omega) \mathbf{J}. \quad (4.53)$$

The hermitian form of the second term in the Lindblad operator as the time derivative of $\partial_t [\mathbf{m}(\Omega) \otimes \mathbf{m}(\Omega)]$ can be omitted since the additional term leads to the same result under the matrix trace in Eq. (4.52). The inversion symmetric dissipator leads to the desired localization rate

$$F(\Omega, \Omega') = \frac{D}{\hbar^2} |\mathbf{m}(\Omega) \times \mathbf{m}(\Omega')|^2, \quad (4.54)$$

vanishing only if $\mathbf{m}(\Omega)$ and $\mathbf{m}(\Omega')$ are parallel. Simultaneously, the dissipator (4.52) still leads to Eqs. (4.31), (4.33), (4.34), (4.35), and in the classical limit to Eq. (4.36) where the inversion symmetry should play no role.

4. Orientational coherence experiments

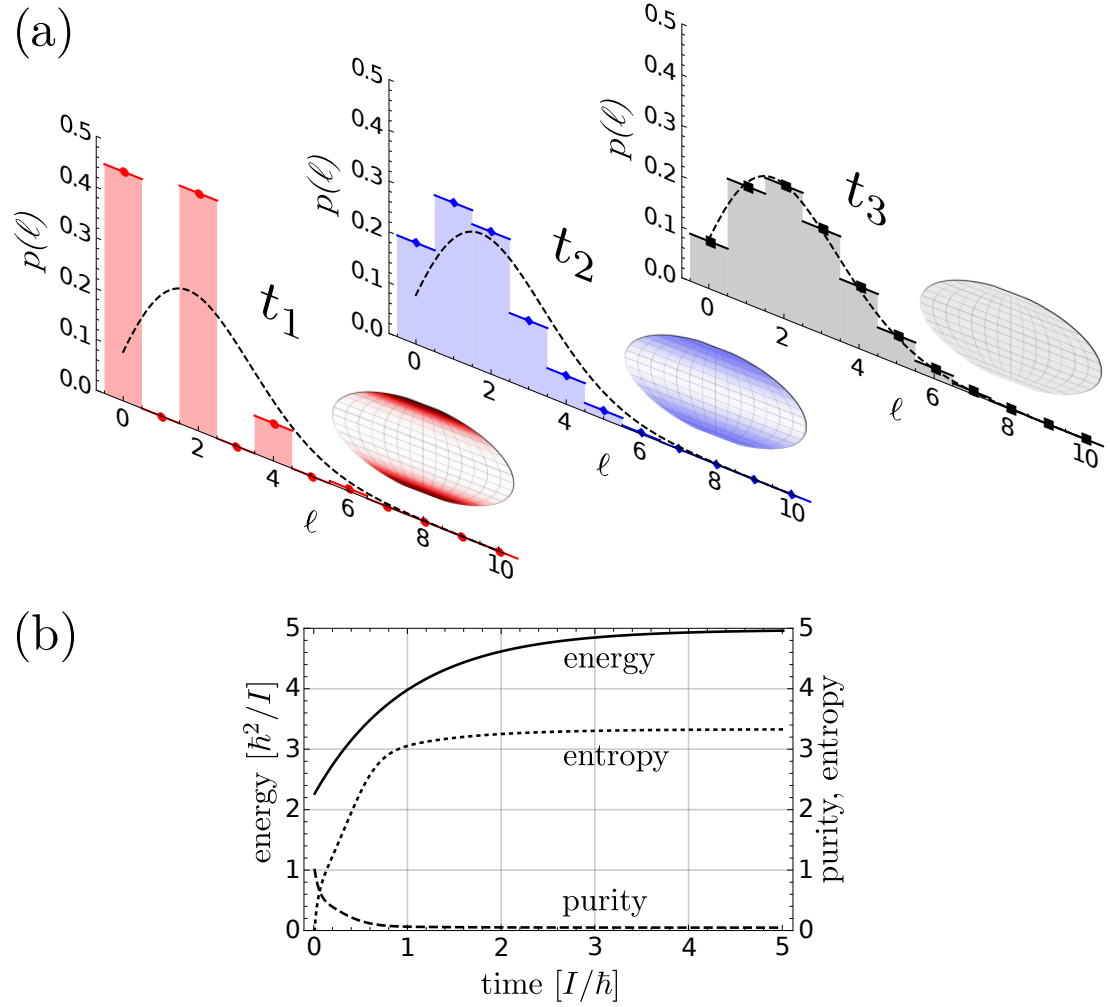


Figure 4.2.: Shown is an exemplary thermalization process of a linear rigid rotor with the free Hamiltonian $H = \mathbf{J}^2/2I$ and the dissipator (4.28), initially in the superposition state (4.50) and with parameters $\xi = 10$, $\Gamma = \hbar/I$, and $\sigma = 0.4$. (a) Snapshots of the rotor state are shown at the times $t_1 = 0$, $t_2 = 0.5 I/\hbar$, and $t_3 = 0.5 I/\hbar$. The histogram depicts the probability for different total angular momentum states $p_\ell = \sum_{m=-\ell}^{\ell} \langle \ell m | \rho | \ell m \rangle$ and shows the typical even to odd structure of orientational superposition states with polar symmetry. The Gibbs state, represented by a dashed line, is a reasonable approximation even for steady state temperatures deep in the quantum regime like $k_B T = 5\hbar^2/I$. The insets are Mollweide projections of the state in the orientational basis $\langle \Omega | \rho | \Omega \rangle$. (b) Plotted are the energy expectation value $\langle H \rangle$ (solid line), the von Neumann entropy $-\text{tr}(\rho \log \rho)$ (dotted line), and the purity $\text{tr}(\rho^2)$ (dashed lines) over time.

4.3. Classicalizing modifications applied on orientational degrees of freedom

As mentioned in the beginning of the chapter, the enormous progress in the manipulation and control of nano-sized rigid rotors and the prospect to reach the quantum regime promise to open up a new playing field for the study of quantum effects on the mesoscopic scale. Naturally, one may want to assess the macroscopicity for those kinds of experiments and therefore a formulation of the MMM for spatio-orientational degrees of freedom is needed. Even though the discussion will be close to the example case of rigid rotors, such a spatio-orientational MMM can be applied to all orientational mechanical degrees of freedom, for example a particle in a ring trap or the like. The general spatio-orientational MMM generator and its applications are published in Refs. [43, 65].

4.3.1. Orientational degrees of freedom under classicalizing modifications

Neglecting the spatial displacements in the MMM, since all relevant processes take place far above the femtometer scale, one can write the MMM generator (2.8) as [13]

$$\frac{1}{\tau_e} \mathcal{M}_{\sigma\rho} = -\frac{1}{2\tau_e} \left(\frac{2\sigma_q^2}{\pi\hbar^2} \right)^{3/2} \int d^3\mathbf{s} [\mathbf{M}(\mathbf{s}), [\mathbf{M}(\mathbf{s}), \rho]], \quad (4.55)$$

with the Lindblad operator

$$\mathbf{M}(\mathbf{s}) = \sum_n \frac{m_n}{m_e} e^{-(\mathbf{s}-\mathbf{r}_n)^2 \sigma_q^2 / \hbar^2}. \quad (4.56)$$

Since all the atoms in a rigid body can be assumed to be sufficiently localized and distinguishable from each other this approximation in first quantization of the Lindblad operator is allowed. As in Sec. 4.2.1 the $3N$ degrees of freedom are reduced to collective ones: The center-of-mass position \mathbf{R}_{cm} and the orientation Ω . The individual position of any atom in the rotor is then $\mathbf{r}_n = \mathbf{R}_{\text{cm}} + \mathbf{R}(\Omega)\mathbf{r}_n^{(0)} + \Delta\mathbf{r}_n$. The $\mathbf{r}_n^{(0)}$ are the equilibrium positions of the atoms while $\Delta\mathbf{r}_n$ are the displacements caused for example by phonon modes. These are on a much smaller length scale (typically femtometers) than the lattice constants and therefore negligible. This completes the reduction of degrees of freedom.

The Lindblad operator (4.56) becomes

$$\begin{aligned} \mathbf{M}(\mathbf{s}) &= \frac{1}{m_e} \int d^3\mathbf{r} \varrho[\mathbf{R}^T(\Omega)\mathbf{r}] e^{-(\mathbf{s}-\mathbf{R}_{\text{cm}}-\mathbf{r})^2 \sigma_q^2 / \hbar^2} \\ &= \frac{1}{m_e} \left(\frac{\hbar^2}{4\pi\sigma_q^2} \right)^{3/2} \int d^3\mathbf{k} e^{-\hbar^2 k^2 / 4\sigma_q^2 + i\mathbf{k}\cdot(\mathbf{s}-\mathbf{R}_{\text{cm}})} \tilde{\varrho}[\mathbf{R}^T(\Omega)\mathbf{k}], \end{aligned} \quad (4.57)$$

with the mass density

$$\varrho(\mathbf{r}) = \sum_n m_n \delta(\mathbf{r} - \mathbf{r}_n^{(0)}). \quad (4.58)$$

4. Orientational coherence experiments

I denote the Fourier transform of $\varrho(\mathbf{r})$ as $\tilde{\varrho}(\mathbf{k})$ that is normalized to the overall mass of the rotor, $\tilde{\varrho}(0) = M$, and often referred to as the form factor. If $\hbar/\sigma_q \gg 5\text{\AA}$, i.e. the modification-induced momentum translation cannot resolve the crystal structure of the nanorotor, a continuous mass density can be used as an approximation. Inserting the operator (4.57) into Eq. (4.55) results eventually in

$$\frac{1}{\tau_e} \mathcal{M}_{\sigma\rho} = \frac{\hbar^3}{\tau_e m_e^2 \sqrt{2\pi\sigma_q^2}} \int d^3\mathbf{k} e^{-\hbar^2 k^2 / 2\sigma_q^2} \times \left[e^{-i\mathbf{k}\cdot\mathbf{R}_{\text{cm}}} \tilde{\varrho}[\mathbf{R}^T(\Omega)\mathbf{k}] \rho \tilde{\varrho}^*[\mathbf{R}^T(\Omega)\mathbf{k}] e^{i\mathbf{k}\cdot\mathbf{R}_{\text{cm}}} - \frac{1}{2} \{ |\tilde{\varrho}[\mathbf{R}^T(\Omega)\mathbf{k}]|^2, \rho \} \right]. \quad (4.59)$$

The Lindblad generator (4.59) leads to decoherence both in the center-of-mass and in the orientation. While the absolute orientation always impacts the spatial decoherence the other way around this is not the case: The decay of orientational coherences with respect to Ω and Ω' depends only on the relative orientation $\tilde{\Omega}(\Omega, \Omega')$, defined by $\mathbf{R}(\tilde{\Omega}) = \mathbf{R}^T(\Omega')\mathbf{R}(\Omega)$. This is made evident by tracing out the center-of-mass degrees of freedom in Eq. (4.59) leading to

$$\frac{1}{\tau_e} \langle \Omega | \text{tr}_{\text{cm}}(\mathcal{M}_{\sigma\rho}) | \Omega' \rangle = -F(\Omega, \Omega') \langle \Omega | \text{tr}_{\text{cm}}(\rho) | \Omega' \rangle. \quad (4.60)$$

The localization rate

$$F(\Omega, \Omega') = \frac{\hbar^3}{2\tau_e m_e^2 \sqrt{2\pi\sigma_q^2}} \int d^3\mathbf{k} e^{-\hbar^2 k^2 / 2\sigma_q^2} |\tilde{\varrho}[\mathbf{R}^T(\Omega)\mathbf{k}] - \tilde{\varrho}[\mathbf{R}^T(\Omega')\mathbf{k}]|^2 \quad (4.61)$$

is always real since for complex form factors, $\tilde{\varrho}(\mathbf{k}) = \tilde{\varrho}^*(-\mathbf{k})$, the imaginary part of the integrand is odd and vanishes together with the Gaussian after integration. By simply rotating \mathbf{k} with $\mathbf{R}(\Omega)$ we observe that the localization function indeed only depends on $\mathbf{R}(\tilde{\Omega}) = \mathbf{R}^T(\Omega')\mathbf{R}(\Omega)$.

For azimuthally symmetric particles the orientational degree of freedom consists only of the direction of the symmetry axis $\mathbf{m}(\Omega)$ so that the relative orientation $\tilde{\Omega}$ reduces to a single angle $\alpha = \arccos[\mathbf{m}(\Omega) \cdot \mathbf{m}(\Omega')]$. In the cases of cylinders and spheroids of radius R and length L the resulting localization rate (4.61) is shown in Fig. 4.3, calculated with help of the continuous form factors

$$\tilde{\varrho}_{\text{cyl}}(\mathbf{k}) = \frac{2M}{R|\mathbf{e}_3 \times \mathbf{k}|} J_1(R|\mathbf{e}_3 \times \mathbf{k}|) \text{sinc}\left(\frac{L}{2}\mathbf{e}_3 \cdot \mathbf{k}\right), \quad (4.62)$$

and

$$\tilde{\varrho}_{\text{sph}}(\mathbf{k}) = M \sqrt{\frac{9\pi}{2}} \frac{J_{3/2}\left(\sqrt{R^2|\mathbf{e}_3 \times \mathbf{k}|^2 + L^2|\mathbf{e}_3 \cdot \mathbf{k}|^2/4}\right)}{\sqrt{R^2|\mathbf{e}_3 \times \mathbf{k}|^2 + L^2|\mathbf{e}_3 \cdot \mathbf{k}|^2/4}}, \quad (4.63)$$

so that $\mathbf{e}_3 = \mathbf{m}(0)$ is the symmetry axis in both cases; $J_n(\cdot)$ are Bessel functions.

4.3. Classicalizing modifications applied on orientational degrees of freedom

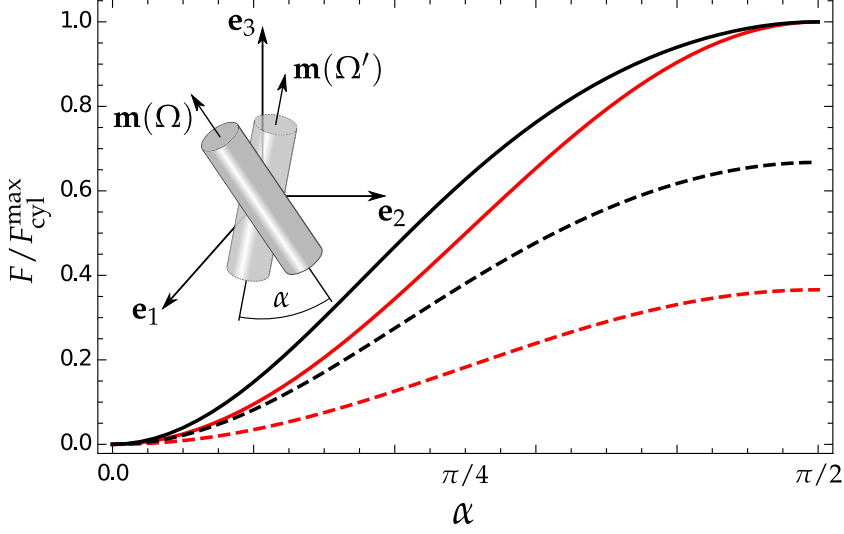


Figure 4.3.: Orientational localization rate (4.61) for a cylinder (solid lines) and a spheroid (dashed lines) as a function of the relative orientation $\alpha = \arcsin|\mathbf{m}(\Omega) \times \mathbf{m}(\Omega')|$. Two cases are studied: If $\hbar/\sqrt{2}\sigma_q = L$ (red lines) the localization rate is still proportional to $|\mathbf{m}(\Omega) \cdot \mathbf{m}(\Omega')|$, even though we are no longer in the regime $L, R \ll \hbar/\sigma_q$ that leads to Eq. (4.64). Going further to $\hbar/\sqrt{2}\sigma_q = L/10$ (black lines) this simple $\sin^2(\alpha)$ dependence is eventually lost. The curves in both length scenarios are normalized to the maximum localization rate of the cylinder in the respective case and extensions are chosen as $L/R = 20$ motivated by real experimental scenarios [57, 59].

The limit of $L, R \ll \hbar/\sigma_q$ leads for both geometries to a sinusoidal dependence of the localization rate (4.61) on α ,

$$F(\Omega, \Omega') \simeq \frac{\sigma_q^4 M^2}{2\tau_e m_e^2 \hbar^4} \left(\frac{R^2}{a} - \frac{L^2}{b} \right)^2 |\mathbf{m}(\Omega) \times \mathbf{m}(\Omega')|^2, \quad (4.64)$$

with numerical constants $a_{\text{cyl}} = 4$, $b_{\text{cyl}} = 12$ and $a_{\text{sph}} = 5$, $b_{\text{sph}} = 20$. This sinusoidal dependence in $|\mathbf{m}(\Omega) \times \mathbf{m}(\Omega')|^2 = \sin^2 \alpha$ was also found for environmentally induced decoherence processes in the limit of small anisotropies [130]. It is noteworthy that in the same limit the localization rate scales with the *tenth* power of the particle size at a fixed density, regardless of the shape, as follows from a dimensional analysis of Eq. (4.61). On the other hand, the rate (4.64) vanishes for isotropic tensors of inertia, i.e. for cylinders with $R = L/\sqrt{3}$ and for spheroids with $R = L/2$ (turning them into spheres).

4.3.2. Linear- and angular-momentum diffusion

While the macroscopicity measure defined via Eq. (2.58) is aimed at experiments exhibiting true quantum phenomena, the underlying MMM can also be tested by simply

4. *Oriental coherence experiments*

monitoring the energy increase of an isolated system or systems at thermal equilibrium. Especially the CSL model, a particular MMM, is predominantly examined by these kind of experiments [37–45]. At the end of the day, it is the linear- and angular-momentum diffusion-limit of the generator (4.59) that will be investigated to assess the modification-induced heating. This limit can be obtained states for sufficiently well localized in position and orientation around Ω_0 , i.e. if $\langle \mathbf{R}_{\text{cm}}\Omega | \rho | \mathbf{R}'_{\text{cm}}\Omega' \rangle \simeq 0$ unless $|\mathbf{R}_{\text{cm}} - \mathbf{R}'_{\text{cm}} + \mathbf{R}(\Omega_0)[\mathbf{R}(\tilde{\Omega}) - \mathbb{1}]\mathbf{r}_n^{(0)}| \ll \hbar/\sigma_q$ for all n . For such small relative orientations one may expand the rotation matrix with up to three small and commuting rotations as

$$\mathbf{R}(\tilde{\Omega}) \simeq \mathbb{1} + \epsilon_{ijk} d\Omega_i \mathbf{e}_k \otimes \mathbf{e}_j, \quad (4.65)$$

where $d\Omega_i$ denotes the angle of rotation around the \mathbf{e}_i axis.

An expansion of the generator (4.59) into the lowest order of $|\mathbf{R}_{\text{cm}} - \mathbf{R}'_{\text{cm}}|$ and $d\Omega_i$ decouples the diffusion in center-of-mass and orientation. The resulting localization rate is therefore given by a sum,

$$\langle \mathbf{R}_{\text{cm}}\Omega | \mathcal{M}_{\sigma\rho} | \mathbf{R}'_{\text{cm}}\Omega' \rangle \simeq -[F_{\text{cm}}(\mathbf{R}_{\text{cm}} - \mathbf{R}'_{\text{cm}}, \Omega_0) + F_{\text{rot}}(\Omega, \Omega')] \langle \mathbf{R}_{\text{cm}}\Omega | \mathcal{M}_{\sigma\rho} | \mathbf{R}'_{\text{cm}}\Omega' \rangle. \quad (4.66)$$

The respective rates are

$$F_{\text{cm}}(\mathbf{R}, \Omega_0) = \frac{\sigma_q^2}{\tau_e \hbar^2} \mathbf{R} \cdot \mathbf{R}(\Omega_0) \mathbf{A}_{\text{cm}} \mathbf{R}^T(\Omega_0) \mathbf{R}, \quad (4.67a)$$

$$F_{\text{rot}}(\Omega, \Omega') = \frac{1}{2\tau_e} d\Omega \cdot \mathbf{A}_{\text{rot}} d\Omega, \quad (4.67b)$$

with the geometry tensors

$$\mathbf{A}_{\text{cm}} = \frac{1}{\pi^{3/2} m_e^2} \left(\frac{\hbar^2}{2\sigma_q^2} \right)^{5/2} \int d^3\mathbf{k} e^{-\hbar^2 k^2 / 2\sigma_q^2} |\tilde{\varrho}(\mathbf{k})|^2 \mathbf{k} \otimes \mathbf{k}, \quad (4.68a)$$

$$\mathbf{A}_{\text{rot}} = \frac{1}{\pi^{3/2} m_e^2} \left(\frac{\hbar^2}{2\sigma_q^2} \right)^{5/2} \int d^3\mathbf{k} e^{-\hbar^2 k^2 / 2\sigma_q^2} [\mathbf{k} \times \nabla_{\mathbf{k}} \tilde{\varrho}(\mathbf{k})] \otimes [\mathbf{k} \times \nabla_{\mathbf{k}} \tilde{\varrho}(\mathbf{k})]. \quad (4.68b)$$

Those geometry tensors generalize the geometry factor for center-of-mass momentum diffusion in a single direction defined in Ref. [138].

If we are interested in symmetric rotors, with symmetry axis \mathbf{e}_3 and invariant under spatial inversion, like cylinders or spheroids, we can simplify the geometry tensors (4.68) to

$$\mathbf{A}_{\text{cm}} = \frac{\tau_e}{\sigma_q^2} [D_{\perp} \mathbb{1} + (D_{\parallel} - D_{\perp}) \mathbf{e}_3 \otimes \mathbf{e}_3], \quad (4.69a)$$

$$\mathbf{A}_{\text{rot}} = \frac{2\tau_e D_{\text{rot}}}{\hbar^2} (\mathbf{e}_1 \otimes \mathbf{e}_1 + \mathbf{e}_2 \otimes \mathbf{e}_2), \quad (4.69b)$$

4.3. Classicalizing modifications applied on orientational degrees of freedom

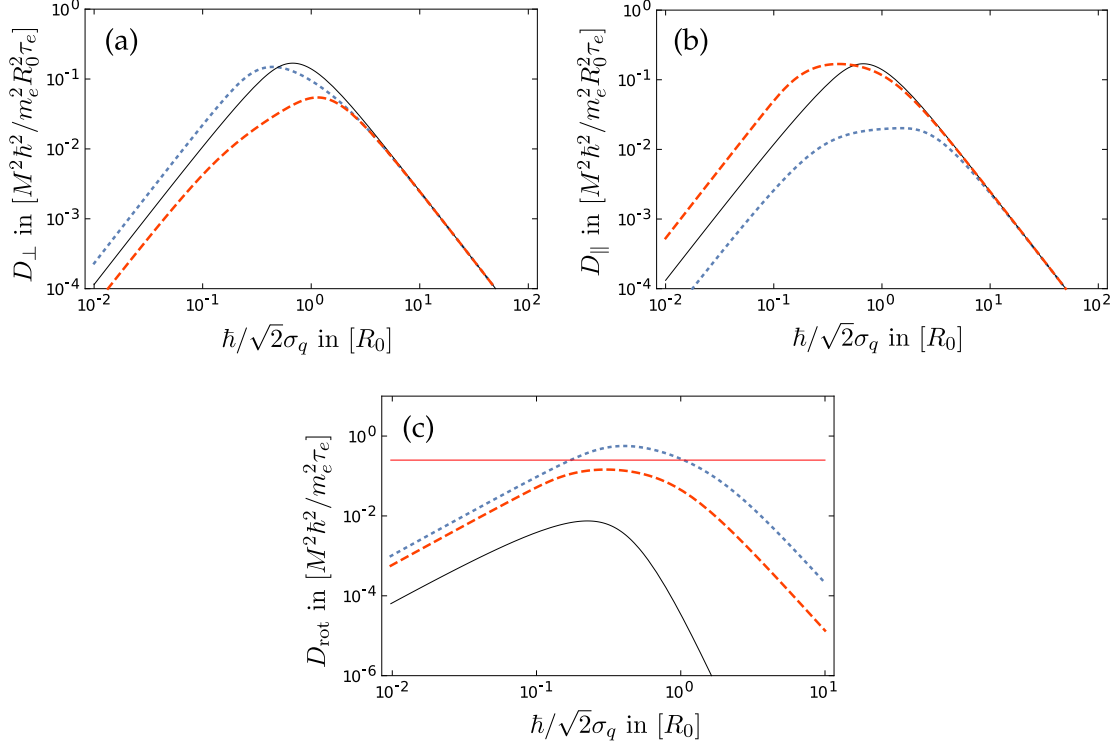


Figure 4.4.: Diffusion coefficients D_{\perp} , D_{\parallel} , and D_{rot} of a cylinder defined via Eq. (4.69) and reported in App. C.2. All curves are for bodies with the same volume $V = \sqrt{3}\pi R_0^3$ to ensure comparability and are plotted against $\hbar/\sqrt{2}\sigma_q$ in units of R_0 . The black solid curve corresponds to a cylinder with minimal anisotropy, $L/R = \sqrt{3}$, the blue dotted lines to a rod with $L/R = 8\sqrt{3}$, and the red dashed curves to a disc with $L/R = \sqrt{3}/8$. The linear diffusion coefficient in (a) and (b) show that the center-of-mass diffusion is strongest perpendicular to the main extension of the particle. This way, the smallest overlap in the indistinguishable mass density is achieved and thus the average distance is maximized. (c) As expected, the rotational diffusion is smallest for an isotropic tensor of inertia, $L/R = \sqrt{3}$. While the diffusion of an elongated rod can in principle increase without bound even for constant mass, it is bounded at the value (4.75) for flat discs as indicated by the horizontal red line.

with

$$D_{\parallel} = \frac{1}{\pi^{3/2} m_e^2 \sigma_q^3 \tau_e} \left(\frac{\hbar^2}{2} \right)^{5/2} \int d^3 \mathbf{k} e^{-\hbar^2 k^2 / 2\sigma_q^2} |\tilde{\varrho}(\mathbf{k})|^2 k_3^2, \quad (4.70a)$$

$$D_{\perp} = \frac{1}{\pi^{3/2} m_e^2 \sigma_q^3 \tau_e} \left(\frac{\hbar^2}{2} \right)^{5/2} \int d^3 \mathbf{k} e^{-\hbar^2 k^2 / 2\sigma_q^2} |\tilde{\varrho}(\mathbf{k})|^2 k_1^2, \quad (4.70b)$$

$$D_{\text{rot}} = \frac{\hbar^2}{2\pi^{3/2} m_e^2 \tau_e} \left(\frac{\hbar^2}{2\sigma_q^2} \right)^{5/2} \int d^3 \mathbf{k} e^{-\hbar^2 k^2 / 2\sigma_q^2} |k_1 \partial_{k_2} \tilde{\varrho}(\mathbf{k}) - k_2 \partial_{k_1} \tilde{\varrho}(\mathbf{k})|^2, \quad (4.70c)$$

inheriting the symmetries of the mass density $\varrho(\mathbf{r})$. The resulting localization rates

4. Orientational coherence experiments

(4.67) are

$$F_{\text{cm}}(\mathbf{R}, \Omega_0) = \frac{D_{\perp}}{\hbar^2} R^2 + \frac{D_{\parallel} - D_{\perp}}{\hbar^2} [\mathbf{R} \cdot \mathbf{m}(\Omega_0)]^2, \quad (4.71a)$$

$$F_{\text{rot}}(\Omega, \Omega') = \frac{D_{\text{rot}}}{\hbar^2} |\mathbf{m}(\Omega) \times \mathbf{m}(\Omega')|^2. \quad (4.71b)$$

Moreover, in the case of symmetric rotors invariant under spatial inversion the diffusive limit of the MMM generator can be written with help of the symmetry axis $\mathbf{e}_3 = \mathbf{m}(0)$ in relatively compact form as

$$\begin{aligned} \frac{1}{\tau_e} \mathcal{M}_{\sigma\rho} = & -\frac{D_{\perp}}{\hbar^2} \sum_{i=1}^3 [\mathbf{R}_{\text{cm},i}, [\mathbf{R}_{\text{cm},i}, \rho]] - \frac{D_{\parallel} - D_{\perp}}{\hbar^2} [\mathbf{R}_{\text{cm}} \cdot \mathbf{m}(\Omega_0), [\mathbf{R}_{\text{cm}} \cdot \mathbf{m}(\Omega_0), \rho]] \\ & - \frac{15D_{\text{rot}}}{16\pi\hbar^2} \int_{S_2} d^2\mathbf{n} [[\mathbf{n} \cdot \mathbf{m}(\Omega)]^2, [[\mathbf{n} \cdot \mathbf{m}(\Omega)]^2, \rho]], \end{aligned} \quad (4.72)$$

where the linear terms in the orientational double commutator vanish due to the symmetry of $\varrho(\mathbf{r})$. Note that Eq. (4.72) fully incorporates the periodic configuration space of orientational degrees of freedom. If one is not required to fulfill those periodicity conditions, e.g. because the particle is aligned by an external potential, a simple quadratic expansion in the Euler angles α, β describes diffusion of a tightly localized orientational distribution with terms $\sim [\alpha[\alpha, \rho]]$ and $\sim [\beta[\beta, \rho]]$.

The MMM generator (4.72) leads to linear and angular momentum diffusion as evident from

$$\frac{1}{\tau_e} \langle \mathcal{M}_{\sigma}^{\dagger} \mathbf{P}_{\text{cm}} \rangle = 0, \quad \frac{1}{\tau_e} \langle \mathcal{M}_{\sigma}^{\dagger} \mathbf{J} \rangle = 0, \quad (4.73)$$

and

$$\frac{1}{\tau_e} \langle \mathcal{M}_{\sigma}^{\dagger} \mathbf{P}_{\text{cm}}^2 \rangle = 2D_{\parallel} + 4D_{\perp}, \quad \frac{1}{\tau_e} \langle \mathcal{M}_{\sigma}^{\dagger} \mathbf{J}^2 \rangle = 4D_{\text{rot}}, \quad (4.74)$$

as follows from direct calculation using the commutation relations given in Tab. 4.1.

The D_{\parallel} , D_{\perp} , D_{rot} resemble diffusion coefficients. For a cylinder those are reported in App. C.2 and plotted in Fig. 4.4 as a function of the localization length \hbar/σ_q . Even though the diffusion in center-of-mass and orientation decouple in Eq. (4.66) the strength of the center-of-mass diffusion components still relies heavily on the orientation of the rotor: As a rule of thumb the diffusion is strongest in the direction for which spatial displacements lead to the smallest overlap of the resulting mass distribution with the original one. In general, the effect of the MMM generator (4.59) on coherences increases with the average spatial distance of the involved mass densities.

An analytical assessment of the diffusion coefficients in App. C.2 shows that elongated rods would be more suitable to test the direct heating due to rotational diffusion since the diffusion coefficient of flat disks with same volume is bounded by

$$D_{\text{rot}}^{\text{max}} = \hbar^2 M^2 / 4\tau_e m_e^2 \quad (4.75)$$

4.3. Classicalizing modifications applied on orientational degrees of freedom

as $R\sigma_q/\hbar \rightarrow \infty$. On the other hand, the diffusion of long rods with same volume increases without bound and approaches asymptotically $D_{\text{rot}} \sim \sqrt{2\pi}\sigma_q\hbar LM^2/24\tau_e m_e^2$ as $L\sigma_q/\hbar \rightarrow \infty$. The diffusion coefficients of spheroidal particles are not analytically accessible, but they show the same qualitative dependency in r_c . If in an experiment a temperature increase of an isolated system could be measured to be below a certain rate $\Gamma_{\perp} = 2D_{\perp}/M$, $\Gamma_{\parallel} = 2D_{\parallel}/M$, or $\Gamma_{\text{cm}} = 2D_{\text{rot}}/M$ one could exclude MMM parameter via the functional dependence of the diffusion coefficients.

4.3.3. Diffusion of planar rotors

The simplest rotational system is an inversion symmetric planar rotor with a single orientational degree of freedom $\alpha \in [-\pi, \pi)$. Ignoring the center-of-mass degrees of freedom in the diffusion generator (4.72) and restricting all rotations to the \mathbf{e}_1 - \mathbf{e}_2 -plane, one arrives at the full master equation

$$\partial_t \rho = -\frac{i}{\hbar} \left[\frac{\mathbf{p}_{\alpha}^2}{2I}, \rho \right] + \frac{2D_{\text{rot}}}{\hbar^2 \pi} \int_0^{2\pi} d\phi [\cos^2(\phi - \alpha) \rho \cos^2(\phi - \alpha) - \frac{1}{2} \{\cos^4(\phi - \alpha), \rho\}], \quad (4.76)$$

where the angular momentum operator has only a component perpendicular to the plane of motion, $\mathbf{J} = \mathbf{e}_3 \mathbf{p}_{\alpha}$.

Once again, it is convenient to express the time evolution with help of the Wigner function (4.42) to arrive at

$$\partial_t w_m(\alpha) = -\frac{\hbar m}{I} \partial_{\alpha} w_m(\alpha) + D_{\text{rot}} \frac{w_{m-2}(\alpha) - 2w_m(\alpha) + w_{m+2}(\alpha)}{(2\hbar)^2}. \quad (4.77)$$

Note how Eq. (4.77) gives the same discretized form of a second-order angular momentum derivative as in Eq. (4.43) resembling the diffusion that was already found for thermalization, except for the fact that next-to-nearest angular momentum states are involved because of the inversion symmetry. This symmetry is also responsible for the simple form of the free time evolution, $\partial_t w_m(\alpha) = -\hbar \partial_{\alpha} w_m(\alpha)/I$, the general time evolution for the Wigner function of a planar rotor is far more complex [139].

The time evolution (4.77) can be solved explicitly via a twofold Fourier transformation as

$$w_m(\alpha; t) = \sum_{\ell \in \mathbb{Z}} \int_{-\pi}^{\pi} d\alpha' w_{m-2\ell} \left(\alpha - \alpha' - \frac{\hbar m t}{I}; t=0 \right) T_t(\alpha', \ell), \quad (4.78)$$

with the kernel

$$T_t(\alpha', \ell) = \frac{e^{-D_{\text{rot}} t / 2\hbar^2}}{2\pi} \sum_{k \in \mathbb{Z}} e^{ik(\alpha' + \ell \hbar t / I)} I_{\ell} \left[\frac{D_{\text{rot}} t}{2\hbar^2} \text{sinc} \left(\frac{\hbar k t}{I} \right) \right], \quad (4.79)$$

involving modified Bessel functions $I_{\ell}(\cdot)$. Consistent to the previous findings (4.74) this solution shows angular momentum diffusion $\partial_t \langle \mathbf{p}_{\alpha}^2 / 2I \rangle = D_{\text{rot}} / I$ which, thanks to the free unitary time evolution, enhances the spatial dispersion as shown in Fig. 4.5.

4. Orientational coherence experiments

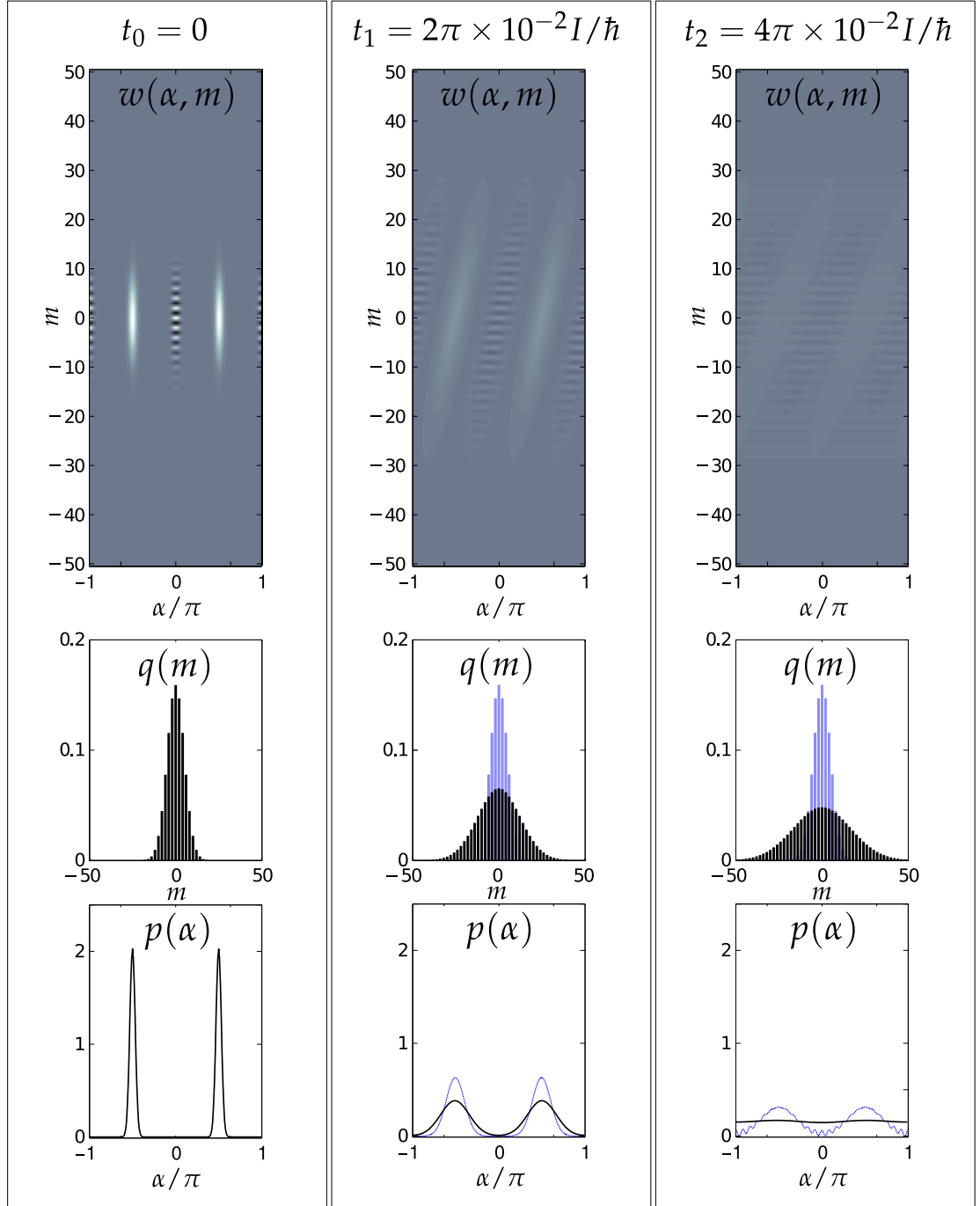


Figure 4.5.: The time evolution of the Wigner function (4.80) with initial width $\sigma_\alpha = 0.1$. The diffusion constant is chosen as $D_{\text{rot}} = 10^3 \hbar^3 / I$ and the snapshots are taken at $t_0 = 0$, $t_1 = 2\pi \times 10^{-2} I / \hbar$, and $t_2 = 4\pi \times 10^{-2} I / \hbar$. Since the MMM cannot distinguish between the two wave packets of the superposition (displaced by $\Delta\alpha = \pi$) the oscillating structure between the wave packets is only broadened but not destroyed. The marginals $p(\alpha) = \sum_m w_m(\alpha; t)$ and $q(m) = \int d\alpha w_m(\alpha; t)$ are compared with the undisturbed solution, $D_{\text{rot}} = 0$, depicted in blue.

4.3. Classicalizing modifications applied on orientational degrees of freedom

The initial state in Fig. 4.5 is $\psi_0(\alpha) \propto \exp[-\cos^2 \alpha/4\sigma_\alpha]$ that is a spatial superposition of wave packets at $\alpha = \pm\pi/2$, simply because it is an inversion symmetric body. The respective Wigner function reads

$$w_m(\alpha; 0) = \frac{(-1)^m}{2\pi I_0(1/4\sigma_\alpha^2)} I_m \left[\frac{\cos(2\alpha)}{4\sigma_\alpha^2} \right]. \quad (4.80)$$

The indirect enhancement of the orientational spread can be quantified via the variance of the unit vector in the plane $\sigma_{\mathbf{e}_\alpha}^2(t) = 1 - \langle \mathbf{e}(\alpha) \rangle_t^2$, with $\mathbf{e}(\alpha) = (\cos \alpha, \sin \alpha)$ [129]. Evaluation of this variance with help of the solution (4.78) leads to

$$\sigma_{\mathbf{e}_\alpha}^2(t) = 1 - (1 - \sigma_0^2(t)) \exp \left\{ -\frac{D_{\text{rot}} t}{2\hbar^2} \left[1 - \text{sinc} \left(\frac{2\hbar t}{I} \right) \right] \right\}, \quad (4.81)$$

with the unperturbed variance

$$\sigma_0^2(t) = 1 - \left[\left\langle \cos \left(\alpha + \frac{\mathbf{p}_\alpha t}{I} \right) \right\rangle_0^2 + \left\langle \sin \left(\alpha + \frac{\mathbf{p}_\alpha t}{I} \right) \right\rangle_0^2 \right]. \quad (4.82)$$

As such, the undisturbed variance experiences revivals of its initial value that are suppressed by the MMM on the time scale $2\hbar^2/D_{\text{rot}}$. Since this is true for any initial state it can be used to falsify MMM parameter even without a genuine orientational superposition state as will be shown in the next subsection.

4.3.4. Application: Orientational state revivals

In Ref. [65] we proposed an experiment showing a macroscopic quantum phenomenon with help of the discreteness of angular momenta. The experimental procedure involves a tight alignment of a silicon nanorod or a double-walled carbon nanotube, thin enough to be approximated as a linear rotor, in an optical trap that is abruptly turned off, see Fig. 4.6. The orientation state of the freely falling particle disperses but returns periodically to its initial state. This can easily be understood with help of the unitary time evolution operator for the orientational dynamics

$$U(t)|jm\rangle = \exp \left[-i \frac{\mathbf{J}^2}{2I\hbar} t \right] |jm\rangle = \exp \left[-i \frac{\hbar j(j+1)}{2I} t \right] |jm\rangle. \quad (4.83)$$

Since all $j(j+1)$ are even integers the time evolution operator turns into the identity operator when the smallest angular momentum $j = 1$ performed one complete rotation at $T_{\text{rev}} = 2\pi I/\hbar$ and at integer multiples $k T_{\text{rev}}$ with $k \in \mathbb{N}$. Since *all* angular momenta perform full rotations at the revival time T_{rev} , it is not necessary to be anywhere near the quantum mechanical ground state of the rotor.

The orientation of the rotor can be measured with help of the scattered light of a weak plane-wave probe pulse of nanosecond duration, as demonstrated in [57], that collapses the state to a definite orientation. The intensity of the scattered light is proportional to the expectation value $\langle \cos^2 \alpha \rangle$ if its polarization is parallel to that of the trapping laser

4. Orientational coherence experiments

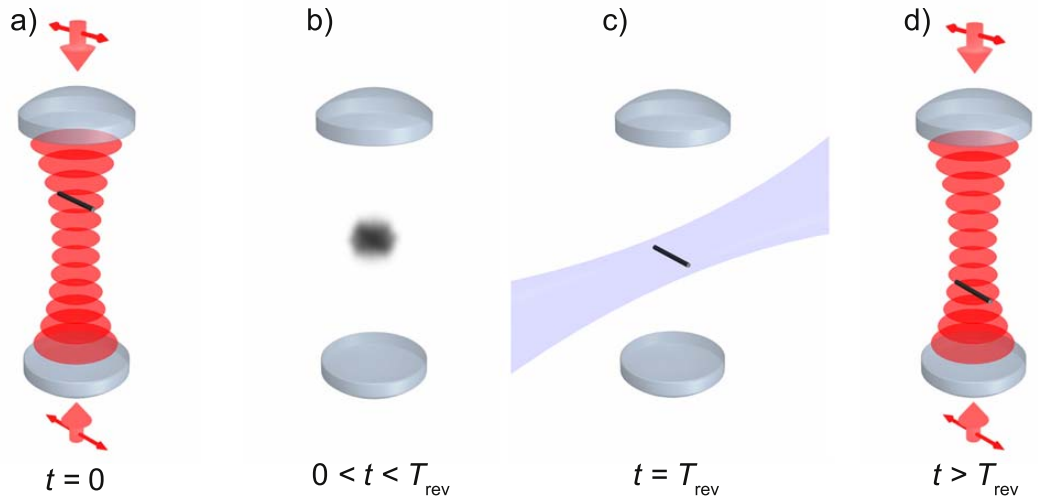


Figure 4.6.: Experimental scheme for the observation of quantum revivals: (a) The rotor is tightly aligned with the field polarization of two counter-propagating linearly polarized laser beams. (b) The trap is switched off and the orientational quantum state disperses to a quasi-uniform distribution. (c) At integer multiples of the revival time T_{Rev} the initial state is recovered which can be detected by the total light scattered from a plane-wave probe pulse. (d) The rotor is recaptured by the trapping lasers, transferred back to the initial configuration (a), and the scheme can be executed repeatedly.

that serves to localize the initial state close around the polar angle $\beta = 0$. Recapturing the rotor and transferring it to the initial position enables one to repeat this protocol. The resulting statistics of the scattered light should show a relative alignment at the revival times compared to times before and after where the orientation is evenly distributed due to the dispersion. Naturally, these revivals are suppressed by orientational decoherence, for example described by the dissipator (4.28), but also from hypothetical MMM as described in the last subsection. Thus, whenever revivals are observed, MMM parameter are falsified empirically. So far, revivals have been experimentally observed for free molecules [126, 128] and molecules dispersed in Helium droplets [127], but the sheer mass of the here proposed silicon nanorods or double-walled carbon-nanotubes would substantially contribute to the test of MMM and therefore lead to a high macroscopicity of the quantum test.

To prove this point, I will estimate the macroscopicity in the sense of the original measure by simply calculating the expectation value $\langle \cos^2 \alpha \rangle$ as a function of the MMM parameter. Since we are still talking about a proposal and no data is available from an actual experiment the hypothesis test proposed in Sec. 2.3 cannot yet be used, but the estimation with an expectation value will suffice in the limit of many measurements, as discussed in Sec. 2.4.4. Further, I will simplify from revivals of a linear rotor to revivals of a planar rotor, underestimating the effect of MMM and therefore the macroscopicity.

The Fourier transform of the mass density of a cylinder (4.62) can be approximated

4.3. Classicalizing modifications applied on orientational degrees of freedom

for $L \gg R$, the limit leading to a linear rotor, as

$$\tilde{\rho}[\mathbf{R}^T(\Omega)\mathbf{k}] \simeq M \text{sinc} \left[\frac{L}{2\hbar} \mathbf{k} \cdot \mathbf{m}(\Omega) \right], \quad (4.84)$$

where in the case of a planar rotor the axis of symmetry simply revolves as $\mathbf{m}(\alpha) = \cos(\alpha)\mathbf{e}_1 + \sin(\alpha)\mathbf{e}_2$. Inserting into the MMM generator (4.59) leads to

$$\begin{aligned} \frac{1}{\tau_e} \mathcal{M}_{\sigma\rho} &= \frac{\hbar^2 M^2}{2\pi\tau_e\sigma_q^2 m_e^2} \int_0^\infty dk k \int_0^{2\pi} d\phi e^{-\hbar^2 k^2 / 2\sigma_q^2} \\ &\times \left[\text{sinc} \left(\frac{kL}{2} \cos[\alpha - \phi] \right) \rho \text{sinc} \left(\frac{kL}{2} \cos[\alpha - \phi] \right) - \frac{1}{2} \left\{ \text{sinc}^2 \left(\frac{kL}{2} \cos[\alpha - \phi] \right), \rho \right\} \right] \end{aligned} \quad (4.85)$$

Now, instead of using the Wigner function I will turn to its Fourier transform, the characteristic function of the planar rotor,

$$\chi(\alpha, m) = \int_{-\pi}^{\pi} d\alpha' e^{im\alpha'} \langle \alpha' - \alpha/2 | \rho | \alpha' + \alpha/2 \rangle. \quad (4.86)$$

The master equation with the generator (4.85) then translates to

$$\partial_t \chi(\alpha, m) = -\frac{m\hbar}{I} \partial_\alpha \chi(\alpha, m) - g(\alpha) \chi(\alpha, m), \quad (4.87)$$

with

$$\begin{aligned} g(\alpha) &= \frac{\hbar^2 M^2}{4\pi\tau_e\sigma_q^2 m_e^2} \int_0^\infty dk k \int_0^{2\pi} d\phi e^{-\hbar^2 k^2 / 2\sigma_q^2} \\ &\times \left\{ \text{sinc} \left[\frac{Lk}{2} \cos \left(\frac{\alpha}{2} + \phi \right) \right] - \text{sinc} \left[\frac{Lk}{2} \cos \left(\frac{\alpha}{2} - \phi \right) \right] \right\}^2. \end{aligned} \quad (4.88)$$

It can be easily integrated,

$$\chi(\alpha, m; t) = \exp \left[-\int_0^t dt' g \left(\alpha - \frac{m\hbar}{I} t' \right) \right] \chi_I(\alpha, m; t). \quad (4.89)$$

At the revival time T_{rev} this leads to

$$\chi(\alpha, m; T_{\text{rev}}) = \left\{ \exp \left[-\frac{nI}{\hbar} \int_0^{2\pi} d\alpha' g(\alpha + \alpha') \right] (1 - \delta_{m,0}) + \exp \left[-\frac{2\pi nI}{\hbar} g(\alpha) \right] \delta_{m,0} \right\} \chi(\alpha, m; 0), \quad (4.90)$$

where $\chi_I(\alpha, m; t) = \chi(\alpha - m\hbar t/I, m; 0)$ is the solution regarding only the unitary part of the time evolution.

The characteristic symbol of the measurement observable $\cos^2 \alpha$ is

$$\eta(\alpha, m) = \frac{\delta(\alpha)}{4} (\delta_{m,-2} + 2\delta_{m,0} + \delta_{m,2}). \quad (4.91)$$

4. Orientational coherence experiments

Assuming tight alignment at $t = 0$, $\langle \cos^2 \alpha \rangle_0 = 1$, the calculation of the overlap at the n th revival leads to

$$\begin{aligned} \langle \cos^2 \alpha \rangle_n &= \int_0^\alpha d\alpha \sum_m \chi \left(\alpha, m; \frac{2\pi n I}{\hbar} \right) \eta(\alpha, m) \\ &= \frac{1}{2} + \frac{1}{2} \exp \left[-n\theta \left(\frac{L\sigma_q}{\hbar} \right) \frac{t_{\text{rev}}}{\tau} \left(\frac{M}{m_e} \right)^2 \right], \end{aligned} \quad (4.92)$$

with

$$\begin{aligned} \theta(x) &= \int_0^\infty du \frac{u e^{-u^2/2}}{8\pi^2} \int_0^{2\pi} d\phi \int_0^{2\pi} d\alpha \\ &\times \left\{ \text{sinc} \left[\frac{ux}{2} \cos \left(\alpha - \frac{\phi}{2} \right) \right] - \text{sinc} \left[\frac{ux}{2} \cos \left(\alpha + \frac{\phi}{2} \right) \right] \right\}^2. \end{aligned} \quad (4.93)$$

As such, all information from the MMM parameter σ_q is encoded in θ and maximalization with respect to σ_q leads to $\theta_m \simeq 0.12$ as long as L is long enough so that $\hbar/\sigma_q \sim L$ does not lead to incompatible heating effects. For example we are on the safe side with $L = 50 \text{ nm}$ and $M = 10^6 \text{ amu}$ and assuming a visibility of $f = 2\langle \cos^2 \alpha \rangle_{10} - 1 = 0.8$ at the tenth revival leads to a macroscopicity of $\mu \geq 17.5$ according to Eq. (2.16). This is still over two orders of magnitude larger on the logarithmic scale than the current record derived for molecule interferometry in Sec. 2.4.3, and is on par with highly ambitious center-of-mass interference proposals [140] that are without the benefits that orientational revival experiments possess, like the recyclability of the nanorotor and the invariance of the revivals regarding its absolute position.

4.4. Discussion

The expressions derived in this chapter allow one to describe the classicalization process of a quantum rigid rotor caused by MMM, both in center-of-mass and in orientational degrees of freedom. Additionally, for those orientational degrees of freedom the generic decoherence, diffusion, and friction mechanics due to interaction with an environment was derived.

The description of orientational collapse with the generator (4.59), as the natural generalization of the orientation-fixed MMM generator studied in Ref. [138], allows for even more insight in the mechanism of spontaneous collapse because of the complex interplay of relative center-of-mass positions and orientations of the different states in a superposition. Since the relevant quantity for the strength of the collapse is the average spatial distance of the superposed mass densities the main impact comes from the center-of-mass position. But there may be a way to use the additional minor orientational dependence to assess subtleties in the action of the collapse models.

A likely starting point is the different scaling behavior of the center-of-mass and orientational diffusion allowing one in principle to extract the values of MMM parameters

from the diffusion constants. However, one has to be careful since exclusion of parameters is only valid in one direction: One can never preclude that the observed decoherence or diffusion has an ordinary source, meaning it is caused by standard quantum mechanics, hence the conclusion to have found the ‘true’ parameters of collapse models is highly dubious [42].

The thermalization process of orientational degrees of freedom due to Eq. (4.28) is fully described by the respective diffusion and friction tensors; they can be determined either by a dedicated measurement or by a microscopic calculation (the classical expressions are for example reported in [137]). The thermalization process itself leads to equilibrium states very close to the expected Gibbs states that would be an exact solution in a flat configuration space. Deviations of the exact equilibrium state from the Gibbs state already disappear very near to the quantum ground state, see for example Fig. 4.2, most likely precluding any experimental verification. On the other hand, the thermalization of orientational degrees of freedom is exceptional in the sense that due to the periodic configuration space a steady state can occur even without any potential. The master equation (4.28) is the first quantum mechanical description of orientational thermalization and promises to be an important tool in the description of levitated nano-sized objects, be it only to estimate the effect of small deviations from perfectly spherical shapes if only center-of-mass degrees of freedom are considered.

Both generators (4.59) and (4.28) from MMM and from environmental interactions, respectively, can be straightforwardly implemented in any setup involving quantum rotational systems. In both cases even analytical solutions were obtained, be it only for the resulting steady state. But already for the linear rotor the resources needed for numerical calculations of the dynamics are immense since the dimension of the Hilbert space to be considered increases more than quadratically in the occupied total angular momentum J . This means that for truly mesoscopic systems with ten thousands of occupied J new numerical techniques have to be developed to effectively calculate the input of the generators. That is, as long as one wants to study quantum effects like quantum revivals [65], otherwise the classical descriptions would obviously suffice.

The proper implementation of the periodicity of orientational degrees of freedom allows one to correctly describe the MMM-induced collapse and quantum mechanical thermalization for all imaginable initial states distributed over all orientations. This is not the case for the linearized diffusion and friction terms that are commonly utilized by simply using the Cartesian Caldeira-Leggett dissipator (4.21) and substituting the positions by angles and the momenta by sort of a Cartesian conjugate of the angles, or the analogous procedure for Eq. (4.72), see for example Refs. [141, 142]. It is immediately clear that this fails as soon as the state is no longer tightly aligned in one specific orientation which is inevitably the case when the derived generators are applied. Thus, the usage of the generators (4.59) and (4.28) for the description of the decoherence of orientational revival experiments [65] is paramount. Compared to their center-of-mass counterparts these kind of experiments promise to operate on a whole new level practicability-wise, due to their robustness, recyclability, and the modest cooling requirements.

5. Conclusion and outlook

The bulk of this thesis was concerned with the extension of the macroscopicity measure of Nimmrichter and Hornberger [51] by means of a general Bayesian hypothesis test applicable to any conceivable mechanical superposition experiment. It turns out that this Bayesian inference approach brings along a lot of benefits, such as the coverage of different measurement protocols (quantum random walks (QRWs) of different lengths or molecule interferometry with varying laser intensity) and the automatic incorporation of statistical errors, while simultaneously being uninformative and objective with help of Jeffreys' prior. The hypothesis test is directly applicable to vastly different quantum tests, as demonstrated with interfering Bose-Einstein condensates (BECs), atomic QRW, and entangled nanobeams, while the study of molecule interferometry, being an example of an ideal interference experiment, shows the close connection to the old definition of macroscopicity from Ref. [51]. In the case of Ramsey interference with BEC and the QRW, the master equations resulting from the minimally invasive, macrorealist modifications of quantum mechanics (MMM) are qualitatively identical to conventional decoherence channels, rendering the found analytical solutions relevant beyond the scope of collapse models and macroscopicity.

The measure defined in Sec. 2.3.3 is independent from derived quantum criteria like visibilities, Leggett-Garg or Bell correlators, and entanglement witnesses. Together with the option to combine all kinds of events to a single likelihood of the classicalization time parameter τ_e this opens up new possibilities for unheard of quantum tests, in particular for tests of collapse models. Since the MMM are basically a type of continuous spontaneous localization (CSL) model for all experiments studied in this thesis the theoretical descriptions can be directly transferred to exclude these most widely used collapse models. Moreover, the hypothesis test can combine different CSL tests via Bayesian updating to draw a combined picture similar to the exclusion curves shown in Fig. 2.1. The formulation of a hypothesis test together with Bayesian updating as alternative to exclusion curves may even be extended to other fields of physics, e.g. the falsification of chameleon fields [143].

Studying the dynamics of orientational degrees of freedom on mesoscopic scales is a new direction to explore the range of quantum physics. The results derived in this thesis regarding the diffusion, friction, and thermalization of rigid quantum rotors and the formulation of MMM in orientational degrees of freedom pave the way for the correct interpretation of experiments to come. The correct incorporation of the periodic and curved configuration space is an immense improvement for the description of these kinds of experiments and allows one for the first time to handle scenarios involving the whole range of the orientational phenomena like state revivals that are possible due to the discrete nature of angular momentum eigenstates. The latter promise to be a serious

5. *Conclusion and outlook*

alternative to the established center-of-mass tests. The discussions in Sec. 4 were focused on the description of rigid nanorotors motivated by the large quantity of recent experiments [57–62] that will benefit from those findings in the future. But all results are also directly transferable to experiments probing the orbital angular momentum of massive particles for example enforced by circular traps.

That said, the work on orientational degrees of freedom is not yet complete. To obtain the dynamics of rigid rotors one currently relies on numerical computations if an external potential or diffusion is present in addition to the free motion. When entering the mesoscopic regime those numerical approaches consume immense resources because of the huge Hilbert space and the necessity to preserve the discreteness of the angular momenta. Appropriate semiclassical approximations for analytical or at least numerical methods are thus highly desired.

A. Experimental data from LUMI

Set 1 (P=0.2 W)				Set 2 (P=0.2 W)				Set 3 (P=0.4 W)				Set 4 (P=0.4 W)				Set 5 (P=0.4 W)				Set 6 (P=0.6 W)									
x	S	N	d	N	0	x	S	N	d	N	0	x	S	N	d	N	0	x	S	N	d	N	0	x	S	N	d	N	0
-1	143	137	0	244	169	1	172	173	2	218	182	-1	148	113	-1	93	113												
24	154	191	23	244	229	24	223	226	24	143	125	25	179	177	24	94	106												
50	178	147	50	178	256	51	189	173	50	190	174	49	111	147	50	108	143												
77	227	198	75	203	194	75	264	230	76	254	177	76	156	203	76	109	124												
101	188	213	101	191	200	102	224	205	102	130	153	102	109	178	102	123	105												
127	253	263	127	193	159	128	220	175	129	255	285	128	139	137	127	121	119												
154	206	222	154	210	182	154	186	225	154	209	180	154	119	155	153	82	71												
180	201	207	180	183	213	179	196	261	180	256	251	180	133	134	180	136	96												
207	127	187	207	165	186	206	119	216	207	186	219	207	178	167	205	149	172												
232	155	167	232	149	195	233	155	139	232	160	162	233	126	125	232	109	115												
258	141	153	258	191	143	258	192	181	258	139	154	258	192	196	258	95	136												
284	232	243	283	175	167	283	194	205	284	114	95	284	107	126	283	97	126												
310	220	215	310	226	191	310	263	227	309	195	173	310	166	98	309	141	108												
337	272	242	336	195	233	335	183	159	336	213	253	336	90	123	335	138	117												
362	207	213	361	209	190	362	208	231	362	189	221	362	146	150	362	129	188												
388	178	166	388	215	196	389	172	117	388	202	225	388	105	165	387	169	162												
414	135	140	414	216	206	413	148	145	413	130	149	415	137	105	414	168	142												
440	195	203	440	194	215	440	142	137	440	161	144	441	170	166	440	114	144												
466	226	170	465	222	214	465	143	193	466	99	97	467	153	172	466	83	140												
491	227	177	491	257	226	491	185	217	491	224	166	491	132	162	492	72	137												
517	242	363	518	262	201	518	248	232	518	200	209	517	141	137	518	118	149												
544	277	226	543	201	188	544	195	172	543	255	245	543	145	116	544	147	165												
570	162	234	570	204	263	570	192	134	569	235	196	570	149	157	569	143	165												
596	144	208	596	158	168	596	171	141	595	151	179	595	121	117	596	113	104												
622	206	249	621	211	171	622	201	146	622	148	125	622	150	247	622	146	60												
648	208	206	647	225	201	648	133	158	647	100	152	648	129	154	648	122	136												
674	214	166	674	200	192	673	195	221	673	112	152	675	173	125	675	186	151												
700	293	276	700	174	200	700	215	224	700	188	203	700	143	121	699	147	169												
725	179	151	725	247	258	726	169	251	726	198	188	727	162	131	726	159	164												
751	195	154	752	199	196	752	161	145	751	225	255	752	177	108	752	110	144												
778	133	156	778	178	216	777	183	151	777	145	162	778	142	129	777	114	144												
804	152	154	803	194	219	804	176	164	804	177	159	805	181	174	804	103	135												
830	153	174	830	214	232	830	192	212	830	169	167	830	172	153	830	129	173												
855	180	176	856	242	208	856	271	325	856	165	181	856	135	168	857	144	105												
882	235	234	882	237	235	882	221	250	882	195	246	882	130	145	882	170	128												
907	183	171	908	244	241	908	172	196	908	168	176	908	161	92	909	209	229												
934	194	146	933	245	234	934	232	233	934	200	204	934	136	147	934	115	102												
959	134	184	960	153	200	960	185	182	960	167	162	960	129	123	960	100	106												
986	171	160	986	201	204	986	132	148	986	155	151	986	187	135	986	94	150												
1012	211	234	1012	253	253	1012	205	146	1012	142	169	1012	187	183	1011	128	95												
1038	174	208	1038	202	244	1038	215	199	1037	262	176	1038	151	166	1037	116	89												
1063	229	227	1064	230	187	1064	246	202	1064	218	160	1064	106	122	1064	135	149												

Figure A.1.: Shown are the counts for different laser powers as function of the grating position x_S in [nm] used for Bayesian inference in Sec. 2.4.3.

A. Experimental data from LUMI

Set 7 (P=0.6 W)			Set 8 (P=0.8 W)			Set 9 (P=0.8 W)			Set 10 (P=0.8 W)			Set 11 (P=1.0 W)			Set 12 (P=1.0 W)				
x	S	N d	N O	x	S	N d	N O	x	S	N d	N O	x	S	N d	N O	x	S	N d	N O
-1	121	164	0	207	225	1	143	136	0	189	104	-1	188	145	-2	64	145		
24	146	116	24	236	179	23	189	223	24	117	115	24	209	139	24	167	139		
49	135	119	49	211	207	50	171	224	50	147	120	50	185	212	49	210	212		
76	167	116	76	100	135	76	119	131	76	108	152	76	136	154	76	178	154		
101	144	120	101	96	173	102	105	149	101	131	153	103	115	177	101	189	177		
127	165	127	127	144	163	128	190	235	127	94	130	128	115	137	127	216	137		
154	143	112	154	229	140	154	122	195	154	189	103	154	108	169	154	184	169		
180	160	210	179	188	215	179	218	222	179	111	133	180	184	186	180	131	186		
207	97	193	207	204	146	206	189	195	206	194	142	206	271	178	206	126	178		
233	122	178	232	184	118	232	160	158	233	200	160	231	222	183	232	100	183		
258	97	100	258	139	121	257	145	147	258	146	138	258	306	272	258	157	272		
284	90	126	284	172	136	283	201	166	284	173	177	285	279	232	284	179	232		
309	134	145	310	109	193	309	207	236	310	126	165	310	293	199	310	179	199		
335	170	150	336	186	215	336	168	268	337	81	133	336	164	192	336	152	192		
361	236	215	362	162	246	361	198	273	362	96	131	362	139	290	362	172	290		
387	135	163	388	99	197	388	140	125	388	57	105	388	175	215	387	224	215		
414	122	139	414	136	175	414	153	114	414	124	116	414	181	208	413	130	208		
440	132	164	441	154	152	441	181	183	441	116	121	440	190	195	441	99	195		
466	103	103	466	177	183	465	210	171	466	180	181	466	317	199	467	142	199		
492	96	138	491	195	210	492	329	248	492	136	139	492	222	221	492	187	221		
518	117	148	518	265	258	517	278	252	518	165	110	518	258	179	518	112	179		
544	146	158	544	229	209	544	223	196	543	172	140	543	205	202	544	179	202		
571	131	167	569	155	135	569	180	208	570	102	157	570	205	193	570	250	193		
596	139	163	596	140	179	596	119	191	597	91	106	595	140	229	596	236	229		
622	142	143	622	115	121	622	145	168	622	97	162	622	167	233	622	158	233		
648	153	126	648	119	147	648	91	187	648	174	146	647	157	187	647	128	187		
674	99	121	674	154	209	674	178	257	673	140	135	673	162	197	674	144	197		
700	130	168	700	227	219	700	282	271	699	132	94	700	195	203	700	89	203		
727	126	178	725	226	195	725	247	193	726	127	123	726	187	212	727	136	212		
752	154	149	752	211	151	752	214	154	752	153	160	752	139	135	752	155	135		
778	127	105	778	117	141	778	127	132	778	163	101	778	290	216	777	195	216		
803	170	107	803	130	109	804	130	148	804	146	134	804	178	190	804	200	190		
830	160	128	829	116	146	830	137	154	830	100	150	830	161	170	830	185	170		
856	213	139	855	140	191	857	131	193	856	133	175	857	148	160	856	209	160		
883	249	186	882	116	210	882	155	207	882	61	153	882	135	193	882	130	193		
908	132	201	908	138	157	908	168	229	908	97	105	908	77	109	908	135	109		
934	175	193	934	125	142	934	125	132	934	114	225	934	102	155	934	131	155		
961	108	148	959	178	150	960	126	138	960	143	145	960	204	209	960	117	209		
986	130	171	986	159	148	985	216	154	985	167	91	987	229	158	986	189	158		
1012	94	142	1012	128	127	1011	176	175	1013	201	185	1012	180	139	1011	217	139		
1038	116	188	1038	202	165	1037	289	216	1038	143	148	1038	168	164	1038	269	164		
1063	144	131	1064	214	276	1064	218	245	1064	141	148	1063	171	139	1064	172	139		

Figure A.2.: Shown are the counts for different laser powers as function of the grating position x_S in [nm] used for Bayesian inference in Sec. 2.4.3.

Set 13 (P=1.0 W)			Set 14 (P=1.2 W)			Set 15 (P=1.2 W)			Set 16 (P=1.2 W)			Set 17 (P=1.2 W)			Set 18 (P=1.4 W)				
x	S	N d	N O	x	S	N d	N O	x	S	N d	N O	x	S	N d	N O	x	S	N d	N O
-1	117	116	0	201	212	-1	137	112	1	194	119	1	155	152	0	189	138		
25	166	144	25	183	193	23	212	251	24	100	90	24	155	137	23	258	200		
50	144	157	50	163	220	49	184	225	51	47	53	50	94	158	49	158	179		
76	101	125	76	197	189	76	237	193	76	78	88	76	109	114	76	182	178		
102	94	127	102	184	274	102	240	191	102	59	95	101	122	165	101	123	175		
129	65	112	128	195	209	129	249	183	129	146	120	128	157	200	128	146	202		
154	124	165	154	220	256	154	222	230	153	174	240	154	135	148	154	159	150		
180	152	132	180	215	215	181	221	234	181	163	216	179	100	138	180	173	197		
206	184	154	205	212	179	206	210	191	206	181	121	206	133	129	206	205	168		
232	188	141	232	222	201	232	159	175	232	142	112	232	147	137	232	154	158		
257	147	142	258	156	222	258	155	192	257	196	151	257	125	156	258	215	209		
284	149	143	284	135	192	284	183	274	283	198	161	284	179	109	284	182	267		
309	118	109	310	160	198	309	207	137	309	160	205	309	166	161	310	263	197		
336	120	146	335	157	179	337	229	194	335	205	198	337	111	194	335	235	183		
363	92	126	362	127	215	361	259	269	362	153	224	362	109	100	362	217	204		
388	107	149	387	200	214	388	239	227	387	133	131	389	90	108	387	183	257		
415	141	147	413	240	201	414	211	224	414	102	113	414	107	120	414	165	209		
440	144	134	440	239	213	440	212	231	439	136	184	439	185	145	440	198	289		
465	119	122	467	212	200	466	186	259	465	191	229	466	142	148	467	228	161		
491	190	109	492	223	204	492	198	299	492	301	221	493	233	228	491	264	247		
519	281	151	518	204	218	518	179	228	517	336	312	517	199	174	517	210	206		
544	192	131	544	135	242	544	181	187	544	253	198	543	173	133	544	249	224		
570	94	126	570	108	169	570	210	224	570	74	152	569	111	107	570	251	217		
595	95	117	596	147	183	596	236	211	596	113	111	597	96	143	596	171	212		
621	119	113	621	225	217	623	249	202	621	114	208	621	127	160	622	182	227		
648	108	124	648	293	208	648	273	249	648	122	181	648	153	150	648	201	205		
675	136	176	673	298	249	673	229	273	674	138	196	674	136	193	674	175	231		
699	239	216	700	238	206	700	177	209	699	213	269	699	142	143	699	188	212		
725	125	125	726	180	165	726	243	251	726	244	231	725	102	145	727	221	294		
753	151	139	751	142	186	751	187	213	751	164	155	752	139	101	752	226	225		
778	201	101	777	168	226	778	143	183	778	186	116	778	160	125	778	226	195		
804	180	100	804	148	265	803	190	205	804	186	163	802	126	176	804	261	217		
829	83	117	829	186	216	830	192	184	829	146	172	829	98	118	830	309	186		
857	105	117	856	225	215	855	268	220	855	176	208	856	150	194	855	194	173		
882	139	117	882	222	199	881	261	228	882	159	225	881	109	197	883	215	200		
908	88	172	908	295	252	908	211	203	908	138	201	908	88	83	907	193	217		
934	91	132	933	247	193	934	203	210	934	124	156	934	107	85	934	189	267		
960	137	91	960	193	225	959	142	146	959	137	172	959	117	140	959	212	246		
985	127	101	987	238	212	985	138	149	985	131	119	986	134	132	984	226	173		
1012	201	119	1013	184	261	1012	167	189	1012	256	208	1012	263	180	1013	200	197		
1038	164	116	1038	228	262	1039	167	212	1038	221	204	1039	216	167	1038	267	219		
1064	168	165	1064	163	218	1064	184	194	1065	216	254	1064	150	164	1064	256	243		

Figure A.3.: Shown are the counts for different laser powers as function of the grating position x_S in [nm] used for Bayesian inference in Sec. 2.4.3. The most leftwards columns at $P = 1$ W are depicted in Fig. 2.5 (c).

A. Experimental data from LUMI

Set 19 (P=1.4 W)			Set 20 (P=1.6 W)			Set 21 (P=1.6 W)			Set 22 (P=1.8 W)			Set 23 (P=1.8 W)		
x	S	N	x	S	N	x	S	N	x	S	N	x	S	N
0	241	221	0	174	140	1	198	151	0	116	184	0	150	216
25	293	226	24	195	185	25	221	173	24	204	183	24	172	116
50	227	201	50	153	174	49	243	206	50	155	144	50	105	121
76	193	208	76	200	192	76	139	166	77	134	169	76	135	148
102	180	211	102	160	186	102	172	202	102	123	157	102	172	139
128	204	200	127	166	237	128	227	182	128	131	134	128	150	151
154	178	269	154	185	193	154	179	173	154	140	130	154	140	156
179	207	206	179	186	184	179	144	231	180	195	208	179	151	165
207	324	284	206	149	184	206	158	171	206	153	162	205	118	105
232	227	268	233	148	110	232	128	140	232	191	181	233	120	152
258	247	198	258	154	106	258	175	146	257	167	151	258	110	151
283	248	305	284	145	146	283	142	139	284	164	113	285	113	102
310	260	265	309	209	190	309	176	116	311	105	85	310	161	173
337	227	255	337	195	183	337	211	200	335	146	159	336	157	150
363	152	226	361	185	160	363	177	227	362	153	152	362	131	180
387	176	232	388	201	224	387	169	149	388	141	113	387	158	160
415	193	223	414	180	155	414	175	172	414	117	152	414	169	160
440	194	213	440	158	125	440	116	163	440	131	123	440	138	171
467	249	218	466	147	153	466	184	164	465	153	145	466	114	123
492	238	218	492	188	170	491	186	180	492	152	147	491	142	153
517	274	229	517	246	226	517	240	233	518	133	161	517	168	154
544	271	244	543	198	204	544	248	212	545	136	200	544	116	174
570	220	231	570	213	191	570	180	153	570	126	231	570	143	170
595	239	207	596	164	145	596	155	160	596	135	193	595	158	163
622	217	209	621	189	186	621	108	152	623	135	132	622	123	198
648	245	246	648	111	195	648	140	180	647	196	129	648	109	141
674	158	189	674	194	195	673	151	168	674	157	208	674	176	241
700	139	194	700	168	194	700	160	232	701	168	154	701	155	134
726	273	309	726	219	232	727	235	232	727	123	131	725	135	153
751	278	219	752	211	194	752	164	210	752	182	178	752	133	118
777	254	215	777	200	148	778	136	146	778	175	154	777	152	127
804	237	259	804	149	165	805	159	180	805	95	143	803	159	152
830	248	216	830	140	117	830	188	197	830	185	205	829	127	142
856	180	208	855	171	174	855	145	203	855	165	171	856	116	147
882	179	211	881	192	245	882	168	195	882	126	178	882	136	151
909	183	241	908	163	191	908	202	192	907	171	161	908	143	145
934	169	199	933	199	178	934	210	170	935	145	209	934	125	153
959	212	242	959	116	148	960	132	185	960	198	179	960	122	135
985	201	188	985	166	169	987	143	148	987	125	142	986	142	118
1011	268	181	1012	163	173	1012	92	96	1011	140	162	1013	143	148
1037	238	209	1037	155	172	1037	173	189	1038	163	148	1039	155	187
1064	195	195	1063	174	179	1064	212	163	1064	191	182	1064	145	166

Figure A.4.: Shown are the counts for different laser powers as function of the grating position x_S in [nm] used for Bayesian inference in Sec. 2.4.3.

B. Quantum experiments in presence of classicalizing modifications

B.1. BEC Interference

Here, I will sketch the straightforward manner in which the several correlation functions and count-statistics required in Sec. 3.1 are calculated in second quantization. Every correlation function $\langle C_K \rangle$ of K th order is an already normally ordered combination of K creation operators $c_{j,\text{out}}^\dagger = \int dx \psi_{j,\text{out}}(x) \psi^\dagger(x)$ (and corresponding annihilation operators). For the balanced beamsplitter the spatial mode functions are $\psi_{a,\text{out}}(x) = [\psi_a(x) - \exp(i\alpha)\psi_b(x)]/\sqrt{2}$ and $\psi_{b,\text{out}}(x) = [\exp(-i\alpha)\psi_a(x) + \psi_b(x)]/\sqrt{2}$. The operator in the correlation functions then can be expressed as

$$C_K =: \prod_{k=1}^K c_{j_k,\text{out}}^\dagger c_{j_{k+K},\text{out}} = \int dx_1 \dots dx_{2K} F_K(x_1, \dots, x_{2K}), \quad (\text{B.1})$$

with

$$F_K(x_1, \dots, x_{2K}) =: \prod_{k=1}^K \psi_{j_k,\text{out}}(x_k) \psi_{j_{k+K},\text{out}}^\dagger(x_k) \psi^\dagger(x_k) \psi(x_{k+K}). \quad (\text{B.2})$$

Using the canonical commutator relations one can explicitly calculate the time evolution of any $F_K(x_1, \dots, x_{2K})$ under MMM with the generator (3.21) without dispersion as

$$\begin{aligned} \langle F_K(x_1, \dots, x_{2K}) \rangle_T &= \langle F_K(x_1, \dots, x_{2K}) \rangle_0 \\ &\times \exp \left\{ \frac{T}{2\tau} \sum_{\mu,\nu=1}^K \left[2e^{-(x_\mu - x_{\nu+K})^2 \sigma_q^2 / 2\hbar^2} - e^{-(x_\mu - x_\nu)^2 \sigma_q^2 / 2\hbar^2} - e^{-(x_{\mu+K} - x_{\nu+K})^2 \sigma_q^2 / 2\hbar^2} \right] \right\}. \end{aligned} \quad (\text{B.3})$$

In the limit $\hbar/\sigma_q \gg w_x$ one can expand the exponential functions in curly brackets with respect to σ_q . Plugging all back into the definition (B.1) the expectation value can be rewritten in a compact form with help of $2K \times 2K$ matrices M_K as

$$\frac{\langle C_K \rangle_T}{\langle C_K \rangle_0} = \int \frac{dx_1 \dots dx_{2K}}{(2\pi w_x^2)^K} \exp \left[-\frac{1}{2} \mathbf{x} \cdot M_K \mathbf{x} \right] = \frac{1}{w_x^{2K} |M_K|^{1/2}}, \quad (\text{B.4})$$

with $|M_K|$ being the determinant of M_K . The last step is possible since M_K is per construction real and symmetric and thus diagonalizable via unitary matrices.

B. Quantum experiments in presence of classicalizing modifications

For example, in the case of the DFS this Gaussian matrix takes on the form

$$M_K = \frac{\sigma_q^2 T}{\hbar^2 \tau_e} \begin{pmatrix} 1 + \frac{\hbar^2 \tau_e}{w_x^2 \sigma_q^2 T} & 1 & \dots & -1 & -1 \\ 1 & 1 + \frac{\hbar^2 \tau_e}{w_x^2 \sigma_q^2 T} & \dots & -1 & -1 \\ \vdots & \vdots & \ddots & \vdots & \vdots \\ -1 & -1 & \dots & 1 + \frac{\hbar^2 \tau_e}{w_x^2 \sigma_q^2 T} & 1 \\ -1 & -1 & \dots & 1 & 1 + \frac{\hbar^2 \tau_e}{w_x^2 \sigma_q^2 T} \end{pmatrix}. \quad (\text{B.5})$$

Integration yields the depletion term

$$\frac{\langle C_K \rangle_{T, \text{DFS}}}{\langle C_K \rangle_{0, \text{DFS}}} = \left(1 + 2K \frac{w_x^2 \sigma_q^2 T}{\hbar^2 \tau_e} \right)^{-1/2} \simeq H \left(\sigma_q, \frac{\tau_e}{K} \right), \quad (\text{B.6})$$

where I expressed the result in terms of the function H from Eq. (3.13) to account for the opposite regime of strong depletion, $\sigma_q w_x \gg \hbar$. The K -th order decay rate saturates at K/τ_e , only leading to small deviations for $\sigma_q w_x \simeq \hbar$ that are irrelevant on the logarithmic scale. In the same way correlation functions for the PS can be computed, where terms can involve $k < K$ mixed pairs $\psi_a \psi_b^*$ or $\psi_b \psi_a^*$. The calculation of the expectation values (B.4) then leads to dephasing with the factor $D(\sigma_q, \tau_e/k^2)$, while terms without mixed pairs are only affected by the depletion $H(\sigma_q, \tau_e/K)$. The count statistics (3.30) are N th order correlation functions with an additional vacuum state squeezed in which does not alter the calculation.

B.2. Mechanical entanglement of photonic crystals

B.2.1. Characteristic functions and symbols of mechanical oscillator states

The characteristic function of the initial oscillator state (3.93) for $\phi = 0$ can be calculated straightforwardly as

$$\begin{aligned} \chi^{\pm 1}(\mathbf{Q}, \mathbf{P}) &= \frac{1}{2} \exp \left[-\frac{1}{4\hbar \varrho V_m} (\mathbf{P} \cdot \Omega^{-1} \mathbf{P} + \varrho^2 V_m^2 \mathbf{Q} \cdot \Omega \mathbf{Q}) \right] \\ &\times \left(1 - \frac{1}{4\hbar \varrho V_m} \left[\sum_{\lambda=1,2} (\pm 1)^\lambda (\Omega^{-1/2} \mathbf{P})_\lambda \right]^2 - \frac{\varrho V_m}{4\hbar} \left[\sum_{\lambda=1,2} (\pm 1)^\lambda (\Omega^{1/2} \mathbf{Q})_\lambda \right]^2 \right), \end{aligned} \quad (\text{B.7})$$

with $\Omega = \text{diag}(\Omega_1, \Omega_2)$. In a similarly straightforward manner, one obtains the characteristic symbols of the effect (3.122) as

$$\begin{aligned} \eta^{\pm 2}(\mathbf{Q}, \mathbf{P}) &= \frac{1}{2} \delta(\mathbf{Q}) \delta(\mathbf{P}) - \frac{1}{8\pi^2 \hbar^2} \exp \left[-\frac{1}{4\hbar \varrho V_m} (\mathbf{P} \cdot \Omega^{-1} \mathbf{P} + \varrho^2 V_m^2 \mathbf{Q} \cdot \Omega \mathbf{Q}) \right] \\ &\times \left[1 \pm_2 \cos \theta \left(\frac{P_1 P_2}{\hbar \varrho V_m \sqrt{\Omega_1 \Omega_2}} + Q_1 Q_2 \frac{\varrho V_m \sqrt{\Omega_1 \Omega_2}}{\hbar} \right) \right. \\ &\left. \pm_2 \sin \theta \left(P_1 Q_2 \sqrt{\frac{\Omega_2}{\hbar^2 \Omega_1}} - P_2 Q_1 \sqrt{\frac{\Omega_1}{\hbar^2 \Omega_2}} \right) \right]. \end{aligned} \quad (\text{B.8})$$

B.2.2. The geometric factor $U_{<}(\sigma)$

There are two regions where the geometric factor $U_{<}(\sigma)$ from Eq. (3.119) can be calculated analytically: If the momentum kicks of the MMM can not resolve the crystal structure, $\hbar/\sigma_q \gg 5\text{\AA}$, one is able to approximate $\varrho(\mathbf{r})$ with a continuous mass density for which the geometric factor (3.119) can be calculated for the longitudinal mode (3.124) as

$$\begin{aligned} U_{<}(\sigma) \simeq U(\sigma) &= \frac{2\varrho^2 \hbar^7}{m_e^2 \sigma_q^7 L_z^3} \left(1 - e^{-L_x^2 \sigma_q^2 / 2\hbar^2} + \frac{\sqrt{\pi} L_x \sigma_q}{\sqrt{2}\hbar} \text{erf} \left[\frac{L_x \sigma_q}{\sqrt{2}\hbar} \right] \right)^2 \\ &\times \left[\sqrt{2\pi} \left(h \left[\frac{L_z \sigma_q}{\hbar}, 0 \right] + e^{-L_z^2 \sigma_q^2 / 2\hbar^2} \text{Re} \left\{ h \left[\frac{L_z \sigma_q}{\hbar}, \frac{L_z \sigma_q}{\hbar} \right] \right\} \right) \right. \\ &\left. - \left(1 + e^{-L_z^2 \sigma_q^2 / 2\hbar^2} \right) \frac{L_z \sigma_q}{\hbar} \left(\pi^2 - 2 \frac{L_z^2 \sigma_q^2}{\hbar^2} \right) \right], \end{aligned} \quad (\text{B.9})$$

since the cutoff q_c plays no role for such low σ_q . It includes the factor

$$h[a, b] = \sqrt{\frac{\pi}{2}} (i3a^2 + \pi b^2 - i\pi^2) \exp \left[\frac{(\pi/a - ib)^2}{2} \right] \text{erf} \left[\frac{i\pi/a + b}{\sqrt{2}} \right], \quad (\text{B.10})$$

which is real for $b = 0$.

If \hbar/σ_q is much smaller than the lattice constant all contributions in the geometric factor (3.119) involving more than a single atom at once are suppressed by the Gaussian $g_\sigma(s, q)$ in Eq. (2.8). Then each atom is affected by the MMM individually and the geometric factor reads

$$U_{<}(\sigma) = N \frac{m_{Si}^2}{4\hbar^2 m_e^2} \text{erf} \left(\frac{q_c}{\sqrt{2}\sigma_q} \right)^2 \left[\sigma_q^2 \text{erf} \left(\frac{q_c}{\sqrt{2}\sigma_q} \right)^2 - \sqrt{\frac{2}{\pi}} \sigma_q q_c e^{-q_c^2 / 2\sigma_q^2} \right], \quad (\text{B.11})$$

which involves an averaged mode function (3.124) over the whole crystal, $\sum_n \mathbf{w}^2(\mathbf{r}_n) \approx N/2$. The diffusion increases quadratically with σ_q until the momentum displacements are strong enough to remove the particles from the crystal instead of decohering its state and in the limit that $\sigma_q \ll q_c$ one obtains $U_{<}(\sigma) \simeq N m_{Si}^2 \sigma_q^2 / 4\hbar^2 m_e^2$, as long as $\hbar/\sigma_q \ll 5\text{\AA}$.

C. Orientational coherence experiments

C.1. Orientational decoherence, diffusion and thermalization

C.1.1. Orientational Fokker-Planck equation of rigidly connected classical particles

Starting from the Fokker-Planck equation of the single particle (4.22) one can write the dissipator for the collective phase space distribution $w(\mathbf{r}_1, \dots, \mathbf{r}_N, \mathbf{p}_1, \dots, \mathbf{p}_N)$ as

$$\partial_t^{\mathcal{L}} w = \sum_{n=1}^N \gamma_n [\nabla_{\mathbf{p}_n} \cdot (\mathbf{p}_n w) + k_B T m_n \nabla_{\mathbf{p}_n}^2 w]. \quad (\text{C.1})$$

Analogously to the rigid body approximation (4.25) for the operators \mathbf{I} now reduce the degrees of freedom of the classical positions and momenta via

$$\mathbf{r}_n = \mathbf{R}(\Omega) \mathbf{r}_n^{(0)}, \quad \text{and} \quad \mathbf{p}_n = m_n \mathbf{I}^{-1}(\Omega) \mathbf{J} \times \mathbf{r}_n, \quad (\text{C.2})$$

which is consistent with $\mathbf{J} = \sum_n \mathbf{r}_n \times \mathbf{P}_n$. Inserting the positions and momenta (C.2) into Eq. (C.1) and exploiting

$$\nabla_{\mathbf{p}_n} = (\nabla_{\mathbf{p}_n} \otimes \mathbf{J}) \nabla_{\mathbf{J}} = -\mathbf{r}_n \times \nabla_{\mathbf{J}} \quad (\text{C.3})$$

leads to the orientational Fokker-Planck equation (4.36). From this we can identify the diffusion tensor

$$\mathbf{D}(\Omega) = k_B T \sum_{n=1}^N m_n \gamma_n (r_n^2 \mathbb{1} - \mathbf{r}_n \otimes \mathbf{r}_n). \quad (\text{C.4})$$

Like the quantum mechanical counterpart for isotropic friction and diffusion it leads to the inequality $D_i + D_j \geq D_k$, for (i, j, k) permutations of $(1, 2, 3)$, since

$$\sum_{n=1}^N m_n \gamma_n \mathbf{r}_n \otimes \mathbf{r}_n = \frac{1}{2} \text{tr}[\mathbf{D}(\Omega)] \mathbb{1} - \mathbf{D}(\Omega) > 0. \quad (\text{C.5})$$

In contrast to the quantum mechanical case, it is clear how to implement directed diffusion in the classical Eq. (C.1): replacing $\nabla_{\mathbf{p}_n} \rightarrow \mathbf{n}_n \cdot \nabla_{\mathbf{p}_n}$ and $\mathbf{p}_n \rightarrow \mathbf{n}_n \cdot \mathbf{p}_n$ in Eq. (C.1) allows one to specify for every constituent n a specific direction in which friction and diffusion take place. The resulting Fokker-Planck equation is the same as Eq. (4.36) but the diffusion tensor now reads

$$\mathbf{D}(\Omega) = k_B T \sum_{n=1}^N \gamma_n m_n (\mathbf{n}_n \times \mathbf{r}_n) \otimes (\mathbf{n}_n \times \mathbf{r}_n). \quad (\text{C.6})$$

C. Orientational coherence experiments

The friction tensor is given by $\Gamma(\Omega) = \mathbf{D}(\Omega)\mathbf{I}^{-1}(\Omega)/k_{\text{B}}T$. In this case the eigenvalues can assume arbitrary values.

C.1.2. General predictions and the classical limit of the orientational Caldeira-Leggett dissipator

The Heisenberg equations of motion for the expectation values (4.31)-(4.34) can be calculated most easily via index notation and exploitation of the rules given in Tab. 4.1. For example, applying the dissipator (4.28) to the angular momentum components \mathbf{J}_μ results in

$$\begin{aligned}
\mathcal{D}^\dagger \mathbf{J}_\mu &= - \sum_{k=1}^3 \frac{2\tilde{D}_k}{\hbar^2} \left[\frac{i\beta\hbar}{4} \left(\epsilon_{\nu\lambda\alpha} \mathbf{J}_\beta \mathbf{I}_{\lambda\beta}^{-1} d_{k,\alpha} [\mathbf{J}_\mu, d_{k,\nu}] - [\mathbf{J}_\mu, d_{k,\nu}] \epsilon_{\nu\alpha\lambda} d_{k,\alpha} \mathbf{I}_{\lambda\beta}^{-1} \mathbf{J}_\beta \right) \right. \\
&\quad \left. + [d_{k,\nu}, [d_{k,\nu}, \mathbf{J}_\mu]] + \mathcal{O}(\hbar^2) \right] \\
&= - \sum_{k=1}^3 \frac{2\tilde{D}_k}{\hbar^2} \left[-\frac{\beta\hbar^2}{4} \left(\mathbf{J}_\beta \mathbf{I}_{\lambda\beta}^{-1} d_{k,\lambda} d_{k,\mu} + d_{k,\lambda} d_{k,\mu} \mathbf{I}_{\lambda\beta}^{-1} \mathbf{J}_\beta - \mathbf{I}_{\mu,\beta}^{-1} \mathbf{J}_\beta - \mathbf{J}_\beta \mathbf{I}_{\mu,\beta}^{-1} \right) \right. \\
&\quad \left. + i\hbar \underbrace{[d_{k,\nu}, \epsilon_{\nu\mu\lambda} d_{k,\lambda}]}_{=0} + \mathcal{O}(\hbar^2) \right] \\
&= \underbrace{\sum_{k=1}^3 \beta \tilde{D}_k \left(d_{k,\lambda} d_{k,\mu} \mathbf{I}_{\lambda\beta}^{-1} - \mathbf{I}_{\mu,\beta}^{-1} \right)}_{=-\Gamma_{\mu\beta}} \mathbf{J}_\beta + \mathcal{O}(\hbar), \tag{C.7}
\end{aligned}$$

where $d_{a,b} \equiv d_{a,b}(\Omega)$ and $\mathbf{I}_{a,b}^{-1} \equiv \mathbf{I}_{a,b}^{-1}(\Omega)$. The calculation of $\mathcal{D}^\dagger \mathbf{J} \otimes \mathbf{J}$ follows along the same lines.

The consistency of the classical limit of the dissipator (4.28) with the Fokker-Planck equation (4.36) is verified with help of the the Wigner function of the orientation state [136]

$$w(\Omega, \mathbf{m}) = \int_{-\pi}^{\pi} d\alpha' \int_{-\pi/2}^{\pi/2} d\beta' \int_{-\pi}^{\pi} d\gamma' \frac{\sqrt{\sin \beta'_+ \sin \beta'_-}}{4\pi^3} e^{i(m_\alpha \alpha' + 2m_\beta \beta' + m_\gamma \gamma')} \langle \Omega'_- | \rho | \Omega'_+ \rangle, \tag{C.8}$$

where

$$\Omega'_\pm = (\alpha'_\pm, \beta'_\pm, \gamma'_\pm) = ((\alpha \pm \alpha'/2) \bmod 2\pi, (\beta \pm \beta'/2) \bmod \pi, (\gamma \pm \gamma'/2) \bmod 2\pi), \tag{C.9}$$

and $\mathbf{m} = (m_\alpha, m_\beta, m_\gamma)$ are the discrete eigenvalues of the canonical momentum operators according to Eq. (4.12).

The derivation of the classical limit of the (angular momentum) diffusive part in the dissipator (4.28), i.e. $\mathbf{A}_k = \mathbf{d}_k(\Omega)$, was already demonstrated in Ref. [132]. Since the part inducing orientational diffusion, i.e. $\mathbf{A}_k = i\hbar \mathbf{I}_0^{-1} \mathbf{R}^T(\Omega) \mathbf{J} \times \mathbf{r}_n^{(0)} / 4k_{\text{B}}T$, vanishes completely

C.1. Orientational decoherence, diffusion and thermalization

because of the proportionality $\sim \hbar^2$ it suffices to calculate the mixed terms \mathcal{D}^f that are responsible for the friction,

$$\mathcal{D}^f \rho = -\frac{i}{2k_B T \hbar} \sum_k \tilde{D}_k \left[(\mathbf{d}_k(\Omega) \times \boldsymbol{\sigma}) \cdot \mathbf{d}_k(\Omega) + \mathbf{d}_k(\Omega) \cdot (\boldsymbol{\sigma}^\dagger \times \mathbf{d}_k(\Omega)) \right], \quad (\text{C.10})$$

with the abbreviation $\boldsymbol{\sigma} = \mathbf{I}^{-1}(\Omega) \mathbf{J} \rho$. We can circumvent the exact calculation including this term by introducing a placeholder $\boldsymbol{\Sigma}(\Omega, \mathbf{p}')$ for the respective characteristic symbol, thus

$$\langle \Omega'_- | \boldsymbol{\sigma} | \Omega'_+ \rangle = \sum_{\mathbf{m}'} e^{-i(m'_\alpha \alpha' + 2m'_\beta \beta' + m'_\gamma \gamma')} \boldsymbol{\Sigma}(\Omega, \mathbf{p}'). \quad (\text{C.11})$$

Inserting Eq. (C.10) into Eq. (C.8) then leads to

$$\begin{aligned} & \partial_t^{\mathcal{D}} w(\Omega, \mathbf{m}) \\ &= \sum_{\mathbf{m}'} \int_{-\pi}^{\pi} d\alpha' \int_{-\pi/2}^{\pi/2} d\beta' \int_{-\pi}^{\pi} d\gamma' \frac{\sqrt{\sin \beta'_+ \sin \beta'_-}}{8i\pi^3 k_B T \hbar} e^{i[(m_\alpha - m'_\alpha)\alpha' + 2(m_\beta - m'_\beta)\beta' + (m_\gamma - m'_\gamma)\gamma']} \\ & \quad \times \sum_k \tilde{D}_k \left\{ [\mathbf{d}_k(\Omega'_-) \times \boldsymbol{\Sigma}(\Omega, \mathbf{p}')] \cdot \mathbf{d}_k(\Omega'_+) + \mathbf{d}_k(\Omega'_-) \cdot [\boldsymbol{\Sigma}^*(\Omega, \mathbf{p}') \times \mathbf{d}_k(\Omega'_+)] \right\}. \quad (\text{C.12}) \end{aligned}$$

The expansion in powers of \hbar is now performed by substituting $m_\alpha \alpha' = p_\alpha \tilde{\alpha}$ which transfers the \hbar -dependence completely to the second line in Eq. C.12. Since we must compensate \hbar^{-1} an expansion of \mathbf{d}_k in first order of \hbar suffices,

$$\mathbf{d}_k \left(\Omega \pm \frac{\hbar \tilde{\Omega}}{2} \right) \simeq \mathbf{d}_k(\Omega) \pm \frac{\hbar \tilde{\alpha}}{2} \mathbf{e}_3 \times \mathbf{d}_k(\Omega) \pm \frac{\hbar \tilde{\beta}}{2} \mathbf{n}_\xi(\Omega) \times \mathbf{d}_k(\Omega) \pm \frac{\hbar \tilde{\gamma}}{2} \mathbf{n}_3(\Omega) \times \mathbf{d}_k(\Omega), \quad (\text{C.13})$$

where $\mathbf{e}_3, \mathbf{n}_\xi, \mathbf{n}_3$ are the rotation axes introduced in Sec. 4.1.1. Inserting into Eq. C.12 leaves only contributions with dependence on $\tilde{\Omega}$ that can be expressed by derivatives in \mathbf{J} (compare with Eq. (4.6)). Dropping again the Ω -dependence of the vectors, one

C. Orientational coherence experiments

arrives at

$$\begin{aligned}
\partial_t^{\mathcal{D}} w(\Omega, \mathbf{m}) &\simeq - \sum_k \tilde{D}_k \sum_{\mathbf{p}'} \int_{-\pi}^{\pi} d\tilde{\alpha} \int_{-\pi/2}^{\pi/2} d\tilde{\beta} \int_{-\pi}^{\pi} d\tilde{\gamma} \frac{\sqrt{\sin \tilde{\beta}_+ \sin \tilde{\beta}_-}}{8\pi^3 k_B T} \\
&\times \left\{ \partial_{\mathbf{J} \cdot \mathbf{e}_3} [(\mathbf{d}_k \times \text{Re}\{\boldsymbol{\Sigma}(\Omega, \mathbf{p}')\}) \cdot (\mathbf{e}_3 \times \mathbf{d}_k) - [(\mathbf{e}_3 \times \mathbf{d}_k) \times \text{Re}\{\boldsymbol{\Sigma}(\Omega, \mathbf{p}')\}] \cdot \mathbf{d}_k] \right. \\
&+ \partial_{\mathbf{J} \cdot \mathbf{n}_\xi} [(\mathbf{d}_k \times \text{Re}\{\boldsymbol{\Sigma}(\Omega, \mathbf{p}')\}) \cdot (\mathbf{n}_\xi \times \mathbf{d}_k) - [(\mathbf{n}_\xi \times \mathbf{d}_k) \times \text{Re}\{\boldsymbol{\Sigma}(\Omega, \mathbf{p}')\}] \cdot \mathbf{d}_k] \\
&+ \left. \partial_{\mathbf{J} \cdot \mathbf{n}_3} [(\mathbf{d}_k \times \text{Re}\{\boldsymbol{\Sigma}(\Omega, \mathbf{p}')\}) \cdot (\mathbf{n}_3 \times \mathbf{d}_k) - [(\mathbf{n}_3 \times \mathbf{d}_k) \times \text{Re}\{\boldsymbol{\Sigma}(\Omega, \mathbf{p}')\}] \cdot \mathbf{d}_k] \right\} \\
&\times e^{i[(p_\alpha - p'_\alpha)\tilde{\alpha} + 2(p_\beta - p'_\beta)\tilde{\beta} + (p_\gamma - p'_\gamma)\tilde{\gamma}]} \\
&= - \underbrace{\sum_{\mathbf{p}'} \int_{-\pi}^{\pi} d\tilde{\alpha} \int_{-\pi/2}^{\pi/2} d\tilde{\beta} \int_{-\pi}^{\pi} d\tilde{\gamma} \frac{\sqrt{\sin \tilde{\beta}_+ \sin \tilde{\beta}_-}}{4\pi^3} e^{i[(p_\alpha - p'_\alpha)\tilde{\alpha} + 2(p_\beta - p'_\beta)\tilde{\beta} + (p_\gamma - p'_\gamma)\tilde{\gamma}]} }_{=1} \\
&\times \frac{1}{k_B T} \sum_k \tilde{D}_k \partial_{\mathbf{J}} \cdot (\mathbf{d}_k \otimes \mathbf{d}_k - \mathbb{1}) \text{Re}\{\boldsymbol{\Sigma}(\Omega, \mathbf{p}')\} \\
&= \frac{1}{k_B T} \partial_{\mathbf{J}} \cdot [\mathbb{D}(\Omega) \text{Re}\{\boldsymbol{\Sigma}(\Omega, \mathbf{p}')\}] \simeq \frac{1}{k_B T} \partial_{\mathbf{J}} \cdot [\mathbb{D}(\Omega) \mathbb{I}^{-1}(\Omega) \mathbf{J} w(\Omega, \mathbf{m})]. \tag{C.14}
\end{aligned}$$

As advertised, the mixed term leads to the term in Eq. (4.36) responsible for friction.

Finally, I will verify that the Gibbs state $\rho_G = \exp[-\mathbb{H}/2k_B T]/Z$ approximates the steady state for high temperatures implying that $\mathcal{D}\rho_G = \mathcal{O}(1/T)$. Defining the transformation

$$F(\mathbf{A}_k) = e^{-\mathbb{H}/k_B T} \mathbf{A}_k e^{-\mathbb{H}/k_B T} = \sum_{n=0}^{\infty} \frac{(-k_B T)^{-n}}{n!} [\mathbb{H}, \mathbf{A}_k]_n, \tag{C.15}$$

with the n -fold commutator $[A, B]_n = [A, [A, \dots, [A, B] \dots]]$, one finds

$$\begin{aligned}
\mathcal{D}\rho_G/Z &= \sum_k \frac{2\tilde{D}_k}{\hbar^2} \left(\mathbf{A}_k \cdot \frac{e^{-\mathbb{H}/2k_B T}}{Z} \mathbf{A}_k^\dagger - \frac{1}{2} \mathbf{A}_k^\dagger \cdot \mathbf{A}_k \frac{e^{-\mathbb{H}/2k_B T}}{Z} - \frac{1}{2} \frac{e^{-\mathbb{H}/2k_B T}}{Z} \mathbf{A}_k^\dagger \cdot \mathbf{A}_k \right) \\
&= \sum_k \frac{2\tilde{D}_k}{\hbar^2} \left[\mathbf{A}_k \cdot F(\mathbf{A}_k^\dagger) - \frac{1}{2} \mathbf{A}_k^\dagger \cdot \mathbf{A}_k - \frac{1}{2} F(\mathbf{A}_k^\dagger \cdot \mathbf{A}_k) \right] \frac{e^{-\mathbb{H}/2k_B T}}{Z}. \tag{C.16}
\end{aligned}$$

The term in the square brackets is of order $1/T^2$ since the zeroth and first order cancel. Together with the T -dependence of the \tilde{D}_k any corrections of the Gibbs state are proportional to $1/T$ and thus get diminished with increasing temperature.

C.1.3. Planar rotor

Here, I show how to calculate the steady state (4.41). Plugging the Lindblad operator (4.39) into Eq. (4.28) leads to

$$\begin{aligned} \mathcal{D}\rho = \sum_k \frac{2D}{\hbar^2} \left[\mathbf{a}_k \rho \mathbf{a}_k - \rho + \frac{\hbar}{4ik_B T I} (\mathbf{a}_k \rho \mathbf{b}_k^\dagger - \mathbf{b}_k \rho \mathbf{a}_k) \right. \\ \left. + \frac{\hbar^2}{16k^2 B T^2 I^2} \left(\mathbf{b}_k \rho \mathbf{b}_k^\dagger - \frac{1}{2} \{ \mathbf{b}_k^\dagger \mathbf{b}_k, \rho \} \right) \right], \end{aligned} \quad (\text{C.17})$$

with

$$\mathbf{a} = \mathbf{e}_r(\alpha) = \begin{pmatrix} \cos \alpha \\ \sin \alpha \end{pmatrix} \quad \text{and} \quad \mathbf{b} = \mathbf{e}_\phi(\alpha) \mathbf{p}_\alpha = \begin{pmatrix} -\sin \alpha \\ \cos \alpha \end{pmatrix} \mathbf{p}_\alpha. \quad (\text{C.18})$$

Since the free time evolution demands the steady state to be of the form (4.40) it suffices to calculate the coupling of the populations $\langle m | \mathcal{D}\rho | m \rangle$. Using $\langle \alpha | m \rangle = e^{-im\alpha} / \sqrt{2\pi}$, and consequently

$$\begin{aligned} \langle m_1 | \mathbf{a} | m_2 \rangle &= \frac{1}{2} \begin{pmatrix} \delta_{m_1-1, m_2} + \delta_{m_1+1, m_2} \\ i\delta_{m_1-1, m_2} - i\delta_{m_1+1, m_2} \end{pmatrix} \\ \langle m_1 | \mathbf{b} | m_2 \rangle &= \frac{\hbar m_2}{2} \begin{pmatrix} -i\delta_{m_1-1, m_2} + i\delta_{m_1+1, m_2} \\ \delta_{m_1-1, m_2} + \delta_{m_1+1, m_2} \end{pmatrix} \\ \langle m_1 | \mathbf{b}^\dagger \mathbf{b} | m_2 \rangle &= \hbar^2 m_1 m_2 \left[\delta_{m_1, m_2} + \frac{1}{2i} (\delta_{m_1-2, m_2} + \delta_{m_1+2, m_2}) \right], \end{aligned} \quad (\text{C.19})$$

one ends up with

$$\begin{aligned} \langle m | \mathcal{D}\rho^{\tilde{m}} | m \rangle &= \sum_{\tilde{m} \in \mathbb{Z}} \rho_{\text{eq}}^{\tilde{m}} \frac{2D}{\hbar^2} \left[\frac{1}{2} (\delta_{\tilde{m}, m+1} + \delta_{\tilde{m}, m-1}) - \delta_{\tilde{m}, m} + \frac{\hbar^2 \tilde{m}}{4k_B T I} (\delta_{\tilde{m}, m+1} - \delta_{\tilde{m}, m-1}) \right. \\ &\quad \left. + \frac{\hbar^4 \tilde{m}^2}{32k_B^2 T^2 I^2} (\delta_{\tilde{m}, m+1} + \delta_{\tilde{m}, m-1} - 2\delta_{\tilde{m}, m}) \right]. \end{aligned} \quad (\text{C.20})$$

As $\langle m | \mathcal{D}\rho_{\text{eq}} | m \rangle$ must vanish for every m , we can deduce

$$\begin{aligned} \rho_{\text{eq}}^{(\pm 1)} &= \frac{2\rho_{\text{eq}}^{(0)}}{1 + 1/\xi + 1/4\xi^2} \\ \rho_{\text{eq}}^{(\pm 2)} &= \frac{(2 + 1/2\xi^2)\rho_{\text{eq}}^{(1)} - \rho_{\text{eq}}^{(0)}}{1 + 2/\xi + 1/\xi^2} \\ \rho_{\text{eq}}^{(\pm 3)} &= \frac{(2 + 2/\xi^2)\rho_{\text{eq}}^{(2)} - (1 - 1/\xi + 1/4\xi^2)\rho_{\text{eq}}^{(1)}}{1 + 3/\xi + 9/4\xi^2} \\ &\vdots \end{aligned} \quad (\text{C.21})$$

C. Orientational coherence experiments

and so on. This is solved by

$$\rho_{\text{eq}}^{\tilde{m}} = \prod_{k=1}^{|\tilde{m}|} \frac{(2\xi - k + 1)^2}{(2\xi + k)^2} \rho_{\text{eq}}^0 = \left(\frac{2\xi}{|\tilde{m}|} \right)^2 \left(\frac{2\xi + |\tilde{m}|}{|\tilde{m}|} \right)^{-2} \rho_{\text{eq}}^0, \quad (\text{C.22})$$

where $\rho_{\text{eq}}^0 = 1/Z$ provides the normalization. In the limit of high temperatures, i.e. $\xi \rightarrow \infty$, one can use

$$\binom{n}{k} \stackrel{n \gg k, 1}{\simeq} \frac{n^k}{k!} \stackrel{k \gg 1}{\simeq} \frac{e^k}{\sqrt{2\pi k}} \left(\frac{n}{k} \right)^k \quad (\text{C.23})$$

to obtain

$$\left(\frac{2\xi}{|\tilde{m}|} \right)^2 \left(\frac{2\xi + |\tilde{m}|}{|\tilde{m}|} \right)^{-2} \simeq \left(1 + \frac{|\tilde{m}|}{2\xi} \right)^{-2|\tilde{m}|} = \underbrace{\left[\left(1 + \frac{|\tilde{m}|}{2\xi} \right)^\xi \right]^{-2|\tilde{m}|/\xi}}_{\simeq e^{|\tilde{m}|/2}} \simeq e^{-|\tilde{m}|^2/\xi}, \quad (\text{C.24})$$

being the Gibbs distribution except for normalization.

C.1.4. Linear rotor

In close analogy to the previous subsection, I show how to calculate the steady state (4.49) of the linear rotor. The Lindblad dissipator takes on the form (C.17) but with the operators

$$\mathbf{a} = \begin{pmatrix} \cos \alpha \sin \beta \\ \sin \alpha \sin \beta \\ \cos \beta \end{pmatrix} = \begin{pmatrix} \sqrt{\frac{2\pi}{3}} [Y_{1,-1}(\alpha, \beta) - Y_{1,1}(\alpha, \beta)] \\ i\sqrt{\frac{2\pi}{3}} [Y_{1,-1}(\alpha, \beta) + Y_{1,1}(\alpha, \beta)] \\ \sqrt{\frac{4\pi}{3}} Y_{1,0}(\alpha, \beta) \end{pmatrix} \quad \text{and} \quad \mathbf{b} = -\mathbf{a} \times \mathbf{L}. \quad (\text{C.25})$$

Here, the $Y_{l,m}(\alpha, \beta)$ are spherical harmonics and with help of the Wigner 3-j-symbol one can determine the transition coefficients as

$$\langle \ell_1, m_2 | Y_{\ell', m'}(\alpha, \beta) | \ell_2, m_2 \rangle = \sqrt{\frac{(2\ell_1 + 1)(2\ell_2 + 1)(2\ell' + 1)}{4\pi}} \times \begin{pmatrix} \ell_1 & \ell_2 & \ell' \\ 0 & 0 & 0 \end{pmatrix} \begin{pmatrix} \ell_1 & \ell_2 & \ell' \\ -m_1 & m_2 & m' \end{pmatrix}. \quad (\text{C.26})$$

The selection rules of the Wigner 3-j symbols require, among other things, that $|\ell_1 - \ell_2| \leq \ell'$. Since $\ell' = 1$ in any case, fortunately only nearest neighbors are coupled in the total angular momentum. This can be expanded one step further when application of the angular momentum operator \mathbf{J} is required¹ which leads to

$$\begin{aligned} \mathbf{J}_1 | \ell, m \rangle &= \frac{\hbar}{2} (c_+ | \ell, m + 1 \rangle + c_- | \ell, m - 1 \rangle) \\ \mathbf{J}_2 | \ell, m \rangle &= \frac{\hbar}{2i} (c_+ | \ell, m + 1 \rangle - c_- | \ell, m - 1 \rangle) \\ \mathbf{J}_3 | \ell, m \rangle &= \hbar m | \ell, m \rangle, \end{aligned} \quad (\text{C.27})$$

¹Explicit calculation shows that those next-neighbor terms eventually cancel.

with $c_{\pm} = \sqrt{\ell(\ell+1) - m(m \pm 1)}$.

With Eqs. (C.26) and (C.27) it is in principle possible to formulate similar general transition rates like in the case of the planar rotor (C.20). The execution is straightforward but results in a huge expression that will not be reported here. Instead I will show the explicit couplings for the first three total angular momenta,

$$\begin{aligned}\rho_{\text{eq}}^{0m} &= \rho_{\text{eq}}^{1m} \left(1 + \frac{2}{\xi} + \frac{1}{\xi^2} \right) \\ \rho_{\text{eq}}^{1m} &= \frac{\rho_{\text{eq}}^{0m} + \rho_{\text{eq}}^{2m} (2 + 6/\xi + 9/2\xi^2)}{3 + 3/2\xi^2} \\ \rho_{\text{eq}}^{2m} &= \frac{\rho_{\text{eq}}^{1m} (2 - 2/\xi + 1/2\xi^2) + \rho_{\text{eq}}^{3m} (3 + 12/\xi + 12/\xi^2)}{5 + 15/2\xi^2} \\ &\vdots\end{aligned}\tag{C.28}$$

so that the reader can convince himself that

$$\rho_{\text{eq}}^{\ell m} = \prod_{k=1}^{\ell} \frac{(2\xi - k + 1)^2}{(2\xi + k + 1)^2} \rho_{\text{eq}}^{0m} = \binom{2\xi}{\ell}^2 \binom{2\xi + \ell + 1}{\ell}^{-2} \rho_{\text{eq}}^{0m}\tag{C.29}$$

indeed solves the coupling (C.28). With Eq. (C.23) one can reconfirm the limit for $\xi \rightarrow \infty$ as

$$\binom{2\xi}{\ell}^2 \binom{2\xi + \ell + 1}{\ell}^{-2} \simeq \left(1 + \frac{\ell + 1}{2\xi} \right)^{-2\ell} = \underbrace{\left[\left(1 + \frac{\ell + 1}{2\xi} \right)^{\xi} \right]^{-2\ell/\xi}}_{\simeq e^{-(\ell+1)/2}} \simeq e^{-\ell(\ell+1)/\xi}.\tag{C.30}$$

C.2. Diffusion coefficients for cylinders

The diffusion coefficients of a cylinder of length L and radius R , defined via Eq. (4.69), are

$$D_{\parallel} = \frac{\lambda \hbar^2}{2r_c^2} \frac{M^2}{m_0^2 R_c^2 L_c^2} h_1(L_c) \left\{ 1 - e^{-R_c^2} [I_0(R_c^2) + I_1(R_c^2)] \right\},\tag{C.31a}$$

$$D_{\perp} = \frac{\lambda \hbar^2}{2r_c^2} \frac{M^2}{m_0^2 R_c^2 L_c^2} h_2(L_c) e^{-R_c^2} I_1(R_c^2),\tag{C.31b}$$

$$\begin{aligned}D_{\text{rot}} &= \frac{\lambda \hbar^2}{2} \frac{M^2}{m_0^2 R_c^2 L_c^2} \left(\frac{R_c^2}{2} h_1(L_c) \left\{ 1 - 2e^{-R_c^2} \left[I_0(R_c^2) + \left(1 - \frac{5}{3R_c^2} \right) I_1(R_c^2) \right] \right\} \right. \\ &\quad \left. + \frac{L_c^2}{3} e^{-R_c^2} I_1(R_c^2) [h_2(L_c) - 2] + \left\{ 1 - e^{-R_c^2} [I_0(R_c^2) + 2I_1(R_c^2)] \right\} [h_1(L_c) - h_2(L_c)] \right),\end{aligned}\tag{C.31c}$$

C. *Orientalional coherence experiments*

where $I_0(\cdot), I_1(\cdot)$ denote modified Bessel functions. I abbreviated $R_c = R/\sqrt{2}r_c$, $L_c = L/2r_c$,

$$h_1(L_c) = 1 - e^{-L_c^2}, \quad \text{and} \quad h_2(L_c) = \sqrt{\pi}L_c \text{erf}(L_c) - h_1(L_c), \quad (\text{C.32})$$

with $\text{erf}(\cdot)$ the error function. Note, that the spatial diffusion coefficient along the cylinder's symmetry axis (C.31a) was already derived in Ref. [138].

Danksagung

Zuerst muss ich mich bei der gesamten Arbeitsgruppe in Duisburg für die angenehme Atmosphäre während und ausserhalb der Arbeitszeiten bedanken. Besondere Erwähnung verdienen dabei natürlich Benjamin, Stefan und Klaus wegen ihres Vertrauens in meine Fähigkeiten, ihrer ausdauernden Geduld und ihrer fachlichen Unterstützung. Damit haben sie entscheidend zum Gelingen dieses Projektes beigetragen.

Für die großartige Unterstützung fernab des Arbeitsplatzes danke ich meiner Familie und meinen Freunden. Den größten Rückhalt gab mir dabei Birthe, der ich nicht genug dafür danken kann.

Bibliography

- [1] M. Planck, *Zur Theorie des Gesetzes der Energieverteilung in Normalspectrum*, Verh. Deutsch. Phys. Gesell. **2**, 237–245 (1900).
- [2] W. Heisenberg, *Über den anschaulichen Inhalt der quantentheoretischen Kinematik und Mechanik*, Z. Phys. **43**, 172–198 (1927).
- [3] H. P. Robertson, *The uncertainty principle*, Phys. Rev. **34**, 163 (1929).
- [4] H. D. Zeh, *On the interpretation of measurement in quantum theory*, Found. Phys. **1**, 69–76 (1970).
- [5] M. Schlosshauer, *Decoherence, the measurement problem, and interpretations of quantum mechanics*, Rev. Mod. Phys. **76**, 1267 (2005).
- [6] K. Hornberger, *Introduction to decoherence theory*, in *Entanglement and Decoherence*, pages 221–276, Springer, 2009.
- [7] L. De Broglie, *La mécanique ondulatoire et la structure atomique de la matière et du rayonnement*, J. Phys. Radium **8**, 225–241 (1927).
- [8] D. Bohm, *A suggested interpretation of the quantum theory in terms of "hidden" variables. I*, Phys. Rev. **85**, 166 (1952).
- [9] L. Disi, *Gravitation and quantum-mechanical localization of macro-objects*, Phys. Lett. A **105**, 199 – 202 (1984).
- [10] G. C. Ghirardi, A. Rimini, and T. Weber, *Unified dynamics for microscopic and macroscopic systems*, Phys. Rev. D **34**, 470 (1986).
- [11] L. Diósi, *Models for universal reduction of macroscopic quantum fluctuations*, Phys. Rev. A **40**, 1165 (1989).
- [12] G. C. Ghirardi, P. Pearle, and A. Rimini, *Markov processes in Hilbert space and continuous spontaneous localization of systems of identical particles*, Phys. Rev. A **42**, 78 (1990).
- [13] A. Bassi, K. Lochan, S. Satin, T. P. Singh, and H. Ulbricht, *Models of wave-function collapse, underlying theories, and experimental tests*, Rev. Mod. Phys. **85**, 471 (2013).
- [14] A. Einstein, *Über einen die Erzeugung und Verwandlung des Lichtes betreffenden heuristischen Gesichtspunkt*, Ann. Phys. **322**, 132–148 (1905).

Bibliography

- [15] C. Jönsson, *Elektroneninterferenzen an mehreren künstlich hergestellten Feinspalten*, Z. Phys. **161**, 454–474 (1961).
- [16] E. Schrödinger, *Die gegenwärtige Situation in der Quantenmechanik*, Sci. Nat. **23**, 823–828 (1935).
- [17] J. S. Bell, *On the einstein podolsky rosen paradox*, Physics Physique Fizika **1**, 195 (1964).
- [18] J. F. Clauser, M. A. Horne, A. Shimony, and R. A. Holt, *Proposed experiment to test local hidden-variable theories*, Phys. Rev. Lett. **23**, 880 (1969).
- [19] M. Arndt and K. Hornberger, *Testing the limits of quantum mechanical superpositions*, Nat. Phys. **10**, 271–277 (2014).
- [20] A. Peters, K. Y. Chung, and S. Chu, *Measurement of gravitational acceleration by dropping atoms*, Nature **400**, 849 (1999).
- [21] M. Zawisky, M. Baron, R. Loidl, and H. Rauch, *Testing the world’s largest monolithic perfect crystal neutron interferometer*, Nucl. Instrum. Methods Phys. Res. **481**, 406–413 (2002).
- [22] S. Dimopoulos, P. W. Graham, J. M. Hogan, and M. A. Kasevich, *Testing general relativity with atom interferometry*, Phys. Rev. Lett. **98**, 111102 (2007).
- [23] H. Müller, S.-w. Chiow, Q. Long, S. Herrmann, and S. Chu, *Atom interferometry with up to 24-photon-momentum-transfer beam splitters*, Phys. Rev. Lett. **100**, 180405 (2008).
- [24] S.-w. Chiow, T. Kovachy, H.-C. Chien, and M. A. Kasevich, *102 k large area atom interferometers*, Phys. Rev. Lett. **107**, 130403 (2011).
- [25] M. Arndt, O. Nairz, J. Vos-Andreae, C. Keller, G. Van der Zouw, and A. Zeilinger, *Wave-particle duality of C 60 molecules*, Nature **401**, 680 (1999).
- [26] S. Gerlich, S. Eibenberger, M. Tomandl, S. Nimmrichter, K. Hornberger, P. J. Fagan, J. Tüxen, M. Mayor, and M. Arndt, *Quantum interference of large organic molecules*, Nat. Commun. **2**, 263 (2011).
- [27] K. Hornberger, S. Gerlich, P. Haslinger, S. Nimmrichter, and M. Arndt, *Colloquium: Quantum interference of clusters and molecules*, Rev. Mod. Phys. **84**, 157 (2012).
- [28] S. Eibenberger, S. Gerlich, M. Arndt, M. Mayor, and J. Tüxen, *Matter-wave interference of particles selected from a molecular library with masses exceeding 10000 amu*, Phys. Chem. Chem. Phys. **15**, 14696–14700 (2013).
- [29] Y. Shin, M. Saba, T. Pasquini, W. Ketterle, D. Pritchard, and A. Leanhardt, *Atom interferometry with Bose-Einstein condensates in a double-well potential*, Phys. Rev. Lett. **92**, 050405 (2004).

- [30] G.-B. Jo, Y. Shin, S. Will, T. Pasquini, M. Saba, W. Ketterle, D. E. Pritchard, M. Vengalattore, and M. Prentiss, *Long phase coherence time and number squeezing of two Bose-Einstein condensates on an atom chip*, Phys. Rev. Lett. **98**, 030407 (2007).
- [31] T. Berrada, S. van Frank, R. Bücker, T. Schumm, S. J-F, and J. Schmiedmayer, *Integrated Mach-Zehnder interferometer for Bose-Einstein condensates.*, Nat. Commun. **4**, 2077 (2013).
- [32] S. van Frank, A. Negretti, T. Berrada, R. Bücker, S. Montangero, J.-F. Schaff, T. Schumm, T. Calarco, and J. Schmiedmayer, *Interferometry with non-classical motional states of a Bose-Einstein condensate*, Nat. Commun. **5**, 4009 (2014).
- [33] T. Kovachy, P. Asenbaum, C. Overstreet, C. A. Donnelly, S. M. Dickerson, A. Sugarbaker, J. M. Hogan, and M. A. Kasevich, *Quantum superposition at the half-metre scale*, Nature **528**, 530–533 (2015).
- [34] J. R. Friedman, V. Patel, W. Chen, S. Tolpygo, and J. E. Lukens, *Quantum superposition of distinct macroscopic states*, Nature **406**, 43 (2000).
- [35] C. H. van der Wal, A. C. J. ter Haar, F. K. Wilhelm, R. N. Schouten, C. J. P. M. Harmans, T. P. Orlando, S. Lloyd, and J. E. Mooij, *Quantum Superposition of Macroscopic Persistent-Current States*, Science **290**, 773–777 (2000).
- [36] R. Riedinger, A. Wallucks, I. Marinković, C. Löschnauer, M. Aspelmeyer, S. Hong, and S. Gröblacher, *Remote quantum entanglement between two micromechanical oscillators*, Nature **556**, 473 (2018).
- [37] F. Laloë, W. J. Mullin, and P. Pearle, *Heating of trapped ultracold atoms by collapse dynamics*, Phys. Rev. A **90**, 052119 (2014).
- [38] S. Nimmrichter, K. Hornberger, and K. Hammerer, *Optomechanical Sensing of Spontaneous Wave-Function Collapse*, Phys. Rev. Lett. **113**, 020405 (2014).
- [39] M. Carlesso, A. Bassi, P. Falferi, and A. Vinante, *Experimental bounds on collapse models from gravitational wave detectors*, Phys. Rev. D **94**, 124036 (2016).
- [40] J. Li, S. Zippilli, J. Zhang, and D. Vitali, *Discriminating the effects of collapse models from environmental diffusion with levitated nanospheres*, Phys. Rev. A **93**, 050102 (2016).
- [41] D. Goldwater, M. Paternostro, and P. Barker, *Testing wave-function-collapse models using parametric heating of a trapped nanosphere*, Phys. Rev. A **94**, 010104 (2016).
- [42] A. Vinante, R. Mezzena, P. Falferi, M. Carlesso, and A. Bassi, *Improved Non-interferometric Test of Collapse Models Using Ultracold Cantilevers*, Phys. Rev. Lett. **119**, 110401 (2017).

Bibliography

- [43] B. Schriniski, B. A. Stickler, and K. Hornberger, *Collapse-induced orientational localization of rigid rotors*, J. Opt. Soc. Am. **34**, C1–C7 (2017).
- [44] M. Bahrami, *Testing collapse models by a thermometer*, Phys. Rev. A **97**, 052118 (2018).
- [45] S. L. Adler and A. Vinante, *Bulk heating effects as tests for collapse models*, Phys. Rev. A **97**, 052119 (2018).
- [46] G. Björk and P. G. L. Mana, *A size criterion for macroscopic superposition states*, J. Opt. B **6**, 429 (2004).
- [47] J. I. Korsbakken, K. B. Whaley, J. Dubois, and J. I. Cirac, *Measurement-based measure of the size of macroscopic quantum superpositions*, Phys. Rev. A **75**, 042106 (2007).
- [48] F. Marquardt, B. Abel, and J. von Delft, *Measuring the size of a quantum superposition of many-body states*, Phys. Rev. A **78**, 012109 (2008).
- [49] L. C-W and H. Jeong, *Quantification of Macroscopic Quantum Superpositions within Phase Space*, Phys. Rev. Lett. **106**, 220401 (2011).
- [50] F. Fröwis and W. Dür, *Measures of macroscopicity for quantum spin systems*, New J. Phys. **14**, 093039 (2012).
- [51] S. Nimmrichter and K. Hornberger, *Macroscopicity of Mechanical Quantum Superposition States*, Phys. Rev. Lett. **110**, 160403 (2013).
- [52] B. Yadin and V. Vedral, *General framework for quantum macroscopicity in terms of coherence*, Phys. Rev. A **93**, 022122 (2016).
- [53] B. Yadin, F. C. Binder, J. Thompson, V. Narasimhachar, M. Gu, and M. S. Kim, *Operational Resource Theory of Continuous-Variable Nonclassicality*, Phys. Rev. X **8**, 041038 (2018).
- [54] F. Fröwis, P. Sekatski, W. Dür, N. Gisin, and N. Sangouard, *Macroscopic quantum states: Measures, fragility, and implementations*, Rev. Mod. Phys. **90**, 025004 (2018).
- [55] B. Schriniski, S. Nimmrichter, B. A. Stickler, and K. Hornberger, *Macroscopicity of quantum mechanical superposition tests via hypothesis falsification*, Phys. Rev. A **100**, 032111 (2019).
- [56] B. Schriniski, K. Hornberger, and S. Nimmrichter, *Sensing spontaneous collapse and decoherence with interfering Bose–Einstein condensates*, Quantum Sci. Technol. **2**, 044010 (2017).

- [57] S. Kuhn, P. Asenbaum, A. Kosloff, M. Sclafani, B. A. Stickler, S. Nimmrichter, K. Hornberger, O. Cheshnovsky, F. Patolsky, and M. Arndt, *Cavity-assisted manipulation of freely rotating silicon nanorods in high vacuum*, *Nano Lett.* **15**, 5604–5608 (2015).
- [58] T. M. Hoang, Y. Ma, J. Ahn, J. Bang, F. Robicheaux, Z.-Q. Yin, and T. Li, *Torsional optomechanics of a levitated nonspherical nanoparticle*, *Phys. Rev. Lett.* **117**, 123604 (2016).
- [59] S. Kuhn, A. Kosloff, B. A. Stickler, F. Patolsky, K. Hornberger, M. Arndt, and J. Millen, *Full rotational control of levitated silicon nanorods*, *Optica* **4**, 356–360 (2017).
- [60] S. Kuhn, B. A. Stickler, A. Kosloff, F. Patolsky, K. Hornberger, M. Arndt, and J. Millen, *Optically driven ultra-stable nanomechanical rotor*, *Nat. Commun.* **8**, 1670 (2017).
- [61] R. Reimann, M. Doderer, E. Hebestreit, R. Diehl, M. Frimmer, D. Windey, F. Tebbenjohanns, and L. Novotny, *GHz rotation of an optically trapped nanoparticle in vacuum*, *Phys. Rev. Lett.* **121**, 033602 (2018).
- [62] J. Ahn, Z. Xu, J. Bang, Y.-H. Deng, T. M. Hoang, Q. Han, R.-M. Ma, and T. Li, *Optically levitated nanodumbbell torsion balance and GHz nanomechanical rotor*, *Phys. Rev. Lett.* **121**, 033603 (2018).
- [63] B. A. Stickler, S. Nimmrichter, L. Martinetz, S. Kuhn, M. Arndt, and K. Hornberger, *Rotational cavity cooling of dielectric rods and disks*, *Phys. Rev. A* **94**, 033818 (2016).
- [64] C. Zhong and F. Robicheaux, *Shot-noise-dominant regime for ellipsoidal nanoparticles in a linearly polarized beam*, *Phys. Rev. A* **95**, 053421 (2017).
- [65] B. A. Stickler, B. Papendell, S. Kuhn, B. Schriniski, J. Millen, M. Arndt, and K. Hornberger, *Probing macroscopic quantum superpositions with nanorotors*, *New J. Phys.* **20**, 122001 (2018).
- [66] B. A. Stickler, B. Schriniski, and K. Hornberger, *Rotational friction and diffusion of quantum rotors*, *Phys. Rev. Lett.* **121**, 040401 (2018).
- [67] A. J. Leggett, *Testing the limits of quantum mechanics: motivation, state of play, prospects*, *J. Phys. Condens. Matter* **14**, R415 (2002).
- [68] D. Petz and C. Ghinea, *Introduction to quantum Fisher information*, in *Quantum probability and related topics*, pages 261–281, World Scientific, 2011.
- [69] S. Nimmrichter, *Macroscopic matter wave interferometry*, Springer, 2014.
- [70] G. Lindblad, *On the generators of quantum dynamical semigroups*, *Commun. Math. Phys.* **48**, 119–130 (1976).

Bibliography

- [71] A. S. Holevo, *A note on covariant dynamical semigroups*, Rep. Math. Phys. **32**, 211–216 (1993).
- [72] A. S. Holevo, *On conservativity of covariant dynamical semigroups*, Rep. Math. Phys. **33**, 95–110 (1993).
- [73] A. Bassi, K. Lochan, S. Satin, T. P. Singh, and H. Ulbricht, *Models of wave-function collapse, underlying theories, and experimental tests*, Rev. Mod. Phys. **85**, 471–527 (2013).
- [74] C. Curceanu, B. C. Hiesmayr, and K. Piscicchia, *X-rays help to unfuzzy the concept of measurement*, Adv. Phys. **4**, 263–266 (2015).
- [75] M. Bilardello, S. Donadi, A. Vinante, and A. Bassi, *Bounds on collapse models from cold-atom experiments*, Phys. A **462**, 764–782 (2016).
- [76] S. L. Adler, *Lower and upper bounds on CSL parameters from latent image formation and IGM heating*, J. Phys. A **40**, 2935 (2007).
- [77] H.-P. Breuer, F. Petruccione, et al., *The theory of open quantum systems*, Oxford University Press on Demand, 2002.
- [78] W. Von der Linden, V. Dose, and U. Von Toussaint, *Bayesian probability theory: applications in the physical sciences*, Cambridge University Press, 2014.
- [79] J. K. Ghosh and R. Ramamoorthi, *Bayesian Nonparametrics*, Springer Series in Statistics **16** (2003).
- [80] L. Schwartz, *On bayes procedures*, Probab. Theory Relat. Fields **4**, 10–26 (1965).
- [81] A. W. Vaart and J. A. Wellner, *Weak convergence and empirical processes: with applications to statistics*, Springer, 1996.
- [82] L. Le Cam and G. L. Yang, *Asymptotics in statistics: some basic concepts*, Springer Science & Business Media, 2012.
- [83] W. H. Press, S. A. Teukolsky, W. T. Vetterling, and B. P. Flannery, *Numerical recipes 3rd edition: The art of scientific computing*, Cambridge university press, 2007.
- [84] H. Jeffreys, *The theory of probability*, OUP Oxford, 1998.
- [85] S. Kullback and R. A. Leibler, *On information and sufficiency*, Ann. Math. Stat. **22**, 79–86 (1951).
- [86] J. M. Bernardo, *Reference posterior distributions for Bayesian inference*, J. Royal Stat. Soc. B , 113–147 (1979).
- [87] M. Ghosh et al., *Objective priors: An introduction for frequentists*, Stat. Sci. **26**, 187–202 (2011).

- [88] R. A. Fisher, *Statistical methods and Scientific Inference*, Oxford: Oxford University Press, 1990.
- [89] Y. Fein and S. Gerlich, *private communication*.
- [90] K. Hornberger, S. Gerlich, H. Ulbricht, L. Hackermüller, S. Nimmrichter, I. V. Goldt, O. Boltalina, and M. Arndt, *Theory and experimental verification of Kapitza–Dirac–Talbot–Lau interferometry*, New J. Phys. **11**, 043032 (2009).
- [91] K. Walter, *Coherence and Decoherence in High-mass Matter-wave Interferometry*, Doctoral thesis, 2016.
- [92] K. Hornberger, S. Uttenthaler, B. Brezger, L. Hackermüller, M. Arndt, and A. Zeilinger, *Collisional decoherence observed in matter wave interferometry*, Phys. Rev. Lett. **90**, 160401 (2003).
- [93] K. Hornberger and J. E. Sipe, *Collisional decoherence reexamined*, Phys. Rev. A **68**, 012105 (2003).
- [94] D. M. Stamper-Kurn, G. E. Marti, and H. Müller, *Verifying quantum superpositions at metre scales*, Nature **537**, E1 (2016).
- [95] T. Kovachy, P. Asenbaum, C. Overstreet, C. Donnelly, S. Dickerson, A. Sugarbaker, J. Hogan, and M. Kasevich, *Kovachy et al. reply*, Nature **537**, E2 (2016).
- [96] Bose, *Plancks Gesetz und Lichtquantenhypothese*, Z. Phys. **26**, 178–181 (1924).
- [97] A. Einstein, *Quantentheorie des einatomigen idealen Gases*, SB Preuss. Akad. Wiss. phys.-math. Klasse (1924).
- [98] M. H. Anderson, J. R. Ensher, M. R. Matthews, C. E. Wieman, and E. A. Cornell, *Observation of Bose-Einstein condensation in a dilute atomic vapor*, Science **269**, 198–201 (1995).
- [99] K. B. Davis, M.-O. Mewes, M. R. Andrews, N. J. van Druten, D. S. Durfee, D. Kurn, and W. Ketterle, *Bose-Einstein condensation in a gas of sodium atoms*, Phys. Rev. Lett. **75**, 3969 (1995).
- [100] F. Laloë and W. J. Mullin, *Quantum Properties of a Single Beam Splitter*, Found. Phys. **42**, 53–67 (2012).
- [101] M. Naraschewski, H. Wallis, A. Schenzle, J. Cirac, and P. Zoller, *Interference of Bose condensates*, Phys. Rev. A **54**, 2185 (1996).
- [102] E. P. Gross, *Structure of a quantized vortex in boson systems*, Il Nuovo Cimento (1955-1965) **20**, 454–477 (1961).
- [103] L. Pitaevskii, *Vortex lines in an imperfect Bose gas*, Sov. Phys. JETP **13**, 451–454 (1961).

Bibliography

- [104] J. Javanainen and M. Wilkens, *Phase and Phase Diffusion of a Split Bose-Einstein Condensate*, Phys. Rev. Lett. **78**, 4675–4678 (1997).
- [105] C. J. Bordé, *Atomic clocks and inertial sensors*, Metrologia **39**, 435 (2002).
- [106] A. Sørensen, L.-M. Duan, J. Cirac, and P. Zoller, *Many-particle entanglement with Bose-Einstein condensates*, Nature **409**, 63 (2001).
- [107] A. S. Sørensen and K. Mølmer, *Entanglement and Extreme Spin Squeezing*, Phys. Rev. Lett. **86**, 4431–4434 (2001).
- [108] B. Lücke, J. Peise, G. Vitagliano, J. Arlt, S. Lu, G. Tóth, and C. Klempt, *Detecting Multiparticle Entanglement of Dicke States*, Phys. Rev. Lett. **112**, 155304 (2014).
- [109] B. Schriniski, *Makroskopizität von Quantenexperimenten mit Bose-Einstein-Kondensaten*, Master thesis, 2015.
- [110] F. T. Arecchi, E. Courtens, R. Gilmore, and H. Thomas, *Atomic Coherent States in Quantum Optics*, Phys. Rev. A **6**, 2211–2237 (1972).
- [111] R. J. Glauber, *Coherent and incoherent states of the radiation field*, Phys. Rev. **131**, 2766 (1963).
- [112] M. Kitagawa and M. Ueda, *Squeezed spin states*, Phys. Rev. A **47**, 5138–5143 (1993).
- [113] J. Ma, X. Wang, C. P. Sun, and F. Nori, *Quantum spin squeezing*, Phys. Rep. **509**, 89–165 (2011).
- [114] G. Tóth, *Multipartite entanglement and high-precision metrology*, Phys. Rev. A **85**, 022322 (2012).
- [115] G. Tóth and I. Apellaniz, *Quantum metrology from a quantum information science perspective*, J. Phys. A **47**, 424006 (2014).
- [116] O. Hosten, R. Krishnakumar, N. Engelsens, and M. Kasevich, *Quantum phase magnification*, Science **352**, 1552–1555 (2016).
- [117] X. Wang, A. Miranowicz, Y.-x. Liu, C. Sun, and F. Nori, *Sudden vanishing of spin squeezing under decoherence*, Phys. Rev. A **81**, 022106 (2010).
- [118] G. Tóth, C. Knapp, O. Gühne, and H. J. Briegel, *Spin squeezing and entanglement*, Phys. Rev. A **79**, 042334 (2009).
- [119] A. J. Leggett and A. Garg, *Quantum mechanics versus macroscopic realism: Is the flux there when nobody looks?*, Phys. Rev. Lett. **54**, 857 (1985).
- [120] C. Emary, N. Lambert, and F. Nori, *Leggett-garg inequalities*, Rep. Prog. Phys. **77**, 016001 (2013).

- [121] S. E. Venegas-Andraca, *Quantum walks: a comprehensive review*, Quantum Inf. Process. **11**, 1015–1106 (2012).
- [122] C. Robens, W. Alt, D. Meschede, C. Emary, and A. Alberti, *Ideal Negative Measurements in Quantum Walks Disprove Theories Based on Classical Trajectories*, Phys. Rev. X **5**, 011003 (2015).
- [123] A. L. Fetter and J. D. Walecka, *Theoretical mechanics of particles and continua*, Courier Corporation, 2003.
- [124] B. Farid and R. W. Godby, *Cohesive energies of crystals*, Phys. Rev. B **43**, 14248–14250 (1991).
- [125] K. Børkje, A. Nunnenkamp, and S. Girvin, *Proposal for entangling remote micromechanical oscillators via optical measurements*, Phys. Rev. Lett. **107**, 123601 (2011).
- [126] M. D. Poulsen, E. Peronne, H. Stapelfeldt, C. Z. Bisgaard, S. S. Viftrup, E. Hamilton, and T. Seideman, *Nonadiabatic alignment of asymmetric top molecules: Rotational revivals*, J. Chem. Phys. **121**, 783–791 (2004).
- [127] B. Shepperson, A. A. Søndergaard, L. Christiansen, J. Kaczmarczyk, R. E. Zillich, M. Lemeshko, and H. Stapelfeldt, *Laser-induced rotation of iodine molecules in helium nanodroplets: revivals and breaking free*, Phys. Rev. Lett. **118**, 203203 (2017).
- [128] E. F. Thomas, A. A. Søndergaard, B. Shepperson, N. E. Henriksen, and H. Stapelfeldt, *Hyperfine-Structure-Induced Depolarization of Impulsively Aligned I₂ Molecules*, Phys. Rev. Lett. **120**, 163202 (2018).
- [129] T. Fischer, *Decoherence of the orientation state*, Doctoral Thesis, 2014.
- [130] B. A. Stickler, B. Papendell, and K. Hornberger, *Spatio-orientational decoherence of nanoparticles*, Phys. Rev. A **94**, 033828 (2016).
- [131] C. Zhong and F. Robicheaux, *Decoherence of rotational degrees of freedom*, Phys. Rev. A **94**, 052109 (2016).
- [132] B. Papendell, B. A. Stickler, and K. Hornberger, *Quantum angular momentum diffusion of rigid bodies*, New J. Phys. **19**, 122001 (2017).
- [133] A. O. Caldeira and A. J. Leggett, *Path integral approach to quantum Brownian motion*, Phys. A **121**, 587–616 (1983).
- [134] K. Hornberger and B. Vacchini, *Monitoring derivation of the quantum linear Boltzmann equation*, Phys. Rev. A **77**, 022112 (2008).
- [135] B. Vacchini and K. Hornberger, *Quantum linear Boltzmann equation*, Phys. Rep. **478**, 71–120 (2009).

Bibliography

- [136] T. Fischer, C. Gneiting, and K. Hornberger, *Wigner function for the orientation state*, New J. Phys. **15**, 063004 (2013).
- [137] L. Martinetz, K. Hornberger, and B. A. Stickler, *Gas-induced friction and diffusion of rigid rotors*, Phys. Rev. E **97**, 052112 (2018).
- [138] S. Nimmrichter, K. Hornberger, and K. Hammerer, *Optomechanical sensing of spontaneous wave-function collapse*, Phys. Rev. Lett. **113**, 020405 (2014).
- [139] J. P. Bizarro, *Weyl-Wigner formalism for rotation-angle and angular-momentum variables in quantum mechanics*, Phys. Rev. A **49**, 3255 (1994).
- [140] J. Bateman, S. Nimmrichter, K. Hornberger, and H. Ulbricht, *Near-field interferometry of a free-falling nanoparticle from a point-like source*, Nat. Commun. **5**, 4788 (2014).
- [141] S. Bera, B. Motwani, T. P. Singh, and H. Ulbricht, *A proposal for the experimental detection of CSL induced random walk*, Sci. Rep. **5**, 7664 (2015).
- [142] J. Jeknić-Dugić, I. Petrović, M. Arsenijević, and M. Dugić, *Dynamical stability of the one-dimensional rigid Brownian rotator: The role of the rotators spatial size and shape*, J. Phys. Condens. Matter **30**, 195304 (2018).
- [143] M. Jaffe, P. Haslinger, V. Xu, P. Hamilton, A. Upadhye, B. Elder, J. Khoury, and H. Müller, *Testing sub-gravitational forces on atoms from a miniature in-vacuum source mass*, Nat. Phys. **13**, 938 (2017).